Karlsruher Institut für Technologie

UNSAM
UNIVERSIDAD
NACIONAL DE
SAN MARTÍN

Hybrid Universality Model Development and Air Shower Reconstruction for the Pierre Auger Observatory

Zur Erlangung des akademischen Grades eines

Doktors der Naturwissenschaften

an der Fakultät für Physik des
Karlsruher Instituts für Technologie (KIT)
und
das Institut für Technologie "Prof. Jorge A. Sábato" der
Nationalen Universität von San Martín (UNSAM)

vorgelegte

Dissertation

von

MSc. Johannes Hulsman
aus Leiden, Niederlanden

Tag der mündlichen Prüfung: 20-Dezember-2019

Referent: Prof. Dr. Alberto Daniel Supanitsky

Korreferent: Prof. Dr. Dr. h.c. Johannes Blümer

Betreuer: Dr. M. A. Roth

Karlsruher Institut für Technologie

UNSAM
UNIVERSIDAD
NACIONAL DE
SAN MARTÍN

Hybrid Universality Model Development and Air Shower Reconstruction for the Pierre Auger Observatory

Tesis presentada para optar por el título de

Doctor en Ciencias Naturales

del Instituto de Tecnología "Prof. Jorge A. Sábato" de la
Universidad Nacional de San Martín (UNSAM)
y de
Instituto de Tecnología de Karlsruhe (KIT)

por

MSc. Johannes Hulsman
de Leiden, los Países Bajos

Día del examen: 20-Diciembre-2019

Director: Prof. Dr. Alberto Daniel Supanitsky

Co-Director: Prof. Dr. Dr. h.c. Johannes Blümer

Colaborador: Dr. M. A. Roth

Karlsruher Institut für Technologie

UNSAM
UNIVERSIDAD
NACIONAL DE
SAN MARTÍN

Hybrid Universality Model Development and Air Shower Reconstruction for the Pierre Auger Observatory

For the attainment of the academic degree of

Doctorate in Science

at the Faculty of Physics at
Karlsruhe Institute of Technology (KIT)
and
Institute of Technology "Prof. Jorge A. Sábato" at
National University of San Martín (UNSAM)

the submitted

Dissertation

of

MSc. Johannes Hulsman
of Leiden, Netherlands

Day of the oral examination: 20-December-2019

Referee: Prof. Dr. Alberto Daniel Supanitsky

Co-referee: Prof. Dr. Dr. h.c. Johannes Blümer

Advisor: Dr. M. A. Roth

Abstract

Cosmic rays have been studied for more than 100 years, providing valuable information on the measured spectrum and theories to particle propagation and interaction. Potential sources, which could also serve possible acceleration mechanisms, include active galactic nuclei, gamma-ray bursts and supernova shock fronts. Due to our increased understanding of cosmic ray physics and technological improvements on a detector level, measurements have progressed towards even higher energies than before. To understand their origin, it is pertinent to understand their mass composition, energy spectrum and arrival direction. Laboratory-based particle accelerators and low energy cosmic ray experiments have elucidated our understanding of particle interaction, providing insight on possible acceleration and propagation models. However, ultra-high cosmic rays at 10^{20} eV are significantly above the highest energies achievable by the Large Hadron Collider (LHC) (about two orders of magnitude between the center-of-mass energies). They are also very rare; with an incident flux of 1 particle per km^2 per century at 10^{20} eV. Accelerator-based models can be extrapolated to the highest energies. However, it is pertinent for large-scale detectors to be able to measure unique properties of cosmic rays interacting with the detection medium.

The Pierre Auger Observatory (Auger) is the largest cosmic ray detector to date, covering an area of more than 3000 km^2. It utilizes surface, underground and fluorescence techniques to measure the macroscopic properties of extensive air showers (initiated by a cosmic ray particle interacting with a nucleus in the atmosphere). Through the fluorescence technique the longitudinal profile can be directly observed. From its maximum, X_{max}, the cosmic ray mass can be inferred. However, due to specific operational conditions it has a duty cycle of $\approx 15\%$, limiting the statistics of more energetic events. The surface and underground detectors can measure data with a duty cycle of $\approx 100\%$. Most surface detectors are distributed in a triangular grid with a spacing of 1500 m. A small fraction is distributed in an infilled grid with a spacing of 750 m. Furthermore, each surface detector in the filled grid is paired with an underground detector. Their combined information provides another mass composition sensitive parameter -the muon content. Air shower universality capitalizes on the universal shape of the longitudinal profile, irrespective of primary or hadronic model. It encapsulates the underlying shower physics and allows for a reconstruction based on mass-composition sensitive shower parameters (the shower maximum X_{max}, maximum of muon production depth X^{μ}_{max} and relative muon content R_{μ}) seen through unique features in the time and signal distributions. The universality approach allows for a highly modular reconstruction algorithm, set as a function of primary energy, mass and geometry.

The major focus of this work was the development of the a new signal and time model for secondary particles at ground seen by the Water Cherenkov Detector (WCD) and Muon Detector (MD), as well as dedicated efforts to effectively process large quantities of simulated air showers. Reconstructed air shower simulations were studied and compared for contemporary high energy hadronic interaction models. In this work, I show how I could successfully model the signal in the detector corresponding to air showers between 10^{17} eV and 10^{20} eV with uncertainties below the 5% level. The temporal distribution is also successfully modelled, mostly within the 3% level. A novelty, the maximum muon production depth, X^{μ}_{max}, has been successfully introduced into the MD universality models. With the newly obtained WCD and MD, I could prove that the muon content, R_{μ}, is a global shower variable. Furthermore, first analysis was performed on hybrid reconstructions for the infilled detector setup. Preliminary resolutions of the shower parameters X_{max} and X^{μ}_{max} are of the order 40 gcm^{-2} and 50 gcm^{-2} respectively, which can be further enhanced. Also, the quality of R_{μ} has greatly improved, with an uncertainty of only 10%. This work sets an important basis for future analyses (mass composition and shower physics) with data from the WCD and MD. Results obtained in this work could also be used for new detector systems, such as the Scintillator Surface Detector (SSD) (part of the AugerPrime upgrade).

Zusammenfassung

Kosmische Strahlungen werden seit mehr als 100 Jahren untersucht und haben seitdem viel über deren gemessenes Energiespektrum, Teilchenausbreitung und -interaktion informiert. Beispiele für potenzielle Quellen, die möglicherweise auch als Beschleunigungsmechanismen eine Rolle spielen könnten, sind aktive galaktische Kerne, Gammastrahlungausbrüche und Supernova-Schockfronten. Aufgrund unser verbessertes Verständnis in der Physik der kosmischen Strahlung und technologische Detektorverbesserungen, werden stets mehr Messungen von hochenergetischen kosmische Teilchen ausgeführt. Zum Nachweisen deren Ursprungs ist das Verständnis von ihrer Massenzusammensetzung, Energiespektrum und Ankunftsrichtung essentiell. Laborteilchenbeschleuniger und niederenergetische Experimente von kosmische Strahlungen haben unser Verständnis von Teilcheninteraktionen verbessert und bieten Einsicht zu mögliche Beschleunigungs- und Propagationsmodelle. Jedoch sind ultrahochenergetische kosmischen Strahlungen von 10^{20} eV deutlich höher als die, die am LHC erreicht werden (etwa zwei Größenordnungen zwischen den Massenschwerpunktenergien). Dazu sind diese auch sehr selten; mit einen Teilchenfluss von nur 1 Partikel pro km^2 pro Jahrhundert. Obwohl hadronische Interaktionsmodelle, abgeleitet von Beschleunigerdaten, bis zu den höchsten Energien extrapoliert werden können, ist es für großflächige Detektoren wichtig einzigartige Eigenschaften kosmischer Strahlungen, die mit dem Detektionsmedium interagieren, zu messen.

Das Pierre Auger Observatorium (Auger) ist bisher das größte Detektor zur Messung von kosmische Strahlungen und umfasst eine Fläche von mehr als 3000 km^2. Es verwendet Oberflächen-, Untergrund- und Fluoreszenztechniken, um die makroskopischen Eigenschaften von ausgedehnten Luftschauern zu messen (initiiert durch ein kosmisches Strahlungsteilchen, das mit einem Kern in der Atmosphäre interagiert). Durch die Fluoreszenztechnik kann das longitudinale Profil direkt beobachtet werden. Mit dessen Maximum, $X_{\max}$, kann die Masse der kosmischen Strahlung abgeleitet werden. Aufgrund spezifischer Betriebsbedingungen hat es jedoch eine Betriebsdauer von 15%, was die Statistik hochenergetischer Ereignisse einschränkt. Die Oberflächen- und Untergrunddetektoren können Daten mit einer Betriebsdauer von 100% messen. Die Meisten sind in einem dreieckigen Raster mit einem Abstand von 1500 mm verteilt, wovon ein kleiner Teil in einem ausgefüllten Array mit einen Abstand von 750 mm verteilt ist. Dabei ist jedes Oberflächendetektor (im ausgefüllten Array) mit einem Untergrunddetektor gekoppelt. Die kombinierte Informationen liefert einen weiteren massenkompositionssensitiven Parameter; das Myongehalt. Luftschaueruniversalität nutzt die universelle Form des longitudinalen Profils aus, was unabhängig vom Primärteilchen oder Hadronmodell ist. Es berücksichtigt die grundeliegende Schauerphysik

und ermöglicht eine Rekonstruktion basierend auf massenkompositionssensitiven Schauerparametern; das Luftschauermaximum $X_{\max}$, das Maximum der Myonenproduktionstiefe $X^{\mu}_{\max}$ und das relative Myongehalt R_{μ}). Diese sieht erkennt durch einzigartige Merkmale in der Zeit- und Signalverteilung. Der Universalitätsansatz ermöglicht einen hochmodularen Rekonstruktionsalgorithmus, was nur von der Primärenergie, Masse und Geometrie abhängig ist.

Der Schwerpunkt dieser Arbeit liegt auf der Entwicklung eines neuen Signal- und Zeitmodells für Sekundärpartikel am Boden, die von den WCDs und MDs gesehen werden, sowie zweckbestimmte Bemühungen zur effektiven Verarbeitung großer Mengen simulierter Luftschauer. Rekonstruierte Schauersimulationen werden untersucht und mit den neusten hochenergetischen hadronischen Interaktionsmodellen verglichen. In dieser Arbeit zeige ich, wie ich Luftschauer zwischen 10^{17} eV und 10^{20} eV mit Unsicherheiten unter 5% erfolgreich modellieren konnte. Die Zeiterteilung wird ebenfalls erfolgreich modelliert, meistens mit Unisicherheiten unter 3%. Eine Novum, die Myon-Produktionstiefe, $X^{\mu}_{\max}$, wurde erfolgreich zu den MD-Universalitätsmodelle integriert. Mit den neuen WCD und MD Modellen konnte ich beweisen, dass der Myongehalt, R_{μ}, eine globale Luftschauervariable ist. Darüber hinaus wurden erste Hybridrekonstruktionsanalysen für den ausgefüllten Detektoraufbau durchgeführt. Die Auflösungen der Luftschauerparameter $X_{\max}$ und $X^{\mu}_{\max}$ sind in Größenordnung von beziehungsweise ≈ 40 gcm^{-2} und ≈ 50 gcm^{-2}. Auch die Qualität von R_{μ} hat sich stark verbessert, mit einer Unsicherheit von nur 10%. Diese Arbeit bildet eine wichtige Grundlage für zukünftige Analysen (Massenzusammensetzung und Luftschauerphysik) mit WCD- und MD-Daten. Die in dieser Arbeit erzielten Ergebnisse könnten auch für neue Detektorsysteme wie das SSD verwendet werden (Teil des AugerPrime Upgrades).

Resumen

Los estudios de rayos cósmicos desarrollados durante más de 100 años han proporcionando información valiosa sobre el espectro de energías y sobre las teorías de propagación e interacción de partículas. Entre las potenciales fuentes, que también proveerían los mecanismos de aceleración, se encuentran núcleos activos galácticos, destellos de rayos gamma y frentes de choque producidos por supernovas. Debido a nuestra mejor comprensión de la física de rayos cósmicos y a las mejoras tecnológicas de los detectores, las máximas energías medibles se han incrementado. Para entender el origen de los rayos cósmicos necesitamos conocer su composición, espectro de energía y direcciones de arribo. Los aceleradores de partículas y los experimentos de rayos cósmicos de baja energía han contribuido al esclarecimiento de nuestro conocimiento sobre la interacción de partículas, proporcionando información sobre posibles modelos de aceleración y propagación. Sin embargo, los rayos cósmicos de ultra alta energía, de 10^{20} eV, están significativamente por encima de las energías más altas alcanzables por el LHC (aproximadamente dos órdenes de magnitud en el sistema centro de masa). Además, son muy poco frecuentes; el flujo incidente es de 1 partícula por km^2 por siglo a 10^{20} eV. Los modelos basados en aceleradores pueden extrapolarse a altas energías. Sin embargo, es pertinente que los detectores a gran escala puedan medir las propiedades únicas de los rayos cósmicos que interactúan con el medio de detección.

El Observatorio Pierre Auger es el detector de rayos cósmicos más grande hasta la fecha, cubriendo un área de más de 3000 km^2. Utiliza detectores de superficie, subterráneos y de fluorescencia para medir las propiedades macroscópicas de las lluvias de partículas (iniciadas por un rayo cósmico que interactúa con un núcleo de la atmósfera). Mediante la técnica de fluorescencia se puede observar directamente el perfil longitudinal. De su máximo, $X_{textmax}$, se puede inferir la masa de los rayos cósmicos. Sin embargo, debido a las condiciones operativas específicas, tiene un ciclo de trabajo del $\approx$ 15%, lo que limita la estadística de los eventos de más alta energía. Los detectores de superficie y subterráneos pueden tomar datos con un ciclo de trabajo del 100%. La mayoría de los detectores de superficie están distribuidos en una arreglo triangular con un espaciado de 1500 m. Una pequeña fracción se distribuye en un arreglo más denso con una separación entre detectores de 750 m. Además, cada detector de superficie en el arreglo se empareja con un detector subterráneo. Su información combinada proporciona otro parámetro sensible a la composición: el contenido de muones de las lluvias. La universalidad de las lluvias atmosféricas aprovecha la forma universal del perfil longitudinal, independiente del primario o modelo hadrónico. Encierra la física de la lluvia subyacente y permite una reconstrucción basada en parámetros de la lluvia sensibles a la composición (el máximo de la lluvia $X_{textmax}$, la profundidad del máximo de producción

de muones X^{μ} y el contenido relativo de muones R_{μ}) visto a través de características únicas en las distribuciones de tiempo y señal. El enfoque de universalidad permite un algoritmo de reconstrucción altamente modular, como función de la energía del primario, su masa y la geometría.

El enfoque principal de este trabajo fue el desarrollo de un nuevo modelo de señal y de distribución evolución temporal para las partículas secundarias que llegan a la superficie terrestre y que son detectadas por los WCD y MD, así como los esfuerzos dedicados a procesar efectivamente grandes cantidades de lluvias simuladas. Se estudiaron simulaciones de lluvias reconstruidas y se compararon con modelos contemporáneos de interacciones hadrónicas de alta energía. En este trabajo, muestro cómo es posible modelar la señal en las lluvias entre 10^{17} eV y 10^{20} eV con incertidumbres por debajo del 5%. La distribución temporal también se modela con éxito, mayormente dentro del 3%. Como innovación, la profundidad atmosférica del máximo de producción de muones, X^{μ}_{max}, se ha incorporado con éxito a los modelos de universalidad de MD. Desarrollando un modelo para los respectivos detectores, se pudo probar que el contenido de muones, R_{μ}, es una variable global de la lluvia. Además, se realizó un primer análisis de la reconstrucción de eventos híbridos para la configuración de detectores en el arreglo más denso. Las resoluciones de los parámetros de la lluvia X_{max} y X^{mu}_{max} son del orden de 40 gcm^{-2} y 50 gcm^{-2}, respectivamente. Además, la calidad de R_{μ} reconstruido ha sido mejorada, alcanzando una incertidumbre de sólo 10%. Este trabajo establece una base importante para futuros análisis (de composición y física de las lluvias) con datos del WCD y MD. Los resultados obtenidos en este trabajo también podrían ser utilizados para nuevos sistemas de detección, como el SSD (parte de la actualización de AugerPrime).

Acronyms

This is a list of acronyms used within this work sorted alphabetically according to the short version.

AERA	Auger Engineering Radio Array
AMIGA	Auger Muon Detectors for the Infill Ground Array
Auger	Pierre Auger Observatory
CDAS	Central Data Acquisition System
CLF	Central Laser Facility
CMB	Cosmic Microwave Background
EAS	extensive air shower
FADC	flash analog to digital converter
FD	Fluorescence Detector
GDAS	Global Data Assimilation System
HEAT	High Elevation Auger Telescopes
LDF	lateral distribution function
LHC	Large Hadron Collider
MD	Muon Detector
PMT	Photo-Multiplier Tube
RD	Radio Detector
SSD	Scintillator Surface Detector
UHECR	ultra-high energy cosmic ray
VEM	vertical-equivalent muon
WCD	Water Cherenkov Detector

Contents

CHAPTER 1

Introduction

1.1 History of Cosmic Rays

In 1912, Victor Hess discovered an increase of "particle radiation" by looking at the discharge rate of particles within an electrometer in a balloon flight at 5300 m. He found that the discharge rate was fourfold compared to the ground and thus concluded that part of the radiation is of cosmic origin [1]. Robert Millikan referred to these particles as "cosmic rays" (CR) and believed those to be photons with his experiment. However, Jacob Clay showed while sailing from Indonesia to the Netherlands that the cosmic ray intensity varied with latitude, indicating that cosmic rays are deflected by earth's magnetic field [2]. In other words, cosmic ray particles are predominantly charged particles. Further studies revealed that the primary composition is dominated by protons.

Initially, cosmic rays were the only source of studying high energy particles. They therefore contributed in the early stages of particle physics theory. While Victor Hess proved the existence of cosmic rays, he did not measure these particles directly. He actually measured the secondary particles of cosmic ray interactions with the atmosphere. Pioneering work in 1929 by Skobelzyn showed that cloud chambers could be used to track these high energy particles directly. As a result, the positron (by Anderson), the e^+e^- pair production (by Blackett and Occhialini) and muon (Neddermeyer and Anderson) could be discovered [3].

In 1938, W. Kolhoster discovered coincidence signals of Geiger-Müller tubes seperated by 75 m. He concluded that the particles in the tubes are secondaries from cosmic rays interacting with the atmosphere. Similarly, P. Auger studied the coincidence of particles with Wilson chambers and Geiger-Müller tubes with a larger separation at an altitude of 3500m and concluded that these particles are secondaries generated in the atmosphere from a *single* primary comsic ray [4, 5]. This confirmed the existence of cosmic ray *air showers*. In 1954, Walter Heitler developed a theoretical description of an extensive air shower [6, 7], later discussed in section 1.4.

To improve CR studies, large detector arrays were built since the mid 1940s. Improvements in the development of photo-multipliers shifted the use of Geiger-Müller tubes towards scintillator and Cherenkov detectors. In the 1960s, the largest CR detector setup was the array of the MIT group at Volcano Ranch (New Mexico). It consisted of 20 scintillation detectors, covering 12 km^2, recording the first event at 10^{20} eV [8]. Around the the same time,

in 1966, Kenneth Greisen, Vadim Kuzim and Georgiy Zatsepin theorized an upper-limit of the particle energy from distant sources, resulting in a flux suppression. This is known as the *Greisen-Zatsepin-Kuzmin* (GZK) cut-off, predicting that ultra-high energy cosmic ray (UHECR) would interact with the Cosmic Microwave Background (CMB) (rediscovered in 1964) and lose a significant fraction of their energy over long distances. Protons would lose their energy through pion production, whereas heavier nuclei lose energy through photo-disintegration. Using protons, it was found that for energies above $5 * 10^{19}$ eV particles could experience these interactions, resulting in a flux suppression of the tail of the energy spectrum. UHECRs, in the suppression region, arriving to Earth must therefore originate within $\approx 100\,\mathrm{Mpc}$ [9, 10].

The rarity of ultra high energy events motivated the construction of bigger detector setups, such as Haverah Park (12 km^2) [11], Yakutsk (10 km^2) [12] and *Akeno Giant Air Shower Array* (AGASA) (100 km^2) [13]. The *High Resolution Fly's Eye* (HiRes) provided first evidence of the flux suppression with its fluorescence detectors [14, 15]. However, this could not be confirmed by AGASA [16]. More recent experiments include the Auger (3000 km^2) [17] and Telescope Array (900 km^2) [18]. After more than 15 years of data collection, the existence of the flux suppression could be confirmed. However, no conclusive result was found as to whether it is due to the GZK effect or an exhaustion of strong acceleration sources.

The introduction of high energy collider detectors provided a more controlled environment and thus paved the way for more discoveries than cosmic ray itself could provide (wrt. particle discoveries and interactions). As a result, the cosmic ray and particle physics communities focus on different aspects. Particle physicists study and describe the particle interactions whereas the cosmic ray physicists would provide new insight to particle properties and interactions [3]. Their respective studies therefore depend on each other; especially beyond collider physics energies. In addition to its contribution to particle physics, cosmic ray particles play the role as messenger particles. Their charge, composition, arrival direction and energy provide insight to several key questions towards the understanding the universe. Where do they come from? How do they propagate/accelerate? How are they produced?

1.2 Energy Spectrum

The cosmic ray flux decreases with increasing energies. Their energies range from 10^9 eV to the highest measured at a few 10^{20} eV. At 10^9 eV, as much as 1000 particles (on average) arrive each second per m^2, whereas at 10^{18} eV, only one particle arrives each km^2 per year (per century at 10^{20} eV). The flux is maximal at 20 GeV below which particles are suppressed by the heliospheric magnetic field from the solar wind [19], i.e. they are deflected before arriving to the Earth's atmosphere.

For higher energies, the particle flux can be described by a power law of the form:

$$\frac{dN}{dE\, d\Omega\, dA\, dt} \propto E^{-\gamma}, \tag{1.1}$$

where N is the number of particles with their respective energy E, solid angle Ω, area A and time t. The spectral index γ changes at different energies, yielding spectral features such as the steepening of the first knee, the second knee, an ankle and the suppression at the highest energies. These features can be seen in figure 1.1.

On average the spectral index of the spectrum is about $\gamma \approx 3$. At the knee, at 3-5×10^{15} eV, the spectral index changes from $\gamma = 2.7$ to $\gamma = 3.1$. As the KASCADE experiment showed

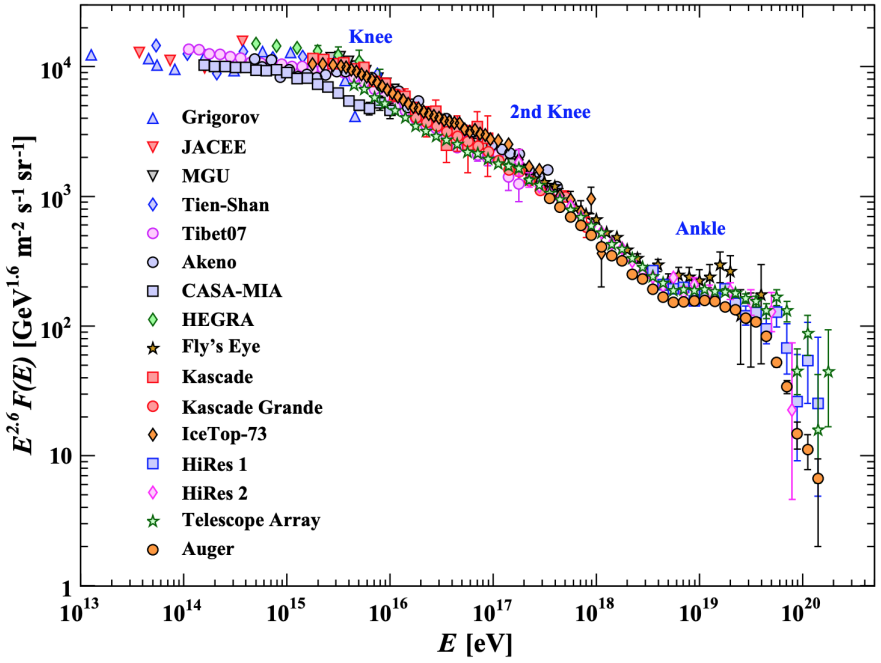

Figure 1.1: Cosmic Ray energy spectrum measured by various experiments. The flux has ben scale by $E^{2.6}$ to emphasize the spectral features such as the knee, ankle and cut-off [20].

in reference [21], the steepening of the spectrum originates from the decline of light cosmic ray (Z<6), transitioning towards heavier nuclei. However, at $(8.3 \pm 0.8) \times 10^{16}$ eV, the spectral index increases to $\gamma = 3.24$. A second knee was also found around 3×10^{17} eV with a similar spectral index of $\gamma = 3.2$ [22]. Accounting for all systematic uncertainties, these two features are unlikely, however not excluded, to coincide. A flattening of the spectrum appears around 5×10^{18} eV, referred to as the ankle. It has a spectral index of $\gamma = 2.6 - 2.8$ [23] and could be attributed to the transition of galactic to extragalactic particles.

The origin of these spectral features are not fully understood and are thus subject to the astrophysical models used. Possible scenarios are:

- In reference [24] the ankle feature is explained through **two population sources**. Lighter particles are assumed to originate from a different source population compared to heavier nuclei, which dominate the spectrum at larger energies. The model is able to describe the spectrum seen by Auger if the injection spectra of nuclei is hard ($\gamma_g \leq 1.6$), the maximum nuclei energy in the sources is $\approx 5Z \times 10^{18}$ eV and if an *ad hoc* light component of extragalactic origin is added with an injection spectrum of $\gamma = -2.7$ [24]. This implies that the transition of galactic to extragalactic cosmic rays occurs below the ankle (see figure 1.2b).

- Another model, discussed in reference [25], predicts the particle spectrum below the ankle to originate through **photo-disintegration**. Particles produced in the source environment are surrounded by turbulent magnetic fields and photon energies much higher than the CMB. This acts as a filter where high energy particles can escape, whereas low energy particles disintegrate into nucleons with energy $\approx \frac{1}{A}$ from the original nucleon (with mass A). As a result, below the ankle, the flux is dominated by light nuclei from higher energy nuclei. Above the ankle, the flux depends on the accelerator and propagation of the particles to earth. Accounting for realistic magnetic

and photon fields, the model described in reference [25] also explains the ankle seen in figure 1.1. This can be seen in figure 1.3a. Figure 1.3b shows that the mass composition seen in data from the Pierre Auger Observatory (described in chapter 2) is in agreement with the photo-disintegration model.

- The **mixed composition model** predicts galactic cosmic rays to be dominant before the ankle, later transitioning to extragalactic particles. The magnetic rigidity R[1] is relevant to interpret changes in the particle spectrum from propagation and acceleration in magnetic fields [26]. Particles with the same rigidity and injection vector will always follow the same path given a certain magnetic field. If protons can be accelerated to a maximum energy in a source then they will be first to cut off. This is followed by helium, carbon... or $E_{\max}(Z) = ZeR$. This is known as the Peters Cylce [27] and is represented in figure 1.2a for energies above 10^{18} eV. Figures 1.2c and 1.2d show the transition of light nuclei towards heavier nuclei with increasing energy. This model describes the features for the galactic and extragalatic component well. However, it cannot explain the origin of the ankle. This suggests a possible third class of particles.

- The **dip model** is a combination of the *pair-production dip*:

$$p + \gamma_{CMB} \rightarrow p + e^- + e^+, \tag{1.2}$$

where the proton p interacts with a CMB photon γ_{CMB}, creating an electron-positron pair, and the *GZK-cutoff*:

$$\begin{aligned} p + \gamma_{CMB} &\xrightarrow{\Delta^+} p + \pi^0 \\ p + \gamma_{CMB} &\xrightarrow{\Delta^+} n + \pi^+. \end{aligned} \tag{1.3}$$

The model claims extragalactic protons to be already dominant below energies of the ankle. However, they are suppressed due to the pair-production. As both features depend on proton interactions, the mass composition is expected to be proton dominated. Finally, the model only allows for a nuclei mixture of no more than 10-15% [28]. This is disfavored (however not excluded) by mass composition results seen in figures 1.2c and 1.2d, which favor heavier compositions.

Note, these astrophysical models already highlight that the mass composition and energy are key observables towards understanding the features seen in the energy spectrum.

1.3 Arrival Directions

The two-population source, mixed composition, photo-disintegration and dip model offer plausible explanations to the spectral features and the transition from galactic to extragalactic cosmic rays. At the highest energies, near the flux suppression, an exhaustion of sources is expected. Possible sources are illustrated in the Hillas plot in figure 1.4. In it, the maximum particle energy is calculated through $E_{\max} \approx ZBR$ for a given particle charge Z, magnetic field strength B and accelerating system size R. The solid and dashed lines indicate the acceleration requirement of a 10^{20} eV proton and iron respectively. Currently, the most promising UHECR sources include active galactic nuclei (AGN) and gamma ray burst (GRB). More exotic sources include pulsars (neutron stars with strong magnetic fields).

[1] defined as $R = \frac{Pc}{Ze}$, P is the particle momentum and Ze its charge.

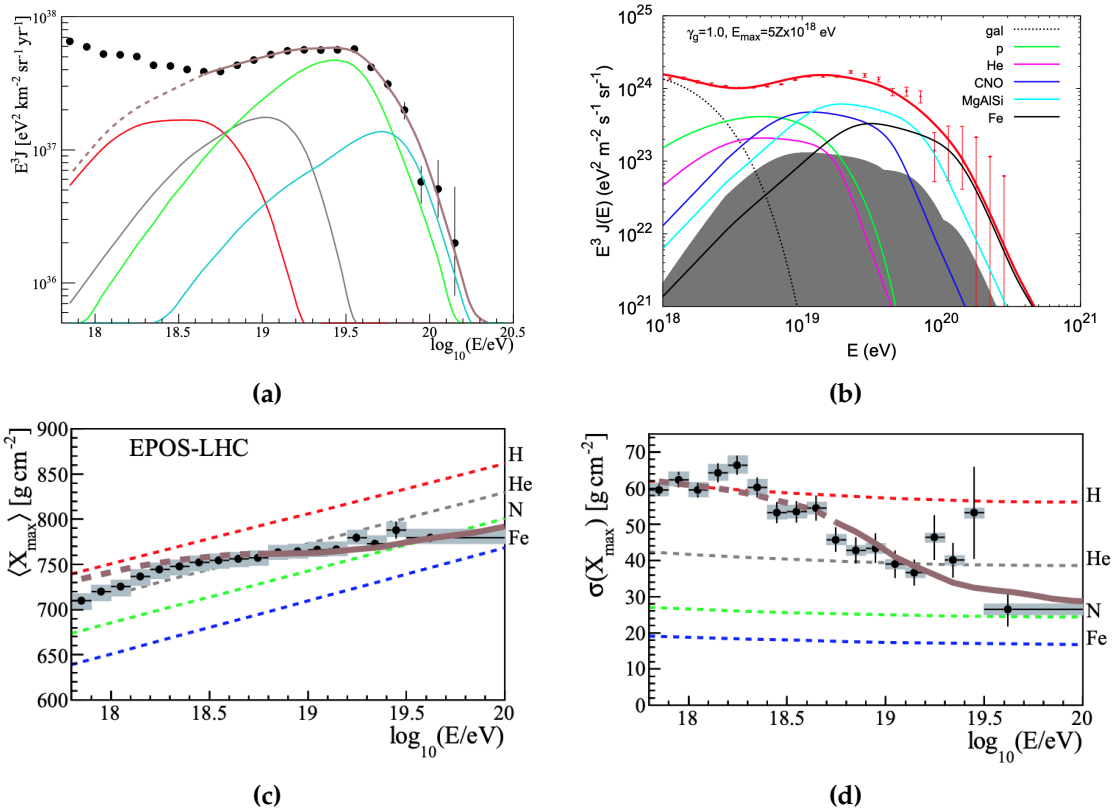

Figure 1.2: Simulated energy spectrum of UHECRs for the **a)** mixed composition [29] and **b)** two population source model [24]. Average mass composition variables **c)** $X_{\max}$ and **d)** $\sigma(X_{\max})$ are compared to their their respective prediction (UHECR-air interactions simulated with EPOS-LHC). Details on mass composition variables are discussed in 1.4. Data points are obtained from the Pierre Auger Observatory (section 2).

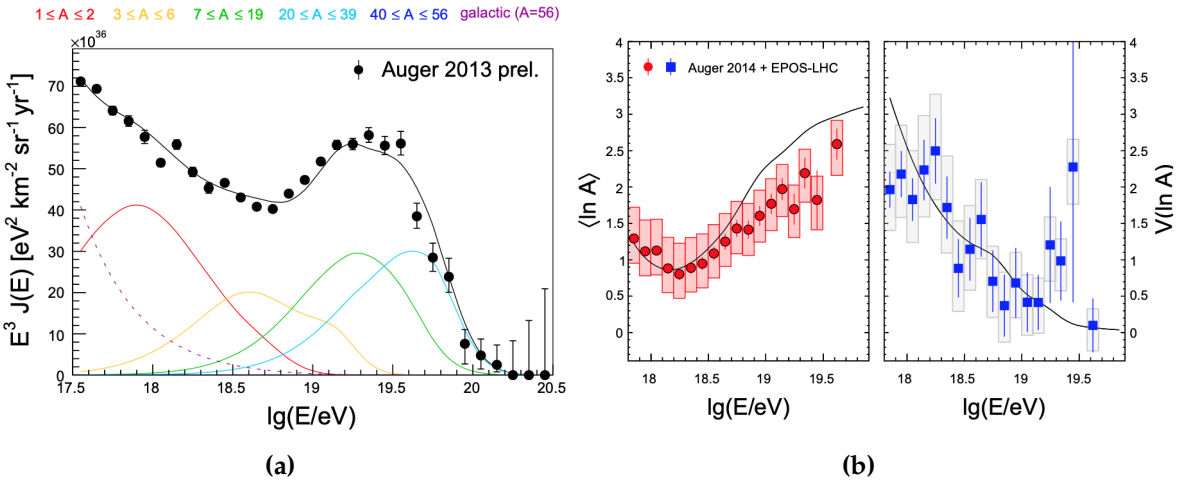

Figure 1.3: Prediction for the cosmic ray **a)** flux and **b)** mass composition assuming the photo-disintegration model [25] in comparison with Auger data. Estimates for the composition are based on simulated air showers using EPOS-LHC. Statistical uncertainties are represented by the error bars. The shaded boxed indicate the experimental systematic uncertainties of the composition.

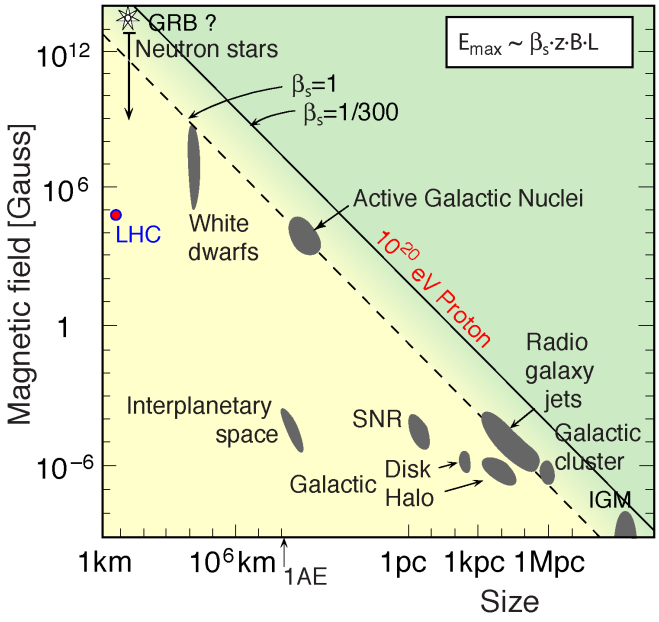

Figure 1.4: The Hillas plot illustrates candidate sources for UHECRs. Solid (Dashed) diagonal lines indicate the requirements for a proton (iron) acceleration of 10^{20} eV [32].

At the time of this writing, no point sources were found as the deflection of charged cosmic rays in galactic and extraglactic magnetic fields makes their source identification challenging. However, it is possible to infer this through studies on medium scale and large scale anisotropy. Recently, Auger reported an anisotropy on an intermediate angular scale [30]. It was found that CRs above 3.9×10^{19} eV most likely correlate to starburst galaxies with a statistical significance of 4σ. Starburst galaxies undergo a high rate of star formation, generating an extreme environment for the particles to be accelerated to the highest energies.

Above 8×10^{18} eV, a large-scale anisotropy was found by Auger at a level of 5.2σ [31]. This is visualized by the normalized events as a function of right ascension in figure 1.5b and the sky map in figure 1.5a. The distribution is best compatible with a dipolar modulation with an amplitude of $6.5^{1.3}_{-0.9}$% in the direction $\alpha_d = 100 \pm 10°$ in right ascension and $\delta = -24^{+12°}_{-13}$ in declination. Its magnitude and direction strongly suggest particles originating from extragalactic sources as opposed to from within the Galaxy (through a combination of less prominent inhomogeneously distributed sources) [31].

1.4 Extensive Air Showers

To accommodate for the low cosmic ray flux at the highest energies (see figure 1.1) large detectors are built, increasing the sampling area. The most effective approach is to use the Earth's atmosphere as a calorimeter. Upon entering the Earth's atmosphere, cosmic ray particles interact with air nuclei and produce a cascade of secondaries. This process is known as an extensive air shower (EAS).

Particles in EASs can be subdivided into three components (depicted in figure 1.6): (i) hadronic, (ii) the electromagnetic and (iii) muonic component. After the first UHECR inter-

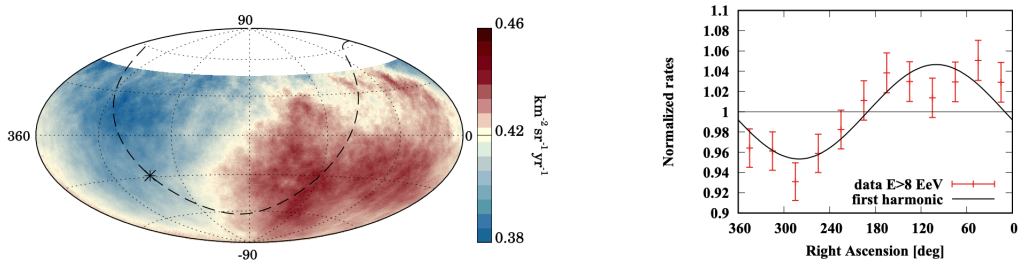

(a) **(b)**

Figure 1.5: a) Sky map showing CR integral flux above 8×10^{18} eV observed by Auger in equatorial coordinates. The galactic center and plane are marked with an asterisk and dashed line respectively. **b)** Normalized rate of events as a function of right ascension. The solid line shows the agreement of the dipole modulation with the data. The dashed line corresponds to a constatn function. Error bars are 1σ uncertainties. [31]

action with air, 75% of the energy goes to the mesons and baryons, creating the *hadronic cascade* [33]. It only dominates in the early part of the air shower development and consists of (p,n,Λ,$K^{\pm}$,K^0,$\pi^{\pm}$,π^0). These subsequently feed the other components with energy. When the average meson energy decreases, it becomes more likely for it to decay rather than to interact. The critical energy depends on particle type and medium. Their order of magnitude is $O^{\pi^{\pm}}_{crit}(100\,\text{GeV})$, $O^{K^{\pm}}_{crit}(1000\,\text{GeV})$, $O^{K^0}_{crit}(200\,\text{GeV})$ and $O^{\mu^{\pm}}_{crit}(700\,\text{GeV})$. This is the stage where muons are mostly produced. The electromagnetic component consists mostly of $e^{\pm}$ and γ. It is fed by photons from π^0 decays, which keep multiplying through pair production and Bremsstrahlung. After each interaction, 25% of the energy is fed from the hadronic cascade into the electromagnetic channel[2]. At ground, about 90% of the shower energy is carried by the electromagnetic component. In reference [34], the particle components are discussed for a simple semi-empirical cascade model (Heitler model). In section 3.2.1 the particle components are discussed in more detail for air shower universality analyses (discussed in chapters 4 and 5).

1.4.1 The electromagnetic shower

Heitler presented a simple model for electromagnetic cascade showers in reference [6]. These were later enhanced with more physical processes. However, these models are not as accurate as detailed simulations. Nevertheless, the Heitler model clearly illustrates the physical features seen in electromagnetic air showers.
A schematic of an electromagnetic cascade is illustrated in figure 1.7a, accounting for two physical processes (also depicted in figure 1.6). It shows how the leading particle (a photon) interacts with a nucleus, creating an e^+e^- pair. These $e^{\pm}$ create photons through Bremsstrahlung (affected by the field of another charged particle). In every step, the particle number is doubled, whereas the energy is shared equally between the particles. In other words, the shower consists of 2^n particles after n steps. Note, it is assumed that the electromagnetic particle interacts after a depth of d=ln(2)λ_r, where $\lambda_r \approx 37\,\text{gcm}^{-2}$. The particle production continues until the particle energy is below the critical energy E_c (85 MeV in air). Here, energy losses through ionization dominates, limiting further particle production [34].

[2] i.e. After 3 generations, more than 50% of the shower energy is associated to the electromagnetic shower component.

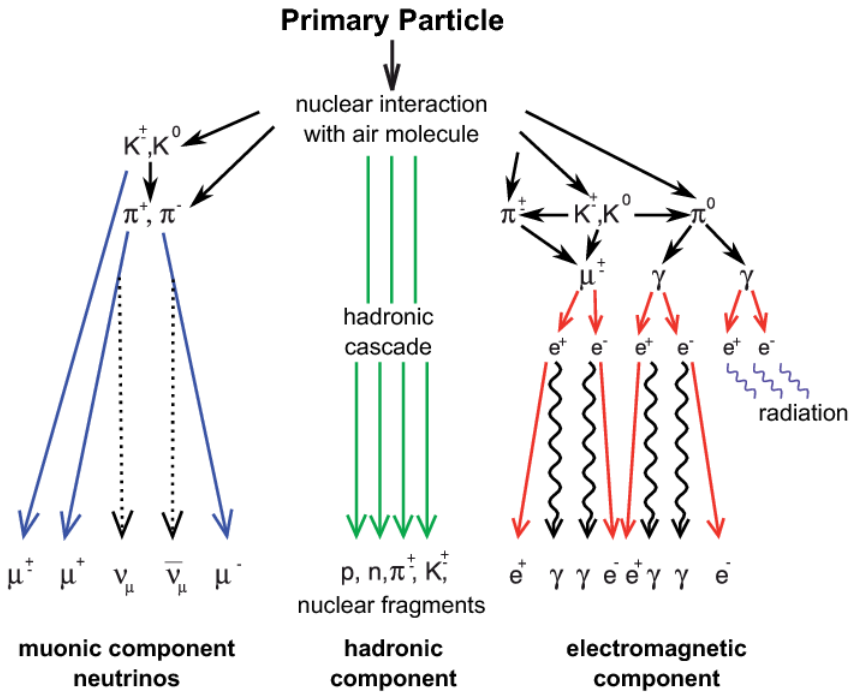

Figure 1.6: Schematic illustration of an EAS and its components [35].

Following the assumptions in the Heitler model, the total number of particles, $N_{\max}$, is described as

$$N_{\max}^{\text{Heitler}} = \frac{E_0}{E_c}, \tag{1.4}$$

where E_0 the energy of the primary particle. Here, the maximum shower depth $X_{\max}$ is

$$X_{\max}^{\text{Heitler}} = X_0 \ln\left(\frac{E_0}{E_c}\right), \tag{1.5}$$

where X_0 is the radiation length in air (36.7 gcm^{-2}). As discussed in [34], equations (1.4) and (1.5) overestimate $N_{\max}$ with respect to detailed simulations, whereas $X_{\max}$ is in fair agreement. Inaccuracies in the model arise, e.g., by not accounting for the attenuation. Also, $e^{\pm}$ mostly do not deposit exactly half their energy into a single Bremsstrahlung photon. Nevertheless, it is clear that the total particle number depends on the primary energy (i.e. $N_{\max} \propto E_0$) and that the maximum atmospheric shower depth, $X_{\max}$, is proportional to $\ln(E_0)$.

1.4.2 The hadronic shower

Hadronic air showers are modelled similarly to the Heitler approach (see the schematic in figure 1.7b). The atmosphere is imagined to be composed of layers with a fixed thickness $\lambda_I \ln(2)$, where λ_I is the interaction length of strongly interacting particles[3]. An interaction of protons with an air molecule produces N_{ch} charged particles and $\frac{1}{2}N_{ch}$ neutral pions. Neutral pions almost immediately decay into two photons, feeding the electromagnetic channel of the air shower. The charged pions continue to produce more pions until their respective energies are below the critical energy E_c^{π}. Pions with energies below E_c^{π} are expected to decay before reaching the next interaction point, yielding muons. E_c^{π} scales with the number of

[3]The assumption that λ_I is constant a good approximation for pions in the range of 10-1000 GeV [34]

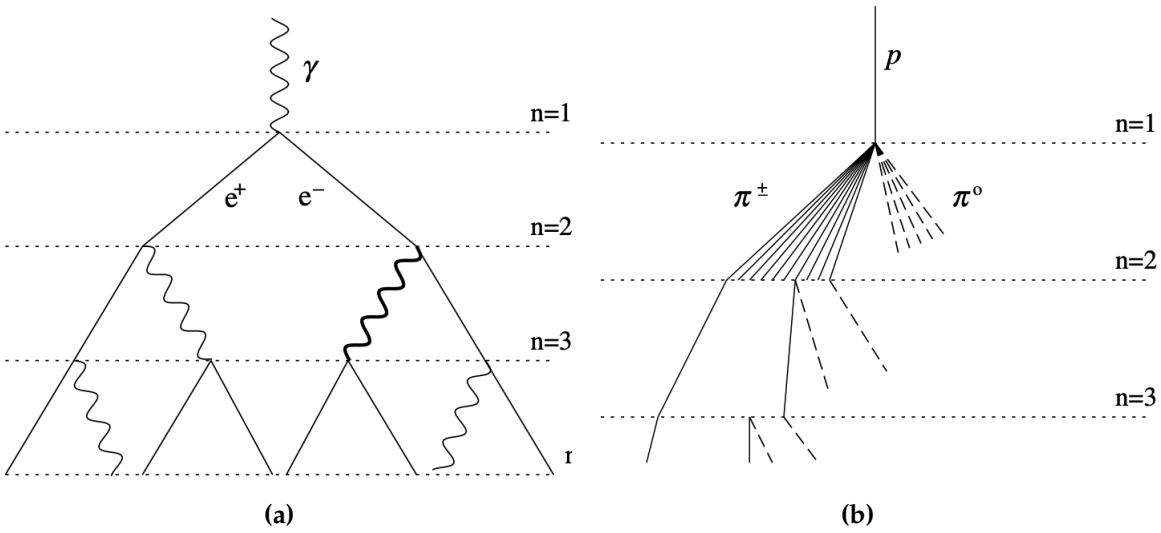

Figure 1.7: Schematic view of **a)** an electromagnetic and **b)** hadronic cascade. The dashed lines in **b)** indicate decayed neutral pions, producing an EM subshower. [34]

atmospheric layers (or integrated atmospheric density) and E_0. Typical values for air showers above 10^{17} eV are 10 GeV [34]. These charged pions then decay into muons and neutrinos

$$\begin{aligned} \pi^+ &\rightarrow \mu^+ + \nu_\mu \\ \pi^- &\rightarrow \mu^- + \bar{\nu}_\mu. \end{aligned} \tag{1.6}$$

As neutral pions contribute to the electromagnetic subshowers, the total energy is calculated through

$$E_0 = E_c^{EM} N_{\max} + E_c^{\pi} N_\mu. \tag{1.7}$$

From the combined information of $N_{\max}$ and N_μ the mass of the primary particle can be inferred.

For air showers induced by heavier nuclei, a superposition model is used. Air showers of nuclei with atomic number A and energy E are described as A proton showers with energy E/A. As a result, the maximum shower development for heavier elements occurs prior to those induced by proton showers with identical energy E. By reducing the energy of each superimposed shower, the critical energy E_c^{π} increases. This changes the number of pions (and hence the number of muons) produced in a shower. As a result, the muon content is a prime indicator to identify the mass of the primary particle. Neutrinos created through these interactions are part of the *invisible energy*. Simulations estimate them to account for 5% of the total energy.

1.4.3 The shower maximum depth

In addition to the muon content, the maximum shower depth $X_{\max}$ provides information on the composition of the primary particle. Applying the superposition model to equation (1.5) already indicates that heavier elements have a smaller $X_{\max}$ for identical energy E. The shower maximum is best described as the integrated air mass:

$$X_{\max} = \int_{z_{\max}}^{\infty} \rho(z) dz. \tag{1.8}$$

The integration is along the shower axis from the top of the atmosphere until the shower maximum. In addition to the particle mass, $X_{\max}$ is found to depend logarithmically on the energy [15]. These dependencies are later used within the scope of this work. In [36], a generalized description for the superposition model is presented. It is

$$\langle X_{\max} \rangle = X_0 + D \lg\left(\frac{E}{E_0 A}\right) + \xi \ln(A) + \delta \ln(A) \lg\left(\frac{E}{E_0}\right), \tag{1.9}$$

where X_0 is the mean depth of proton showers with initial energy E_0. Also, D is the elongation rate. Deviations from the ideal superposition model are accounted for with ξ and δ. The dispersion in $X_{\max}$ is expected to be dominated by shower-to-shower fluctuations:

$$\sigma^2(X_{\max}) = \sigma^2_{sh}(\ln(A)). \tag{1.10}$$

Note, the shower maximum $X_{\max}$ in (1.9) applies only for the electromagnetic component. The production of muons in air shower also yield similar dependencies as seen in (1.9) (albeit with different corrections and elongation rate). $X^{\mu}_{\max}$ is referred to as the *maximum muon production depth*. Its estimator for primary mass is also discussed and later used in this work. In figure 1.8, the longitudinal profiles for different particle components is shown for a proton-induced extensive air shower. It illustrates the particle abundances and their respective shower maximum.

1.4.4 Mass composition

The energy dependency of $\langle X_{\max} \rangle$ measured by Auger and Telescope Array is depicted in figure 1.9a. Their composition is in agreement with each other. Studies shown in reference [38] have revealed that the number of muons are systematically above those predicted by simulations. More recent results, obtained through direct muon measurements at Auger, have found the muon density to be 38% (EPOS-LHC) and 53% (QGSJETII-04) above those predicted by simulations [39] at 10^{18} eV. This is illustrated in figure 1.9b, where ρ_{35} is the muon density at 450 m and $\langle X_{\max} \rangle$ the mean shower depth measured by fluorescent detectors (described in 2.2) at Auger. Furthermore, studies with AGASA data have shown the muon deficit to increase at higher energies. EPOS-LHC and QGSJETII-04 simulations are found to be respectively 49% and 66% lower compared to data obtained from events between $18.83 \leq \log(E/\text{eV}) \leq 19.46$ [40]. The muon deficit in simulations is also confirmed by various other experiments, discussed in reference [41]. They show that the predicted muon content from the latest high energy hadronic interaction models (EPOS-LHC, QGSJETII-04 and Sybill2.3c) is in agreement with data until 10^{16} eV. The deficit increases with increasing energies, whereas the prediction of the electromagnetic shower component remain consistent with data. This complicates mass composition analyses, necessitating hybrid experimental setups, which measure the muon content, electromagnetic content and maximum shower depth.

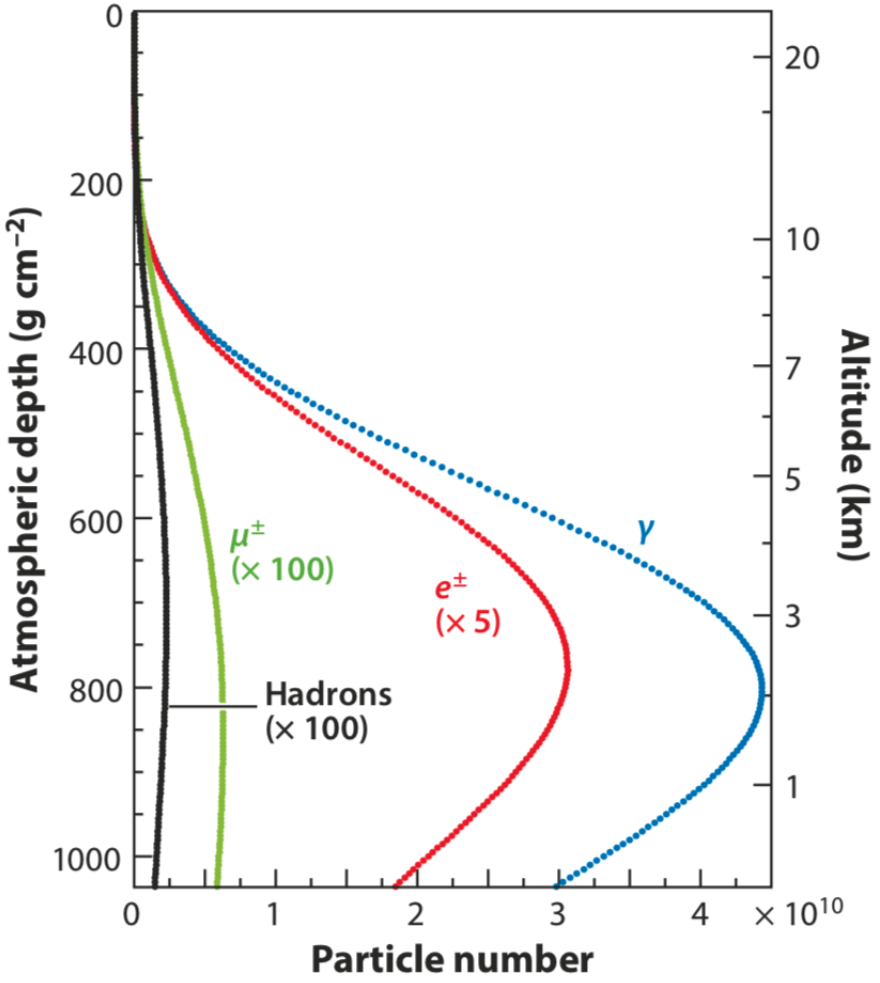

Figure 1.8: Longitudinal profiles of different particle components for a sample vertical extensive air shower at 10^{19} eV. The air shower is simulated with CORSIKA and induced by a proton primary [37].

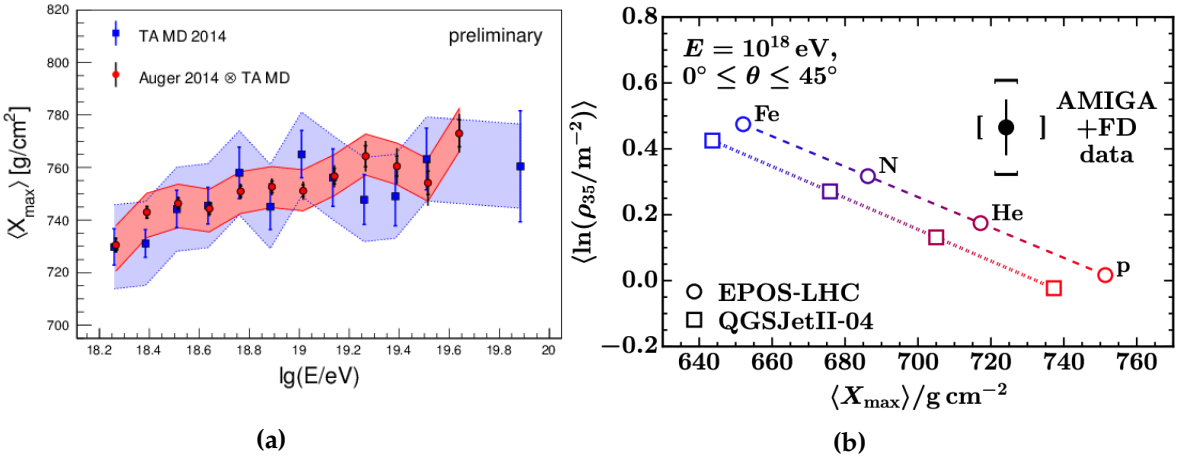

(a) **(b)**

Figure 1.9: a) The mean $X_{\max}$ measured by the Middle Drum detector of TA is compared to the Auger data (accounting for the MD acceptance) [42]. **b)** Average logarithmic muon density $\ln(\rho_{35})$ as a function of mean $X_{\max}$ for air shower simulations with different primary and high energy hadronic models at 10^{18} eV. These are compared to direct measurements with the fluorescence detector ($X_{\max}$) and muon detector ($\ln(\rho_{35})$), part of AMIGA, at Auger. [39]

CHAPTER 2

Pierre Auger Observatory

The Auger is the largest cosmic ray detector in the world. It was conceived to measure and study the characteristics and interactions of extensive air showers initiated by cosmic ray particles with energies above 10^{17} eV with a hybrid detection system. It spans 3000 km^2 over a vast plane in Western Argentina, near the city of Malargue, at an average altitude of 1400 m above sea level. This corresponds to an atmospheric overburden of 875 g cm^{-2}. The principle design features of the Observatory is the more than 1600 water Cherenkov particle detectors (WCD) separated by 1500 m in a triangular grid array accompanied by 24 air Fluorescence Detector (FD) (see figure 2.1). In addition, three high elevation FDs (High Elevation Auger Telescopes (HEAT)) overlook a 23.5 km^2 infilled detector area where the WCDs are separated by 750 m. Its construction began in 2002 and was completed by 2008 with a total exposure exceeding 60,000 km^2 sr yr. It has been collecting data since 2004.

As part of the upgrade initiative to the observatory (also known as *AugerPrime*), three additional detector systems are being developed; muon detectors (MD), SSD and Radio Detector (RD). The muon detectors are part of the Auger Muon Detectors for the Infill Ground Array (AMIGA), designed to detect muons from the cosmic ray shower underground. These detectors will be associated to each WCD (together referred to as a *station*) in the infilled detector array. The SSD will be located atop of each WCD in the standard array grid to simultaneously measure particles with independent detector system and thus identify the particle type. Finally, radio detectors will measure the unique radio signature generated by comic ray showers. Currently, studies are being done at the Auger Engineering Radio Array (AERA). All stations operate autonomously.

2.1 Water Cherenkov Detector

More than 1600 Water Cherenkov Detectors are distributed on the combined 1500 m and 750 m infilled triangular grid array. The detection efficiency at trigger-level is defined by the grid spacing. A coincident detection of at least three neighboring stations is required. As the shower energy increases, more detectors will be triggered. The quality of measurements will therefore improve with more energetic showers (and vice versa). Assuming the standard 1500 m array, full efficiency is achieved for energies larger than $10^{18.5}$ eV. As the station density is higher for the infilled array (750 m), full efficiency is achieved above $10^{17.5}$ eV.

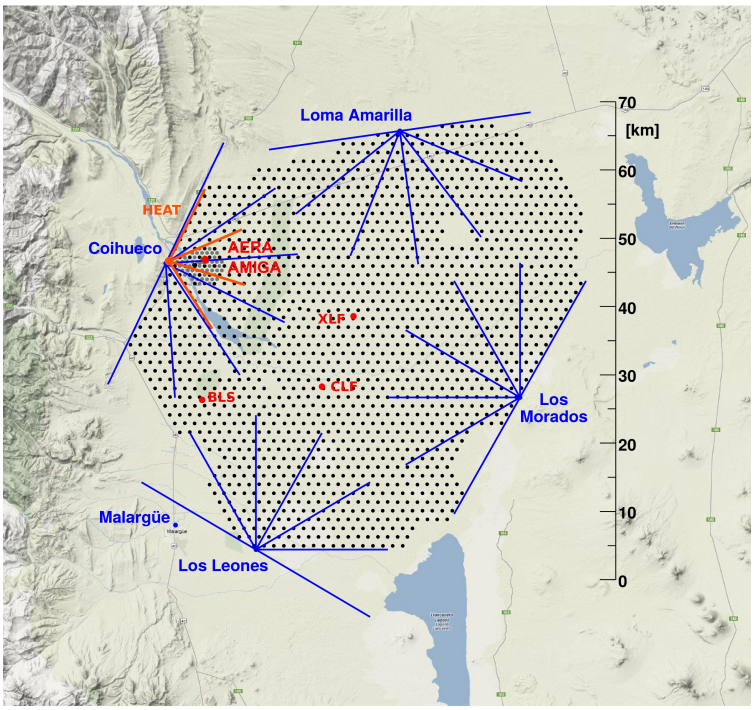

Figure 2.1: Map of Pierre Auger Observatory: ~ 1600 WCDs are distributed on a 3000 km^2 grid area, 1500 m apart from each other. 24 FD telescopes are grouped together into 4 locations (Coihueco, Loma Amarilla, Los Morados, Los Leones) and overlook the entire detector area. The infilled array with 750 m spacing is situated near Coihueco. In the infilled area AERA and AMIGA can be found.

2.1.1 Water Cherenkov Detector Design

Each detector is a cylindrical shaped water tank with a diameter of 3.6 m and 1.6 m height (1.2 m water depth), filled with 12 m^3 ultra-pure water. They are made of polyethylene resin and sealed inside with a liner [17]. They are sensitive to muons, charged electromagnetic particles and energetic photons producing electron-positron pairs in water. As relativistic charged particles traverse through the water, they produce Cherenkov light which is detected by three Photo-Multiplier Tube (PMT)s. Their diameter is 9 inches and are installed at the top surface of the inner liner with a downwards orientation. They are powered by their own solar panel and store excess energy in a battery (to be used at night). Each WCD is equipped with its own electronics, located in a hatch at the top of the tank. It includes a power supply unit, a processor, GPS receiver and a radio transmitter for communication with the Central Data Acquisition System (CDAS). Signals are initially recorded in flash analog to digital converter (FADC) at 40 MHz and then locally calibrated by the electronics. PMT voltages are tuned to match the average event rate of all PMTs of the tank [17]. Figure 2.2a shows an example of such a station.

Naturally, the detector signal is a convolution of the particle arrival distribution from sed shower and the detector response. Signals by the WCD are measured in units of vertical-equivalent muon (VEM); i.e. with respect to a vertically impinging muon that goes through the water column. The signal for a vertically muon is obtained by injecting 1 GeV muons vertically in a WCD with two scintillator plates placed above and below the water tank (acting as an external trigger) [43]. Figure 2.2b shows the calibration histogram (solid line) where the first peak is from the convolution of the trigger on a steeply decreasing distribution from low-energy particles and the second from vertical muons. They only contain data from

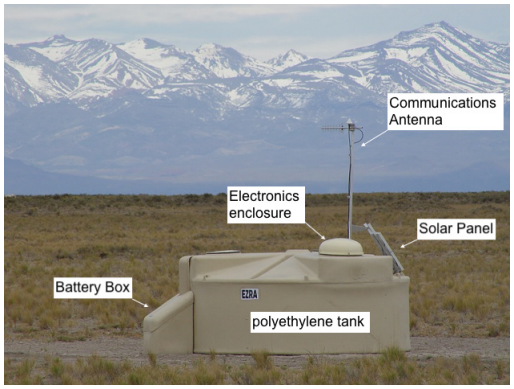

(a)

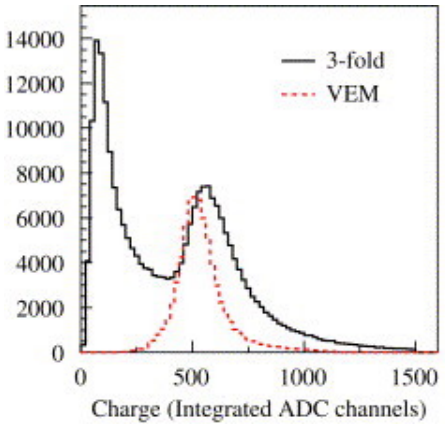

(b)

Figure 2.2: a) Photograph of a WCD in the field, labeled with the relevant detector components. **b)** Charge distribution of a vertical impinging muon (red) compared to the distribution from 3-fold coincidences [43]. The first peak in the 3-fold coincidence is the convolved response of the trigger and low-energy particle spectrum.

3-fold coincidence where all 3 PMTs are triggered. The total detector signal is therefore the integration of the time dependent signal response of all particles in a buffer.

The standard reconstruction (described in reference [44]) uses arrival times of the detector signal to derive the arrival direction of the primary particle. The integrated station signals are then fitted to a lateral distribution function (lateral distribution function (LDF)) where the signal at 1000 m (S_{1000}) serves as an energy estimator. For the infilled array the signal at 450 m is used. At those respective distances shower to shower fluctuations are found to be minimal. The energy estimators are calibrated with events detected simultaneously by the WCD and the FD (also known as hybrid events), since the FD provides a direct measurement on the shower energy. Unfortunately, FD only has a duty cycle of ~15 %, whereas the WCD has a duty cycle of 100 %. The calibration is therefore used to obtain the energy spectrum. More to it in chapter 6.

2.2 Fluorescence Detector

Shower particles passing through the atmosphere generate fluorescence light, through interaction with atmospheric nitrogen, which can be seen by the Fluorescence Detector (FD) [17]. FDs therefore provide a direct measurement of the longitudinal shower profile. As figure 1.8 illustrates, most shower particles are electromagnetic and thus contribute most to the generation of fluorescence light in any shower (about 95 % of fluorescent light is generated by electromagnetic particles).

The detectors are housed in four buildings (Los Leones, Coihueco, Los Morados, Loma Amarilla) at the perimeter of the array, each containing six fluorescence telescopes. Each telescope has a field of view of 30° × 30° in the azimuth and elevation (with a minimum elevation of 1.5°), with a combined field of view of 180° × 30° per building. All detectors are faced inwards towards the surface detector array. This guarantees that a 10^{19} eV shower arriving in the array will be seen at least by one FD telescope. At one of the FD buildings, Coihueco, three additional telescopes have been built for lower energetic showers (down to

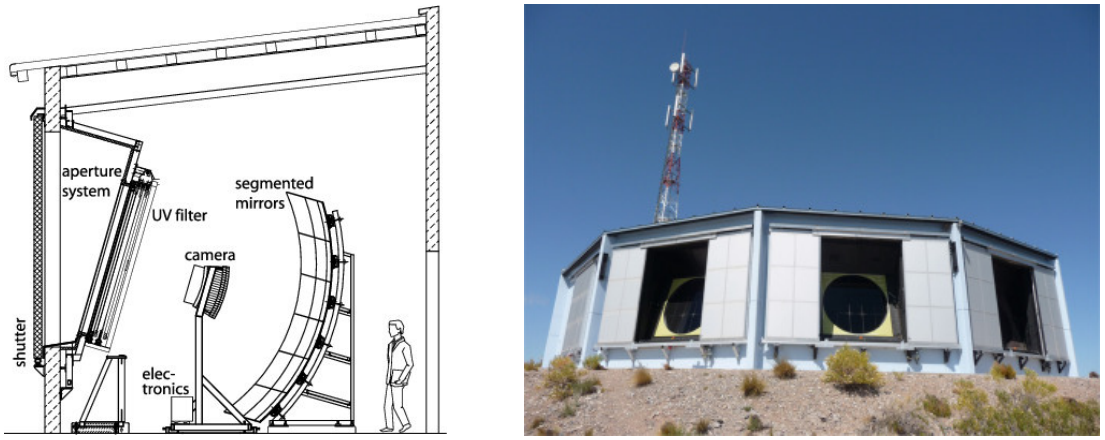

(a) **(b)**

Figure 2.3: a) Interior schematic of a fluorescence detector telescope. **b)** Photograph of an FD building during daytime. (Shutters are normally closed during daytime).

$\sim 10^{17}$ eV). These telescopes are known as the High Elevation Auger Telescopes (HEAT) and can elevate from 29° to 59° (higher than the other telescopes) since low energetic showers develop earlier in the atmosphere. The site of HEAT was strategically chose to be closest to the infilled array (which is near Coihueco). Low energetic showers can therefore also be seen through hybrid measurements.

The telescopes reside in clean, isolated and climate controlled rooms within the FD building. During operating hours, the shutters are opened for the fluorescence light to pass through an aperture and a 1.1 m circular diaphragm. It is coated with a UV band pass filter to reduce background light. The light is then collected by a 13 m^2 segmented curved mirror and reflected onto the camera (as seen in figure 2.3a). It consists of 440 PMT pixels, each equipped with a Winston cone for better light collection [17]. The shutters automatically close during daylight, when moonlight is in the field of view and bad weather conditions. During emergencies, such as a malfunction of the shutters, a curtain drops in front of the aperture.

Due to the opaque nature of the atmosphere, fluorescent light attenuates and diffuses prior to its arrival to the telescope. To correct for this, atmospheric conditions are continuously monitored during FD operating hours at the array. The Central Laser Facility (CLF) and the eXtreme Laser Facility, located close to the center of the array, shoot collimated UV laser pulses vertically into the atmosphere. The telescopes measure the scattered light from the laser pulses, providing information on the properties of the aerosol and possible time offsets with respect to the surface detectors. Each FD building is also equipped with its own weather station to monitor (among many other properties) wind speed, pressure, temperature and cloud coverage (the latter with an infrared camera). Finally, data from the Global Data Assimilation System (GDAS) are used as supplementary information on the atmospheric conditions.

Showers measured by the FD are projected on the camera as a light trace. The shower reconstruction is performed with the temporal light distribution in the camera. Since the light originates predominantly from electromagnetic particles, the Gaisser-Hillas function [45] is used to fit the longitudinal profile. The maximum of the Gaisser-Hillas profile corresponds to the shower maximum (the shower stage where most particles are being produced) at an atmospheric depth of $X_{\max}$. $X_{\max}$ provides a direct estimate on the primary particle mass. The light intensity depends on the energy deposit of the charged particles. The total deposited

energy can therefore be derived by integrating over the shower profile. The calorimetric energy is finally corrected for the "invisible" energy, energy carried away by muons and neutrinos, to provide the energy of the primary. This primary energy is then used to calibrate the energy estimator of the WCD (by using the S_{1000}). For a shower at 10^{19} eV the FD energy resolution is $\sim$10 %, whereas the X_{max} resolution is 20 g cm^{-2}.

Fluorescence detectors can only be operated during dark moonless nights and clear weather. Strong winds, rain/snow and lightning lead to a duty cycle of about 15 % (with longer duty cycles in the winter due to longer nights). It always measures in hybrid mode with the surface detector and thus (through GPS synchronization) provides simultaneous measurements of air showers. At the time of this writing, possible methods to extend the FD duty cycle is being investigated. By reducing the PMT gain, the telescopes can operate for longer nights and thus longer duty cycles. It is expected to increase the FD duty cycle by 50 %.

2.3 Muon Detector

The AMIGA project is an enhancement to the Pierre Auger Observatory. It consists of the infilled WCD array with dedicated muon detectors (MD) (see figure 2.4a). First, only seven WCDs were equipped with muon detectors for the AMIGA project. These are referred to as the Unitary Cell (UC) and serves as the engineering array for the project, providing useful information on soil shielding, detector systematics and module layouts in the field. By early 2020, 72 stations are planned to be constructed and deployed in the infilled array.

Although AMIGA only covers 23.5 km^2, the increased particle flux at lower energies provides for sufficient statistics between the second knee and the ankle. It was designed to enhance the quality of X_{max}, energy and the optimal lateral distance N^{μ}_{450} (analog to S_{1000} for the WCD) for mass composition analyses through direct muon measurement [46]. The study of muon production depth and hence X^{μ}_{max} (maximum muon production depth for an air shower) is also of considerable interest. It has been established (through measurements) that the hadronic models used for shower simulations underestimate the muon production in showers [38]. The independent measurement of muons will therefore enable the study of hadronic interactions at higher energies.

MDs are buried 2.3 m underground, corresponding to an additional vertical atmospheric overburden of $\sim$550 g cm^{-2}. At this depth, electromagnetic particles are effectively not present. The soil shielding also affects the muon energy spectrum, which can be simplified as an energy cut at 1 GeV for vertical muons (the energy increases as a dependency of cosine for inclined muons). The infilled setup of the MDs allow it to operate at full efficiency for energies above $10^{17.5}$ eV for zenith angles below 45°. Since the MDs are located within the infilled area, they are overlooked by the Coihueco and HEAT FD telescopes (the latter also providing information on low energetic showers). They also operate at 100 % duty cycle.

2.3.1 Muon Detector Design

Each muon detector covers in total 30 m^2, divided into 2×5 m^2 and 2×10 m^2 scintillator modules. The modules are buried 5 m from the WCD in an L-shaped pattern (see figure 2.4b) to prevent shadowing and reduce systematic effects on the azimuthal angle of inclined muons. The latter is a consequence of the segmentation of the 2×32 scintillator bars within each

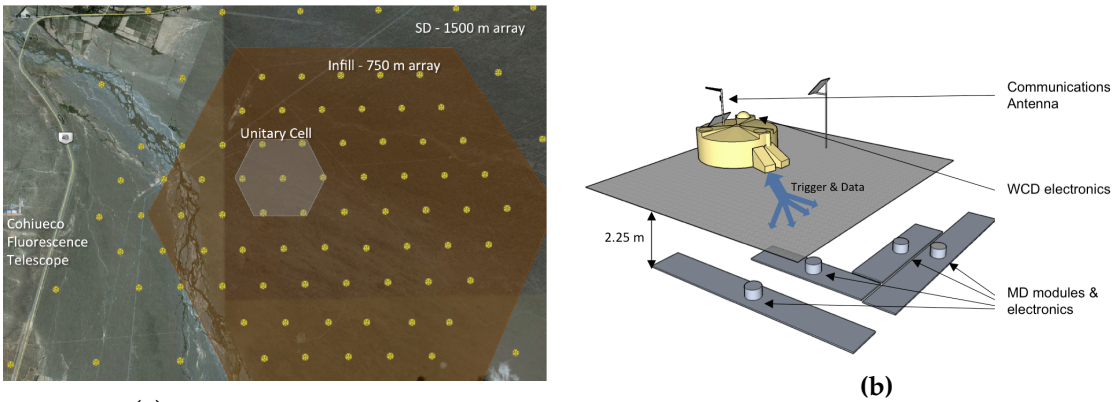

(a) **(b)**

Figure 2.4: a) The colored hexagon denotes the 23.5 km^2 infilled array. Each yellow dot marks a WCD, whereas within the colored band it also denotes a MD. Within the infilled array a smaller hexagonal region is marked. This region is known as the Unitary Cell (UC) and serves as the engineering array for AMIGA. **b)** The rectangular grey boxes below the detector represent the MD modules. The cylindrical box on top of the modules will house the electronics. A triggered WCD will relay the trigger to the MD, which then sends the data to the WCD electronics to be forwarded to the CDAS. Communication between the WCD and MD is with a cable [46].

module; each with dimensions 4cm×1cm×400cm. In total, every MD has 192 scintillator bars. Plastic scintillators were opted for their mechanical quality and durability (considering the soil pressure it is supposed to sustain). They are polystyrene doped with fluor and wrapped with TiO_2 to increase reflectivity. The attenuation length of the bars are ~(5.5±0.5) cm [46]. Generated photons must therefore be transported with an optical fiber to the photo-sensor. Here a 1.2 mm diameter wavelength-shifting (WLS) optical fiber propagates the light to the photo-multiplier. These WLS are glued inside a groove along the scintillator bar and taped with aluminium tape to minimize photon loss (see figure 2.5). These WLS fibers are then bundled tightly together with a PVC casing and attached to a multi-pixel photo-multiplier.

Initially, the MDs were equipped with PMTs. Data from the unitary cell revealed that silicon photo-multipliers (SiPM) are more beneficial. SiPMs consume 10 times less power, saturate less quickly (and can thus be used closer to the shower core) and have no cross talk between pixels compared to its PMT counterpart. Cross talk implies that the signal from one pixel leaks into its neighbouring pixel and thus provides an invalid signal of the scintillator bar the fiber originates from. Within the scope of this work only muon detectors with SiPMs are being considered.

The electronics are divided into two separate units. The primary is located on top of the module underground. They are comprised of the SiPM, the analog front-end, and the digital and micro-controller board. The Field Programmable Gate Array samples the signal at 320 MHz (3.125 ns time bins) and provides a digitized output, with a discriminator, and an analog output (see figure 2.6). The digitized output is then stored in a 2048 bin ring buffer, whereas the analog output is stored in a 1024 bin ring buffer (with 6.25 ns time bins). Upon triggering the WCD, the buffer is sent to the main electronics of the WCD (second unit for MD) to relay and transmit the data to CDAS.

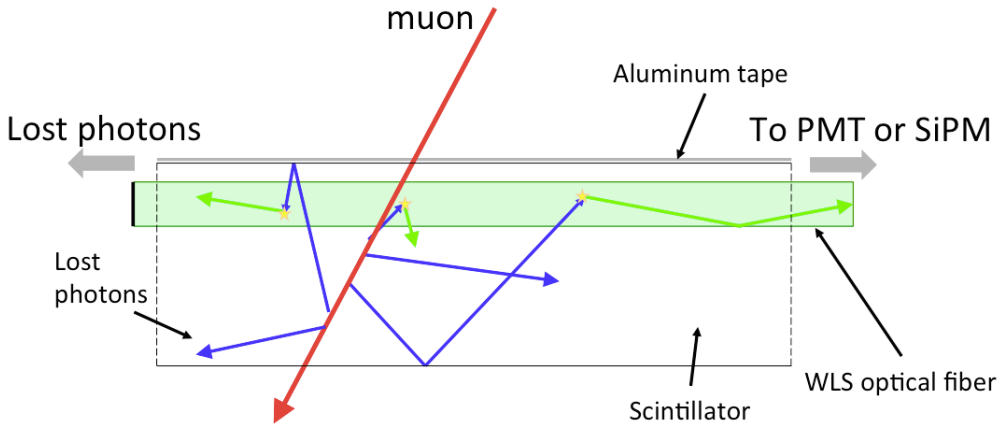

Figure 2.5: Schematic of a muon (red) interacting with a scintillator (transparent). The generated photons are reflected on the inner scintillator walls and passed to the WLS. The top of the bar and the fiber end not going to the photo-multiplier (PMT or SiPM) are covered with aluminium tape. However, photons are still lost (predominantly at the fiber end) [46].

2.3.2 Muon Counting Strategies

With the two data sets (1024 bin and 2048 bin ring buffer) the MD provides two independent muon counting strategies. The *1-bit strategy* uses the digitized 2048 bin output where the discriminator produces signals in the form of "1" and "0", whereby "1" signifies an existing signal above a given discriminator threshold for sed scintillator bar (and vice versa for "0"). Due to the muonic pulse response, they are counted in 12 bin time windows (or 37.5 ns). Shorter time windows cause over-counting, whereas longer bins under-counting. This strategy is very robust as it does not require a detailed knowledge of the signal shape and intensity or any related subsequent analysis (such as deconvolving the signal). It is effectively independent of the interaction point of muons, fiber attenuation and the number of SPEs per muon. Nevertheless, setting the correct discriminator level, time window and counting method is critical to prevent over-/under-counting muons (see figure 2.6). The 1-bit counting strategy searches for "1x" patterns within the 12 bin window, where "x" can be either "1" or "0", and counts it as a muon. Due to the low SiPM noise, choosing a different counting strategy does not provide for an immediate improvement [47].
Inclined muons can cross from one scintillator bar to another and subsequently give a false signal, also known as a clipping corner. This effect is more frequent for inclined showers and depends on the azimuthal orientation with respect to the detector. Clipping corner effects are therefore corrected during the shower reconstruction. A drawback from the 1-bit counting strategy is the hard limit on the detector saturation set by the finite segmentation. With 192 scintillator strips, the MD cannot exceed 192 "1"s at any given time bin. It therefore saturates quickly, a problem which can be resolved by inferring the muon number from the charge distribution of the analog output. The *integrator strategy* integrates the entire signal stored in the 1024 bin ring buffer and converts it (similar to the WCD) into units of single muons. It is independent of clipping corner effects and the finite segmentation of the detector. It will therefore over-count muons less likely and can thus be used closer to the shower core. Nevertheless, depending on the gain, the 1-bit counting strategy is more accurate at larger distances from the shower core. At the time of this writing, shower reconstructions with the SiPM are at its infancy. This is in part due to the incomplete AMIGA array, which would provide more statistics, and the necessity to properly tune and calibrate the SiPMs. More detailed SiPM properties used in subsequent analysis can be found in section 4.1.2.

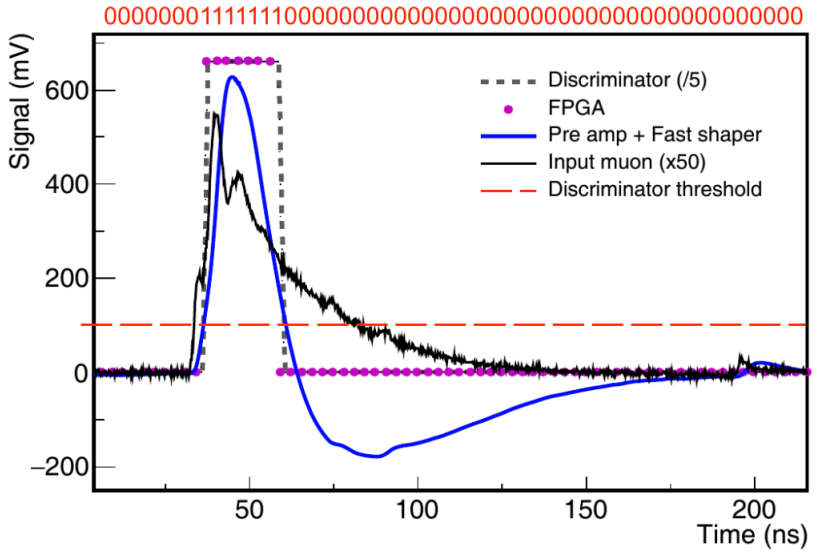

Figure 2.6: A simulated trace of a single muon. The pulse and discriminator level are re-scaled for illustrative purposes. The FPGA outputs a binary trace, where "1" indicates a signal above the discriminator threshold [48].

2.4 Scintillating Surface Detector

The scintillating surface detector (SSD) is the flagship project of the AugerPrime upgrade to the observatory. Its main objective is to sample the shower at the same location as the WCD but with a different detector response to shower particles. This allows for a seperation between muonic and electromagnetic particles, improving mass composition discrimination sensitivity (see reference [49] for further elaboration). Each station will be equipped with an SSD. Currently, construction of the SSDs is in its final phase with deployment underway.

The SSD design is based on a plane of plastic scintillators located above the WCD (see figure 2.7), therefore measuring the same particles as the tank does and thus comparing the amplitude and temporal distribution of signals directly. Signals from the SSD will be dominated by signals from the electromagnetic particles with respect to the WCD, where the signal is dominated by muons and photons [50].

An SSD module is divided into two $\sim 2\,\mathrm{m}^2$ extruded plastic scintillators. Each module is comprised of $12 \times 1.6\,\mathrm{m}$ scintillator bars, 1 cm thick and 10 cm wide, placed next to each other. Holes are drilled along the center of the strips for the WLS fibers. Each fiber passes through two non-consecutive scintillator strips to carry the photons. All fibers are then bundled and mounted to a single photo-multiplier, located in the center of the module. Its electronics are those used for the WCD. As a result, it triggers only whenever the WCD triggers and will also operate at 100 % duty cycle.

A reconstruction algorithm is currently being developed to infer the shower parameters. It will use the same principles as for the reconstruction with the WCD where the S_{1000}^{SSD} serves as an energy estimator. Due to the different signal responses of shower particles with respect to the WCD the slope of the lateral distribution function is expected to be different.

Figure 2.7: A sample photograph of an SSD deployed in the standard array above a WCD.

2.5 Radio Detector

The radio emission produced by air shower particles in the atmosphere is measured by the Auger Engineering Radio Array (AERA). The radio engineering array was conceived to improve the understanding of radio emissions mechanism in air showers, develop optimal hardware for detection and software for reconstruction of shower observables [51]. They measure the emission in a frequency range of 30 MHz – 80 MHz of cosmic ray energies above $\sim 10^{17}$ eV (equivalent to the FD and MD).

AERA is located in the infilled array and was deployed in three phases. First, 24 logarithmic periodic dipole antennas [52] were deployed with a 144 m grid spacing, covering 0.4 km^2. Next, 100 butterfly antennas were deployed with updated hardware and trigger concepts. These were partially distributed with a 250 m and 375 m grid spacing. Finally, 25 antennas were deployed with a 750 m spacing, covering 17 km^2. The latter is intended to measure air showers above 60°. It was found that the lateral distribution of radio emission increases with inclined air showers [53], allowing for larger grid spaces. They are externally triggered by the surface detector and have a 100 % duty cycle. At the time of writing, enough funds were collected to build radio antennas for all WCD stations.

CHAPTER 3

Air Shower Universality

The foundations of reconstructing extensive air shower are the fit to the geometry and lateral distribution function (LDF). The former takes the arrival time of detector signals into account, where the latter describes the radial dependence of the shower signal with respect to the core [54]. Due to changing LDF shapes on a shower to shower basis, the estimators $S_{1000}^{\mathrm{WCD}}/S_{1000}^{\mathrm{SSD}}/N_{\mu,450}^{\mathrm{MD}}$ are used. They describe the shower size (and thus its primary energy) and minimize primary mass dependencies. Energy and geometry are robustly and accurately reconstructed. However, the estimator also leads to poor mass composition discrimination. Information on the underlying physics of the shower development is lost, i.e., physics on the signal and time distribution of secondary particles are effectively unattainable. Air shower universality is based on a phenomenological method which encapsulates the underlying shower physics and allows for a reconstruction based on mass-composition sensitive shower parameters -among those being the shower maximum X_{max}, maximum muon production depth X_{max}^{μ} and relative muon content R_{μ}. It assumes that shower secondaries have the same fractional rate of change with increasing depth at the same shower stage. In other words, the normalized shape of the longitudinal shower profile is expected to be equivalent for all showers.

3.1 Universality for Electromagnetic Cascades

In reference [55], the concepts of shower *age* has been thoroughly studied for pure electromagnetic showers and reevaluated in reference [56]. In the latter, the shower age s and relative evolution stage t are defined as

$$s = \frac{3X}{X + 2X_{\mathrm{max}}}, \tag{3.1}$$

$$t = \frac{X - X_{\mathrm{max}}}{X_0}, \tag{3.2}$$

with $X_0 = 36.7\,\mathrm{g\,cm^{-2}}$ for the radiation length of electrons in air. At $s = 0$ the shower is at its youngest stage and at the top of the atmosphere, $s = 1$ at the shower maximum and at $s = 3$ at its oldest stage. The findings have shown that at the same shower age three distinct universal features emerge.

- The fractional rate of change for the electron size is equivalent for increasing shower depth.
- The energy spectra and relative normalization of most electrons and photons in the showers can be uniquely described by the age parameter.
- The electromagnetic particles (reasonably close to the shower axis) have the same angular and lateral distributions.

In figure 3.1a the energy distribution of electron and positron particles are illustrated. The red lines correspond to different primary species (p, Fe and γ) and different energies (10^{17} eV, 10^{18} eV, 10^{19} eV) whereas the dashed lines correspond to their parameterizations. The plot is subdivided into three shower stages $t = -6$ (young shower stage), $t = 0$ (at shower maximum) and $t = 6$ (old shower stage) all of which indicating universal behaviours, irrespective of primary and energy. Minor deviations seen at the young shower stage (t=-6) is caused by the primary energy.
Figure 3.1b shows the average electron distributions at different electron energies as a function of momentum angle. The red band marks the 3σ statistical error margin. Again, a good agreement is seen between the simulated electron distribution (solid red line) and paramaterization assuming universality (dashed black line).

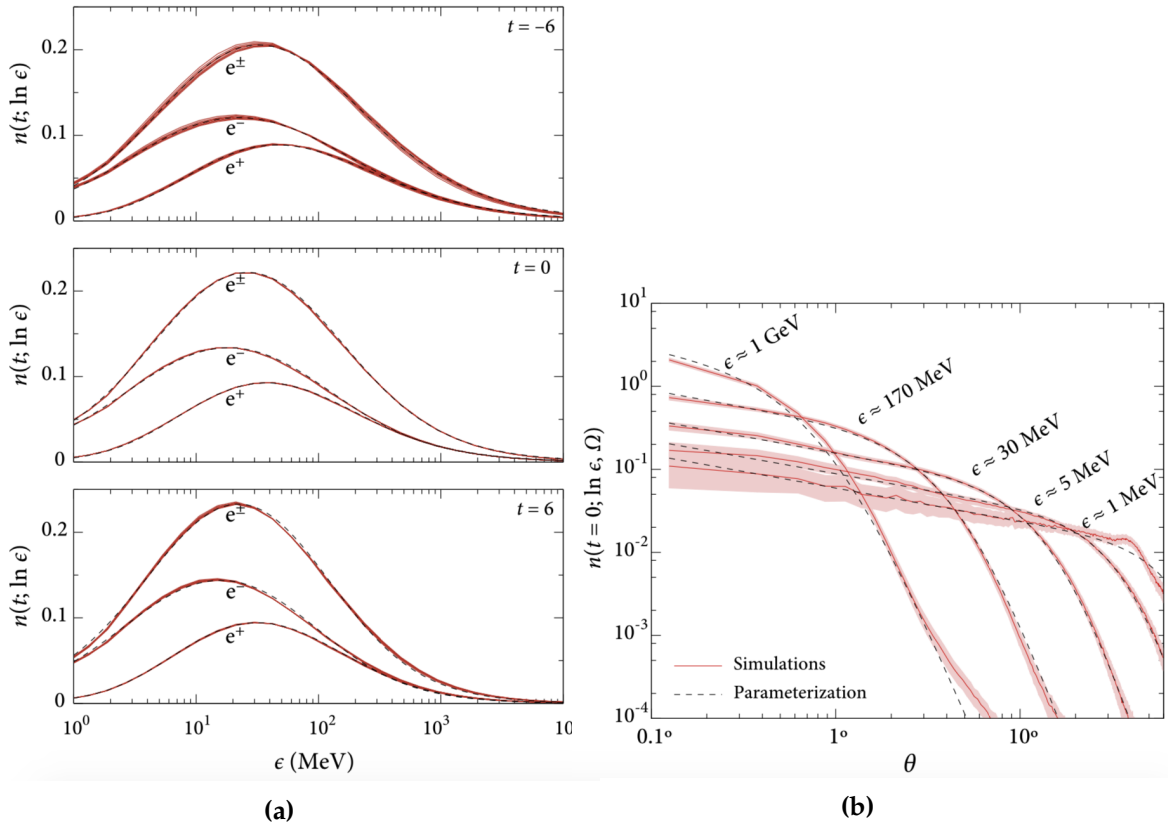

(a) **(b)**

Figure 3.1: a) Energy distribution for different evolution stages $t = -6, 0, 6$ for e^-, e^+ and their sum $e^\pm$. **b)** Normalized average electron distributions. The dashed lines correspond to the parameterization to simulated distributions for different primary species (p, Fe and γ) [56].

To put this into perspective for air showers seen by the Pierre Auger Observatory, the normalized longitudinal profiles (seen by FD) of extensive air showers should exhibit the same universal structures seen earlier in figures 3.1a and 3.1b at the same stage of shower

development. This is shown in figures 3.2a and 3.2b, clearly indicating the universal structure is primary and hadronic model independent as well as energy independent. The signals seen at ground by ground detectors are effectively the projection of the longitudinal profile.

3.2 Universality for Hadrons

As the universality model described in this chapter involves the WCD and MD, the shower stage is described with ΔX -the integrated atmospheric density from the shower maximum to the detector along the shower axis. This convention is most similar to the relative evolution stage t. The shower maximum refers to electromagnetic shower maximum $X_{\max}$ for WCD, whereas it refers to the maximum muon production depth $X^{\mu}_{\max}$ for the MD. The latter is newly introduced within the principles of Universality to study its potential and use for subsequent mass composition analyses. Figures 3.2c and 3.2d show the same study for the Universality of muons and reveals that under strict conditions the principles of Universality are *broken*. Average hadronic model and primary dependencies are within the 5 % level. However, the muon production depth distributions differ at the young (from $-600\,\mathrm{g\,cm^{-2}}$ to $-250\,\mathrm{g\,cm^{-2}}$) and old shower stage (from $250\,\mathrm{g\,cm^{-2}}$ to $600\,\mathrm{g\,cm^{-2}}$). Nevertheless, an overall quasi-Universal behavior is seen. These findings are used as motivation to continue building a Universality-based reconstruction for the MD.

Within the scope of Auger, air showers generated by hadrons are of interest where the added contribution of muons, produced through pion decay, should be accounted for. In previous works (e.g. [57]) a universal description of the signals was attempted by subdividing the arriving shower particles in the detector in: the muonic component, the purely electromagnetic component and the electromagnetic component from muon interactions and muon decay. However, as figure 3.3a shows, no universal signal behaviour is seen between the primaries and energies with deviations of up to 50 %. Equivalent features are also seen for muon signal responses (see figure 3.3b). Simulations have shown that a fraction of the purely electromagnetic component originates from the low-energy hadronic interactions (later referred to as *hadronic jet component*). Its size is directly proportional to the muon content, explaining the differences seen in figure 3.3b.

The muon content is introduced through a normalization factor R_{μ}, linked to the electromagnetic particles of the shower. Any shower can therefore be characterized by only R_{μ}, E, $\Delta X^{(\mu)}$ (ΔX or ΔX^{μ} for $X_{\max}$ or $X^{\mu}_{\max}$ respectively) and geometry.

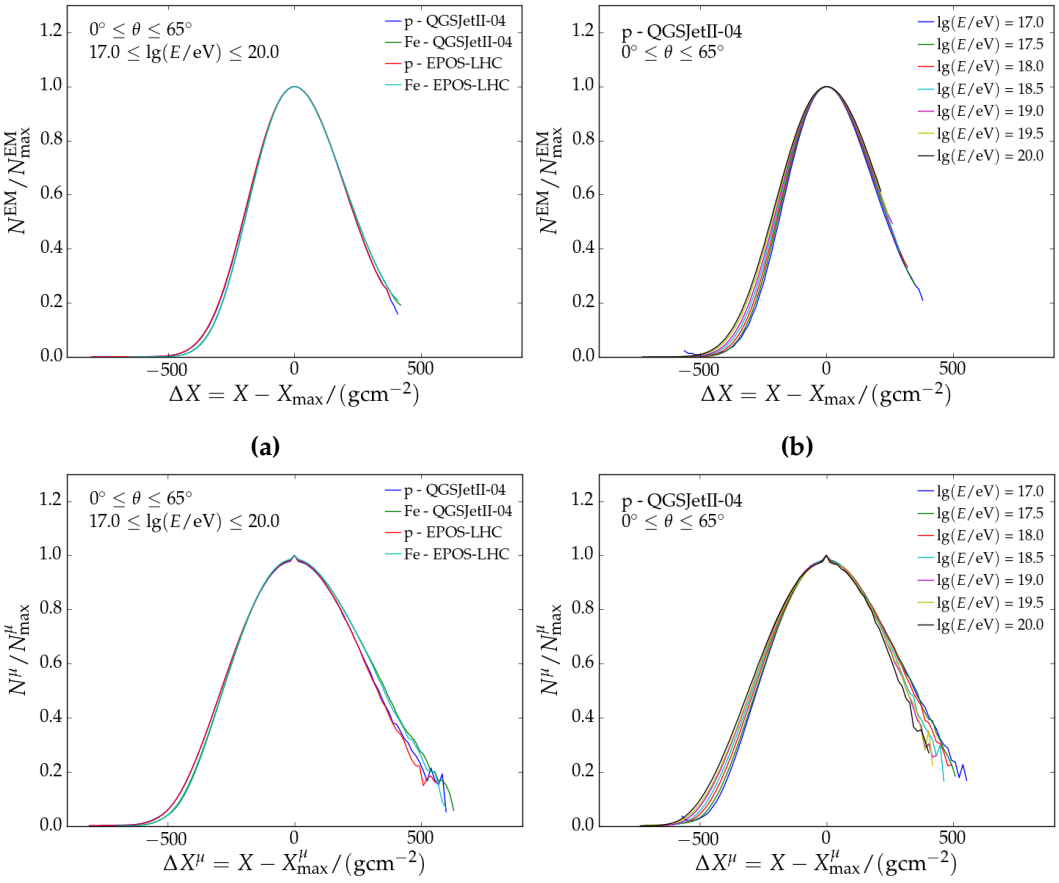

Figure 3.2: Average normalized longitudinal profile for the electromagnetic particles (muon production) for various **a)** hadronic models and primaries and **b)** energies. **c)** and **d)** are the same **a)** and **b)** but for the muon production depth distribution. Cuts seen on the right hand side of the longitudinal profiles are due to the shower arriving to ground. The distinct peak seen with the muon production is a binning artifact. 6720 and 960 showers were used to derive the average longitudinal profiles for each hadronic model (**a)** and **c)**) and energy bin (**b)** and **d)**) respectively.

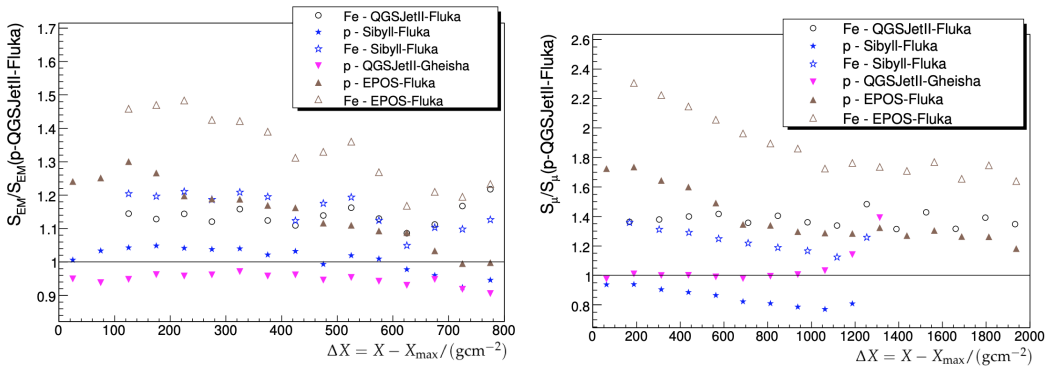

Figure 3.3: A Universality model for the WCD is designed with a proton primary and the hadronic model QGSJETII-03. **a)** The electromagnetic and **b)** muonic signal response both show a non-universal behaviour [57].

3.2.1 Particle Components

The muons and electromagnetic particles are categorized into four components [58]. These are

a. Muons ($\mu^{\pm}$)

b. Purely electromagnetic component

c. Electromagnetic components from muon interactions and muon decay

d. Electromagnetic component from low-energy hadrons

Muons (a) are identified and categorized based on the particle id from CORSIKA. Electromagnetic particles are also identified by their CORSIKA particle id. However, they are further categorized based on their origin and their relation with respect to the mother and grandmother particles. Information on the mother and grandmother particles can only be obtained by enabling the particle history during the CORSIKA simulations. Electromagnetic particles with a muon as a mother or grandmother particle are categorized as (c). Simulationas have shown that many decay products from neutral pions (decaying into photons) and charged pions (decaying into muons and subsequently into electrons) arrive to the detector through low energetic hadronic interactions [58]. They are referred to as hadronic jets and produce excess amount of electromagnetic particles through sub-showers. This feature is reflected in the peak seen in figure 3.4b (explained below).

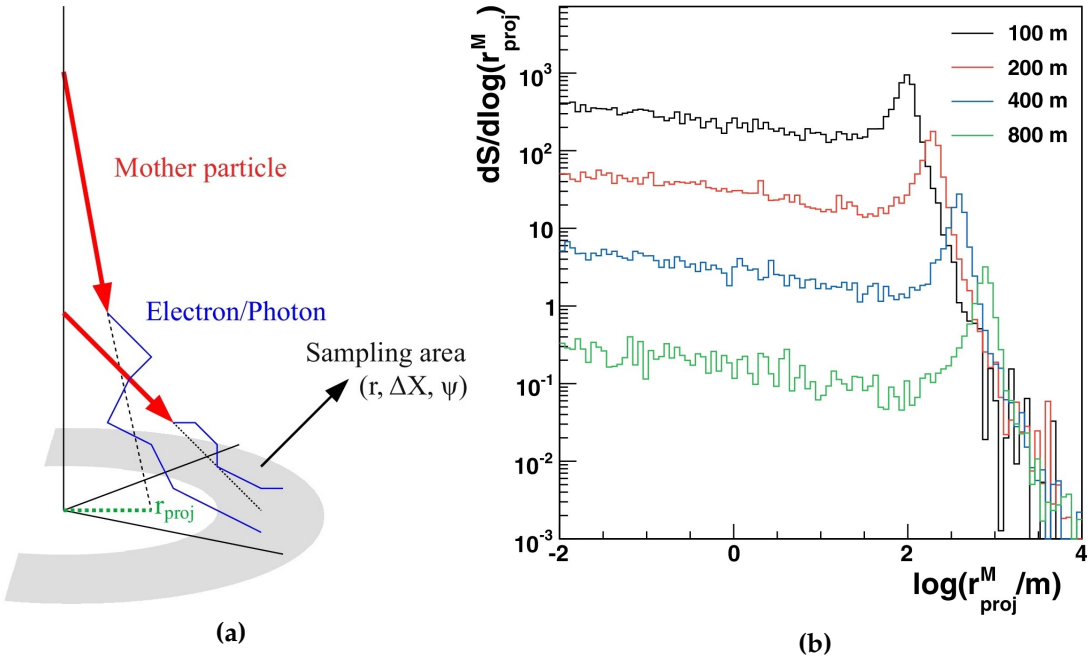

Figure 3.4: a) Example of possible hadronic jets. **b)** Distribution of r_{proj} for electromagnetic particles falling in specified radial distances [59].

Electromagnetic particles are sampled at radial distances of 100 m, 200 m, 400 m and 800 m. Assuming the scenario of a vertical shower at a radial distance of 800 m (±40 m), it is visible from figure 3.4a that the direction of mother particles, when extrapolated to ground, do not always fall within the same sampling area as their daughter particle counterparts. The project radial distance r_{proj} of the mother particles can be calculated and used to produce

the distributions seen in figure 3.4b. The figure is derived from a proton shower at 10^{19} eV, 45° and $X_{max} = 1020\,\mathrm{g\,cm^{-2}}$ (with the CORSIKA history option enabled). It shows a clear peak at the respective distances of the sampling areas. This clearly implies the presence of sub-showers for which the lateral displacement is dominated by the transverse momentum of particles initiating it. The peak-to-plateau ratio increases with increasing distances, showing its importance at larger distances [58]. Particles originating from hadronic jets are identified and later categorized as (d) with

$$\lg(r_{proj}) > \lg(r_{dist}) - 0.05, \tag{3.3}$$

where r_{proj} is the project radial distance of the mother particle and r_{dist} the radial distance of the sampling area. All other electromagnetic particle are categorized as (b). The only exception to equation (3.3) is if the grandmother particle is a photon.

The CORSIKA library used in this work (see section 4.1) is simulated with the history option enabled. However, due to time constraints, it was not possible to implement the aforementioned hadronic jet identification strategy. Instead, a strategy designed to be used for CORSIKA showers without the history option is used. The strategy is based on unique relation seen between the hadronic generation number and the particle weight. The hadronic generation number is a counter introduced to track the number of hadronic interactions that have occurred prior to the arrival of the particle at ground level [60]. Depending on the counter value, charged pion decays increase the counter value by 51. The decay of charged mesons add 31, whereas those from muon decays or interactions add 50. Per CORSIKA convention, the counter ends at 99. Based on these conventions, electromagnetic particles with a generation number above 50 are expected to be from muon decay products (c). This can be recognized in figures 3.5a and 3.5b.

Figures 3.5a and 3.5b show the hadronic generation number distribution for sampling areas at radial distances of 400 m and 800 m. Similar distributions are also seen closer to the core (up to 100 m, albeit with higher particle weight densities). In addition to the band seen above the generation number 50, there are two distinct peaks -below a particle weight of 500 and around 6000. The former is due the hadronic jets with particle weights at 99. By assigning those to (d), the final distribution will be that of the pure electromagnetic particle (b) (shown in figures 3.5c and 3.5d) [58].

The cumulative response of all four components defines the *total signal* and *trace* as

$$S_{tot} = \sum_{i=1}^{4} S_i, \tag{3.4}$$

$$\frac{\delta S_{tot}}{\delta t} = \sum_{i=1}^{4} \frac{\delta S_i}{\delta t}, \tag{3.5}$$

where i refers to the particle components. Each component is treated and modeled individually within the framework. A simplistic, however incorrect, interpretation would be to assume that each component represents a fraction of the total shower development. This implies that each component describes a different stage of the shower. All particle components share the same shower stage parameter (previously illustrated in figure 3.2). For all electromagnetic particles the atmospheric overburden ΔX from the detector to the shower maximum (X_{max}) parallel to the shower axis is used (see schematic in figure 3.6). For muons, ΔX is unsuitable to describe its attenuation. The dominant process for muons depends on

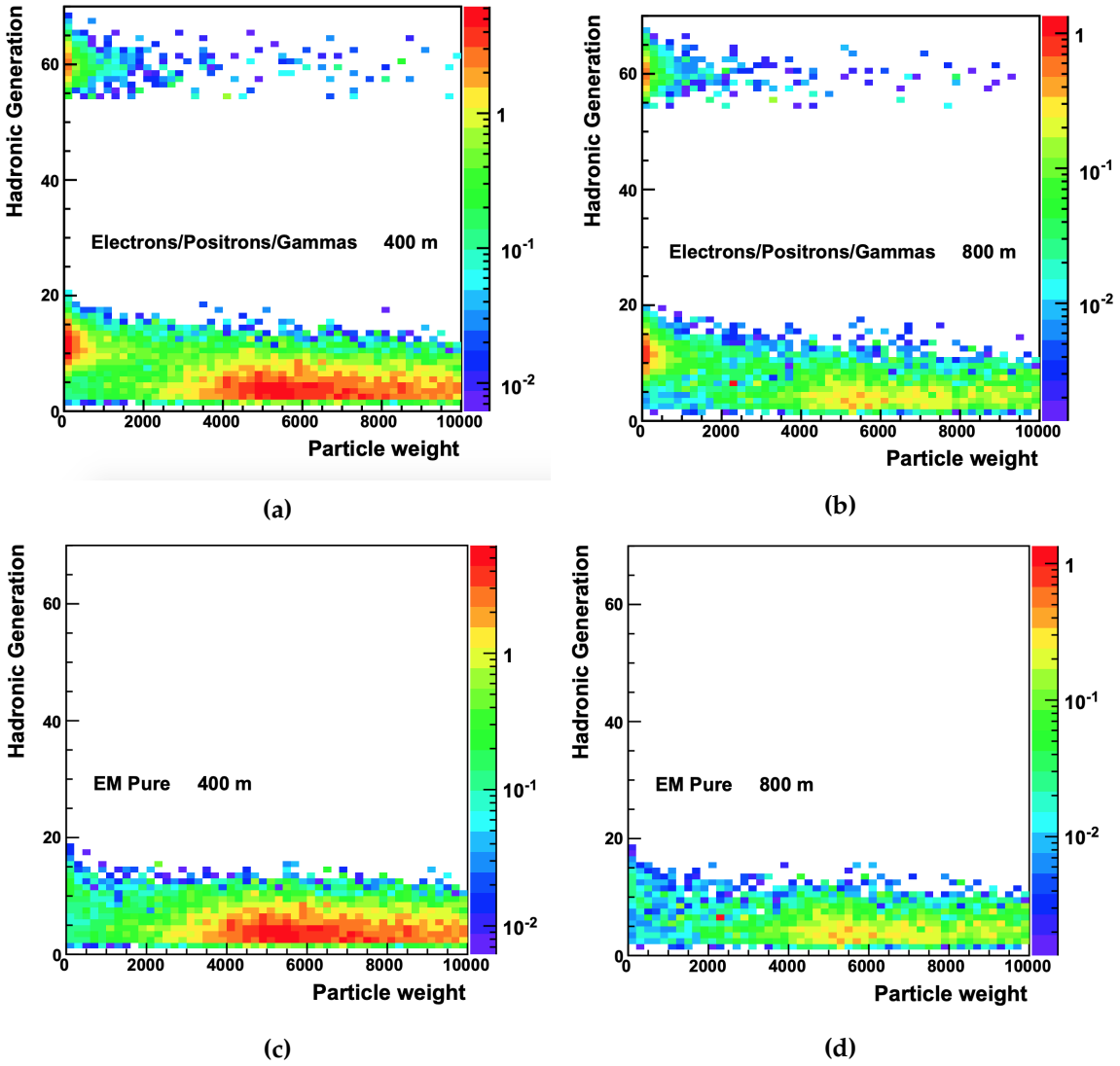

Figure 3.5: Particle weight with respect to the hadronic generation for sampling areas at 400 m and 800 m. **a)** and **b)** refer all electrons, positrons and photons. **c)** and **d)** shows the distribution without the hadronic jets [58].

its decay, which depends on the geometric path length and not the integrated atmospheric density. Therefore, ΔL is introduced to describe the geometric distance between the detector and shower maximum parallel to the shower axis. The shower maximum refers to $X_{\max}$ and $X^{\mu}_{\max}$ for WCD and MD respectively.

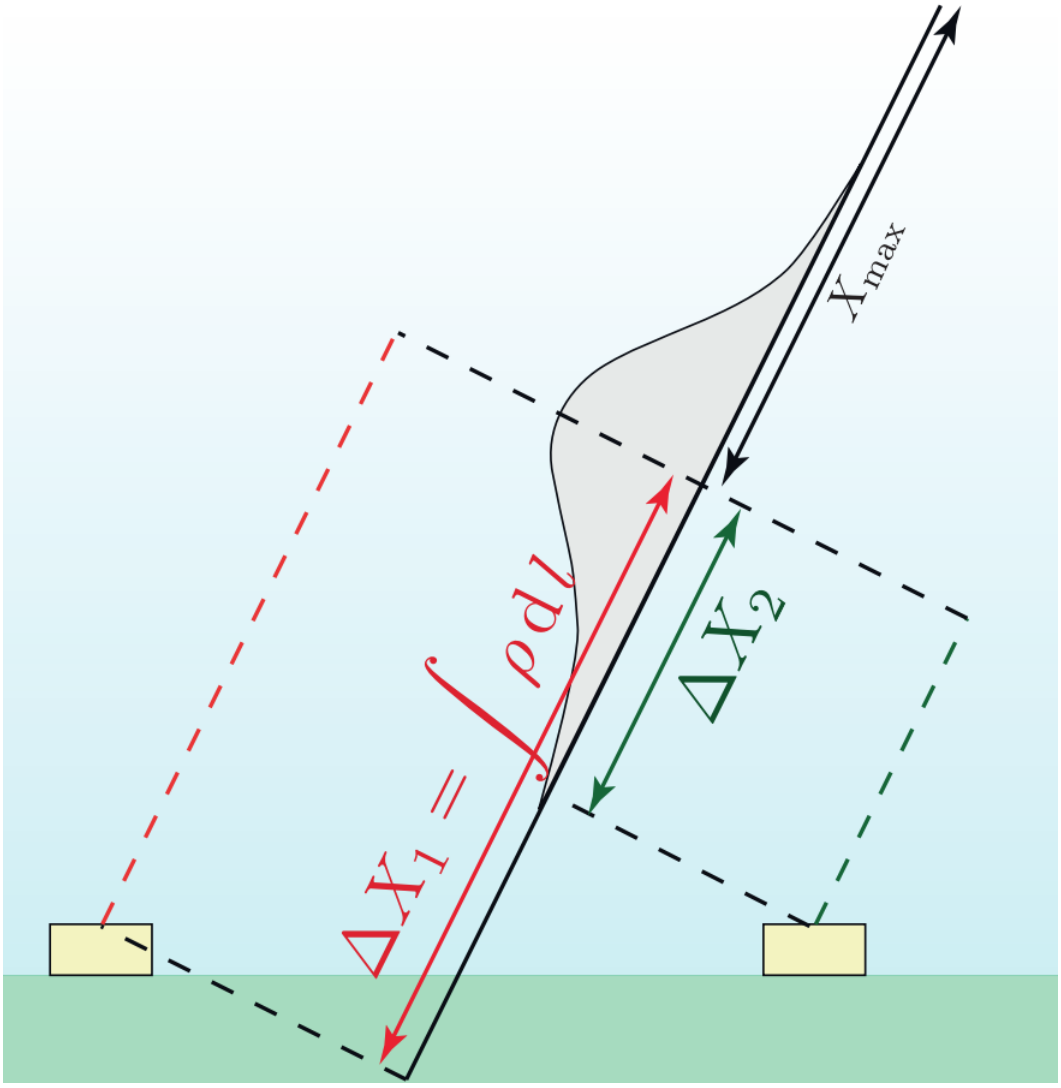

Figure 3.6: Schematic of the definition of the shower stage parameter ΔX. It is defined as the atmospheric overburden between the detector and shower maximum along the the shower axis. ΔX is only used for electromagnetic particles. Muon use ΔL -the geometric analog of ΔX.

CHAPTER 4

Universality Signal Model

With the principles of Universality described in chapter 3 a model describing the signal response for the WCD was developed [59]. Simulated showers were produced with CORSIKA v6.89 [61], a dedicated software which simulates extensive air showers initiated by high energy cosmic rays. Proton induced air showers were simulated with the high-energy hadronic interaction model QGSJETII-03 [62] and used as reference of the Universality signal model. It was designed to be used for the standard array at energies above $10^{18.5}$ eV. Inaccuracies for primaries and hadronic models were found to be better than 5 %-10 %.

In this chapter we introduce and validate an upgrade to the previous Universality signal model. It will be based on the latest hadronic interaction model QGSJETII-04, updated with data from the first LHC run. The new signal model will be extended down to 10^{17} eV to be used for data obtained from the infilled area. For the standard array S_{1000} is used, whereas the infilled array uses S_{450} as an energy estimator. Different energy estimators also implies that the reconstruction systematics are different, albeit using the same method. The extension for Universality signifies that a single model will be able to reconstruct data from the second knee to above the ankle. In addition to the energy extension, an entirely new model for the MD is introduced. It will exploit the quasi-Universal behaviour seen in figure 3.2c and introduce the possibility to reconstruct the maximum muon production depth.

Mass composition specific shower parameters of interest are the maximum shower depth X_{max}, maximum muon production depth X^{μ}_{max}, energy E and muon content R_{μ}. The signal model will be described in terms of these shower parameters as well as geometric and seasonal dependencies.

4.1 Simulations

The simulation is performed using CORSIKA v7.41 [61]. It handles simulation of particle cascades in the atmosphere initiated by cosmic rays such as hadrons or photons. It can handle relevant processes of particles such as their deflection in the magnetic field, energy loss and particle interactions. The atmospheric profiles used in CORSIKA are based on data from the GDAS and local weather information. These are selected prior to simulation with a flag. Primaries with energies of 10^{17} eV are several orders of magnitude larger than

those obtained at LHC (for proton-proton interaction). Simulations above the LHC limits are extrapolated through high-energy hadronic models. Here predictions from QGSJETII-04 [62] and EPOS-LHC [63] are used and studied in detail. Furthermore, the Universality model uses the same unit and coordinate convention as CORSIKA.

The number of secondary particles is proportional to primary energy. Simulating showers above 10^{16} eV become very time consuming despite the increased improvement of computing powers. This is solved by introducing a *thinning* mechanism. Particles below the adjustable fraction

$$\epsilon_{\text{th}} = \frac{E}{E_0} \tag{4.1}$$

for particle energy E and total energy E_0 are reduced to a single particle with a weight factor w_i, i.e., a particle with $w_i = 100$ and $E_i = 10$ GeV represents 100 particles at 10 GeV. Mostly, particles reaching the ground have a weight $w > 1$. The *unthinned* particle number is obtained from a Poisson distribution with a mean w. Their arrival times are smeared to avoid creating artificial muon peaks.

For the infilled array, full efficiency is achieved above $10^{17.5}$ eV ($10^{18.5}$ eV for the standard array). For the WCD, full efficiency is below 65°, whereas it is below 45° for the MD. Within these limits, the signal model is used to reconstruct the air showers. A discrete shower library is used for energies from $\lg(E/\text{eV}) = 17.0$ to $\lg(E/\text{eV}) = 20.0$ in steps of $\Delta \lg(E/\text{eV}) = 0.5$, and θ 0°, 12°, 22°, 32°, 38°, 48°, 56° and 65° (the latter used only for WCD). For each configuration 120 showers were simulated; 10 for each month of the year. For every month, 10 showers are simulated with the atmospheric profiles at the detector site. Accounting for the proton and iron primaries and the hadronic models (QGSJETII-04 and EPOS-LHC) a total of 26880 were used. The library is referred to as the *fixed library*.

Generally, the $\overline{\text{Off}}\underline{\text{line}}$ software framework [64] is used to simulate the time-dependent signal response of the ground detectors. The simulation starts with the CORSIKA simulation files where information on energy, type, momentum and arrival time of all secondaries reaching ground (*observation level*) are stored. To compensate for the small area covered by the WCDs and MDs and the use of *thinned* air showers, information from particles ±10 % of the distance of the station to the shower core is used. At e.g. 1000 m from the shower core, all particles between 900 m and 1100 m are used to form a *pdf*. Particles are then randomly selected from the *pdf* with respect to the ratio of the detector area and collection area (from 900 m to 1100 m here). All particles arriving at sed detector are then simulated for their combined detector response (more to it in sections 4.1.1 and 4.1.2). The $\overline{\text{Off}}\underline{\text{line}}$ framework properly accounts for the simulated particle fluctuations seen in showers. However, within the scope of Universality model development the *average* detector signal distributions (time dependant and total signal) are of interest. $\overline{\text{Off}}\underline{\text{line}}$ does not provide this but it could be obtained by using an array with *dense rings*.

Dense rings are virtual detectors placed in rings on the shower detector plane (the plane perpendicular to the shower axis) (as seen in figure 4.1) and form an ellipse (based on the zenith angle) within the array. They are closely placed to each other to sample the air shower more accurately. The average signal of all detectors in a ring provides a first order estimation of the signal. However, this method washes azimuthal effects for inclined showers away. Particles of inclined showers traverse through different atmospheric profiles, attenuate differently and thus deposit a different signal in the detector. To bypass this bottleneck, identical

stations could be simulated many times (effectively sampling many times from the particle *pdf*). This is computationally inefficient as this method implies that the same CORSIKA shower is simulated multiple times. Due to the architecture of Offline an alternative method is not possible. As a result, the *Universality framework*, designed for the model development, generates the average signal and time responses independently (albeit in a similar method). All particles within ±5 % from the specified shower distance (and azimuth) are averaged and scaled for the detector area, effectively using the previously inaccessible particle *pdf*. Nevertheless, detector responses are still derived from Offline. Particle and signal information are stored in sampling areas to be used when necessary. For the model development, these sampling areas are subdivided into radial distances of 60 m, 100 m, 150 m, 275 m, 450 m, 750 m, 1100 m, 1500 m and azimuth angles of 0°, 45°, 90°, 135° and 180°.

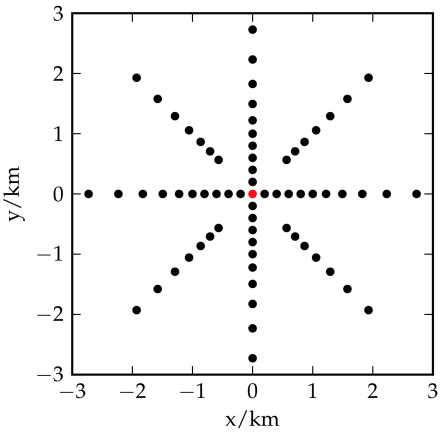

Figure 4.1: Schematic of a dense ring array commonly used in Offline the Universality framework. Coordinates are in the shower detector plane.

4.1.1 WCD Signal Response

The signal response of the WCD is simulated using Geant4. Cherenkov photons produced along the track length of the particles in the water are reflected on the inner Tyvek surface. Photons collected by photomultipliers are calculated. They will produce photoelectrons at the cathode; their photon number and arrival time recorded. Next, the amplification and time delay introduced by the dynode chain and the digitization in the FADC are simulated. Finally, the obtained signals are converted into VEM signal with the derived calibration function (see figure 2.1).

Closer to the shower core more particles penetrate the WCD, each of them to be simulated using Geant4. Computing all stations simultaneously leaves a large memory footprint, resolved by simulating one station at a time. Nevertheless, more particles imply a longer computation time (too long). For a large simulation library (necessary for Universality), using Offline for shower simulation purposes becomes a bottleneck. To resolve this, the tank response is derived from a pre-calculated tabulation.

With Offline, the number of photons that reach the cathode of each PMT is simulated with Geant4 for muons, electrons and photons. Particles are injected between zenith angles of 0° and 88°. Muons have energies between 1 MeV and 2500 GeV, whereas electrons and photons at 0.1 MeV and 100 GeV. The entry position is uniformly sampled in the projected

area of the tank. The probability of muons decaying in the tank is described as a function of energy. Muons, electrons and photons are simulated 10000, 3000 and 1000 times respectively to achieve an accuracy of $< 1\,\%$ for the tank response [65]. All simulated results are written to file and form the *Geant4 LookUp Table* (see schematic in figure 4.2). From CORSIKA showers, all secondary particles arriving to the detector are flagged to be compared with the tabulated signal response. Each particle has its own energy and zenith. These are used to interpolate the number of photoloelectrons produced in sed detector. All photoelectrons from all individual secondaries are summed to form (after calibration into VEM) the detector signal and used during development of the Universality model. Arrival times are stored in 2 ns time bins for a more detailed model description. This method becomes beneficial if electronics are upgraded as there will be no need to change the model (unless the sampling rate exceeds the 500 MHz).

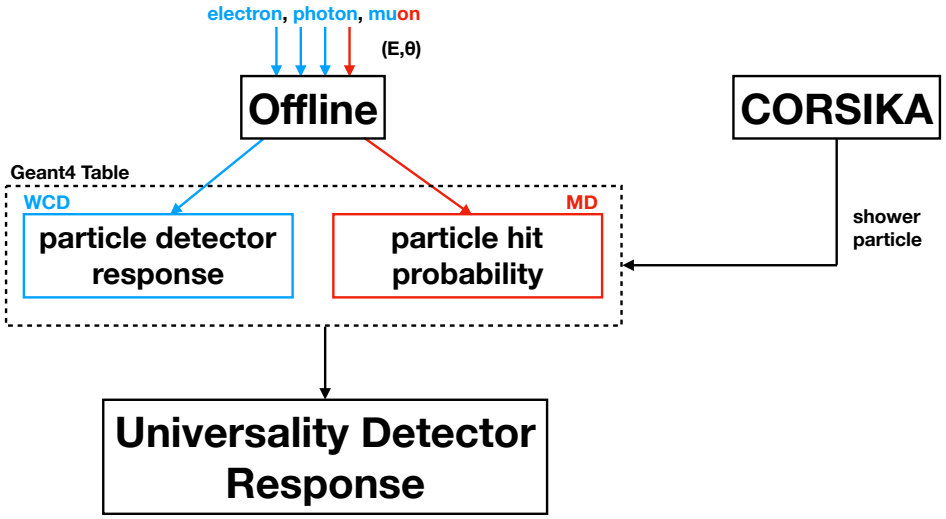

Figure 4.2: Schematic describing how the detector response is obtained. $\overline{\text{Off}}\underline{\text{line}}$ simulates the individual detector responses for muons, electrons and photons (depending on their injected energy and angle). These are stored in tables and called upon by particles from CORSIKA showers. All particles in a detector are superimposed and form the detector response used during development of the Universality model.

Figure 4.3 shows a comparison between the photoelectrons from $\overline{\text{Off}}\underline{\text{line}}$ and through interpolation with the Geant4 lookup tables. Detector signals with the tabulated response are well produced and are within 5 % with respect to a full simulation.

4.1.2 MD Signal Response

At the time of writing, SiPM Geant4 simulations for MD were not available. Geant4 tables only contain the *hit probability* of particles arriving to the module. They are defined as the probability of an injected particle at observation level to exist and impinge the detector after propagating 2.3 m underground. The energy loss is mostly caused through ionization and radiation, depending on incident particle energy. The concept of a hit probability therefore assumes an ideal detector without i) detector segmentation, ii) photon loss in the scintillator and iii) photomultiplier response. We address these issues to provide a more realistic de-

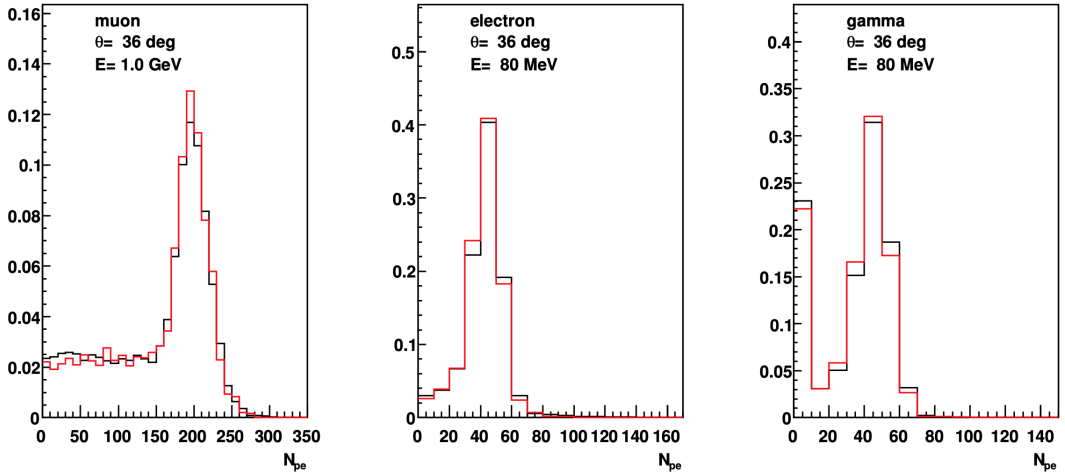

Figure 4.3: Comparison between the distribution of number of photoelectrons (N_{pe}) for muon, electrons and photons at $\theta = 36°$. Photoelectrons from the tabulation (red) are in agreement with the full Geant4 simulation (black) [65]. The left tail for the muon N_{pe} distribution is from muons close to the edge of the tank (corner clipping).

scription of the detector (a quasi-real detector).

Using $\overline{\mathrm{Off}}\underline{\mathrm{line}}$, hit probabilities are calculated for muon energies between 250 MeV and 100 GeV and zenith angles between 0° and 80°. Particles are injected at observation level. Due to the soil[1] shielding muons below 250 MeV are effectively stopped (hit probability at 0 %), whereas those above 100 GeV will always arrive (hit probability at 100 %) -an extract can be seen in figure 4.4. The well known muon energy threshold at 1 GeV can be seen for vertical muons. It increases by cos θ for inclined muons which is a direct consequence of the track length and thus its energy loss. From CORSIKA, incident particle energies of secondaries (at ground) are compared to the tabulated hit probability to extract the interpolated particle probability. The particle probability is then used as a *cut* on a binomial distribution of the form

$$B_{\mathrm{hit}} = \begin{cases} P_{\mathrm{hit}} & \text{for } 0 \leq x \leq P_{\mathrm{hit}} \quad \text{(successful hit)} \\ 1 - P_{\mathrm{hit}} & \text{for } P_{\mathrm{hit}} < x \leq 1 \quad \text{(unsuccessful hit)} \end{cases} . \tag{4.2}$$

After a random toss from a uniform distribution, x, in B_{hit}, particles below the cut (set by their probability P_{hit}) are considered as "a muon", whereas those above are not. The total signal in an ideal MD can then be expressed as

$$N_{\mu}^{\mathrm{ideal}} = \sum_{i=1}^{N_{\mathrm{particles}}} \begin{cases} 1 & \text{for } 0 \leq x \leq P_{\mathrm{hit}} \\ 0 & \text{for } P_{\mathrm{hit}} < x \leq 1 \end{cases} . \tag{4.3}$$

As equations (4.2) and (4.3) indicate, the segmentation of the MDs is not accounted for. It is irrelevant to the integrator strategy (where the signal of all scintillator bars are summed). However, for the 1-bit counting strategy, clipping corner effects ('false' signals due to muon crossing into neighbouring bars) are being ignored. This suggests that, during reconstruction, data from the 1-bit strategy will lead to azimuthal biases up to 20 %. As studies from the unitary cell have revealed [66], these biases can be corrected for during

[1]The soil reflects the one at the site of the Pierre Auger Observatory in Malargue. It is comprised of 66% SiO_2, 13% Al_2O_3, 6% Fe_2O_3 and CaO and 8% other minerals.

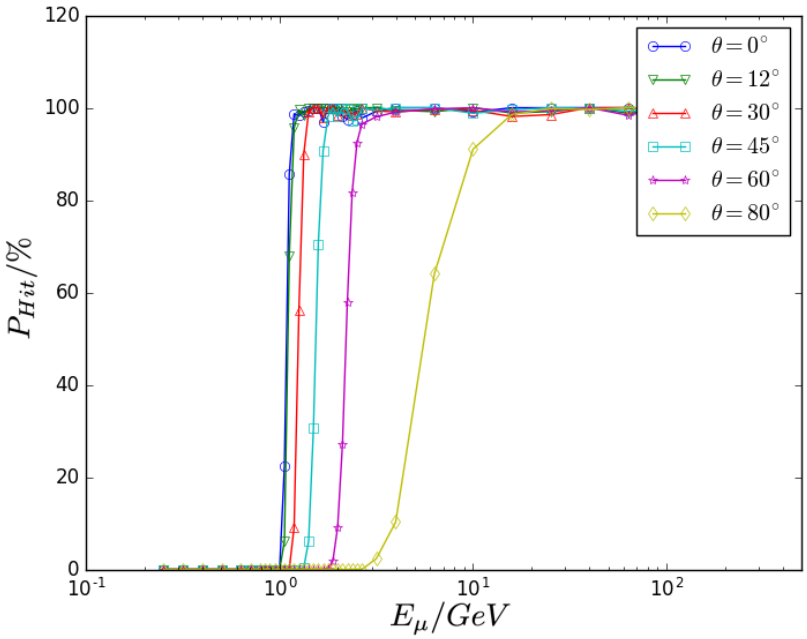

Figure 4.4: Hit probability as a function of energy and zenith of incident muon at a soil depth of 2.5 m.

the reconstruction as a function of shower zenith and detector azimuth. Results are based on data obtained with PMTs. Similar studies for SiPMs are not available and are strongly recommended to be done prior to using the Universality model for MD data. Regardless, for simulation purposes and model development clipping corner effects can be safely ignored.

At this point, muon arrival times correspond exactly to those obtained from CORSIKA. Time delays between the ground level and detector module level range between 8.33 ns ($\theta_p = 0°$) and 48 ns ($\theta_p = 80°$) depending on muon track length. Here muons are assumed to travel at relativistic speeds; their respective time delays described as a function of particle zenith. Additional time delays are also caused by photons travelling through the WLS before arriving to the photonmultiplier. These are included by injecting muons from a uniform distribution along the scintillator strip. The index of refraction for the WLS is 1.49 but since photons do not always propagate along a straight path, the effective index of refraction is determined to be 1.71 [67].

Photons propagating longer distances along the WLS are more attenuated and thus less likely to hit the cathode and pass the discriminator voltage set for the photomultiplier. An end-to-end lab measurement (described in reference [68]) was performed with a prototype SiPM to describe the combined effect of the attenuation and discriminator voltage as a function of photon path length. It is referred to as *detection efficiency* in reference [68]. Similar to the calibration for WCD, two small scintillator plates were placed above and below a sample scintillator bar used for the MD. These small scintillator plates serve as external triggers for atmospheric muons. They are initially placed at the furthest end of the scintillator bar and moved closer to the photomultiplier in 50 cm increments. As seen in figure 4.5, the detection efficiency does not decrease below 90 %. For larger overvoltages ΔV (voltage above which the SiPM operates in Geiger Mode) a better detection efficiency is obtained. However, the increased overvoltage also increases the noise.

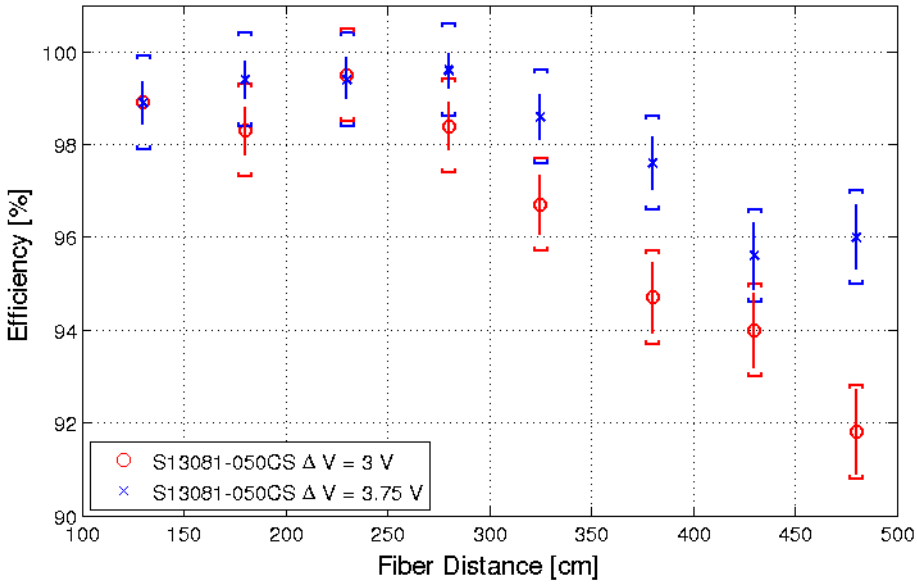

Figure 4.5: Detection efficiency for two different overvoltages ΔV. Larger ΔV increase the efficiency. Vertical lines and brackets represent statistical errors assuming a binomial distribution and systematics errors caused by false triggers respectively [68]

.

Efficiencies for $\Delta V = 3.75$ V are used in subsequent analyses. For the 1-bit strategy, the detector signal is now redefined as

$$N_{\mu}^{\text{1-bit}} = N_{\mu}^{\text{ideal}} \cdot f_{\text{eff}}(x), \tag{4.4}$$

where x is the muon impact distance to the SiPM. In this work, the efficiencies are obtained by interpolating the data seen in figure 4.5. The muon arrival time is defined as

$$t_{\text{1-bit}} = t_{\text{CORSIKA}} + t_{\text{depth}}(\theta_{\mu}) + t_{\text{WLS}}. \tag{4.5}$$

Currently, the only missing ingredient is to convolve the muon signal with the SiPM response function. The current signal and time response reflect those of the particle spectrum from the shower. Convolving with the SiPM pulse shape will change the overall shape of the raw signal trace and consequently (after digitizing) the 1-bit trace. At the time of writing, no definitive counting strategy was developed. Counting strategies generally follow after the definitive pulse shape of the SiPMs used in the array are known. At this stage, only pulse shapes from prototype SiPMs are known and used in this work. It is possible to introduce a prototype 1-bit counting strategy. However, this would be a highly speculative study which could introduce a biased model (only discovered in data, not simulation). It was discussed in section 2.3 that the counting strategy uses an inhibition window of 12bins (expected to be less for SiPMs) -each bin 3.125 ns wide. By assuming a perfect counting procedure (corrected for possible over- and undercounting), each 3.125ns time bin can be redefined as a bin containing the number of muons (not "1" or "0"). The added benefit of this is that the time trace becomes significantly more granular, benefiting the model development of the temporal response (later discussed in chapter 5). During reconstruction with the Universality model the accumulated signals of (in this example) 12 bins are used; as is intended for the 1-bit counting strategy.

Simulating the integrator is based on early measurements with the SiPM. The average signal will be equivalent to the 1-bit strategy. Figures 4.6a and 4.6b are based on data collected

from 10 m^2 modules in the AMIGA engineering array from 16-May-2017 until 30-September-2017. The histogram shown in figure 4.6a shows the charge produced by a single muon for a low gain SiPM. They are fitted with a Gaussian distribution and an empirical function provided by Hamamatsu for comparison. The Gaussian describes charge fluctuations better than the empirical function and is thus opted for further analysis. The normalized pulse shapes, for a low and high gain setup, of a muon can be seen in figure 4.6b. They are characterized by a Landau function modified with an exponential function and scale value to properly describe the tail of the pulse:

$$\frac{\delta S_{\text{pulse}}}{\delta t} = f_{\text{Landau}}(t) \cdot \frac{\exp(-t\alpha)}{\alpha}. \tag{4.6}$$

The integrator signal within the Universality framework is obtained by following the first initial steps as the 1-bit counting strategy (until the muon reaches detector level). Time stamps are recorded in 6.25 ns time bins (as per design; see section 2.3). The muon charge is obtained randomly from the charge distribution seen in figure 4.6a. Next, the muon charge is distributed based on the pulse response (see equation (4.6) and figure 4.6b). It is then calibrated with the mean value from the previously used charge distribution to obtain the number of muons. For low signals (below 5 muons), the calibrated integrator signal can deviate up to 10 % from $N_\mu^{\text{1-bit}}$. This is an expected feature caused by the random charge selection. For large signals this effect is below the 1 % level (due to sufficient particle statistics).

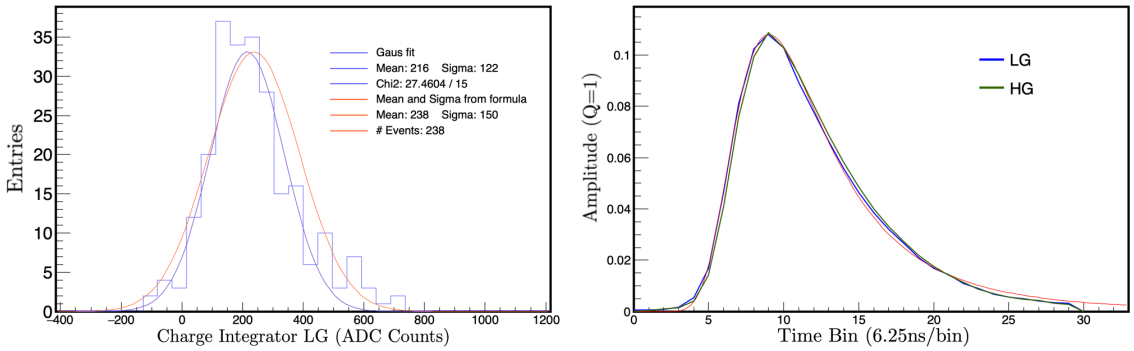

(a) **(b)**

Figure 4.6: a) Low gain charge distribution of a SiPM overlaid with a Gaussian and empirical fit function. **b)** Average normalized signal response function for a low and high gain setup. It is overlaid with a modified Landau function.

For the integrator strategy, the detector signal is defined as

$$N_\mu^{\text{ADC}} = \sum_{i=1}^{N_{\text{particles}}} \sum_{\text{bin}_{\text{start}}}^{\text{bin}_{\text{end}}} S_{\text{pulse}}^{\text{charge}}(t_{\text{bin}}) \cdot f_{\text{eff}}(x) \cdot \begin{cases} 1 & \text{for } 0 \leq x \leq P_{\text{hit}} \\ 0 & \text{for } P_{\text{hit}} < x \leq 1 \end{cases}. \tag{4.7}$$

The arrival time of muons is equivalent to equation (4.5). However, equation (4.7) basically describes the signal distribution of the collection of pulse responses generated by all injected muons. The signal trace is effectively its convolved from, simplified as

$$\frac{\delta S}{\delta t} = \int P_{\text{shower}}(t) \cdot D_{\text{response}}(t - t')\, dt', \tag{4.8}$$

where $P_{\text{shower}}(t)$ is the time distribution of the shower particles and $D_{\text{MD response}}(t)$ the detector response.

4.2 Signal Parameterization

We develop a parameterization for the signal in a WCD and a MD and will discuss both in this section. They are tuned to proton showers using QGSJETII-04 and the phase-space where these detectors operate at full efficiency in the infilled array. For the WCD, the model is tuned for energies above 10^{17} eV[2], zenith angles of $0° - 65°$ and radial distances up to 1500 m in the shower plane. The MD is similarly tuned with the only difference being that zenith angles range between 0° and 56°.

The extensive air showers are characterized by the shower energy E, electromagnetic shower maximum X_{max} (only WCD), maximum muon production depth X^{μ}_{max} (only MD), zenith θ, azimuth ψ, atmospheric air density $\rho^{\text{air}}_{\text{ground}}$ and muon content R_{μ}. This model extends and redesigns an earlier Universality model described in reference [59]. Similar approaches were taken to obtain the WCD and MD signal models. For simplicity, we therefore introduce the convention that any outlined procedure/parameterization is equivalent for both detectors unless stated otherwise. Due to the vast number of parameters, the parameter values are not always shown. These can be found in [69].

The parameterization for the signal is based on the parameterization of the four individual particle components. Following the principles of air shower Universality, we use the particle spectrum as the foundation of the parameterization, which is reflected in the particle density and subsequently the signal size. We therefore begin with the density of particles corrected for the detector area and particle spectrum. This is followed by atmospheric corrections (such a seasonal effects). Azimuthal signal asymmetries from particles propagating through different atmospheric profiles are also accounted for. Finally, the relative contribution of each signal component is accounted for with the introduction of R_{μ}. This ansatz is described by

$$\begin{aligned} S(r,\psi,E,X^{(\mu)}_{\text{max}},R_{\mu},\theta,\rho^{\text{air}}_{\text{ground}}) &= S^{\mu}_{\text{ideal}}(r,\Delta L^{(\mu)},E) \\ &\cdot f^{\mu}_{\text{mod}}(r,\psi,\theta)\ \cdot\ f^{\mu}_{\text{atm}}(r,\rho^{\text{air}}_{\text{ground}})\ \cdot\ f^{\mu}_{\text{conv}}(r,\Delta L^{(\mu)},\psi,\theta)\ \cdot\ f^{\mu}_{R_{\text{fluct}}}(r,R_{\mu}) \\ &+ \sum_{\text{icomp}=2}^{4} S^{\text{icomp}}_{\text{ideal}}(r,\Delta X,E) \\ &\cdot f^{\text{icomp}}_{\text{mod}}(r,\psi,\theta)\ \cdot\ f^{\text{icomp}}_{\text{atm}}(r,\rho^{air}_{\text{ground}})\ \cdot\ f^{\text{icomp}}_{\text{conv}}(r,\Delta X,\psi,\theta)\ \cdot\ f^{\text{icomp}}_{R_{\text{fluct}}}(r,R_{\mu}), \end{aligned} \tag{4.9}$$

where the different terms are:

- $S_{\text{ideal}} \cdot f_{\text{mod}}$: signal for an ideal detector with the correction factor introduced for azimuthal dependencies
- f_{atm}: factor to correct for seasonal and day/night atmospheric changes
- f_{conv}: conversion factor to a realistic detector

[2] Although the model is tuned for energies above 10^{17} eV, it uses showers at 10^{18} eV as reference and normalizes based on signal at that energy.

- $f_{R_{\text{fluct}}}$: correlation factor between the component signal

The bracketed notation seen in e.g. $X_{\max}$ (or $\Delta L^{(\mu)}$) refers to the maximum muon production depth (not to be confused with the muonic shower component).

4.2.1 Conversion to a Real Detector Response - f_{conv}

The signal of an ideal detector is defined as that of a spherical detector with a projected area of 10 m^2, irrespective of the incoming direction of the particle, and the response function of *vertically* arriving particles. This definition serves as an intermediate step to describe the geometric detector effects.

By defining ρ as the particle number for a differential surface area δA

$$\rho = \frac{\delta N}{\delta A}, \tag{4.10}$$

and p_z as the cosine of the angle subtended by the particle momentum with respect to the shower axis ($p_z = \cos \alpha_{pz}$ in figure 4.7), introduced to the particle density through its angular distribution, it is possible to define the ideal detector signal with

$$S_{\text{ideal}}(r, \Delta X, \Delta L^{(\mu)}, \psi, \theta = 0°) = \int_{-1}^{1} \frac{\delta^2 N}{\delta A \delta p_z} \cdot A_v \cdot T_0(r, \Delta X, \Delta L^{(\mu)}, p_z)\, dp_z, \tag{4.11}$$

where A_v refers to the 10 m^2 projected detector area and T_0 to the detector response function. The latter is the convolved response of the particle energy spectrum $\frac{\delta N}{\delta E}$ and detector response of a vertical particle. This can be written as

$$T_0(r, \Delta X, \Delta L^{(\mu)}, p_z) = \int_{E_{min}}^{E_{\max}} \frac{\delta N}{\delta E_p}(r, \Delta X, \Delta L^{(\mu)}, p_z) \cdot S_{\text{detector}}(E_p, \theta_p = 0°)\, dE_p, \tag{4.12}$$

where $S_{\text{detector}}(E, \theta_p = 0°)$ is the detector signal of a vertical particle with energy E_p (extracted from the tabulated signals). As figure 4.7 already hints, the analytical description in equation (4.11) overestimates the ideal signal for inclined showers. Upwards moving particles ($\theta_p > 90°$) must be rejected by introducing a cut at p_z^{cut}. At first glance, this step may seem redundant as T_0 (see equation (4.12)) will naturally be 0 below p_z^{cut}. However, the detectors cannot distinguish between individual particles during data taking. Therefore, T_0 must be parameterized through simulations. The functional shape derived from it is then used in equation (4.11), revealing the necessity for p_z^{cut}.

Using figure 4.7 as reference, we see that p_z^{cut} is at $\cos\theta$. Assuming a radially diffuse shower particle, p_z^{cut} can be generalized with

$$\cos\theta_p = p_z \cos\theta + \sin\theta \cos\psi \sqrt{1 - p_z^2}. \tag{4.13}$$

This is illustrated in figure 4.8 with the black dashed line. As the data points already show, the shower particles are not perfectly diffuse. Equation (4.12) is therefore adjusted with A_{rad}, a correction factor obtained by fitting with

$$\cos\theta_p = p_z \cos\theta + A_{\text{rad}}(r, \theta) \sin\theta \cos\psi \sqrt{1 - p_z^2}. \tag{4.14}$$

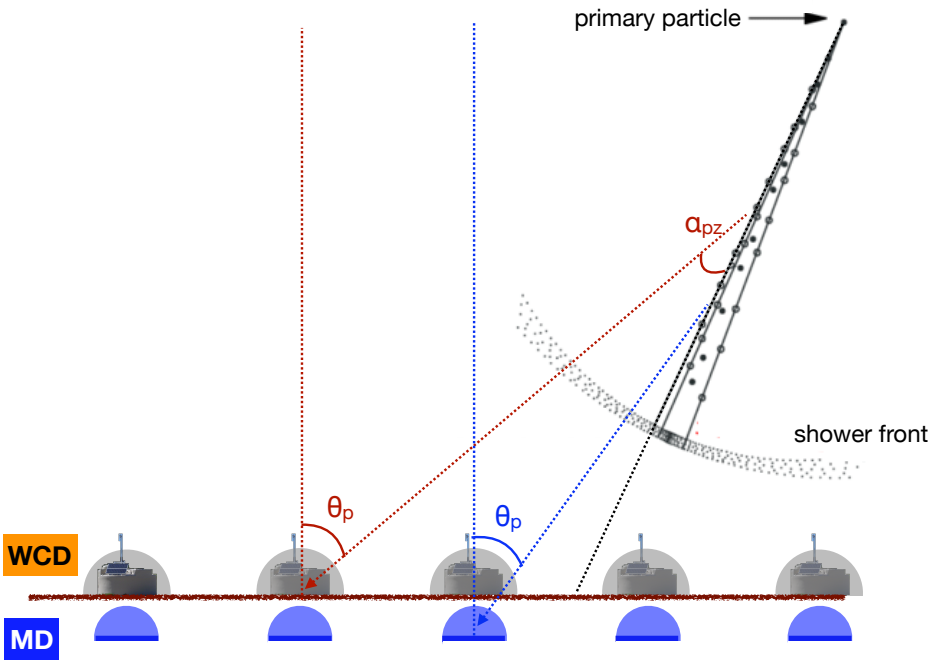

Figure 4.7: Schematic of particles arriving to the WCD and MD from an inclined shower. *Real* detectors are illustrated by a miniature WCD and dark rectangular (MD module), whereas their *ideal* counterparts are the semi-transparent half spheres. The analysis assumes full spheres with a projected area of 10 m^2; half spheres were drawn for illustrative purposes only. θ_p is the particle angle with respect to the detector and p_z the cosine subtended by the particle direction ($\cos \alpha_{p_z}$).

Here, p_z and $\cos \theta_p$ are directly obtained from CORSIKA simulations. The functional shape for A_{rad} is designed to account for radial and zenith dependencies (see figure A.2) and, as the figures in 4.8 show, provide for a very good representation of the diffusive behaviour of shower particles. For vertical showers the relation between p_z and $\cos \theta_p$ is at unity. Minor differences between the MD (figure 4.8c) and WCD (figure 4.8a) are evident for the standard deviation of the average values. This is a feature resulting from the MD being more sensitive to the higher end of the muon energy spectrum, which are generally more boosted (and thus more frequent at higher p_z).

By introducing p_z^{cut} and formulating equation (4.11) more compactly, we obtain

$$S_{\text{ideal}} = \int \frac{\delta S_{\text{ideal}}}{\delta p_z}\, dp_z = N_{\text{norm}} \int_{p_z^{\text{cut}}}^{1} \frac{1}{N} \frac{\delta \rho}{\delta p_z} A_v T_0\, dp_z, \tag{4.15}$$

with A_v and T_0 as the projected area and detector response for a vertical particle. N_{norm} is introduced as a normalization constant for the integral in the range of -1 and 1 to become unity. It is defined as

$$N_{\text{norm}} = S_{\text{ideal}}(r, \Delta X, \Delta L^{(\mu)}) \cdot f_{\text{mod}}(r, \psi, \theta), \tag{4.16}$$

where S_{ideal} and f_{mod} are as defined before (the latter to be further discussed in section 4.2.3). Introducing the normalization factor N_{norm} here is very convenient as we can derive the real signal by only parameterizing the ideal signal for a differential δp_z. The actual projected

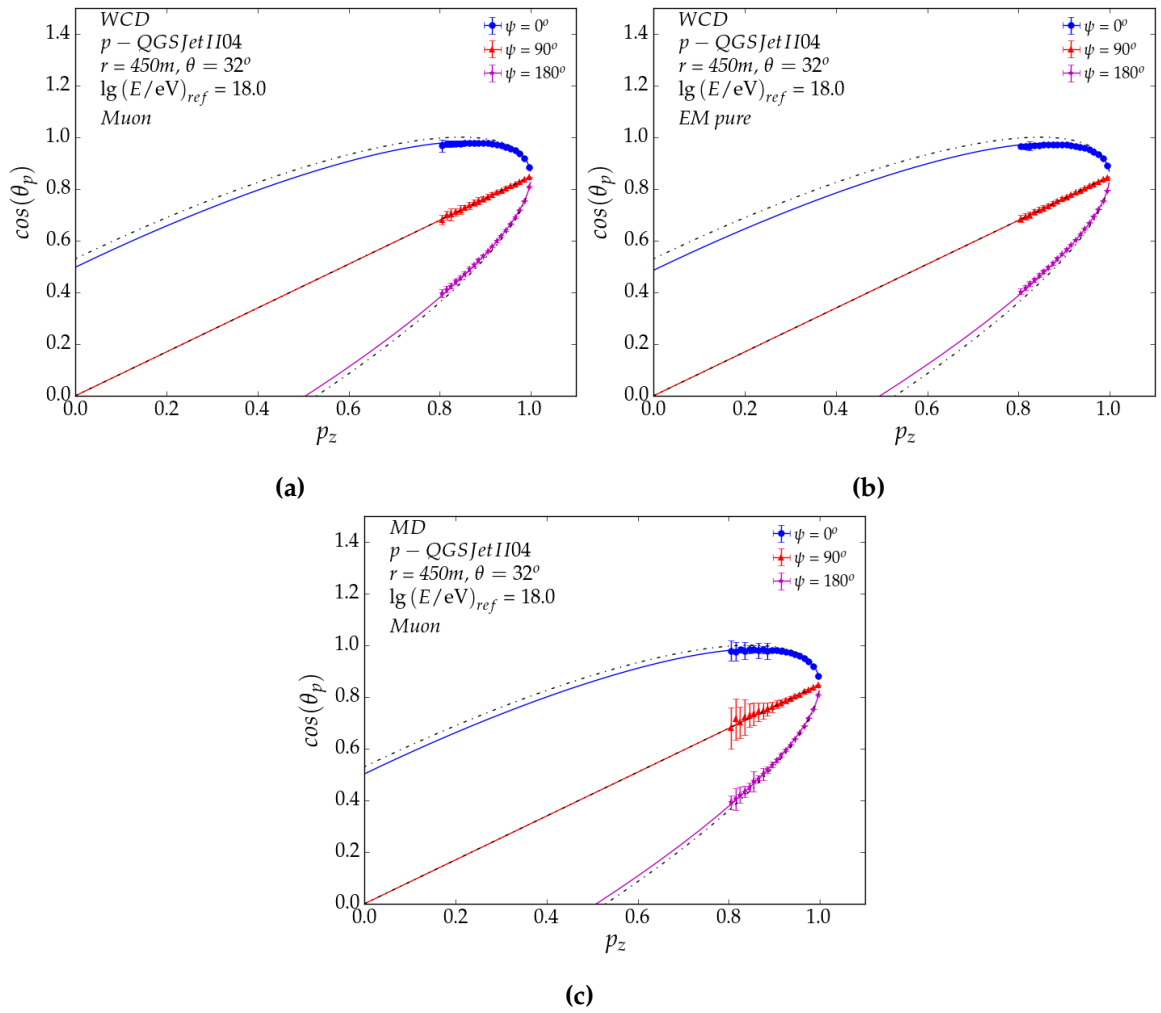

Figure 4.8: Average $\cos\theta_p$ as a function of p_z for the **a)** muonic and **b)** pure electromagnetic component in the WCD and the **c)** muonic component in the MD. The black dashed lines are the expected values for the approximation of a radially diffuse shower particles. The remaining figures for the electromagnetic component from muon particles and hadronic jets can be seen in figure A.1.

detector area with the information from the particle energy spectrum can be combined into a single quantity ($A_{\text{mod}}T_{\text{mod}}$). Therefore, the *real* signal is defined as

$$S_{\text{real}}(r, \Delta X, \Delta L^{(\mu)}, \psi, \theta) = N_{\text{norm}} \int_{p_z^{\text{cut}}}^{1} \frac{\delta S_{\text{ideal}}}{\delta p_z}(p_z, r, \Delta X, \Delta L^{(\mu)}) \cdot A_{\text{mod}}(\theta_p) \cdot T_{\text{mod}}(\theta_p, r, \Delta X, \Delta L^{(\mu)}, p_z)\, dp_z, \tag{4.17}$$

where A_{mod} and T_{mod} are

$$A_{\text{mod}} = \frac{A_{\theta_p}}{A_v}\ ,\ T_{\text{mod}} = \frac{T_{\theta_p}}{T_0}. \tag{4.18}$$

The integral in equation (4.17) is equivalent to the definition of f_{conv}.

The distribution for $\frac{\delta S_{\text{ideal}}}{\delta p_z}$ is obtained from simulations with $\psi = 0°$ and all zenith angles. Showers at the reference energy of 10^{18} eV are used. They are parameterized by first describing the mean of the distribution as a function of r and $\Delta X/\Delta L^{(\mu)}$. Only forward particles

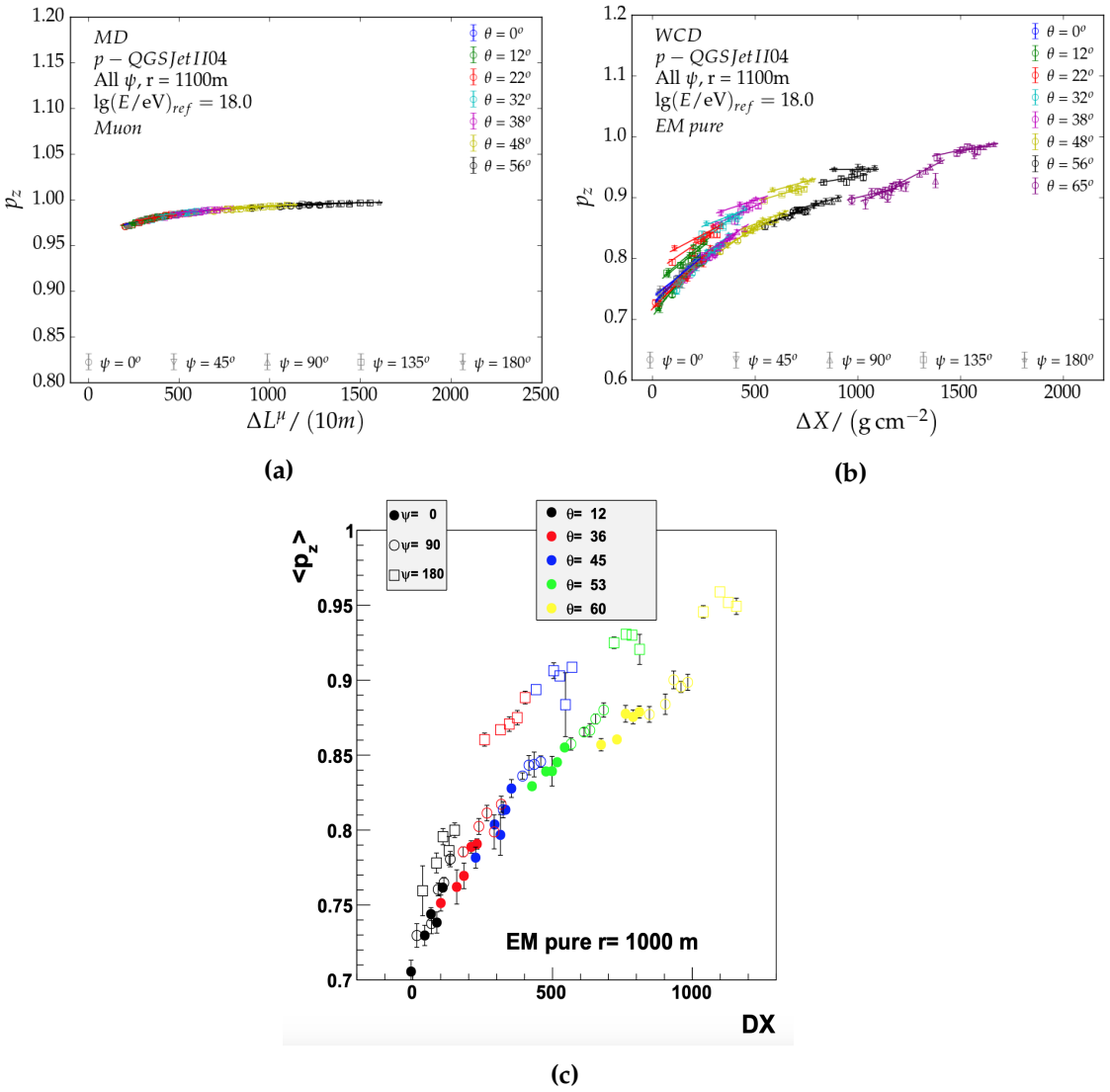

Figure 4.9: Average p_z distribution of the **a)** MD muon and **b)** WCD pure electromagnetic component. For comparison, the same analysis of **b)** is shown in **c)** for an earlier signal model developed with proton QGSJETII-03 as reference [58]. Marker represent the average value of 20 showers with the same zenith. The error bars are their respective RMS.

($0 < p_z < 1$) are used but their distributions will be normalized in the full range (-1,1) [58]. This allows for comparisons to be made between $\psi = 0°$ and $\psi = 90°$ (p_z^{cut} is always 0 for the former; see equation (4.12)). To derive $\frac{\delta S_{\text{ideal}}}{\delta p_z}$, the assumption is made that the change in $\frac{\delta S_{\text{ideal}}}{\delta p_z}$ is only due to the change in $p_z(r, \psi, \Delta X, \Delta L^{(\mu)})$.

The mean for each p_z is obtained by binning 20 showers (of the 960 shower in total -120*8 zenith angle bins) in groups of $\Delta X/\Delta L^{(\mu)}$. These are then individually fitted for every radial distance of the sampling area with a linear function. This is illustrated in figure 4.9 for the muon component of the MD and the electromagnetic component for the WCD. Additional figures for all components of WCD can be seen in figure A.2.

The figures in 4.9 show the mean p_z distribution for all zenith angles (colored), azimuth and the corresponding linear fit. As figure 4.9a shows, muons (as expected) are mostly close

to 1. The slight dip at low ΔL^{μ} is from more vertically inclined showers. For those showers, muons mostly arrive at 1100 m from a younger shower stage. p_z would have been much lower had they originated at a later shower stage (although this scenario is very unlikely and reflected in the average p_z values). No biases are seen between the azimuthal angles.

For comparison we show the p_z distributions of the pure electromagnetic component in the WCD used for the new (figure 4.9b) and old (figure 4.9c) signal model. Note, the latter used proton QGSJETII-03 showers at 10^{19} eV as reference. The normalized p_z distributions are consistent with each other. Their average angular distribution is larger than those for muons (as expected). p_z distributions between $\psi = 0°$ and $\psi = 90°$ agree within fluctuations. For larger ψ angles, the average p_z is biased. This results from p_z^{cut} being larger than the lower limit of the p_z range used to calculate the mean [58] (resulting in the overestimation seen in the figure). This bias is evaded by basing the $\frac{\delta S_{\text{ideal}}}{\delta p_z}$ description solely on p_z for $\psi = 0°$. Its p_z distribution serves as a good unbiased estimate for all ψ angles.

Using the linear pre-fits (lines in figure 4.9), a generalized description for the average p_z is empirically derived for all shower particle components, accounting for radial shower stage dependencies. It is described as

$$p_z = a(r) + \frac{b(r) - a(r)}{\exp(-1) - 1} \cdot \left(\exp\left(\frac{\Delta L^{(\mu)} - 300\ \text{g cm}^{-2}}{500\ \text{g cm}^{-2}} \right) - 1 \right) \tag{4.19}$$

for the muons and

$$p_z = a(r)_{\text{icomp}} + \frac{b(r)_{\text{icomp}} - a(r)_{\text{icomp}}}{\exp(-1) - 1} \cdot \left(\exp\left(\frac{\Delta X_{\text{icomp}} - \Delta X_0}{\Delta X_1 - \Delta X_0} \right) - 1 \right) \tag{4.20}$$

for the electromagnetic particles. $\Delta X_{0,1}$ are constants introduced to minimize the covariance. They (ΔX_0, ΔX_1) are set at (100 g cm^{-2}, 600 g cm^{-2}) and (300 g cm^{-2}, 800 g cm^{-2}) for the pure electromagnetic component and the remaining components respectively. $b(r)$ and $a(r)$ are radially dependant parameters defined as

$$a(r), b(r) = \alpha_0 + \frac{\alpha_1 - \alpha_0}{\exp(\alpha_2) - 1} \cdot \left(\exp(-\alpha_2 r) - 1 \right), \tag{4.21}$$

where α_i are the fit parameters. The figures in 4.10 show the fits to the p_z distribution with equations (4.19) and (4.20). They are shown for the muons in the MD and all shower particle components in WCD. The functional shape is in agreement with its predicted value (well within the 5 % level). The variance of each binned p_z (error bars in figure 4.10) are shown in the figures in A.3. They are equally characterized (albeit with different parameter values) as in equations (4.19), (4.20), and (4.21) and later used for $\frac{\delta S_{\text{ideal}}}{\delta p_z}$.

With the assumption of $\frac{\delta S_{\text{ideal}}}{\delta p_z}$ being only p_z dependant, it is characterized with a gamma function [59]

$$\frac{\delta S_{\text{ideal}}}{\delta p_z^{bin}} \left(p_z^{bin} \right) = \frac{\left(1 - p_z^{bin}\right)^{\alpha} \exp\left((p_z^{bin} - 1)/\beta \right)}{\Gamma(\alpha)\, \beta^{\alpha}\, N_{\text{norm}}}, \tag{4.22}$$

where α and β are defined by

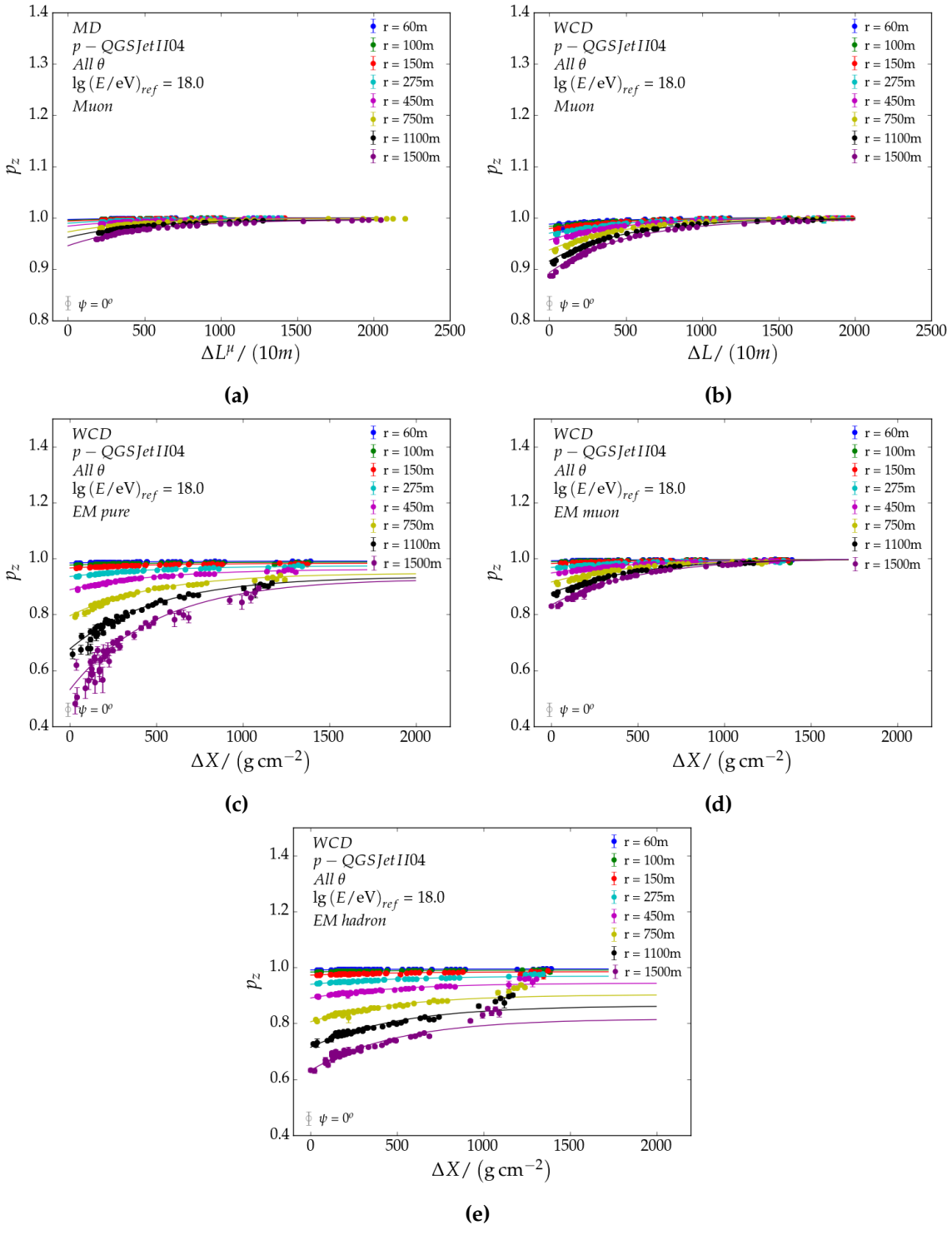

Figure 4.10: Average p_z distributions of 960 showers (all available zenith angles) at 10^{18} eV with respect to the shower stage $\Delta X/\Delta L^{(\mu)}$. Different distributions are shown at various radial distances to the shower core. Solid lines depict their respective model predictions. Their variances (error bars) can be found in the figures in A.3. They are also characterized.

$$\alpha = \left(\frac{1-\mu_{p_z}}{\sigma_{p_z}}\right)^2, \qquad \beta = \frac{\sigma_{p_z}^2}{1-\mu_{p_z}}. \tag{4.23}$$

Here, μ_{p_z} and σ_{p_z} are the previously derived estimators for the mean and variance of the binned p_z. In equation (4.22), N_{norm} is the normalization factor for which $\int_{-1}^{1} \frac{\delta S_{\text{ideal}}}{\delta p_z^i}(p_z)\, dp_z = 1$.

The final result for $\frac{\delta S_{\text{ideal}}}{\delta p_z}$ is illustrated in figure 4.11 for the MD and WCD and their respective particle components. It shows the cumulative $\frac{\delta S_{\text{ideal}}}{\delta p_z}$ distribution of a random sample shower compared to its prediction (960 showers were used for the parameterization) for various radial distances at $\psi = 0°$ (results also apply to all azimuth angles). Clear separations are seen below the 1 % quantile; especially for radial distances close to the core. Predictions for muonic components of the WCD and MD appear to underperform but they are in agreement for 95 % of the distribution (most of them are naturally clustered at p_z=1). Distributions for the electromagnetic particles have smaller biases compared to muons below the 1 % quantile but also fluctuate significantly more. Nevertheless, more than 99 % of their distributions are within the 5 % level of the model prediction. It can be argued to further improve the model to minimize the biases below 150 m. At these distances, the model is within the 10 % level for 95 % of the distribution. Also, depending on shower energy, most detectors at those distances are saturated.

The second factor in the integral in equation (4.17), $A_{\text{mod}}T_{\text{mod}}$, is parameterized with dependencies of r, θ_p and p_z. Dependencies of $\Delta X/\Delta L^{(\mu)}$ are negligible. They are derived from simulated showers at the reference energy of 10^{18} eV for all zenith angles. As before, we use $\psi = 0°$ to minimize biases. Using equation (4.18), $A_{\text{mod}}T_{\text{mod}}$ becomes

$$A_{\text{mod}}T_{\text{mod}} = \frac{A_{\theta_p}T_{\theta_p}}{A_v T_0}, \tag{4.24}$$

where T_{θ_p} is the general expression of equation (4.12) and

$$A_{\theta_p} = A_v \cos\theta_p + A_h \sin\theta_p, \tag{4.25}$$

with the addition of the detector area in the horizontal direction A_h. As a first order approximation, the MD can be considered without A_h (because $A_v >> A_h$) and thus $A_{\theta_p} \approx A_v \cos\theta_p$. Regaedless, equation (4.25) is still used for exactness. $A_{\text{mod}}T_{\text{mod}}$ is derived by first characterizing as second order polynomials in $\cos\theta_p$ for every radial distance and bins of the p_z distribution. The parameters are then characterized for their dependency to the binned p_z^{bin} and subsequently r. The former is found to be

$$p_z^{\text{bin}} = \alpha_1(r) + \frac{\alpha_2(r)-\alpha_1(r)}{\exp\left(-\alpha_3(r)\right)-1} \cdot \exp\left(-\alpha_3(r) \cdot \frac{1-p_z}{1-C_{pz}^{\text{icomp}}}\right), \tag{4.26}$$

where C_{pz}^{icomp} is a particle component dependent constant set at 0.5 and 0.8 for muons and electromagnetic particles respectively. $\alpha_i(r)$ is similarly characterized as

$$\alpha_i^{\text{icomp}} = p_1 + \frac{p_2-p_1}{\exp\left(-p_3\right)-1} \cdot \exp\left(-p_3 \cdot r\right), \tag{4.27}$$

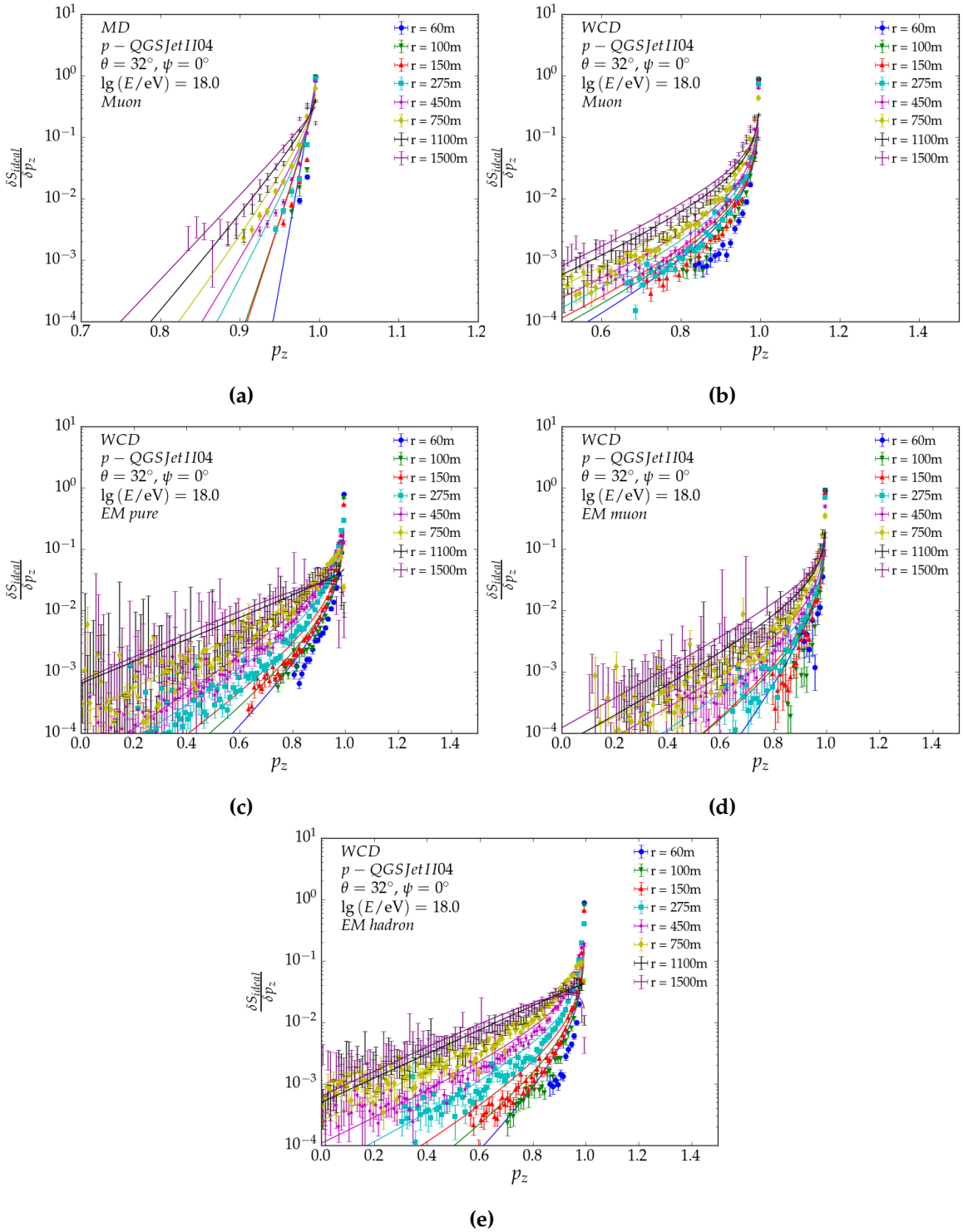

Figure 4.11: Cumulative p_z distributions at various radial distances for a shower at 10^{18} eV and $\theta = 32°$. Distributions at $\psi = 0°$ are used to minimize biases. Solid lines are the model predictions.

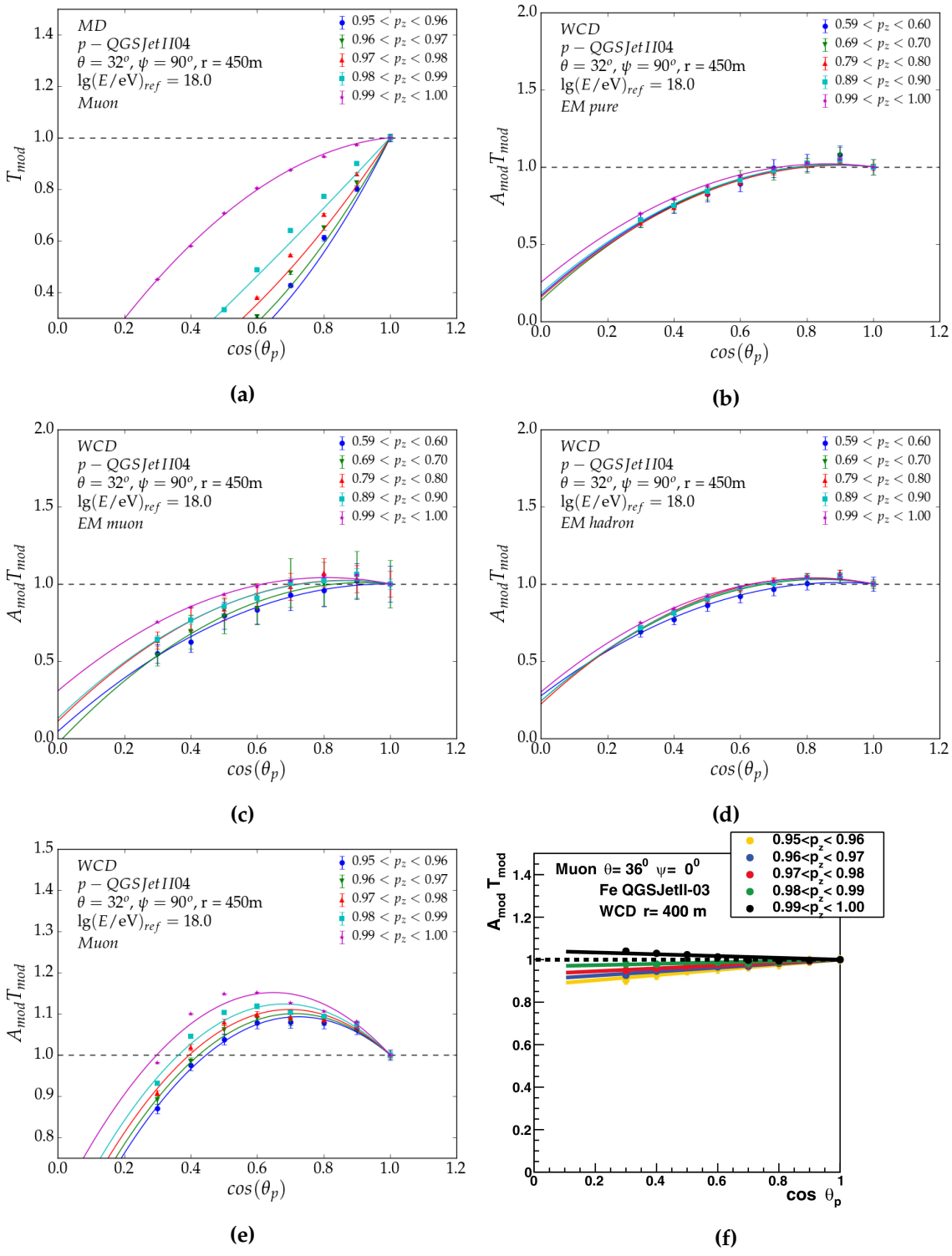

Figure 4.12: Distributions for T_{mod} for **a)** muons in the MD. $A_{\mathrm{mod}}T_{\mathrm{mod}}$ distributions are depicted in **b)-d)** electromagnetic particles and **e)** muons in the WCD. For comparison, **f)** the muonic component in the WCD for the previous signal model is shown [59]. Solid lines are the model predictions with respect to simulated averages. Simulated averages are obtained by binning the p_z distribution. Differences between **e)** and **f)** are from intrinsic high energy hadronic interaction model differences in the muon energy spectra.

with p_i as fit parameters. The figures in 4.12 compare the simulations with the model predictions using the aforementioned characterization. Results for $\psi = 0°$ and $\psi = 90°$ are equivalent (as was already established in figure 4.9b). We show those for $\psi = 90°$ to discuss new features seen with respect to an earlier model (figure 4.12f).

The figures show the average $A_{\text{mod}}T_{\text{mod}}$ distributions for particle angles up to 80° and 88° for the MD and WCD respectively. These upper angle limits are imposed by the limitation of the Geant4 tabulation (discussed in sections 4.1.2 and 4.1.1). Binned p_z are shown where 90 % of its distribution lies (see figure 4.11 for reference). The markers and error bars are the mean and variance of all p_z contained in sed bin. Figures 4.12a to 4.12e are from the currently developed model, whereas figure 4.12f is from the early iteration in reference [59].

Using the approximation of equation (4.25) for the MD we derive that $A_{\text{mod}} \approx \cos\theta_p$ and is thus unitary to $\cos\theta_p$. Figure 4.12a follows this trend with deviations originating from the muon energy spectrum. Muons with $0.99 < p_z < 1$ (pink line) are those which are boosted most and therefore follow the unitary approximation best. These are well described by the model prediction. Figures 4.12b to 4.12d all share the same structure in the WCD due to the equivalent detector response of their particle type (they are all electromagnetic). The signal response of electromagnetic particles is proportional to its total energy deposit ($T_{\text{mod}} = 1$). Their structure is therefore dominated by the projection of the detector surface. Although updated for the current signal model, the shape for $A_{\text{mod}}T_{\text{mod}}$ has not changed with respect to the signal model developed with proton QGSJETII-03. This is expected as there are no significant differences between the spectral features of QGSJETII-03 and QGSJETII-04. Figures 4.12e and 4.12f show the results for the muonic component. Due to their inherently different design approach, they can only be approximately compared.

Figure 4.12f used p_z distributions for iron showers at 400 m and 10^{20} eV. Different zenith and azimuth are shown. However, zenith and azimuth differences can be ignored because all distributions are normalized and differences for ψ are minimal (as mentioned before). The benefit of using iron particles at a large energy is the increased number of particles to process, providing a better estimate on the mean structure. However, a more realistic description of the variance is lost. It is why proton showers at 10^{18} eV are preferred. Nevertheless, this does not result in major differences (as was established with the electromagnetic particle spectra). Both figures show clear differences in their respective trends. Nonetheless, they both yield $A_{\text{mod}}T_{\text{mod}}$ values in the same range (0.8,1.1). These can only be attributed to the intrinsic properties between the high energy hadronic interaction models (muon energy spectral differences are studied in references [70, 71]). We continue with the new description for the muonic component seen in figure 4.12e for subsequent analyses. With the newly obtained characterization for $\frac{\delta S}{\delta p_z}$ and $A_{\text{mod}}T_{\text{mod}}$ we obtain the real detector response S_{real}.

4.2.2 Atmospheric Densities - f_{atm}

Changes in atmospheric densities a few radiation lengths above ground affect the Moliere radius, varying the electromagnetic signal in the detector. They can deviate up to 10 %. Muons (as anticipated) are barely affected (< 1 %) by this -as will be shown later on. Changes in atmospheric densities can be caused by i) fluctuations between day and night, ii) zenith dependent density changes and iii) particles traversing through different effective atmospheric profiles at different ψ -the latter two will be discussed in section 4.2.3.

We derive the correction for f_{atm} by fitting the signal to a Gaisser-Hillas function [45] for each radial distance, ψ and energy E. Furthermore, shower zeniths between 0° and 65° (56°) are used for the WCD (MD). For surface detectors, the Gaisser-Hillas function cannot be applied on a single shower to shower basis. However, it can be used after accounting for all zenith angles. The principle idea is that the detector signal of a single shower at e.g. 450 m represents a specific snapshot of the shower at shower stage $\Delta X/\Delta L^{(\mu)}$. Assuming the exact same shower at different zenith angles, it provides us with different snapshots of the shower at different development stages, eventually resembling a Gaisser-Hillas structure (see the schematic in figure 4.13).

The Gaisser-Hillas function is transformed to depend on shower stage. It is also rewritten such that the covariance is minimized during fitting procedure. For electromagnetic particles the Gaisser-Hillas looks as

$$N(X) = N_{\text{max}} \left(\frac{X - X_0}{X_{\text{max}} - X_0} \right)^{\frac{X_{\text{max}} - X_0}{\lambda}} \cdot \exp\left(\frac{X_{\text{max}} - X}{\lambda} \right), \tag{4.28}$$

where N_{max} is the maximum number of particles observed at the shower maximum. X_0 and λ are energy dependent shower parameters (further discussed in section 4.2.3). Based on a preliminary inspection of the detector signal for all zenith angles, we find the maximal signal at around 400 g cm^{-2} (ΔX_{ref}) for all electromagnetic shower components and 4000 m ($\Delta L^{(\mu)}_{\text{ref}}$) for the muonic component (irrespective of the detector). We use these findings as reference to minimize the covariance, altering equation (4.28) into

$$N_{\text{ref}}(X_{\text{ref}}) = N_{\text{max}} \left(\frac{X_{\text{ref}} - X_0}{X_{\text{max}} - X_0} \right)^{\frac{X_{\text{max}} - X_0}{\lambda}} \cdot \exp\left(\frac{X_{\text{max}} - X_{\text{ref}}}{\lambda} \right). \tag{4.29}$$

Combining equations (4.28) and (4.29) with the additional transformation of $X_i \rightarrow \Delta X_i$ (for X, X_0, X_{ref} and X_{max}) and $N_i \rightarrow S_i$[3] we derive for the pure electromagnetic and electromagnetic from hadronic jets component

$$S^{\text{EM}_{\text{pure}},\text{EM}_{\text{hadron}}}(\Delta X) = S_{\text{ref}} \left(\frac{\Delta X - \Delta X_0}{\Delta X_{\text{ref}} - \Delta X_0} \right)^{\frac{\Delta X_{\text{max}} - \Delta X_0}{\lambda}} \cdot \exp\left(\frac{\Delta X_{\text{ref}} - \Delta X}{\lambda} \right). \tag{4.30}$$

Note that the meaning of S_{max} and $\Delta X^{\mu}_{\text{max}}$ have changed. $\Delta X^{\mu}_{\text{max}}$ currently represents the shower stage where the detector signal is maximal (for a given radial distance). As the schematic in figure 4.13 implies, the detector signal is generally largest for more vertical showers.

For the muonic and electromagnetic from muons component, the expressions are

$$\begin{aligned} S^{\mu}(\Delta L^{(\mu)}) &= S_{\text{ref}} \left(\frac{\Delta L^{(\mu)} - \Delta L_0}{\Delta L_{\text{ref}} - \Delta L_0} \right)^{\frac{\Delta L_{\text{max}} - \Delta L_0}{\lambda_1 + \lambda_2 \Delta L^{(\mu)} + \lambda_3 (\Delta L^{(\mu)})^2}} \cdot \exp\left(\frac{\Delta L_{\text{ref}} - \Delta L^{(\mu)}}{\lambda_1 + \lambda_2 \Delta L^{(\mu)} + \lambda_3 (\Delta L^{(\mu)})^2} \right), \\ S^{EM_{\mu}}(\Delta X) &= S_{\text{ref}} \left(\frac{\Delta X - \Delta X_0}{\Delta X_{\text{ref}} - \Delta X_0} \right)^{\frac{\Delta X_{\text{max}} - \Delta X_0}{\lambda_1 + \lambda_2 \Delta X + \lambda_3 \Delta X^2}} \cdot \exp\left(\frac{\Delta X_{\text{ref}} - \Delta X}{\lambda_1 + \lambda_2 \Delta X + \lambda_3 \Delta X^2} \right), \end{aligned} \tag{4.31}$$

[3] This follows from the approximation that the signal size scales with the particle number, thus preserving the functional shape of equation (4.29)

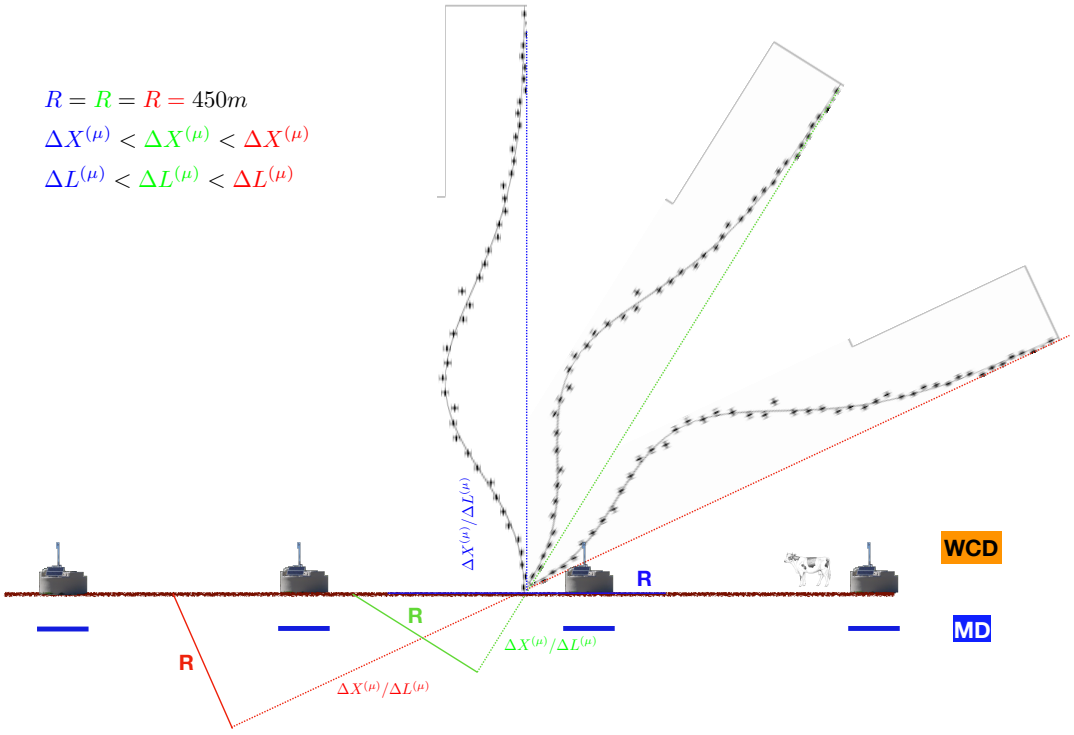

Figure 4.13: Schematic of three identical showers at different inclinations. At e.g. 450 m from the core (shower plane) they provide three different shower stages $\Delta X/\Delta L^{(\mu)}$ which can be interpreted as three snapshots of the shower.

where ΔL_i has the same physical meaning as ΔX_i but in terms of geometric distances. After muons are produced, they can only "disappear" through decay. In addition, they are barely attenuated by the atmosphere[4]. As a result, the tail of the Gaisser-Hillas function will be flatter compared their electromagnetic counterparts. This distinct behaviour cannot be described through equation (4.30) and is therefore characterized by extending λ to $\lambda_1 + \lambda_2\Delta L + \lambda_3\Delta L^2$ (as seen in equation (4.31)). This raised tail structure is also seen for the electromagnetic particles from muons, albeit much softer (here λ is extended to $\lambda_1 + \lambda_2\Delta X + \lambda_3\Delta X^2$). As with λ, λ_i is an energy dependent quantity.

Sample fits for all components at 450 m, $\psi = 90°$ and 10^{18} eV are shown in figure 4.14. Additional fits at 1500 m can be found in figure A.5. For these fits, $\Delta X_0/\Delta L_0^{(\mu)}$ were fixed at $-250\,\mathrm{g\,cm^{-2}}/2500$ m for muons and electromagnetic particles from muons and $-800\,\mathrm{g\,cm^{-2}}$ for the pure electromagnetic and hadronic jet components. This improves the fit stability by minimizing the correlation found between DX_0 and λ [73]. For all components, energies and radial distances the fit is within the 5 % level from simulations. Figures 4.14a and 4.14b show the distinct flat tail. More vertical showers are clustered at younger shower stages (and

[4]Assuming a muon at 1 GeV, it will have a mean decay path of ~ 6 km, equivalent to passing through an atmospheric overburden of approximately 520 $\mathrm{g\,cm^{-2}}$ [72] should the muon arrive to ground.

vice versa for very inclined showers). The offsets seen at $\sim 1500\,\mathrm{g\,cm^{-2}}$ in figure 4.14c is a possible bias from the $\frac{\delta S}{\delta p_z}$ or $A_{\mathrm{mod}} T_{\mathrm{mod}}$ estimation. It was not corrected for as they occur below 0.2 VEM (the WCD trigger threshold is at 1.75 VEM [74]). They have been removed from the fitting procedure.

Fluctuations in atmospheric densities are propagated to the shower stage (defined as $\Delta X = \int \rho dl$ for electromagnetic particle in figure 3.6), effectively changing the shape of the Gaisser-Hillas structure. The average yearly air density is $\langle \rho \rangle = (1.043 \pm 0.014)\,\mathrm{kg\,cm^{-3}}$. The average ground density at the Pierre Auger Observatory is $1.060\,\mathrm{kg\,cm^{-3}}$ [75, 76]. Discrepancies between these two originate from the fitting procedure of the balloon data to derive the matter overburden. Seasonal models used here are in agreement with the actual ground density [77]. They are also equivalent to those used for the previous iteration of the Universality model.

The yearly average Gaisser-Hillas prediction serves as the baseline to compare all showers with their respective monthly atmospheric model. For every month, all showers (for every zenith angle) are bundled to form the *monthly Gaisser-Hillas* structure. Their respective density two radiation lengths [78] above the detector is also calculated. They are shown in figures 4.15 for the highest energetic shower 10^{20} eV at 1500 m and $\psi = 90°$. This to emphasize the rapid increase in particle fluctuations due to atmospheric effects. We only show the muonic component for completeness and to reiterate its independence to seasonal weather conditions (they are below $< 1\,\%$). Shower zenith fluctuations are within the $10\,\%$ limit and originate from the shower to shower fluctuations of the particle. In figure 4.15b we already see that a near $3\,\%$ difference in density changes the signal response of the electromagnetic component by $10\,\%$. Atmospheric effects are less profound in figures 4.15c and 4.15d but deviate up to $5\,\%$. This is due to the late production of electromagnetic particles in the shower with respect to the pure electromagnetic particle component (jets and muons propagate first before they decay).

Atmospheric effects decrease closer to the core, leading to the correction factor

$$f_{\mathrm{atm}}^{\mathrm{radial}}(r) = 1 - \alpha(r) \cdot (\rho - \langle \rho \rangle), \tag{4.32}$$

where ρ is the current air density and $\langle \rho \rangle$ the yearly average. The slope $\alpha(r)$ is characterized by a power-law

$$\begin{aligned} \alpha^{\mu}(r) &= 0, \\ \alpha^{\mathrm{icomp}}(r) &= \beta_1 \cdot r^{\beta_2}, \end{aligned} \tag{4.33}$$

with component sensitive parameters β_i. The new parameters β_i also account for detectors close to the shower core (down to 60 m), useful for low energetic showers.

With the expression in equation (4.32), zenith dependent shifts can be extracted[5]. This is referred to as *type II* corrections (following the same notation as in reference [59]). It is predicted using

$$f_{\mathrm{atm}}(r, \theta) = f_{\mathrm{typeII}} = 1 - \alpha(r) \cdot \left(\rho(\theta) - \langle \rho(0°) \rangle\right), \tag{4.34}$$

[5]For vertical showers, two radiation lengths X_0 is at a higher altitude compared to inclined showers. This in turn reduces the total integrated density along the shower axis and hence the shower age. This can be derived from $X(h) = a_i + b_i \cdot \exp(h/c_i)$ where a_i, b_i, and c_i are atmospheric profile constants. By approximating the atmospheric overburden along the shower axis $X(h, \theta) \approx X(h)/\cos\theta$, you derive a zenith dependent density $\rho(h, \theta) = -\frac{\delta X}{\delta h} \approx \frac{X(h)/\cos\theta - a_i}{c_i}$.

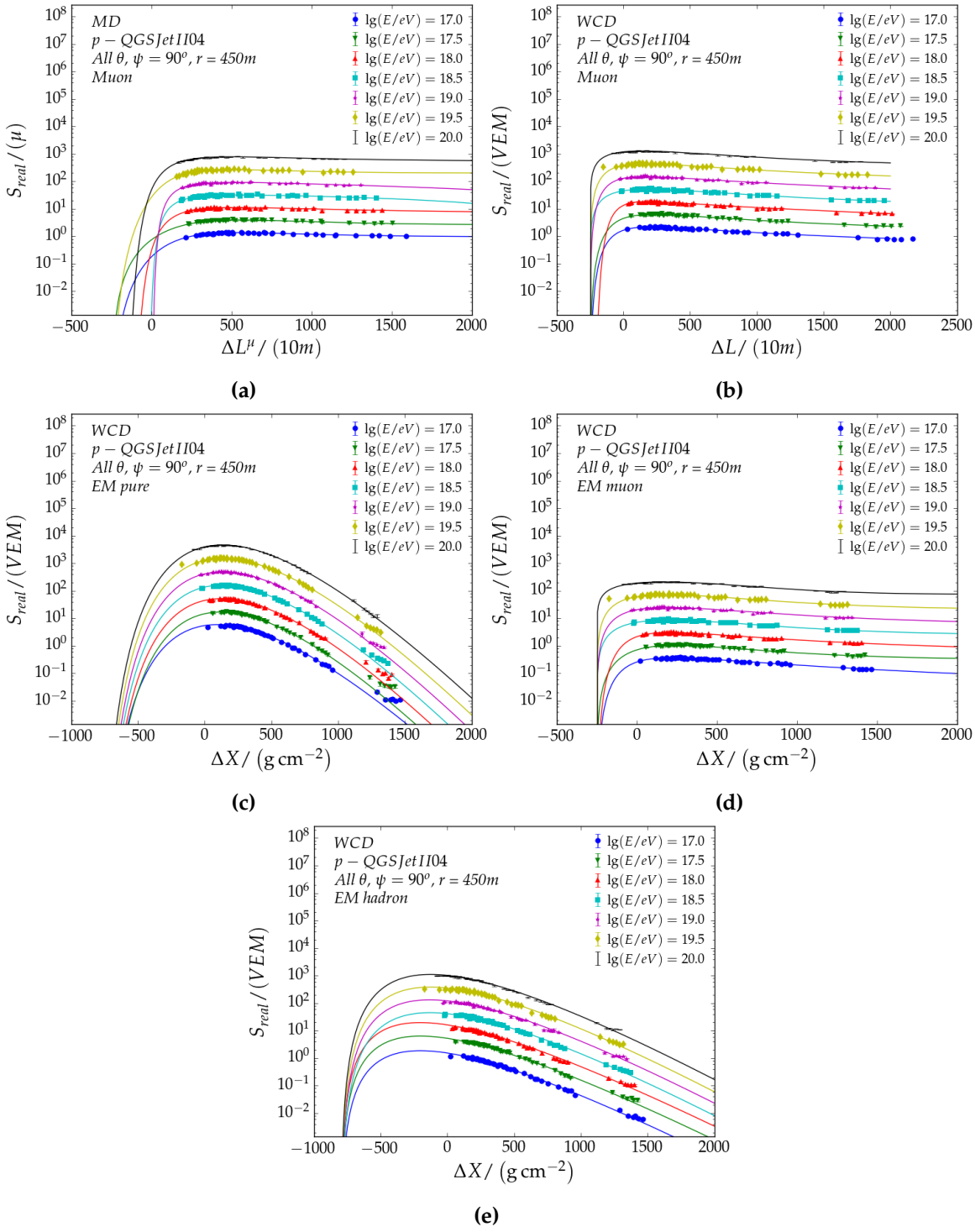

Figure 4.14: Profiles of detector signal with respect to shower stage $\Delta X/\Delta L^{(\mu)}$. Each profile is the result accounts for zenith angles between 0° and 65° (56°) for the WCD (MD). The markers represent the average of 30 showers (error bars are their respective variances). Solid lines are the fitted Gaisser-Hillas function described in equations (4.30) and (4.31).

where $\alpha(r)$ is as defined before in equation (4.33). The yearly average of all vertical showers at specific radial distances for a subset of showers with the same energy is used to derive $\langle\rho(0°)\rangle$ (and $\rho(\theta)$ for all other angles). Their predictions (early iteration and current model) are shown in figures 4.16. Current results are in agreement with the ones obtained in

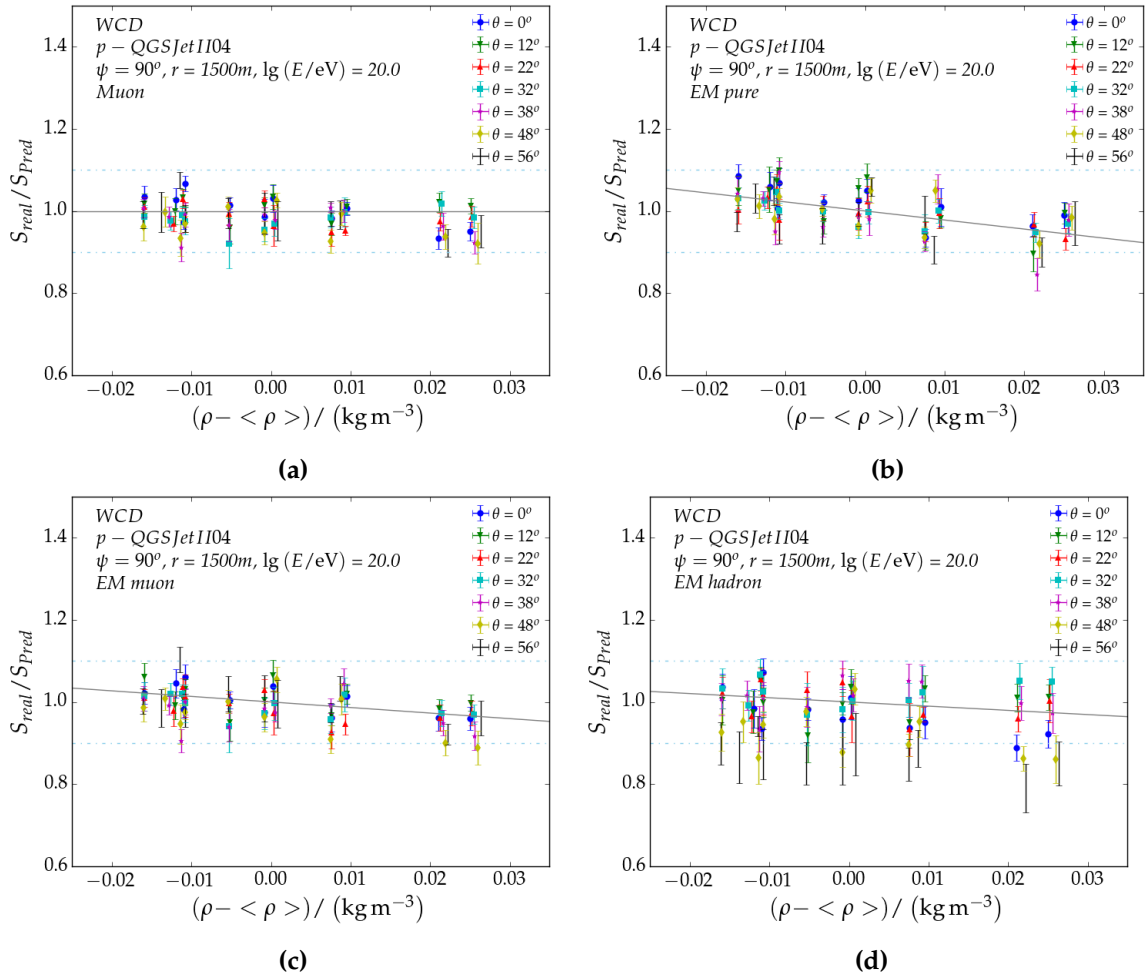

Figure 4.15: The yearly average of WCD signals are compared with the monthly averages for each particle component. Monthly air densities two radiation lengths above ground are used and compared to the yearly average. The muonic component for MD is not shown as muons are barely affected by changes in atmospheric densities (as seen in **a)**). The pure electromagnetic component **b)** is most sensitive with up to a 10 % offset.

reference [59] as they share the same atmospheric models with only minor differences in the electromagnetic spectrum between proton QGSJETII-03 and QGSJETII-04. In subsequent analysis, we will include this correction into the definition of S_{real}, i.e., it will henceforth be defined as $S_{\text{real}} = S_{\text{ideal}} \cdot f_{\text{conv}} \cdot f_{\text{atm}}$.

4.2.3 Azimuthal Asymmetries - f_{mod}

Atmospheric asymmetries originate from particles propagating through different atmospheric profiles. This would not be necessary if the atmosphere were considered uniform. For explanatory purposes, we assume a quasi-real atmospheric model which is divided into four layers of equal density. In this scenario, particles from vertical showers will (on average) always propagate through the same atmospheric layers irrespective of azimuth. For inclined showers, a clear separation between particles upstream ($\psi = 0°$) and downstream ($\psi = 180°$) is anticipated. Upstream particles are more likely to have longer path lengths in the upper layers of the atmosphere where the density is lower. This means that their effective attenuation differs. Returning to the realistic scenario where the density decreases with alti-

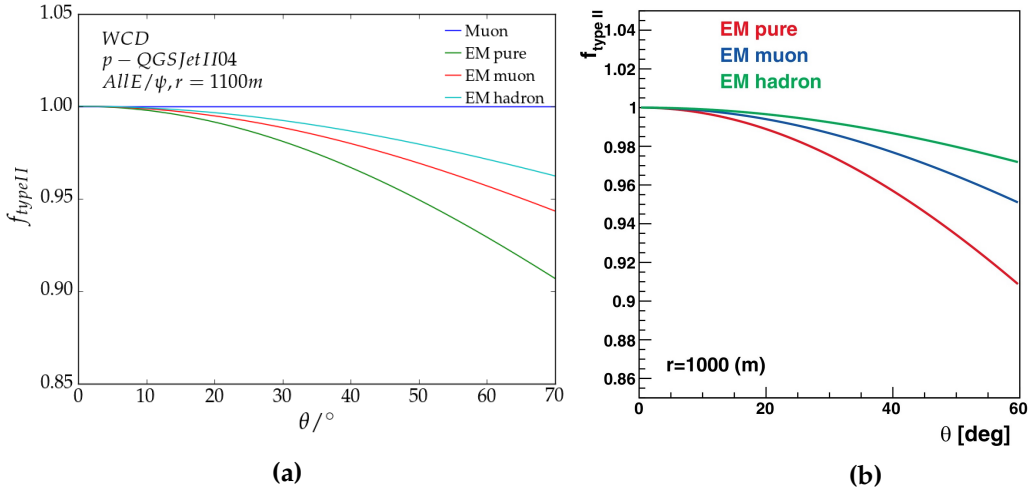

Figure 4.16: Atmospheric overburden change with zenith angles. The f_{typeII} correction shows prediction for the **a)** current model and **b)** previous iteration [59] at 1100 m and 1000 m respectively. Only electromagnetic particles show any form of dependency. The muonic component in **b)** is not shown as there are no seasonal effects (as indicated in **a)**).

tude for every atmospheric layer. We recognize that the ψ modulation becomes more evident.

This difference is characterized by the modulation factor

$$f_{\text{mod}}(\psi) = M_0\,(1 + M_1 \cos\psi), \tag{4.35}$$

for which M_0 is a normalization factor and M_1 the modulation amplitude. Considering its implementation in the signal model ansatz in equation (4.9), we can consider M_0 as $f_{\text{atm}}(r, \theta)$, defined earlier in equation (4.34). By fixing M_0 to $f_{\text{atm}}(r, \theta)$ we also minimize biases for the signal model (they are effectively absorbed into M_1). We obtain M_1 similarly as f_{atm}. The detector signal is fitted for each radial distance and azimuth to a Gaisser-Hillas function (see definitions in equations (4.30) and (4.31)) for all shower zenith angles at the reference energy 10^{18} eV. Signals at $\psi = 90°$ are used as reference for which no modulation is present. Detector signals at different azimuthal angles are then compared to the Gaisser-Hillas prediction where M_1 is included as an additional fit parameter.

The figures 4.17a to 4.17d show this modulation for showers at the reference energy and at 450 m and 1100 m from the shower core. M_1 shows a clear radial and zenith dependency for the pure electromagnetic component in the WCD. It shows that azimuthal signal asymmetries can be as high as 10 %. Asymmetries from the other components are more nuanced. For the muons we see a similar structure between the MD and WCD. Comparing this with figure 4.17e (modulation of the previous iteration), we see a similar structure for the pure electromagnetic component in the WCD. However, we find contradicting structures for the remaining components. The modulation for the electromagnetic particle from hadronic jets and muon decays are flatter. What is most striking is that muons show a modulation of up to 10 % (below 2 % in this work), whereas the pure electromagnetic component is less emphasized at 5 %. The difference in M_1 for the pure electromagnetic component and hadronic jets can be attributed to the change in reference energy. We find the flatter modulation for the muonic and electromagnetic particles from muon decay to be a consequence of the new description for the Gaisser-Hillas function in equation (4.31). The new characterization of the Gaisser-Hillas function accounts for the higher signals seen at late shower stages. The

previous iteration of the signal model did not account for this. The fit parameters (especially the parameter describing the slope of the Gaisser-Hillas function λ) become more biased, which is carried into the description of M_1. Finally, the flatter modulation seen in the current analysis for muons is also anticipated as different atmospheric profiles should not affect the muon spectrum significantly.

M_1 is characterized through simple functional shapes. For each radial distance the zenith dependency is described as a polynomial of θ:

$$M_1(r,\theta) = f_1(r)\left(\frac{\theta}{65^\circ}\right) + f_2(r)\left(\frac{\theta}{65^\circ}\right)^2 + f_3(r)\left(\frac{\theta}{65^\circ}\right)^3, \tag{4.36}$$

where $f_i(r)$ are radially dependent constants characterized as

$$f_i^{\mathrm{WCD}}(r)\Big|_{\mathrm{icomp}} = \alpha_0\left(\exp\left(\frac{\alpha_1}{r}\right) - 1\right) \tag{4.37}$$

for all components in the WCD and

$$f_i^{\mathrm{MD}}(r) = \alpha_0 + \alpha_1 \cdot r + \alpha_2 \cdot r^2 \tag{4.38}$$

for the MD with their respective fit parameters α_i.

With the addition of f_{mod} the signal is predicted for every shower energy and radial distance. S_{pred} of the figures in 4.18 correspond to the signals from the Gaisser-Hillas fit at $\psi = 90^\circ$ multiplied with the predicted estimation of $f_{\mathrm{mod}}(r,\theta)$. Results for the component signals at 450 m from the shower core are shown (see the figures in A.7 for a radial distance of 1100 m). Differences for the muonic component in the MD and WCD are mostly within the 5 % level. For the MD, inclined showers at $\theta = 56^\circ$ deviate up to 10 %. This is a combined effect of the low particle statistics at 10^{17} eV and effective detector area (reduced to almost 50 % of its original surface area). No spread is seen for azimuth angles between $\psi = 0^\circ$ and $\psi = 180^\circ$. This implies a successful correction of the signal modulation. Near equivalent results are seen for the muonic component and electromagnetic particles from muons in the WCD with the exception of the smaller bias at $\theta = 56^\circ$. For the pure electromagnetic component the correction for the modulation is mostly successful. For low energetic inclined showers above $\theta = 56^\circ$ an average offset above 20 % is found. Also, the azimuthal correction fails (seen in the spread for each azimuth). The offset is caused by the tail of the Gaisser-Hillas function. Looking at figure 4.14c, we see that for these showers the WCD detector signal is below 1 VEM. There the Poisson fluctuation dominates over the 20 % offset and failure of the correction for signal modulation. Energies above 10^{18} eV are well described. The electromagnetic component from hadronic jets (figure 4.14e) shows a successful correction for the modulation. However, a clear energy dependency is found (it is also found for the pure electromagnetic component at larger distances)[6]. They are mostly contained within the 10 % level and subsequently accounted for during the characterization of radial and energy dependency of the Gaisser-Hillas function in section 4.2.4. In subsequent analysis, we will include the modulation correction into the definition of S_{real}, i.e., it will henceforth be defined as $S_{\mathrm{real}} = S_{\mathrm{ideal}} \cdot f_{\mathrm{conv}} \cdot f_{\mathrm{atm}} \cdot f_{\mathrm{mod}}$.

[6]It is possible that hadronic jets carry a larger fraction of the primary energy, thus propagating longer through the atmosphere before creating a subshower. Only those subshowers are affected by the atmospheric profile, producing those azimuthal asymmetries. To the "sub-primary" (e.g. pions) the atmosphere is relatively opaque (with respect to EM particles).

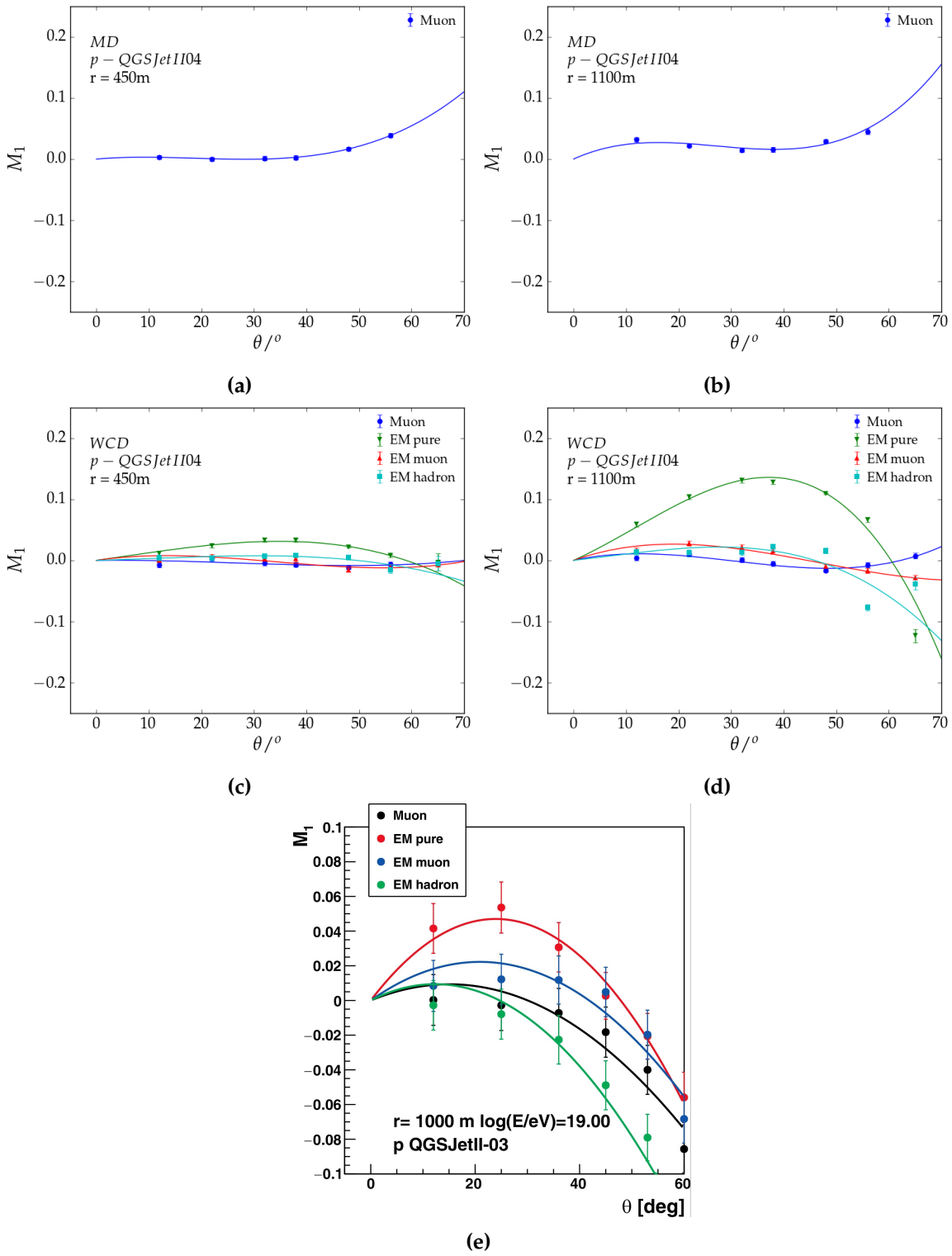

Figure 4.17: M_1 modulation factor for azimuthal asymmetries seen in the detector signal caused by particle propagating through different atmospheric profiles. They are shown in **a)-b)** for MD and **c)-d)** for WCD at 450 m and 1100 m. Showers at the reference energy are used here (10^{18} eV). **e)** shows the modulation of the previous work in reference [59] for an energy at 10^{19} eV and 1000 m from the core. The solid lines are model predictions.

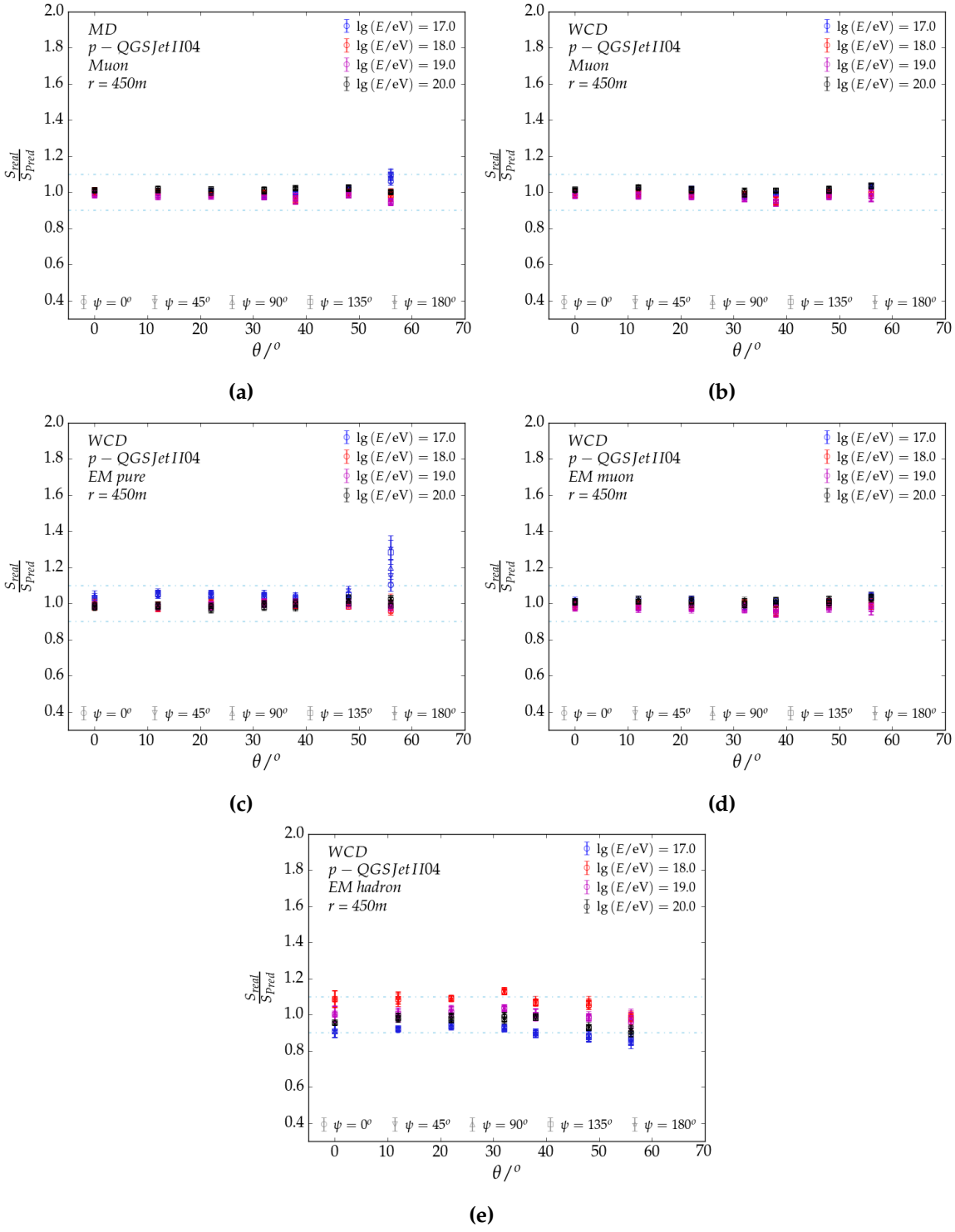

Figure 4.18: Signal biases between the predicted signal (accounting for azimuthal signal modulation) and real detector signal at 450 m from the shower core. The correction for signal modulation is derived from 10^{18} eV showers. All particle components for MD and WCD are in **a)** and **b)-e)** respectively.

4.2.4 Gaisser-Hillas Characterization

In sections 4.2.2 and 4.2.3 the detector signals were fitted to Gaisser-Hillas functions for every radial distance at the reference energy. For convenience, it is shown again in its full description in equation (4.39).

$$
\begin{aligned}
&S^{\mu}(r,E,\Delta L) = \\
&S_{\text{ref}}(r,E)\left(\frac{\Delta L-\Delta L_0}{\Delta L^{(\mu)}_{\text{ref}}(r,E)-\Delta L_0}\right)^{\frac{\Delta L^{(\mu)}_{\text{max}}(r,E)-\Delta L_0}{\lambda_1(r,E)+\lambda_2(r,E)\Delta L+\lambda_3(r,E)\Delta L^2}}\cdot\exp\left(\frac{\Delta L^{(\mu)}_{\text{ref}}(r,E)-\Delta L}{\lambda_1(r,E)+\lambda_2(r,E)\Delta L+\lambda_3(r,E)\Delta L^2}\right),\\
&S^{\text{EM}_{\text{pure}},\text{EM}_{\text{hadron}}}(r,E,\Delta X) = \\
&S_{\text{ref}}(r,E)\left(\frac{\Delta X-\Delta X_0}{\Delta X_{\text{ref}}(r,E)-\Delta X_0}\right)^{\frac{\Delta X_{\text{max}}(r,E)-\Delta X_0}{\lambda(r,E)}}\cdot\exp\left(\frac{\Delta X_{\text{ref}}(r,E)-\Delta X}{\lambda(r,E)}\right),\\
&S^{\text{EM}_{\mu}}(r,E,\Delta X) = \\
&S_{\text{ref}}(r,E)\left(\frac{\Delta X-\Delta X_0}{\Delta X_{\text{ref}}(r,E)-\Delta X_0}\right)^{\frac{\Delta X_{\text{max}}(r,E)-\Delta X_0}{\lambda(r,E)}}\cdot\exp\left(\frac{\Delta X_{\text{ref}}(r,E)-\Delta X}{\lambda_1(r,E)+\lambda_2(r,E)\Delta X+\lambda_3(r,E)\Delta X^2}\right).
\end{aligned}
\tag{4.39}
$$

Radial and energy dependencies are characterized by using detector signals from proton QGSJETII-04 generated showers for the full energy, zenith range, azimuth and radial range. As before, all zenith angles of showers at sed energy and radial distance are used to obtain S_{ref}, $\Delta X_{\text{max}}/\Delta L^{(\mu)}_{\text{max}}$ and λ[7]. ΔX_0 and $\Delta L^{(\mu)}_0$ remain unchanged with respect to those used for the analysis of f_{atm} and f_{mod} (constants found in section 4.2.2). The characterization is derived by first describing its energy dependency. It is then followed by describing the radial characterization of each parameter to the previously obtained functional shape. For compactness, only the muonic component for the MD and pure electromagnetic component from the WCD are illustrated. The remaining components are detailed in Appendix A.7. Radial dependencies are discussed here but their characterizations are found in the Appendix (due to the many parameters involved in the fits).

As the figures in 4.19a and 4.19b point out, the power-law dependency can be clearly recognized. Ideally, this allows for $S_{\text{ref}}(r,E)$ to be defined as

$$
S_{\text{ref}}(r,E) = S_{\text{const}}(r)\cdot\left(\frac{E}{10^{18}\,\text{eV}}\right)^{\gamma}, \tag{4.40}
$$

where $S_{\text{const}}(r)$ is an arbitrary constant and γ the slope of the energy dependency. However, we find this approach to be of first order and only valid for larger energies. At lower energies, this definition introduces biases to γ for the electromagnetic particles from hadronic jets. This is best evaded by introducing an offset $S_{\text{off}}(r)$

$$
S_{\text{ref}}(r,E) = S_{\text{off}}(r) + S_{\text{const}}(r)\cdot\left(\frac{E}{10^{18}\,\text{eV}}\right)^{\gamma(r)}. \tag{4.41}
$$

[7] As simple qualitative check for consistency, common features are anticipated for S_{ref} (energy scaling and LDF structure) [17]. Energy dependent structures are also foreseen for $\Delta X_{\text{max}}/\Delta L^{(\mu)}_{\text{max}}$ and λ.

This is a unique feature from the definition of the hadronic jet component. The transverse momentum of hadrons do not need to be large to reach radial distances close to the core (and create a subshower). As a result, significantly more particles are classified as hadronic jets. Equation (4.40) is therefore inaccurate and improved through the introduction of $S_{\text{off}}(r)$. $S_{\text{off}}(r)$ is a strongly reducing factor for larger radial distances (its characterization is found in the Appendix). This offset holds no validity if the energy approaches zero. Nevertheless, it is well beyond the intended energy of the signal model. Also, showers below 10^{17} eV are not available within the scope of this work. It is therefore not possible to accurately characterize a second order energy dependency to $S_{\text{ref}}(r, E)$. The figures also show the anticipated LDF and is described by $S_{\text{const}}(r)$. In this work, the Nishimura-Kamata-Greisen (NKG) function is used to describe the lateral distribution of all components for all detectors. Equation (4.41) therefore becomes

$$S_{\text{ref}}(r, E) = S_{\text{off}}(r) + \alpha_0 \left(\frac{r}{1000\ \text{m}}\right)^{-\alpha_1} \left(\frac{\alpha_3 + r}{\alpha_3 + 1000\ \text{m}}\right)^{-\alpha_2} \cdot \left(\frac{E}{10^{18}\ \text{eV}}\right)^{\gamma(r)}, \tag{4.42}$$

carrying the most dominant features of the shower signal. α_i are component dependent LDF parameters. The characterization for $S_{\text{off}}(r)$ and $\gamma(r)$ are empirically derived and listed in section A.7.

For $\Delta L^{\mu}_{\text{max}}$ and ΔX_{max}, we find two very unique features. Signals for the muonic component in the MD mostly originate from the late shower stages (the maximum muon production depth is also prior to X_{max}). As a result, the Gaisser-Hillas is heavily dominated by the description of its tail (as seen in figure 4.20a). This feature is more pronounced at larger radial distances, resulting in large $\Delta L^{\mu}_{\text{max}}$. Furthermore, $\Delta L^{\mu}_{\text{max}}$ may also be interpreted as a projection of the maximum muon production along the shower axis (since most muons are produced when pions reach the critical energy). The spatial distribution of muons follow a cone given by

$$\sin \alpha = \frac{p_t}{E_p}, \tag{4.43}$$

where α is the particle angle with respect to the shower axis, p_t the transverse particle momentum, and E_p the particle energy. At a distance r_i, the maximum can be derived by

$$\Delta L^{(\mu)}_{\text{max}} = r_i \cdot \frac{p_t}{p_z}. \tag{4.44}$$

Here, p_z is the cosine of the particle to the shower axis (first introduced in section 4.2.1). $\Delta L^{\mu}_{\text{max}}$ is expected to increase further from the shower axis (and approach 0 at the core). As figure 4.19c shows, the $\Delta L^{\mu}_{\text{max}}$ becomes 0 if $r = 0$. The steep rise for $\Delta L^{\mu}_{\text{max}}$ from 60 m to 1500 m originates from the effective muon energy spectrum seen by the MD (detectors are shielded from low energy muons). For the muonic component in the WCD, a flatter rise is anticipated and found (see figure A.8c). With increasing energy, muons are generated deeper in the atmosphere and more boosted. They are therefore less likely to arrive to a detector at r_i, declining $\Delta L^{\mu}_{\text{max}}$. At 1500 m, $\Delta L^{\mu}_{\text{max}}$ decreases almost by ≈ 3300 m per energy decade. This declination flattens closer to the core, becoming energy independent. In this work, the energy dependency for $\Delta L^{(\mu)}_{\text{max}}$ (MD and WCD) is described with the linear function

$$\Delta L^{(\mu)}_{\text{max}}(r, E) = \alpha_0(r) \cdot (1 + (\lg(E/\text{eV}) - 18) \cdot \alpha_1(r)), \tag{4.45}$$

where $\alpha_i(r)$ are empirically obtained following the reasoning of equation (4.44). For the leading slope parameter λ_1[8], a clear energy dependant structure is seen for larger radial distances.

[8] $\lambda = \lambda_1(r, E) + \lambda_2(r, E)\Delta L + \lambda_3(r, E)\Delta L^2$.

This is a consequence of shower energy dependencies in the shape of the longitudinal profile (see figure 3.2d). At 10^{17} eV, the width of the normalized longitudinal profile can differ as much as 5 % with respect to the average profile for all energies (10 % with respect to the highest energy). This feature is possibly also affected by a fitting artifact for high energy showers. At 10^{20} eV, the maximum muon production depth is closer to the ground. This in turn generates smaller values for $\Delta L^{\mu}_{\max}$, which results in a deteriorated description of the Gaisser-Hillas tail[9]. λ_1 (including λ_2 and λ_3) is characterized with

$$\lambda_i(r, E) = \alpha^i_0(r) \cdot (1 + (\lg(E/\text{eV}) - 18) \cdot \alpha^i_1(r)), \tag{4.46}$$

with its empirically driven description of $\alpha_i(r)$ (see Appendix for their functional shapes). The same description is also used for the electromagnetic particle component from muons. For all electromagnetic particle components in the WCD, the $\Delta X_{\max}$ can be interpreted as a delay (in $g\,cm^{-2}$) by particles produced close to the core at the shower maximum, which diffuse to larger core distances. This delay is expected to approach 0 close to the core (as seen in figure 4.19d). $\Delta X_{\max}$ does not increase above 150 g cm^{-2} for core distances above 750 m. It is expected that the attenuation dominates over the diffusion. An increased shower energy enhances the diffusion, which increases $\Delta X_{\max}$. This feature is most evident close to the core. At $r = 60$ m, the $\Delta X_{\max}$ changes from ≈ 25 g cm^{-2} to ≈ 50 g cm^{-2} for energies at 10^{17} eV and 10^{20} eV respectively. For radial distances beyond 750 m, $\Delta X_{\max}$ is within a 5 % level of 150 g cm^{-2}. It has been characterized by

$$\Delta X_{\max}(r, E) = \alpha_0(r) + \alpha_1(r)(\lg(E/\text{eV}) - 18) + \alpha_2(r)(\lg(E/\text{eV}) - 18)^2, \tag{4.47}$$

where the $\alpha_i(r)$ characterizations carry the radial plateau and suppression of the energy dependency (see Appendix for their functional shapes). λ shows minor energy dependencies as they differ less than 10 % from each other (as seen in figure 4.19f). However, a parabolic structure around $10^{18.5}$ eV is present. Also, the fitted λ values are beyond 3σ from each other closer to the shower core (e.g. at 60 m). This feature is produced by fixing ΔX_0, which is known to be also energy dependent. These energy dependent structures are therefore propagated into λ and described by

$$\lambda(r, E) = \alpha_0(r) + \alpha_1(r)(\lg(E/\text{eV}) - 18) + \alpha_2(r)(\lg(E/\text{eV}) - 18)^2. \tag{4.48}$$

Radial dependent structures $\alpha_i(r)$ are found in the aforementioned Appendix. For the hadronic jet component the same energy characterization is used.

The result of the complete Gaisser-Hillas characterization is shown for each component in figure 4.20. At this point, it accounts for energy, shower stage and geometry (θ, ψ, r). The figures show the profiles of 840 and 960 showers for the MD and WCD respectively. The markers in the figures are the average signal response of 30 showers for each detector specific particle component. The error bars are their respective variance. Dashed lines show the predicted signal to the Gaisser-Hillas function, whereas the solid lines are local fits to the Gaisser-Hillas function. As seen at a radial distance of 450 m (and furthermore at 1500 m in the figures in A.10), a clear agreement is seen for all shower stages, energies, particle components and detectors. Also, the local Gaisser-Hillas fit aligns with the Universality signal model within a 5 % margin. Minor offsets can be seen in the Gaisser-Hillas description for the muon originating electromagnetic particle component. It results from the extrapolation of the derived functional form for λ.

[9] It is common to reformulate the Gaisser-Hillas into a universal shower profile (USP). It divides the Gaisser-Hillas function into a right-handed (R) and left-handed (L) contribution. It is commonly used for muon production depth studies (as in reference [79]). This was briefly used and yielded no improvements.

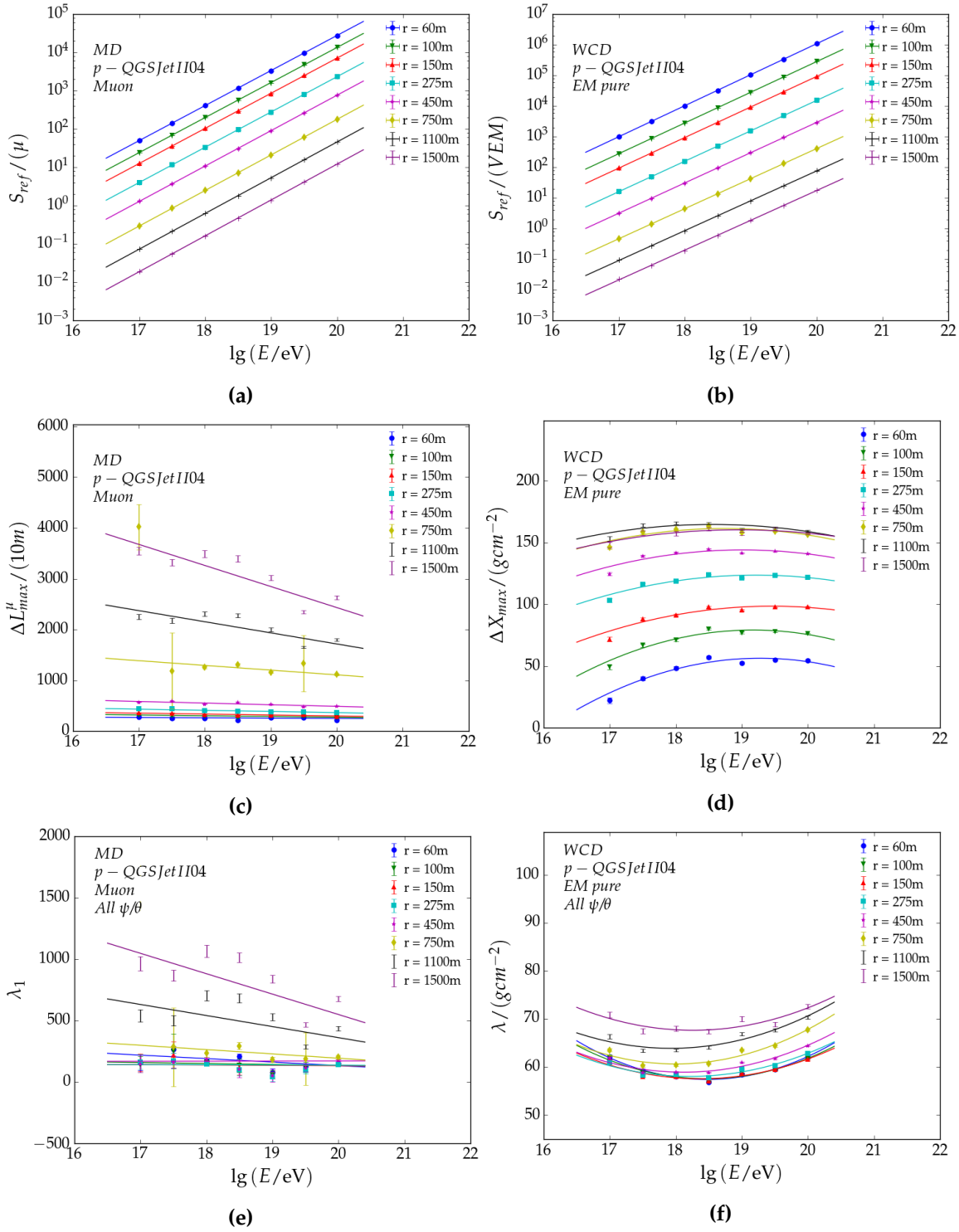

Figure 4.19: Select figures of the Gaisser-Hillas fit parameters S_{ref}, $\Delta L^{(\mu)}_{\text{max}}/\Delta X_{\text{max}}$ and $lambda$. For the muon and electromagnetic component from muons only the leading order parameter λ_1 is shown (see equation (4.39) for more detail). The parameters are shown with respect to energy and radial distance. The markers are the parameter fits to the Gaisser-Hillas function, whereas the solid lines are the predictions of the models used in this work. The error bars of the markers are their respective fit error.

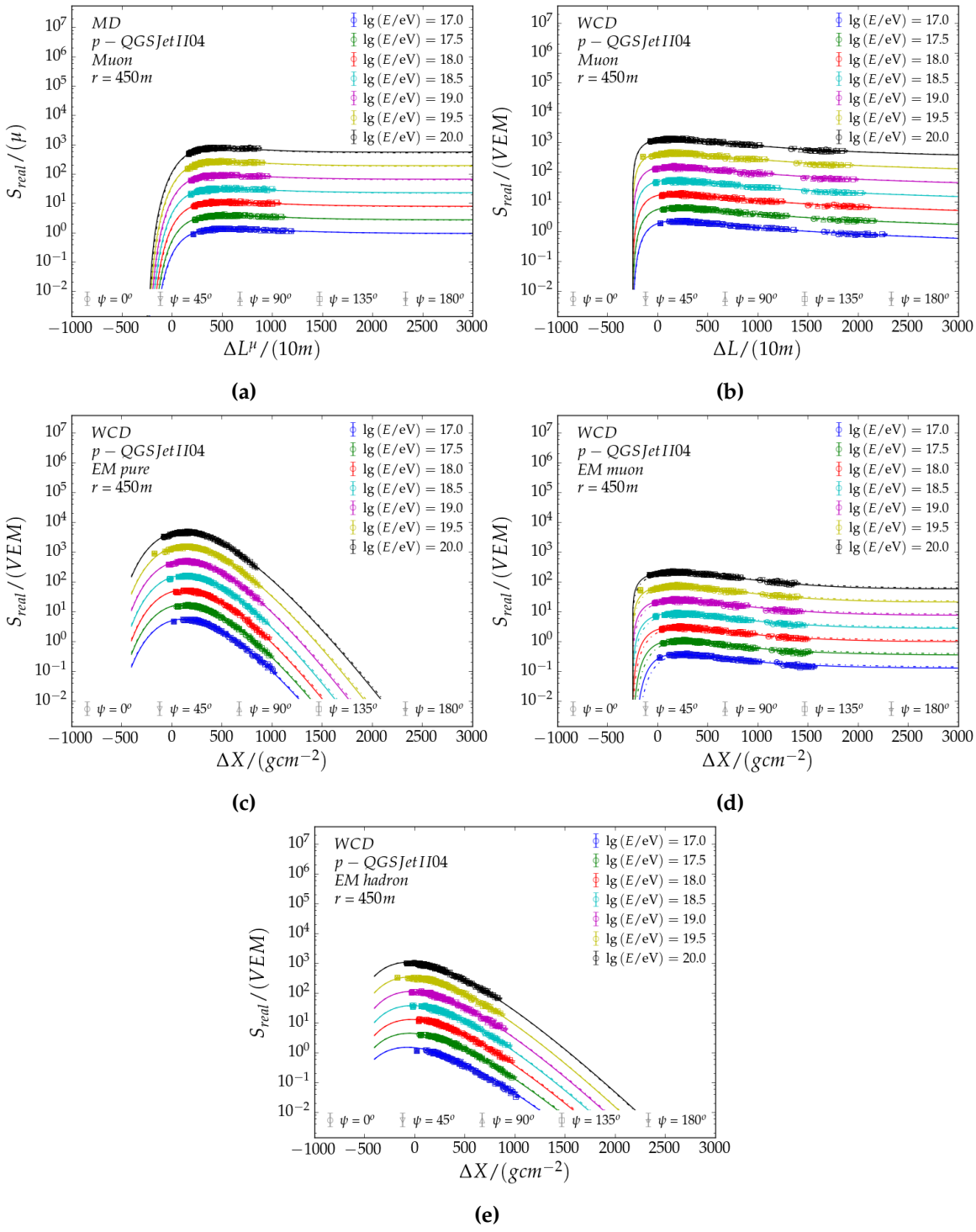

Figure 4.20: Signal as a function of shower stage $\Delta L^{(\mu)}/\Delta X$ for all relevant particle components of MD and WCD. Each point corresponds to the average detector signal of 30 showers. The dashed line refers to a Gaisser-Hillas function fitted. The solid line refers to the predicted signal for sed components. The predicted signal already accounts for geometry and shower parameters.

Nevertheless, differences are below 5 % within the relevant range. This is also valid for signals below 1 VEM.

4.2.5 Component Correlation - $f_{R_{\text{fluct}}}$

At this stage, the Universality model for the MD is complete (its validation will be discussed in section 4.3). It is also complete for each particle component in the WCD. Principally, the reconstruction could be performed with 4 additional free parameters for the particle component abundance R_μ, $R_{\text{EM-pure}}$, $R_{\text{EM-muon}}$ and $R_{\text{EM-Hadron}}$. Here R_i refers to the signal S_i with respect to the reference model and primary S_i^{ref} (proton QGSJETII-04):

$$R_i = \frac{S_i}{S_i^{\text{ref}}}. \tag{4.49}$$

R_i serves as a mass composition indicator for which *1* is a proton and anything higher a heavier nuclei. It is redundant to use all of them because they are (i) highly correlated and (ii) do not provide the reconstruction procedure with information on shower to shower fluctuations between particle components. Both issues are accounted for by characterizing all R_i with respect to the normalization factor of the muonic component R_μ[10].

The correlation is found by comparing the normalization factor R_i for all primaries and hadronic models. During the development of the early iteration of the signal model [77], showers at 10^{19} eV and $\theta = 36°$ were used. From figure 4.20, it can be recognized that a reference zenith of $\theta = 36°$ only provides a fraction of the Gaisser-Hillas function. In this work, the characterization is derived at its respective reference energy of 10^{18} eV. Contrary to the previous iteration, showers up to $\theta = 65°$ are used, therewith using the full range of the Gaisser-Hillas function and thus providing an average correlation for all relevant zenith angles. The pure electromagnetic component and electromagnetic particles from muons could be described by a linear relation to R_μ. Considering the near independent relation between the pure electromagnetic component and muons, a near flat structure is expected. For the electromagnetic particles from muons, the relation should, to some extent, resemble unity. This is recognized in figure 4.21.

Upon comparing the correlation between the current model (figures 4.21b, 4.21d, and 4.21f) and the previous iteration (figures 4.21a, 4.21c, and 4.21e), a clear structure is seen for iron primaries. This structure is hadronic model independent and originates from inclined showers (vertical showers have a higher R_μ with respect to inclined showers). This feature is not seen in the previous iteration due to only looking at 36°. Since the correlation is empirically driven, it was concluded that in terms of universality parameterization, the fluctuations between iron and proton showers are indistinguishable [77]. As a result, the correlation was only characterized (solid black line) with proton QGSJETII-03 showers. Primary dependencies were already hinted by figure 4.21e. In this work, we realize that the previously understood correlation feature is incomplete. The same underlying correlation is found in addition to radial and zenith dependencies. Radial dependencies are only found in the particle components (see figures in A.11), whereas zenith dependencies are found for heavier primary masses.

[10] In other work, this normalization factor is sometimes referred to by N_μ. In this work, we refrain from this notation as it is also used to describe the number of muons.

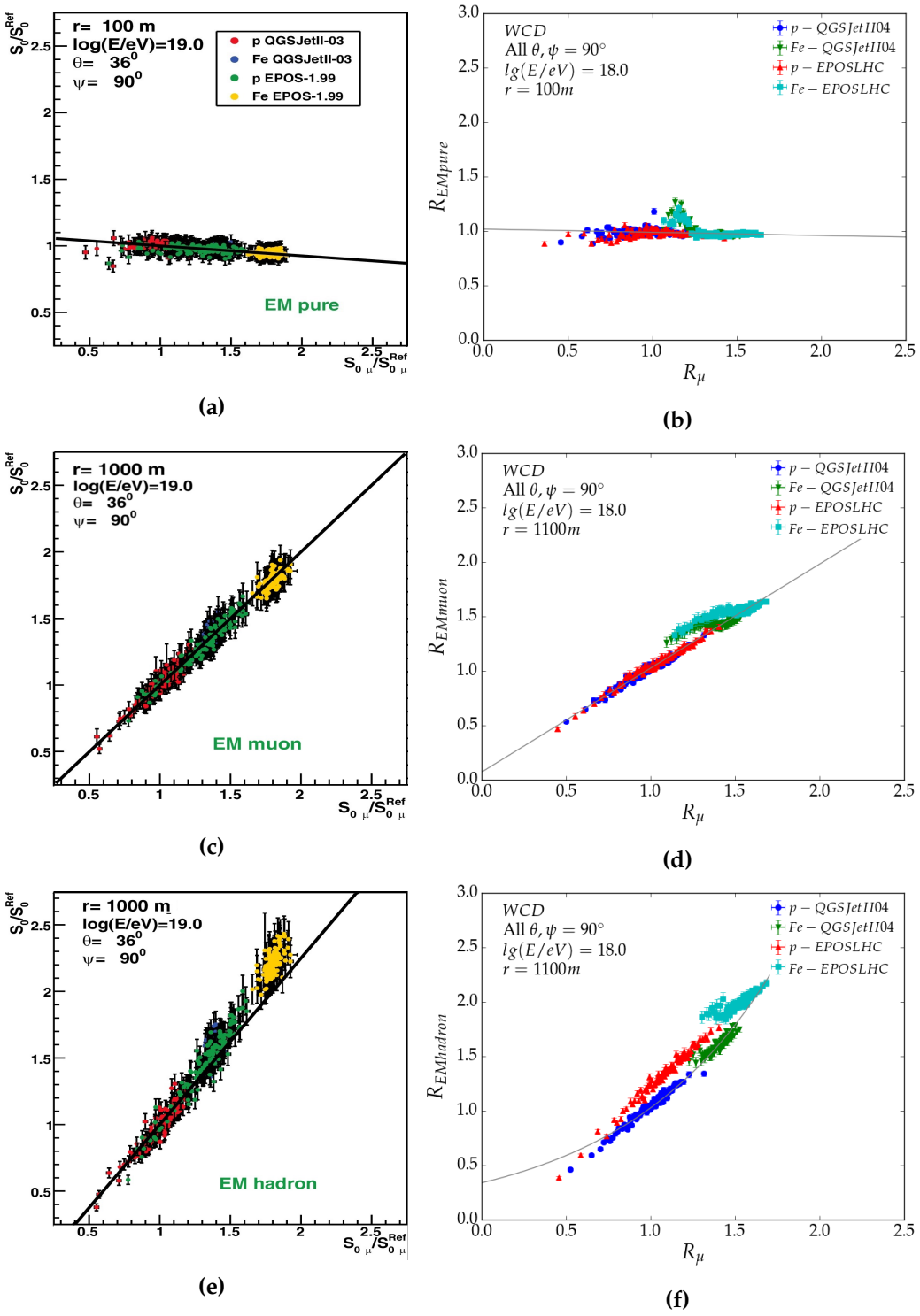

Figure 4.21: Particle component correlations with respect to R_μ. The spread is caused by shower to shower fluctuations. **Left**: Correlation for showers for the previous iteration of the signal model [59]. The correlation is derived from showers at $\theta = 36°$. **Right**: Profile of the correlation for showers with respect to the signal model derived in this work. Zenith angles between $\theta = 0°$ and $\theta = 65°$ are used to derive the characterization for the correlation. Note, the energies differ between the left and right figures. This results from differing reference energies used to develop the model.

It is not clearly understood as to why the electromagnetic particle excess is exclusively seen for inclined iron primary showers. As iron showers develop earlier in the atmosphere, the electromagnetic and muonic shower maximum is higher in the atmosphere (smaller $X_{\max}^{(\mu)}$). The muons therefore propagate longer, decaying more likely into electromagnetic particles. This would explain the excess electromagnetic particles seen in figure 4.21d. However, if these electromagnetic particles interact multiple times prior to reaching ground, its *mother-particle* is not a muon and it will therefore be classified as a pure electromagnetic particle. An excess π^0 production for iron primaries (assuming universality does not hold) would also increase the pure electromagnetic component. However, it would not be zenith dependent. Different shower to shower fluctuations are mainly attributed to intrinsic hadronic model differences. Primaries from EPOS-LHC generate more hadrons with sufficient transverse momenta to create subshowers.

The correlations are characterized for all showers at the reference energy 10^{18} eV for all radial distances. Proton and iron showers from QGSJETII-04 are used to account for primary dependencies. Furthermore, the full zenith range is used during each radial correlation fit, effectively averaging over all zenith angles. Using this approach, it is found that signal biases are within the 10 % level (see section 4.3)[11]. Its prediction is shown by the grey line and shows a very good agreement (with exception of highly inclined iron showers). They are described by

$$R_i(r) = \beta(r)(1 + (R_\mu - 1) \cdot \alpha(r)) \tag{4.50}$$

for the pure electromagnetic and electromagnetic particles from muon component where $\alpha(r)$ and $\beta(r)$ are radial dependent constants. For the hadronic jet component, the correlation is characterized as

$$R_{\text{EM-Hadron}}(r) = \beta(r) \exp\left(\alpha(r) \cdot R_\mu\right). \tag{4.51}$$

Radial characterizations for $\alpha(r)$ and $\beta(r)$ are found in reference A.7.1. Following the characterizations in equations (4.50) and (4.51), the complete Universality signal model becomes

$$S^{\text{WCD}}(E, X_{\max}, r, \theta, \psi, R_\mu, \rho^{\text{air}}_{\text{ground}}) = S^{\text{WCD}}_{\text{ref}} \cdot \sum_{\text{icomp}} R_{\text{icomp}} \cdot f_{\text{icomp}},$$

$$\begin{aligned} S^{\text{WCD}}(E, X_{\max}, r, \theta, \psi, R_\mu, \rho^{\text{air}}_{\text{ground}}) = S_{\text{ref}} \cdot \big[& R_\mu \cdot f_\mu \\ & + \beta_{\text{EM-pure}}(1 + (R_\mu - 1) \cdot \alpha_{\text{EM-pure}}) \cdot f_{\text{EM-pure}} \\ & + \beta_{\text{EM-muon}}(1 + (R_\mu - 1) \cdot \alpha_{\text{EM-muon}}) \cdot f_{\text{EM-muon}} \\ & + \beta_{\text{EM-Hadron}} \exp\left(\alpha_{\text{EM-Hadron}} \cdot R_\mu\right) \cdot f_{\text{EM-Hadron}} \big] \end{aligned} \tag{4.52}$$

for the WCD, and

$$S^{\text{MD}}(E, X^\mu_{\max}, r, \theta, \psi, R_\mu, \rho^{\text{air}}_{\text{ground}}) = S^{\text{MD}}_{\text{ref}} \cdot R_\mu \tag{4.53}$$

for the MD. Here R_μ is as before and $S^{\text{MD,WCD}}_{\text{ref}}$ the detector specific signal at the reference model with the addition of the normalized fractional contribution of each particle component

[11] It is possible to characterize θ dependencies. However, it was opted not to do this without any physical motivation. Alternatively, the reconstruction could be redesigned to account for the component abundances independently R_μ, $R_{\text{EM-pure}}$, $R_{\text{EM-Muon}}$ and $R_{\text{EM-hadron}}$ or redefine the 4 particle components.

f_{icomp}.

The normalization R_μ is a shower dependent quantity and thus equivalent for all detectors (such that $R_\mu^{\text{WCD}} = R_\mu^{\text{MD}}$). This is reflected in figure 4.22 where R_μ^{WCD} and R_μ^{MD} follow the identity line. Larger errors seen for protons result from larger shower to shower fluctuations with respect to iron. The figure also provides two useful implications on the development of the new signal model. First, if the signal of proton QGSJETII-04 showers are not at *1* then the new signal model is flawed. Second, if heavier primaries (iron here) and different hadronic models do not follow the identity line (within 10 %)[12] then the principles of shower Universality are violated. Figures 4.22a and 4.22b show both conditions to be satisfied, providing a strong indication of the validity of the new signal model.

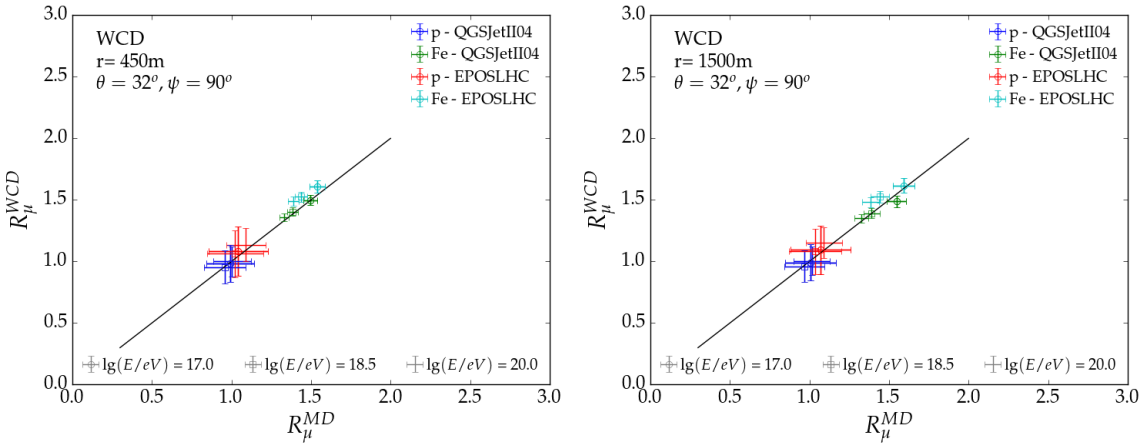

(a) **(b)**

Figure 4.22: Normalization factors R_μ^{MD} and R_μ^{WCD} are compared for different primaries and hadronic models. The solid black line is the identity line, implying that (i) R_μ is a global shower variable, (ii) that the signal model is valid and (iii) that principles of shower Universality are conserved.

4.3 Validation

Following the Universality signal model ansatz in equation (4.9), the signal was divided into 4 particle components, which were then individually characterized to the shower parameters. For the MD only the muonic component had to be modelled. With a complete Universality signal model at hand for the MD and WCD, a final test is performed to validate whether all components reflect the total detector signal. Furthermore, the model is compared with different primaries and hadronic models to confirm if the principles of shower universality still hold (see chapter 3 for more information).

In figure 4.23, high energy hadronic interaction models and primaries are compared at 450 m from the shower core to the reference model (proton QGSJETII-04) for all hadronic components in the WCD. The new signal model for sed component is considered complete if proton QGSJETII-04 showers are always *1*. The model is considered universal if they only scale by the factor R_μ. This horizontal structure is seen for all particle components, implying a complete universal signal model. For iron showers, muon signals are about ≈ 45 % larger.

[12] Due to intrinsic differences between hadronic models.

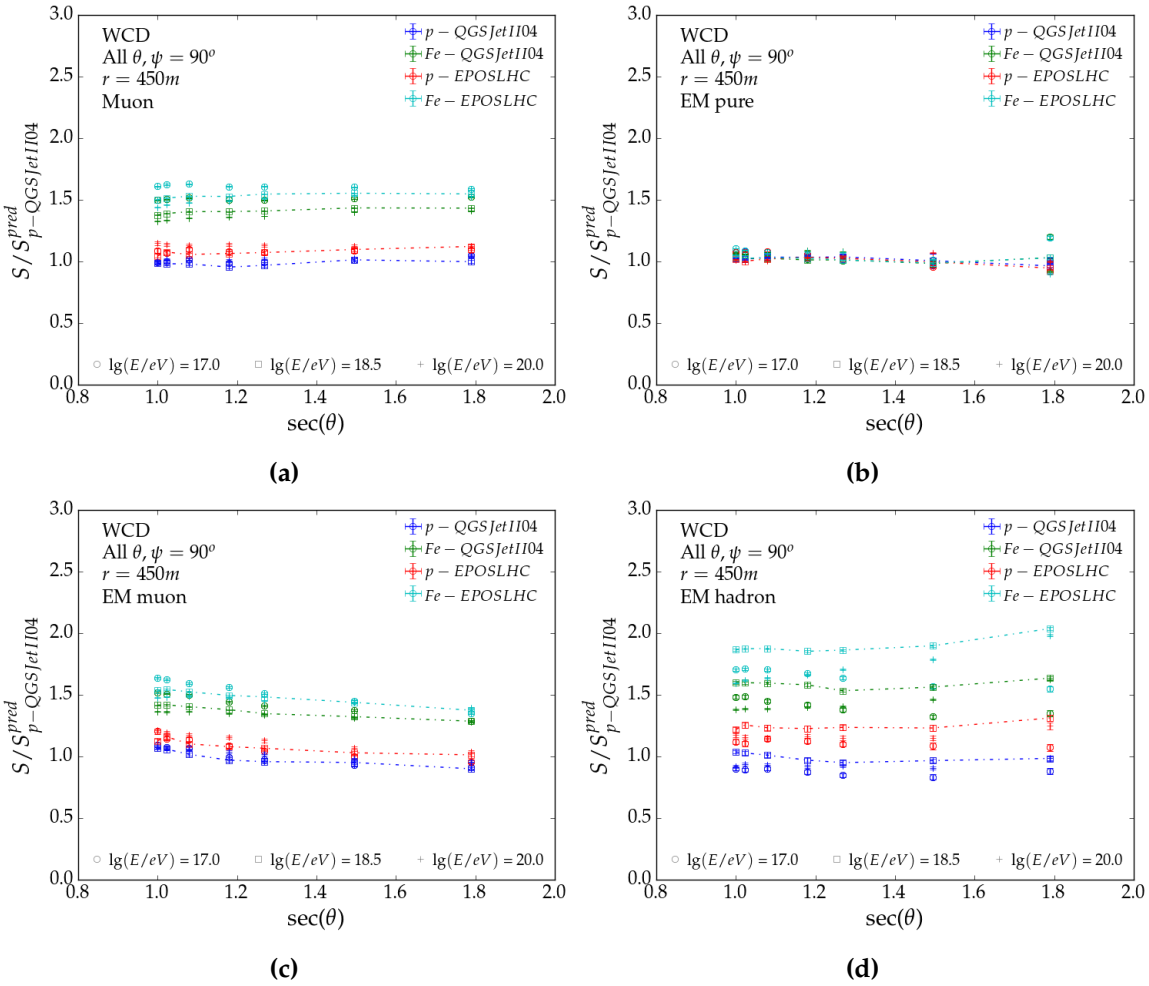

Figure 4.23: Detector signal for each particle component in the WCD with respect to the predicted signal from the proton QGSJETII-04 reference model (blue) at 450 m. Different primaries, high energy hadronic interaction models and energies are illustrated. The flat structure implies Universality, whereas the S/S^{pred} refers to the mass composition sensitive scale factor R_μ.

The excess electromagnetic particles are fully absorbed by the increased muon production (figure 4.23c) and hadronic jets (figure 4.23d). They can increase up to $\approx 50\,\%$ and $\approx 80\,\%$ respectively. However, due to their low relative signal contribution they account for $\approx 15\,\%$ to the total electromagnetic signal (at the radial distance shown in figure 4.23). Similar plots are shown for a radial distance of 1500 m in the figures in A.12.

Recent use of the previous iteration (see figure 4.24c) showed significant biases below 450 m, irrespective of shower energy [44]. Generally, it overestimates for low signal and underestimates for large signals. This may result from the Gaisser-Hillas function used. It did not account for the muon tail properly, possibly introducing a bias. Considering that it was developed for the standard array (1500 m grid space), where energies above $10^{18.5}$ eV are relevant, it is evident that the model is mostly within the 10 % level. However, for energies below $10^{18.5}$ eV, relevant to AMIGA, it cannot be used. In figure 4.24a, the newly developed WCD signal model successfully extends down to energies of 10^{17} eV. For clarity, only extreme energies (10^{17} eV and 10^{20} eV) and a shower at $10^{18.5}$ eV are selected. Model predictions from this work (hollow markers) and MC signal (solid markers) are overlaid on top of each other. Each marker in figures 4.24a and 4.24b represent the mean value of 120 showers at

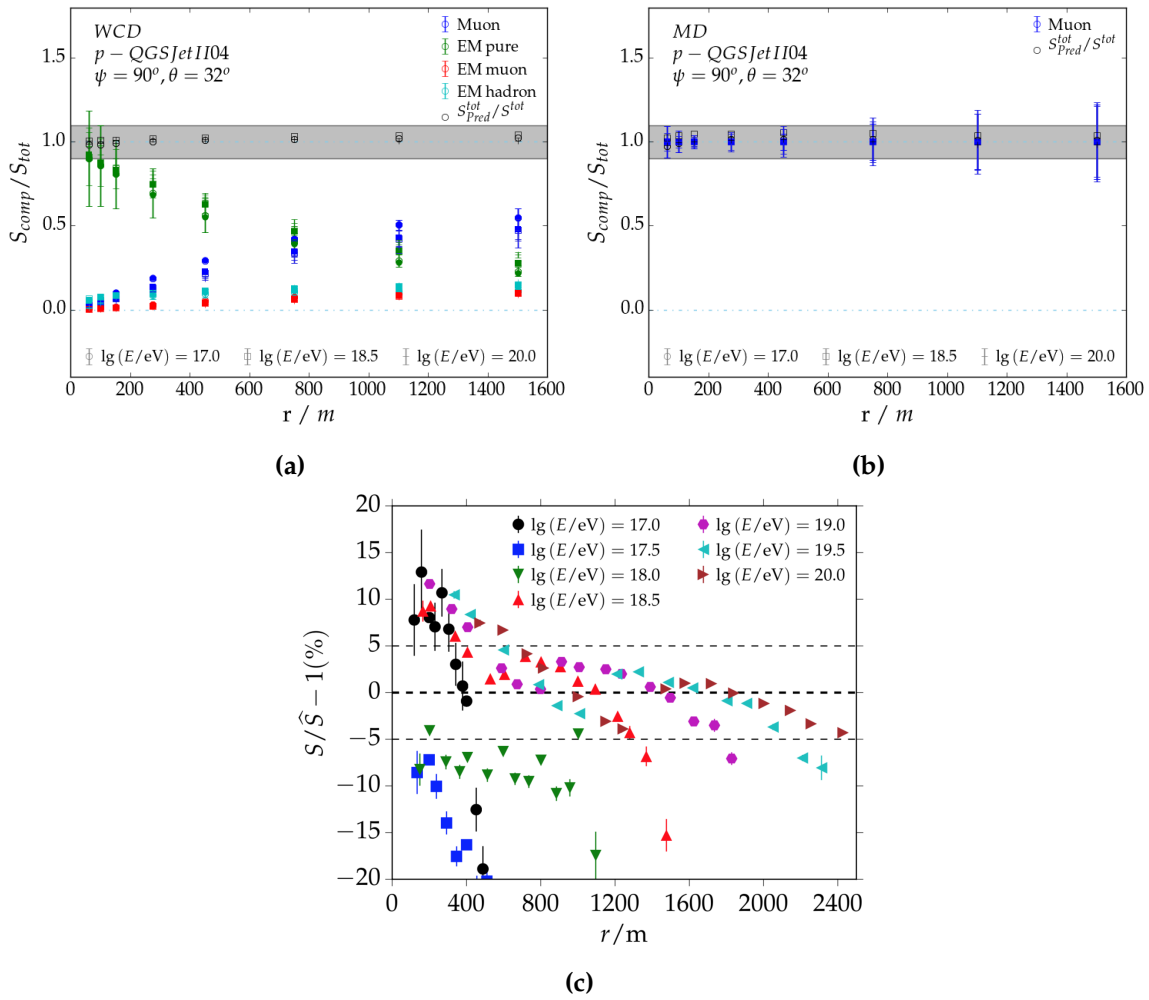

Figure 4.24: Normalized particle component signal in the **a)** WCD and **b)** MD for different energies and radial distances. The predicted particle component fraction is overlaid with MC simulations. Bias of the total signal is also shown. Error bars refer to the particle component variance. **c)** Signal biases using the previous Universality signal model [44, 59].

the selected energy, zenith and sampling area. The error bars are their respective standard deviations.

Figure 4.24a shows how the electromagnetic component dominates the overall signal seen in the WCD. Above 800 m, muons provide the highest fraction to the overall signal. Furthermore, it also indicates that the relative signal contributions of all particle components changes with increasing energy. This is most evidently seen between the muon and pure electromagnetic particle component, where the muon fraction decreases with increasing energy (and the vice versa for the pure electromagnetic particle component). These features are interesting to compare with data for studies of high energy interaction models (more effective with multiple detectors - i.e. MD and SSD). The figure also provides three conclusions: (i) component signals agree with their MC counterparts, (ii) the total signal is mostly within the 5 % level and (iii) the signal model can be successfully used between energies of 10^{17} eV and 10^{20} eV. From figure 4.24b, the same conclusions are drawn for the MD. The Universality signal model can therefore not only be used for 'WCD-only' or 'MD-only' shower reconstructions but also for hybrid Universality reconstructions (later discussed in chapter 6).

CHAPTER 5

Universality Time Model

In addition to the detector signal, the temporal distribution of shower particles provides insight on the mass composition sensitive parameters. In reference [80] it was proven that X_{max} could be measured with surface detectors. The risetime[1] of the signal trace provides key information from the shower front, which depends on the maximum shower development. By using all 4 particle components (see section 3.2.1), shower to shower fluctuations are minimized. Their relative contribution to the total traces is also dictated by R_μ, previously modelled in section 4.2.5. Deriving X_{max} from the temporal distribution provides an increased statistic compared to the FD (which only has a 15 % duty cycle) and aid anisotropy studies if the resolution is better than $\approx 30\,\mathrm{g\,cm^{-2}}$.

Muons propagate differently through the atmosphere compared to electromagnetic particles. They scatter less and therefore are the first particles to arrive to the detector (irrespective of their signal fraction). Due to this delayed effect, particle components are modelled independently. The simulated showers used for the signal model are also used to derive the time model here. From the resampling procedure (discussed in section 4.1), average time traces are derived from all arriving particles in their respective sampling areas, which are of interest here. These are then scaled to the signal in the detector. During time model development, the temporal traces are normalized to eliminate dependencies already accounted for in the signal model. The coordinate system is equivalent as in chapter 4. Shower to shower fluctuations are minimized by using the shower stage $\Delta X/\Delta L$. However, in this work, the temporal signal variance of the particle component is not accounted for.

To emphasize, the *shape* of the temporal structure is important to derive X_{max}, especially the early stage of the trace. On a shower to shower basis, this implies that detectors far from the shower axis are of little use for the reconstruction (further elaboration will follow in chapter 6).

In this chapter, we introduce a new time model for the WCD. It is based on references [65, 80, 81] and extends its use to energies of 10^{17} eV, complimenting the energy range of the signal model and providing a sensitive tool for mass composition analysis between the second knee and ankle. Furthermore, two time models are also developed for the 1-bit and integrator signal trace of the MD. As with the signal model, the MD will be characterized with respect to the muon production depth X^{μ}_{max}. Energy and geometric characteristics are also

[1] The risetime is defined as the time difference between the 10^{th} percentile, t_{10}, to the 50^{th} percentile, t_{50}, of a signal trace.

accounted for, whereas seasonal effects are already included in the signal model[2]. Parameter values can be found in [69].

The majority of the trace should be within the 3 % level for either detector type. Anything above reduces the capacity of the time model to differentiate between $X_{\mathrm{max}}^{(\mu)}$ for mass composition purposes (i.e., its resolution will become poor during reconstruction). This is easily identifiable through time quantiles. Those within 3 % correspond to an X_{max} of $\approx 25\,\mathrm{g\,cm^{-2}}$ in the WCD. For the MD, time quantiles within 3 % imply an X_{max}^{μ} accuracy of $\approx 30\,\mathrm{g\,cm^{-2}}$ and $\approx 20\,\mathrm{g\,cm^{-2}}$ for the 1-bit counting and integrator strategy respectively[3].

The functional shape derives from the convolved response of the detector response and temporal distribution of the particle spectrum. Many functional shapes were studied in references [65, 81] to describe the time dependence (Moyal distribution, Gamma distribution, etc.). However, most were unsuitable to describe the fast rise of the traces (from muons in the shower front). The log-normal describes the trace accurately over a wide range of radial distances. It only fails close to the shower core ($r < 150$ m) for the highest energies. At these distances, the WCD and MD are saturated and cannot be used during the time model reconstruction[4]. Its functional form is

$$\frac{\delta S}{\delta t}(t, t_0, m, s) = \left\{ \begin{array}{cc} 0 & \text{for } t \leq t_0 \\ \frac{1}{(t-t_0)s\sqrt{2\pi}} \exp\left(-\frac{(\ln(t-t_0)-m)^2}{2s^2}\right) & \text{for } t > t_0 \end{array} \right\}, \tag{5.1}$$

where t_0 is the arrival time of the first particle. Its time is with respect to the arrival of the curved shower front, propagating at the speed of light. m and s are the shape parameters (mean and width), discussed later in section 5.2.

To provide an accurate description on the shape and t_0, traces are binned in 2 ns time bins for the WCD. Time bins for the MD remain unchanged. However, for the 1-bit counting strategy, each bin represents the mean number of muons[5]. During reconstruction, these *pdf*s are rebinned into their respective bin width of 25 ns.

Signal traces can be fitted twofold: (i) fitting the complete trace with a χ^2 or (ii) use three time quantiles (t_1,t_{10} and t_{50}) to calculate t_0, m and s. The latter is a practical approach for faster calculations. However, it disregards the tail of the trace which could provide useful information on the late stage of the shower development. In this work, approach (i) is used where the trace is fitted up its 90^{th} percentile. This provides a more complete description on the parameter (and its errors), which is used during the model characterization. First, the origin of times is derived at a reference distance of 450 m. It is then used to derive m and s.

5.1 Time Origin - t_0

In CORSIKA simulations, particle timing starts at the first interaction point X_1. No particle can arrive prior to the arrival of the spherical shower front with its time origin at height of

[2] Seasonal differences change the trace no more than 5 %.

[3] The 10 % level reflects biases up $50\,\mathrm{g\,cm^{-2}}$ and $65\,\mathrm{g\,cm^{-2}}$ for X_{max} and X_{max}^{μ} respectively. X_{max} differences between proton and iron are at the order of $100\,\mathrm{g\,cm^{-2}}$.

[4] The shape has been effectively compromised.

[5] This approach is used as no definitive counting strategy was available for the SiPM. Nevertheless, counting strategy effects can be added at the reconstruction stage.

X_1. X_1 could be used to derive t_0 but in reference [80] it was found that shower particles start their lateral spread after 100 g cm^{-2} – 200 g cm^{-2}. The optimal time origin is therefore between X_1 and $X^{(\mu)}_{\max}$. Using the average signal traces a quasi-physical quantity $D^{(\mu)}_{T_0}$ can be calculated, which is defined as the geometric distance along the shower axis from the shower maximum to the *effective time origin*[6]. The reference core distance r_{ref} is a compromise between the particle statistic and shower front width. Considering the reference energy of 10^{18} eV used during the development of the signal model and intended use for low energetic showers, it was found that 450 m is qualitatively most suitable for the intended use of this model (infilled array). With $D^{(\mu)}_{T_0}$, the expected start time t_0 at all radial distances can be predicted.

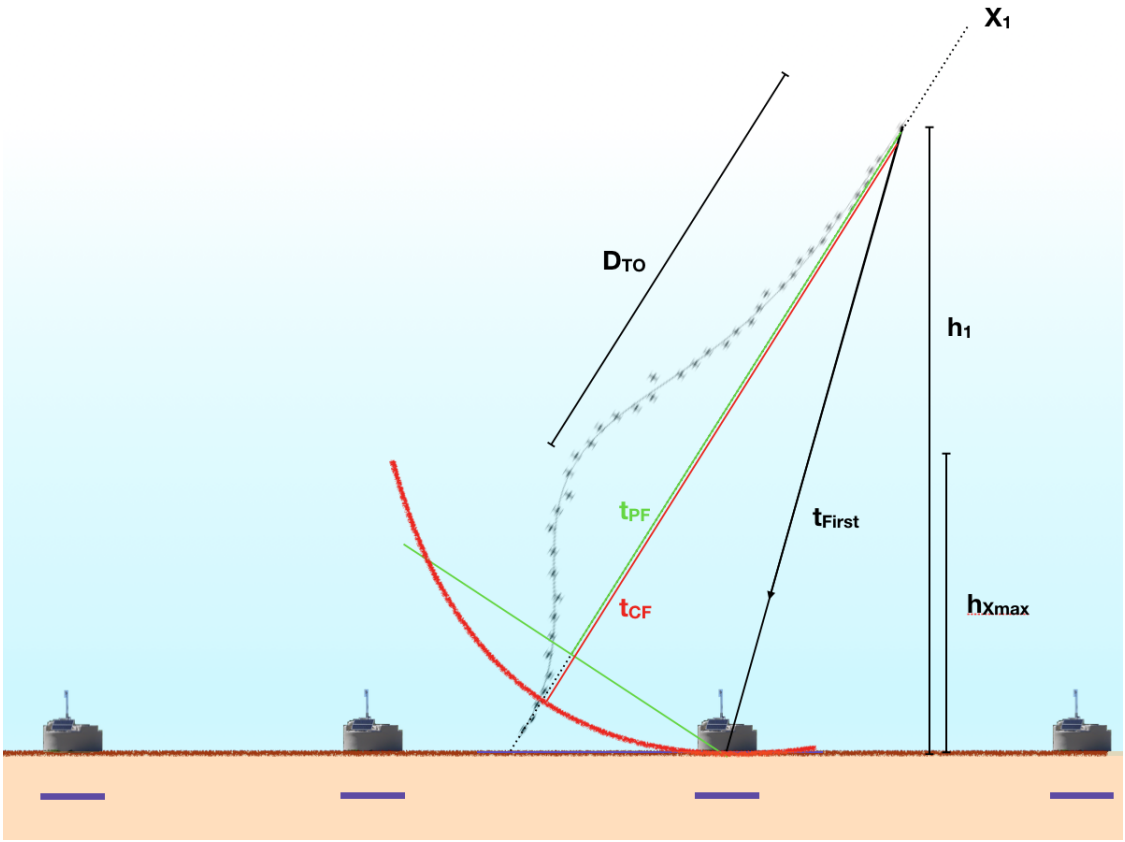

Figure 5.1: Schematic illustration of $D^{(\mu)}_{T_0}$, the geometric distance between the shower maximum and effective time origin.

Figure 5.1 shows a schematic of D_{T0} and its derivation. It can be calculated through

$$D_{T_0} = \frac{h_1 - h_{X^{(\mu)}_{\max}}}{\cos\theta}, \tag{5.2}$$

where h_1 and $h_{X^{(\mu)}_{\max}}$ refer to the vertical height of the effective time origin and shower maximum. The bracketed notation in $h_{X^{(\mu)}_{\max}}$ implies that the same calculation applies to electromagnetic shower maximum ($X_{\max}$) and muon production depth ($X^{\mu}_{\max}$). The height is

[6]This approach replaces X_1. X_1 is correlated to the particle cross section (see reference [82]) and is therefore an interesting choice for subsequent analysis. Although this was not studied during the scope of this work, a correlation between $D^{(\mu)}_{T_0}$ and the particle cross section would not be surprising.

a mere conversion of the atmospheric overburden into km through GDAS. The zenith refers to the elevation of the shower axis. Detectors at a radial distance r are related to t_{pf} and t_{first} through

$$r^2 = d_{\mathrm{pf}}^2 + d_{\mathrm{first}}^2 = \left(t_{\mathrm{pf}}c\right)^2 - \left(t_{\mathrm{first}}c\right)^2, \tag{5.3}$$

where t_{pf} is the arrival time of the plane front and t_{first} the arrival time of the first particle propagating at the speed of light from the effective shower origin to the detector. Assuming a spherical shower front, it is equivalent to t_{cf}. t_0 is defined as $t_0 = t_{\mathrm{first}} - t_{\mathrm{pf}}$. Combining this with equation (5.3) yields

$$d_{\mathrm{pf}} = \frac{r^2 - (t_0 c)^2}{2t_0 c}. \tag{5.4}$$

With it, h_1 can be written as

$$h_1 = \left(d_{\mathrm{pf}} + r \cdot \tan\theta \cos\psi\right) \cdot \cos\theta, \tag{5.5}$$

where ψ is the detector azimuth. After combining equations (5.2), (5.3), (5.4), and (5.5), the final expression for $D_{T_0}^{(\mu)}$ is derived. Equation (5.4) already implies several behavioural features for $D_{T_0}^{(\mu)}$. Closer to the shower core, r and t_0 will approach zero, implying a negative (non-physical) result for the effective shower origin. Detector effects can affect the start time t_0 such that $D_{T_0}^{(\mu)}$ may be outside the atmosphere[7]. Furthermore, errors in t_0 are considered Gaussian but are asymmetrical in D_{T_0} (this has been accounted for in subsequent analysis).

$D_{T_0}^{(\mu)}$ is calculated for showers at 450 m and $\psi = 90°$ characterized with respect to E, θ and $X_{\mathrm{max}}^{(\mu)}$. All particle components have their respective shower origin. The MD provides two different measurements to count muons (1-bit counting strategy and integrator). As a result, their time origin is also computed independently.

Figures 5.2 and 5.3 show the $D_{T_0}^{(\mu)}$ distribution for the MD and WCD with respect to their model predictions (dashed lines). Irrespective of counting strategy, the $D_{T_0}^{\mu}$ in the MD is fairly independent of X_{max}^{μ}. The time origin is mostly around $\sim$100 km, resulting from an additional delay between the particle arrival times and photon arrival times to the photomultiplier[8]. The average delay is of the order of $\sim$13 ns. The integrator (right figures in 5.2) is also affected due to the muon pulse shape. This decreases its perceived time origin (as seen between figures 5.2a and 5.2b). Despite these detector effects, a minor X_{max}^{μ} dependency is seen (emphasized by very inclined showers). This is described by an exponential and linear function for the 1-bit counting strategy and integrator respectively,

$$D_{T_0}^{\mu}(X_{\mathrm{max}}^{\mu}, E, \theta) = \begin{cases} \alpha_1(E,\theta)\ \exp\left(-\alpha_2(E,\theta) X_{\mathrm{max}}^{\mu}\right) & \text{for 1-bit strategy} \\ \alpha_1(E,\theta) + \alpha_2\ (X_{\mathrm{max}}^{\mu} - 650\ \mathrm{g\,cm^{-2}}) & \text{for the integrator} \end{cases} \tag{5.6}$$

Showers for the same energy and zenith are first fitted to the function in equation (5.6). The scale and slope parameters $\alpha_i(E,\theta)$ are energy (weakly) and zenith dependent and empirically characterized and shown in figures B.1; a total of 6720 showers are used. $D_{T_0}^{\mu}$ increases with θ. This results from the shower propagating longer through less dense atmospheric profiles, exponentially increasing the distance to the effective time origin. As figures

[7] At 450 m, $D_{T_0}^{(\mu)}$ may be roughly interpreted as inversely proportional to t_0.

[8] i.e. t_0 becomes $t_0' = t_0 + t_{delay}$

5.2c and 5.2d indicate, the increased energy is coupled to an increased shower depth. This should not (and does not) affect the end result of $D^{\mu}_{T_0}$ as the increased energy also increases the depth at which the lateral spread will begin. This parallel affect is recognized by a shift.

Characterizing $D^{\mu}_{T_0}$ is difficult. Deviations are sometimes above 20 %. However, these should be evaluated with respect to t_0, where they are within the 10 %. It is therefore unnecessary to further improve the characterization of $D^{\mu}_{T_0}$.

In terms of Universality, $D^{\mu}_{T_0}$ of showers of different hadronic models and primaries range between 90 km and 200 km with the model prediction around 150 km for the 1-bit counting strategy. This translates into t_0 differences below 10 %. For the integrator, the spread is smaller with t_0 within the 5 % level.

With the model prediction for t_0 and the MC values for m and s, the signal trace time quantiles t_1, t_{10}, t_{50} and t_{90} are calculated. This serves as an intermediate step for bias checks. These are illustrated in figures B.2 and B.3. Most are within the 5 % level. At shower core distances below 275 m t_1 biases increase up to 30 %. This does not pose a problem as the absolute errors are smaller than the bin width[9].

For the components in the WCD, similar structures are apparent. Only the muonic and pure electromagnetic particle component are depicted in figure 5.3. Those for the remaining two particle components are shown in figure B.1. Only the muonic and the electromagnetic particle component from muons show a clear and compact zenith and $X_{\max}$ dependency as in figure 5.3a. The pure electromagnetic particle component and those from hadronic jets are produced at a later stage and scatter multiple times before arriving to the detector. This distorts the D_{T_0} distribution as seen in figures 5.3b and B.1b. The dependency of D_{T_0} with $X_{\max}$ is characterized as

$$D_{T_0}(X_{\max}, E, \theta) = \begin{cases} \alpha_1(E,\theta)\ \exp\left(-\alpha_2(E,\theta) X_{\max}\right) & \text{Muon and EM-Muon} \\ \alpha_1(E,\theta) + \alpha_2(E,\theta)\ \left(X_{\max} - 650\ \mathrm{g\,cm^{-2}}\right) & \text{EM-Pure and EM-Hadron} \end{cases}, \tag{5.7}$$

with scale and slope parameters $\alpha_i(E,\theta)$ also characterized in Appendix B.1. Weak energy dependencies are found for D_{T_0}, coupled with the $X_{\max}$ shift (see figure 5.3d). D_{T_0} increases with larger energies, signifying a lower t_0.

For the highest energies, the plane front of the pure electromagnetic component arrives almost simultaneously as the muon plane front. At these energies it is more suitable to derive D_{T_0} further from the shower core. In reference [80], a radial distance of 800 m was chosen. Although not studied in this work, it may be more suitable to replace the reference distance r_{ref} with an energy dependent $r_{\mathrm{ref}}(E)$.

D_{T_0} for different primaries and hadronic models are relatively well described by the predicted values. Offsets seen in figures 5.3e and 5.3f are within the 10 % level of t_0. t_1, t_{10}, t_{50} and t_{90} are calculated by combining the predicted t_0 with the MC values for m and s (as previously done with the MD). These are illustrated in figures B.4, B.5, B.6, and B.7. All particle components are within the 5 % level between t_{10} and t_{70}. For the muonic and electromagnetic particles from muon component it was found that t_1 differs by 20 % for core distances below 200 m. Equivalently large biases are also seen for t_{90}. t_1 and t_{90} are within

[9] E.g. assume $t_0 = 8$ ns and $t_0^{\mathrm{pred}} = 6$ ns. Biases are at 25 % but the MD bin width is at 3.125 ns (25 ns for the inhibition window) or 6.25 ns.

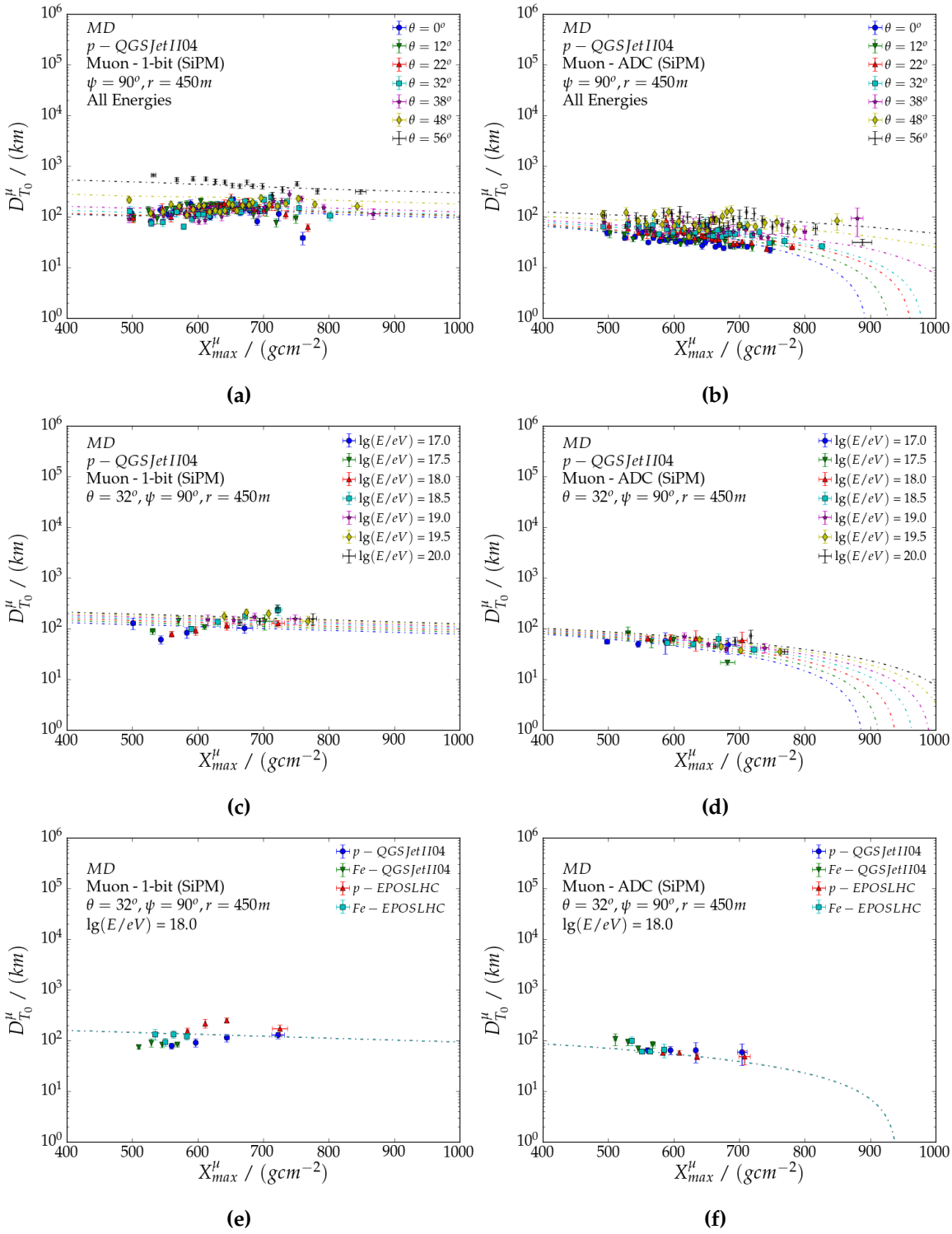

Figure 5.2: $D^{\mu}_{T_0}$ profile distribution for the 1-bit (**left**) and integrator (**right**) counting strategy of the MD. Figures **a)** and **b)** show the zenith dependence, **c)** and **d)** the the energy dependence and **e)** and **f)** the primary and hadronic model dependence. For illustrative purposes, markers represent the the average of 60 showers (sorted for X^{μ}_{max}) with their variances.

the 10 % level for the pure electromagnetic and hadronic jet component. These results can be interpreted as (i) a failure of the log-normal ansatz or (ii) a correct ansatz but a biased MC for late arriving particles. Late particles have large weights, possibly biasing the accumulated

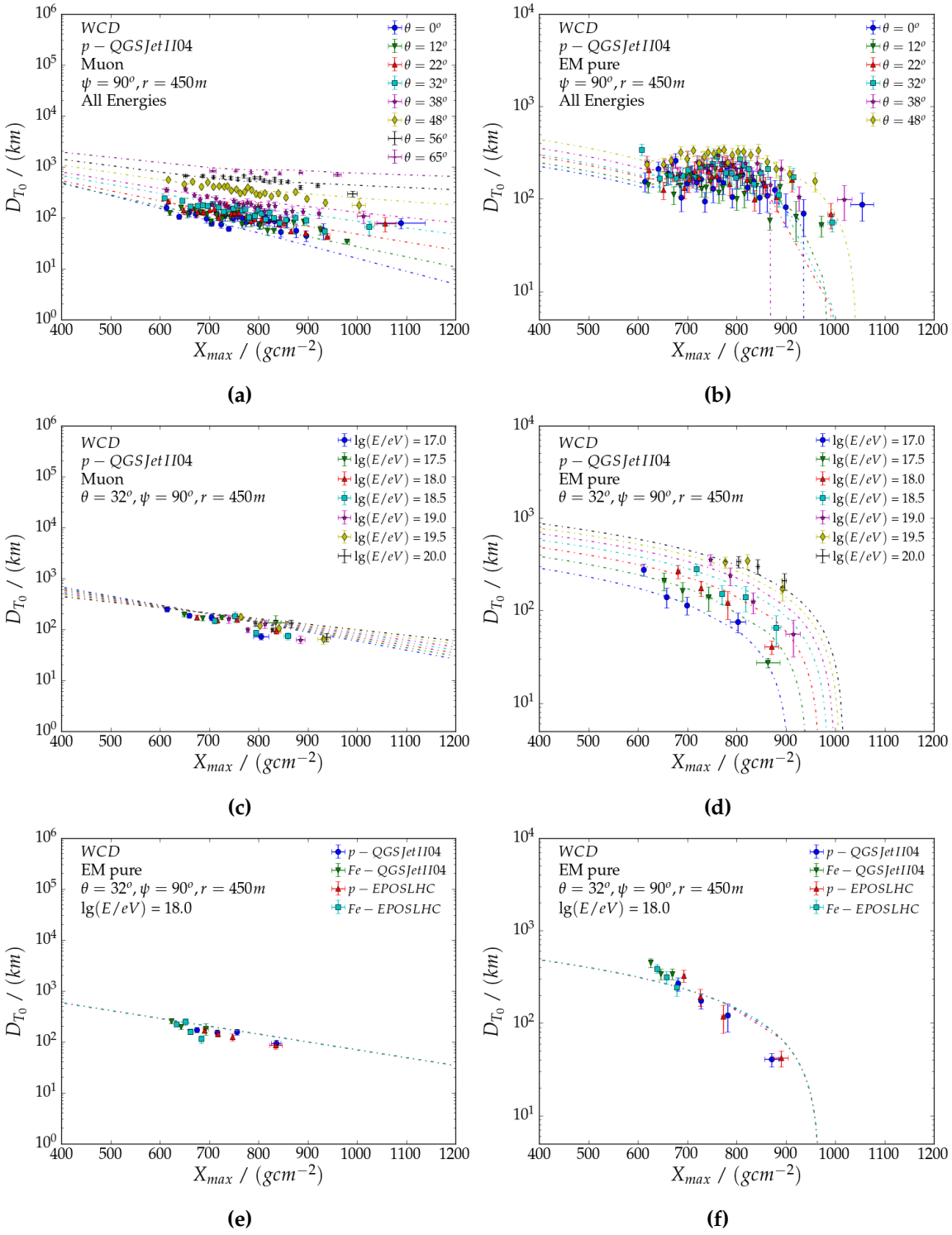

Figure 5.3: D_{T_0} profile distribution for the muonic (**left**) and pure electromagnetic (**right**) particle component of the WCD. Figures **a)** and **b)** show the zenith dependence, **c)** and **d)** the the energy dependence and **e)** and **f)** the primary and hadronic model dependence. For illustrative purposes, markers represent the the average of 60 showers (sorted for $X^{\mu}_{\max}$) with their variances.

delay. No better distribution was found for (i). Also, it is computationally inefficient[10] to

[10]Due to increased simulation time and disk space.

quantify the possible bias of (ii) for all CORSIKA showers. Biases are empirically corrected for in section 5.3.

5.2 Shape Parameters - m, s

Through equations (5.2), (5.3), (5.4) and the parameterization of $D_{T_0}^{(\mu)}$ the start time t_0 is obtained. This is used to calculate m and s, reducing the three-parameter fit of the log-normal in equation (5.1) into a two-parameter fit. $D_{T_0}^{(\mu)}$ biases are propagated into m and s, which are partially corrected for during their respective characterizations. m and s are calculated for all radial and azimuth of all available CORISKA showers.

m and s are empirical characterized based on several anticipated features of the shower development. For increased radial distances, electromagnetic particles are delayed due to multiple scattering, whereas muons with sufficient transverse momenta (with respect to their total energy) to reach far lying detectors are generally produced late in the shower development. Consequently, the mean and width of the time trace will increase. As with the signal model, shower ages are expressed in $\Delta L^{(\mu)}$ for the muonic component and ΔX for all electromagnetic particle components (see section 4.1[11]) to emphasize time sensitive shower parameters. Zenith dependencies are incorporated into $\Delta X / \Delta L^{(\mu)}$. Given a specific radial distance, m and s are expected to decrease with increasing shower age, resulting from the increased path length in the atmosphere. Considering that the atmospheric density decreases exponentially with respect to height, a similar dependency is also expected. Energy dependent features are difficult to envision for the full energy range. From the principles of Universality, at first order, an increased energy translates into a decreased shower age and thus into a smaller m and s.

Following the aforementioned physical motivations, the m, s-characterization in reference [80] is derived by first fitting m and s to

$$f_{m,s}(r, \Delta L) = \alpha_1(r) + \alpha_2(r) \exp\left(\frac{-\alpha_3(r)\Delta L}{1000\,\mathrm{m}}\right) \tag{5.8}$$

for all particle components in all showers and subsequently fit the residuals with respect to energy, zenith and azimuth. With this approach, time quantiles up to t_{50} could be reproduced within the 3 % level. In this work, it is found that the ansatz used in reference [80] and its successor in reference [81], also designed for the WCD, is insufficient to describe the full energy range. Different dependencies were also found for the MD. In this work, they are derived by first fitting m and s with respect to the shower stage $\Delta L^{(\mu)}$ for showers (all zenith angles) with the same energy and at the same radial distance (similar strategy as the Gaisser-Hillas approach in section 4.2). The fit parameters are then characterized for their energy dependencies. Next, m/s of all showers at radial distances r_i are then fitted with respect to energy and shower stage, providing a better estimate on the parameters and their correlations to each other. At this stage, leading order dependencies to the shower parameters have been accounted for. Combined, second order geometric dependencies can bias m/s more than

[11] $\Delta L^{(\mu)}$ is the geometric distance from the shower maximum to the detector along the shower axis.

10 %. As a result, they are characterized by fitting the residuals as in reference [80]. For the WCD, the trace mean m is found to have the functional form of

$$\begin{aligned} &m_{\mathrm{WCD}}(r, \theta, \psi, E, \Delta L) = \\ &\big(\alpha_1(r)(\lg(E/\mathrm{eV}) - 18) + \alpha_2(r)\big) \exp\left(\alpha_3(r)\Delta L\right) + \\ &\alpha_4(r)(\lg(E/\mathrm{eV}) - 18) + \alpha_5(r)\cos\psi + \\ &\alpha_6(r)(\Delta L - \Delta L_{\mathrm{ref}}) + \alpha_7(r) \end{aligned} \tag{5.9}$$

for all particle components. For the muonic ($\Delta\xi = \Delta L$) and electromagnetic particles from muon component ($\Delta\xi = \Delta X$), the trace width s is characterized as

$$\begin{aligned} &s_{\mathrm{WCD}}^{\text{Muon,EM-Muon}}(r, \theta, \psi, E, \Delta\xi) = \\ &\alpha_1(r)\Delta\xi^2 + \big(\alpha_2(r)(\lg(E/\mathrm{eV}) - 18) + \alpha_3(r)\big)\,\Delta\xi + \\ &\alpha_4(r)(\lg(E/\mathrm{eV}) - 18) + \alpha_5(r)\cos\psi + \\ &\alpha_6(r)(\Delta\xi - \Delta\xi_{\mathrm{ref}}) + \alpha_7(r), \end{aligned} \tag{5.10}$$

whereas the for the remaining particle components it is

$$\begin{aligned} &s_{\mathrm{WCD}}^{\text{EM-Pure,EM-Hadron}}(r, \theta, \psi, E, \Delta X) = \\ &\big(\alpha_1(r)(\lg(E/\mathrm{eV}) - 18) + \alpha_2(r)\big)\,\Delta X + \\ &\alpha_3(r)(\lg(E/\mathrm{eV}) - 18) + \alpha_4(r)\cos\psi + \\ &\alpha_5(r)(\Delta X - \Delta X_{\mathrm{ref}}) + \alpha_6(r). \end{aligned} \tag{5.11}$$

Modulations in ψ deviate maximally 10 % with respect to $\psi = 90°$ and are accounted for with the term $\alpha_i(r)\cos\psi$. $\Delta X_{\mathrm{ref}}/\Delta L_{\mathrm{ref}}$ is a reference value of $\Delta X/\Delta L$ for which X_{max} is 650 g cm^{-2}. Parameters $\alpha_i(r)$ are interpolated in r[12].

The counting strategies of the MD do not affect the functional shapes for the m and s. Their trace mean m is found to be

$$\begin{aligned} &m_{\mathrm{MD}}(r, \theta, \psi, E, \Delta L^{\mu}) = \\ &\big(\alpha_1(r)(\lg(E/\mathrm{eV}) - 18) + \alpha_2(r)\big) \exp\left(\alpha_3(r)\Delta L^{\mu}\right) + \\ &\alpha_4(r)(\lg(E/\mathrm{eV}) - 18) + \alpha_5(r)\cos\psi + \\ &\alpha_6(r)(\Delta L^{\mu} - \Delta L^{\mu}_{\mathrm{ref}}) + \alpha_7(r), \end{aligned} \tag{5.12}$$

whereas the trace width s is

$$\begin{aligned} &s_{\mathrm{MD}}(r, \theta, \psi, E, \Delta L^{\mu}) = \\ &\big(\alpha_1(r)(\lg(E/\mathrm{eV}) - 18) + \alpha_2(r)\big)\,\Delta L^{\mu} + \\ &\alpha_3(r)(\lg(E/\mathrm{eV}) - 18) + \alpha_4(r)\cos\psi + \\ &\alpha_5(r)(\Delta L^{\mu} - \Delta L^{\mu}_{\mathrm{ref}}) + \alpha_6(r), \end{aligned} \tag{5.13}$$

where $\Delta L^{\mu}_{\mathrm{ref}}$ is a reference value of ΔL^{μ} for which X^{μ}_{max} is 550 g cm^{-2}. $\alpha_i(r)$ differs between counting strategies and is also interpolated in r.

[12]The interpolation uses the parameter values obtained at the radial distances of the sampling areas. Detector closer than 60 m and further than 1500 m from the shower core are therefore rejected. This is not problematic as detectors are already saturated below 60 m and do not provide a useful time structure at 1500 m.

Figures 5.4 and 5.5 illustrate the newly found characterization for showers at $10^{18.5}$ eV. Each marker depicts the average m/s of 120 showers at distance r_i and zenith θ_i. Errors refer to the variance in m/s and $\Delta L^{(\mu)}$. The dashed blue line corresponds to the model prediction at r_i (labeled next to it in the figure)[13]. Anticipated radial and shower depth dependencies are recognized in the MD in figures 5.4a and 5.4c. They are also seen for all particle components in the WCD (figures 5.5a, 5.5c, B.8a, and B.8c). At the highest energies, they are in agreement with earlier work discussed in references [65, 80, 81]. Between the MD and WCD, it can be recognized that s depends significantly less on shower age and radial distance for the MD. This can be attributed to the detector response but also to the absence of low energetic muons in the tail of the trace, effectively decreasing s for the MD with respect to the WCD. Differences between the 1-bit counting strategy (figure 5.4b) and integrator (figure 5.4b) are also evident, implying that MD detector effects (especially the integrator) are suppressing potential primary sensitive parameters.

The contribution of absent low energetic muons in the MD can be validated with the development of a time model for the SSD. The SSD and MD share a similar design. Furthermore, the SSD is also exposed to the same particle components as the WCD. These shared features can be exploited to highlight the muon energy spectrum effect on s[14].

For the MD and the electromagnetic particles from hadronic jet component in the WCD, showers above 56° are not very well represented by the time model. The functional form of m and s has not been altered to prevent over-fitting. Furthermore, at 56°, biases are most evident for radial distances beyond 1100 m and below 150 m where the time trace signal is too low and saturated respectively. They can be safely ignored[15]. Characterizing the hadronic jet component is difficult due to its inconsistent time structure for very inclined showers (possibly from electromagnetic particles carrying large weights, leading to (nonphysical) peaks in the traces and thus a bad fit). This is a break in Universality for the time profile. However, considering the relative fraction of electromagnetic particles from hadronic jets (below 5 %), its effect becomes minimal.

In terms of Universality, different hadronic models and primaries align very well to the characterization from proton QGSJETII-04. They are indicated as a shift in $\Delta L^{(\mu)}$ along the line of the model prediction. Equivalent results are found for energies between 10^{17} eV and 10^{20} eV. Seasonal effects change the temporal structure of arriving particles less than 1 %. They only change the scale of the signal, which has already been accounted for during the development of the signal model (section 4.2.2).

Combining the characterization for t_0 (from section 5.1), m and s, the time quantiles of the detector traces are calculated. Comparing them to their MC simulation counterpart, it is found that the time trace, irrespective of detector or particle component, is within the 3 % level between t_{30} and t_{70}. Below t_{30} and above t_{70}, time offsets are as large as 15 %. This results from the failure of the log-normal ansatz and is empirically corrected for in section 5.3.

[13] As a reminder, the distribution of shower age for vertical showers is lower compared to inclined showers; i.e., $\Delta L^{(\mu)}(0°) < \Delta L^{(\mu)}(56°)$.

[14] I.e., if the SSD reveals equivalent results as shown in figures 5.4b and 5.4d, then the suppression of s to shower stage and radial distances can be fully attributed to detector properties.

[15] 56° is also beyond design specifications for the MD.

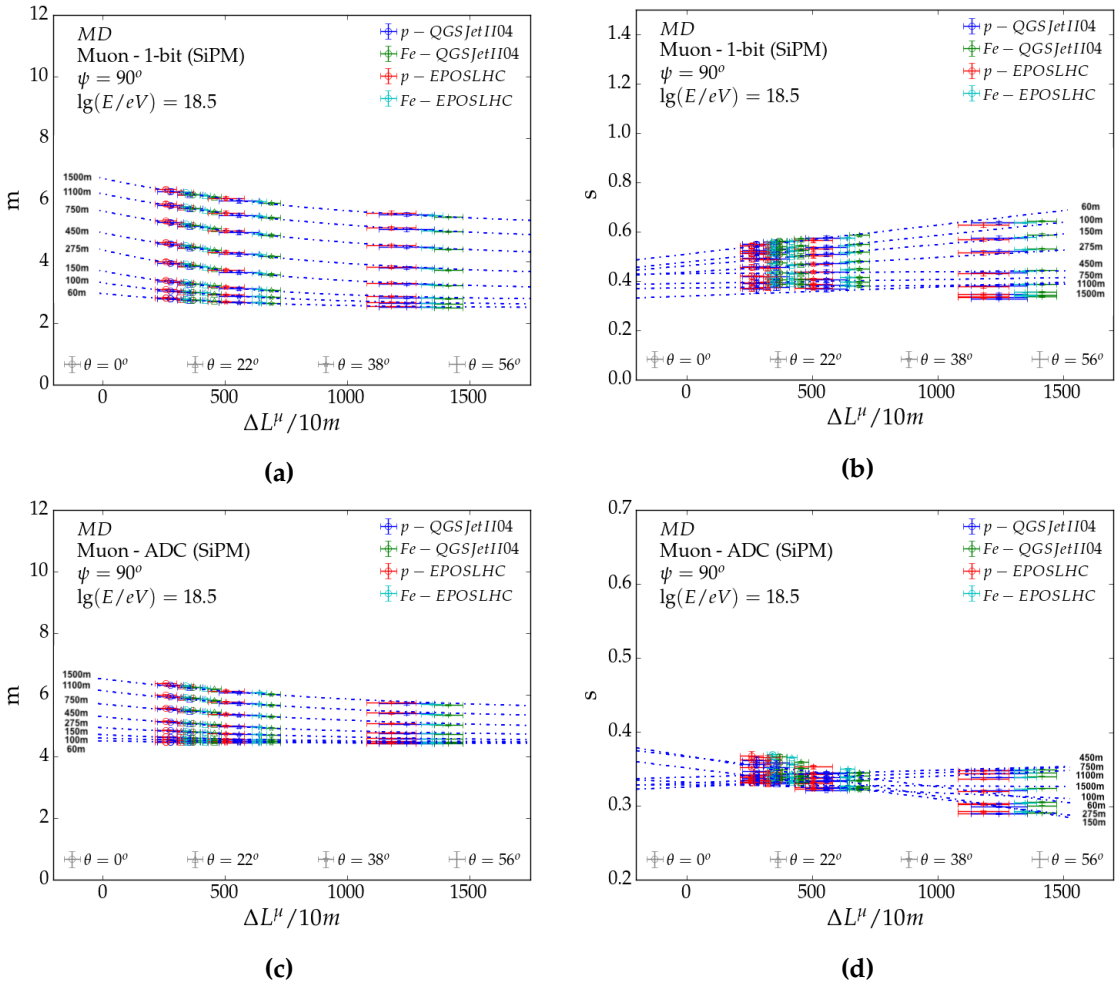

Figure 5.4: m and s parameters for the log-normal trace for the **a)** 1-bit counting strategy and **b)** integrator in the MD at $10^{18.5}$ eV. The blue dashed line represents the model prediction at different radial distances. Markers depict the trace shape for different primaries and hadronic models.

5.3 Time Correction

In section 5.1, the time model derives its *effective time origin* at the reference core distance of 450 m and fits it to a log-normal. As each time bin (up to t_{90}) is used to fit the log-normal, biases at the tails become present. This effect is also present in the previous iteration of the time model in reference [80] where t_1, t_{10} and t_{50} give an *exact*[16] result to t_0, m and s. There, time offsets below t_{30} are smaller compared to this work. However, they are also larger for t_{90} (about 20 % for all particle components together). Unless a better ansatz than the log-normal is found, the time traces are corrected for to be within the necessary 3 % level.

As figures 5.6 and 5.7 (and those in Appendix B.3) show, time offsets depend primarily on radial distance and only little on shower stage. The latter becomes relevant for detectors at radial distances below 150 m. A purely geometric time correction is applied and may be interpreted as a correction to the purely spherical shower front. It is obtained by averaging the time offset for all showers in each sampling area.

[16] three variables, three parameters

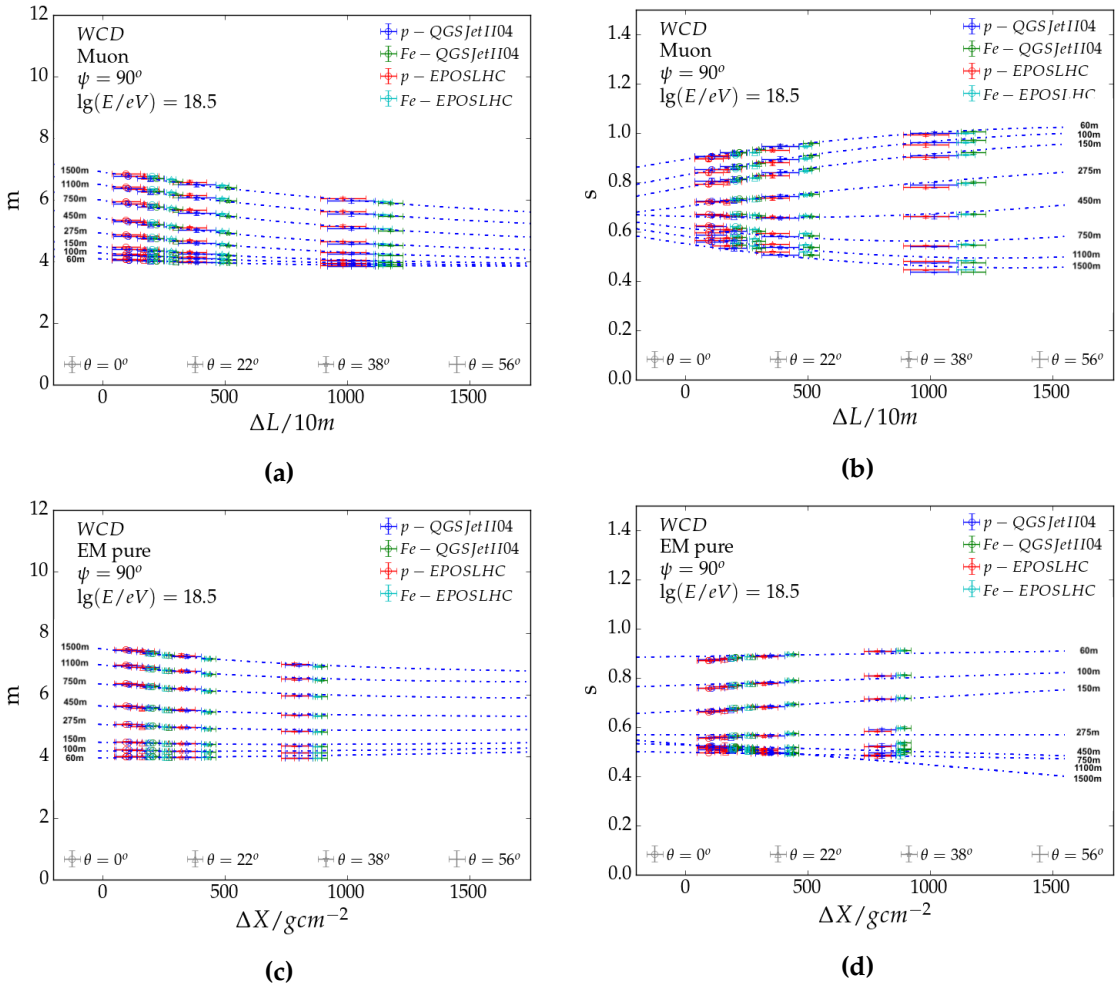

Figure 5.5: m and s parameters for the log-normal trace for the **a)** muonic and **b)** pure electromagnetic particle component in the WCD at $10^{18.5}$ eV. The blue dashed line represents the model prediction at different radial distances. Markers depict the trace shape for different primaries and hadronic models.

For the 1-bit counting strategy in the MD, the predicted time quantiles are overestimated. Their difference increases further away from the reference distance 450 m. An overestimation of time quantiles reflects in an overestimation of $X^{(\mu)}_{\max}$. If the time model, without any further correction, is used together with the signal model then the pairing of the R_μ-$X^{(\mu)}_{\max}$ would yield a bias towards lighter cosmic ray primaries. Equivalent (or even similar) structures are not found for the integrator counting strategy (see figure B.9). All time quantiles are within the 3 % level[17]. The geometric time correction is characterized as

$$t_q = t_q^{\text{pred}} \cdot f_{\text{corr}}(q, r), \tag{5.14}$$

with $f_{\text{corr}}(q, r)$ as

$$f_{\text{corr}}(q, r) = \alpha_1(r) + \alpha_2(r)(q - 0.5) + \alpha_3(r)(q - 0.5)^2, \tag{5.15}$$

where r is the distance to the shower core and q the trace quantile (between 0 % and 100 %). The constant 0.5 results from the smallest biases found at t_{50}. The parabolic form is

[17] The log-normal ansatz needs no more improvements here. Nevertheless, in this work, the geometric time correction is also applied.

derived from the semi-symmetric offset between t_{10} and t_{90}. $\alpha_i(r)$ emphasizes the scale of the geometric offset and is described as

$$\alpha_i^{MD}(r) = p_1 + p_2 r + p_3/r \tag{5.16}$$

with different parameters values p_j for every $\alpha_i^{\mathrm{MD}}(r)$. The ansatz in equation (5.14) is most effective for traces with large detector signals, mostly coupled with *smooth* traces (i.e., a well-defined shape). Those with lower signals are affected by lately arriving particles, identified by peaks in the tail of the trace.

In the right figures of 5.6, the time quantiles are corrected and show a significant improvement. All time quantiles between t_{30} and t_{70} are within the required 3 % level for all energies and radial distances. The extremities of the trace are not within the desired level due to their dependence to the shower stage ΔL^{μ}. This applies only to MD below 150 m. At these distances, the 1-bit counting is saturated within the energy range of interest. MDs are not immediately rejected, as the integrator may not be simultaneously saturated (depending on primary energy).

Similarly to the MD, the particle components in the WCD have their smallest biases between t_{30} and t_{70}. Also, they are always within the 3 % level at 450 m from the shower core. Contrary to the figure 5.6, the predicted trace quantiles of all particle components are overestimated for radial distances below 450 m and underestimated above it. Biases for detectors closer than 275 m are also much larger than those at larger distances. Equal findings are also found for all other particle components (seen in figures B.10, B.10, and B.10).

Using the ansatz in equation (5.15), these offsets are reduced. There $\alpha_i(r)$ is characterized as

$$\begin{aligned} \alpha_1(r) &= p_1 + p_2 \exp\left(p_3 r\right) \\ \alpha_2(r) &= p_1 + p_2 r + p_3/r \\ \alpha_3(r) &= p_1 + p_2 r + p_3 r^2 \end{aligned} \tag{5.17}$$

for the muonic and electromagnetic particle from muon component and

$$\begin{aligned} \alpha_1(r) &= p_1 + p_2 r^2 + p_3/r \\ \alpha_2^{\text{EM-Pure}}(r) &= p_1 + p_2 r + p_3/r \\ \alpha_2^{\text{EM-Hadron}}(r) &= p_1 + p_2 r \\ \alpha_3(r) &= p_1 + p_2 r + p_3 r^2 \end{aligned} \tag{5.18}$$

for the pure electromagnetic and hadronic jet component -all with their respective parameter values p_j.

The right figures in 5.7 show the performance of the time correction for the muonic component (remaining particle components are in figures B.10, B.11, and B.12). Here, time quantiles are also within the 3 % level between t_{30} and t_{70}. Shower stage dependencies in t_{10} and t_{90} are recognized and more emphasized closer to the core. They are not accounted for as their bias in ns is smaller than the half width of the WCD time bin (i.e. 12.5 ns), irrespective of primary energy. Nevertheless, with additional fine tuning for the shower stage, the time model can also be used for electronics upgrades with higher sampling rates (up to maximum sampling rate of 500 MHz). Additional fine tuning would not benefit the 1-bit counting strategy in the MD due to its digitization of the analog signal. It would (in theory) benefit the integrator strategy. However, it is already at the 3 % level and thus unnecessary.

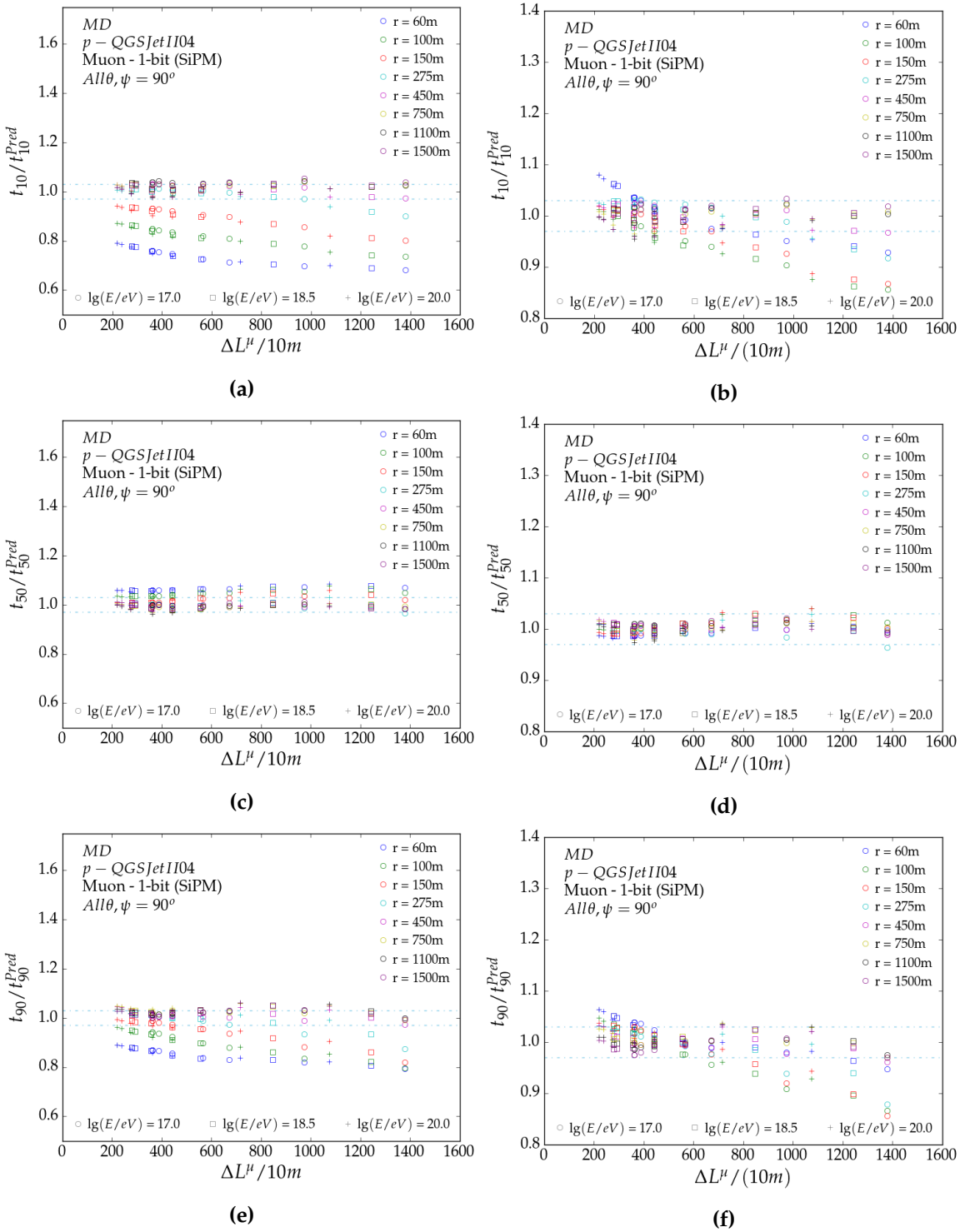

Figure 5.6: Biases between the 1-bit MD MC time quantiles and their respective predicted counterparts for different energies, radial distance and shower stage. **Left** are the biases of the *uncorrected* time quantiles. **Right** are the biases of the corrected time quantiles.

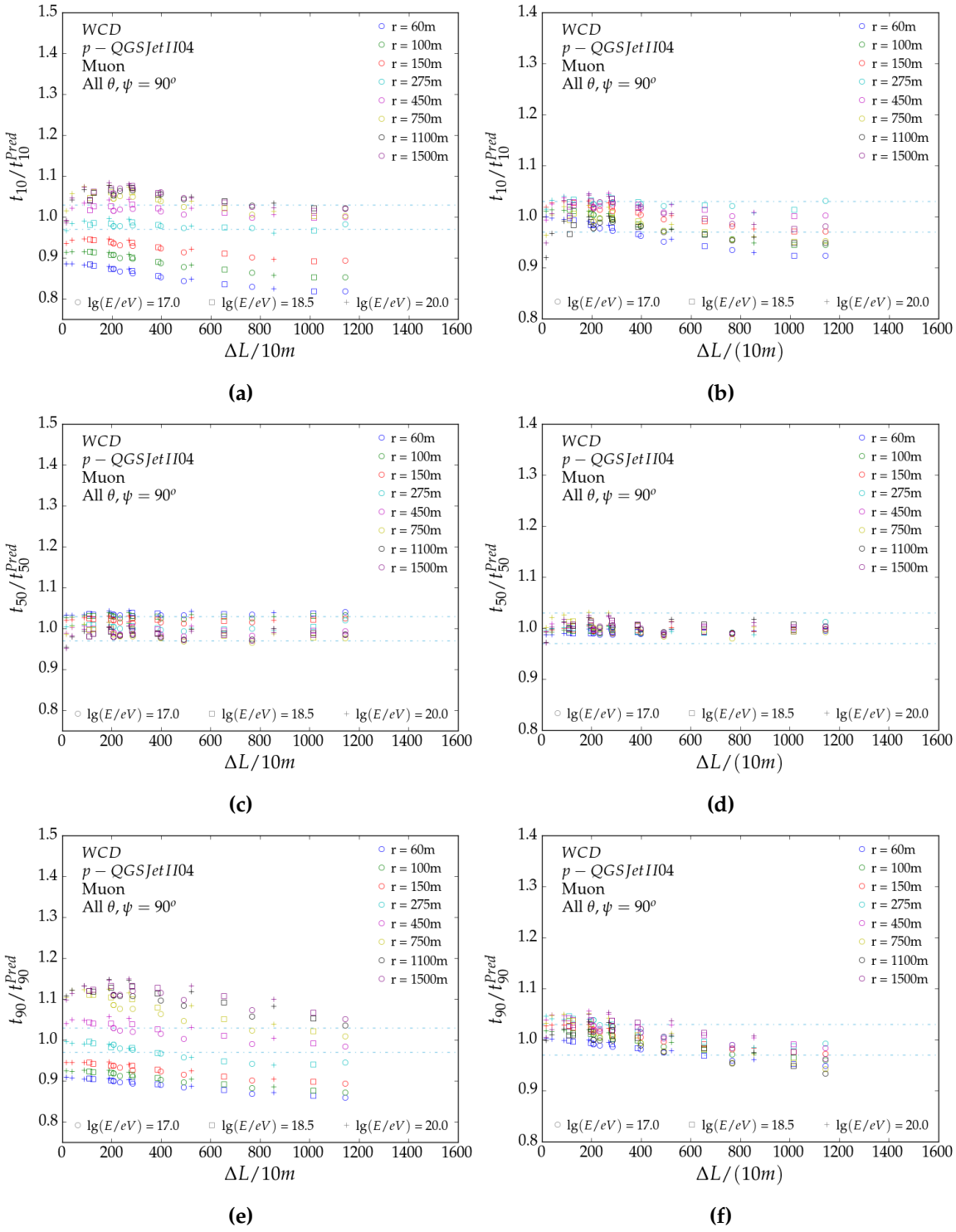

Figure 5.7: Biases between MC time quantiles and their respective predicted counterparts for different energies, radial distance and shower stage. They are illustrated for the muonic particle component in the WCD. **Left** are the biases of the *uncorrected* time quantiles. **Right** are the biases of the corrected time quantiles.

5.4 Validation

The time quantiles are useful indicators to validate the time model. They are mostly within the 3 % level between t_{30} and t_{70} and barely exceed the 10 % level for the rest of the traces. As mentioned in the beginning of this chapter, the 3 % level serves as a useful indicator for the error in $X_{\mathrm{max}}^{(\mu)}$. In reference [80], the time model must satisfy this condition strictly as the determination of X_{max} is only based on three quantiles. As this work utilizes the full trace information up to its 90$^{\mathrm{th}}$ percentile, its complete *shape* is validated here. This is done in figures 5.8 and 5.10 where the trace is integrated up to its quantile q[18] and compared to the one predicted by the time model from this work. They are shown for inclined showers of $\theta = 32°$ at $\psi = 90°$. Various energies and radial distances are depicted. The grey band in the figures refer to a $\pm 25\,\mathrm{g\,cm^{-2}}$ shift in $X_{\mathrm{max}}^{(\mu)}$, providing the necessary limits for the time model to be useful for mass composition purposes. Increasing or decreasing $X_{\mathrm{max}}^{(\mu)}$ affect the signal size, which has already been accounted for in the signal model. It is therefore removed to only emphasize its effect on the trace shape.

As the figures in 5.8 show, the shape of the WCD time model agrees most with the simulations with increasing trace information (or quantile). Biases seen at e.g. 1$^{\mathrm{st}}$ percentile are carried into subsequent quantiles. No significant energy dependencies are seen between 10^{17} eV, $10^{18.5}$ eV and 10^{20} eV. Further away from the core, a "bump" becomes visible between the 1$^{\mathrm{st}}$ and 30$^{\mathrm{th}}$ percentile. This results from the log-normal failure, underestimating the initial rise of the trace (time quantile correction could not correct for this). Here, energy dependencies become more emphasized as the peak flattens for higher energies. This is a favorable result as the shape of time traces at 1100 m are unsatisfactory for low energetic showers.

To minimize the effect of these biases, it is best to perform fits which exceed at least the 30$^{\mathrm{th}}$-percentile. Considering the lower t_{30}-limit and the reduced shape quality at the tail of trace (especially for traces far from the core), an upper limit at the 70$^{\mathrm{th}}$-percentile is set for universality time reconstructions (in chapter 6). In other words, the current WCD time model is most effective if minimally 30 % and maximally 70 % of the trace information is used. With an appropriate *signal time variance model* (signal variance in each time bin of the trace) the full trace information may be employed. The time model is based on the average trace response in a detector, assuming the signal variance in a time bin may be described by a Poisson distribution. This overestimates the signal variance in the bin, increasing the error of the reconstructed shower maximum (further elaboration will follow in chapter 6). Additional fine-tuning of the model can resolve the biases in the 1$^{\mathrm{st}}$ percentiles. However, its contribution to the full trace shape is negligible and thus not further studied in this work.

In terms of Universality, it is apparent that intrinsic differences between the hadronic models produce different outcomes for the trace shape. As these hadronic model differences are largest at the beginning of the trace, it suggests an increased muon production in the early stages of the shower development. This is not recognized in the electromagnetic and muonic longitudinal profiles of figures 3.2a and 3.2c respectively[19]. Although outside the scope of this work, longitudinal profiles for all particle components can help resolve this issue as they are sub-dominant in figure 3.2a.

[18] I.e., its cumulative distribution function.

[19] If anything, it should hint towards mass composition differences.

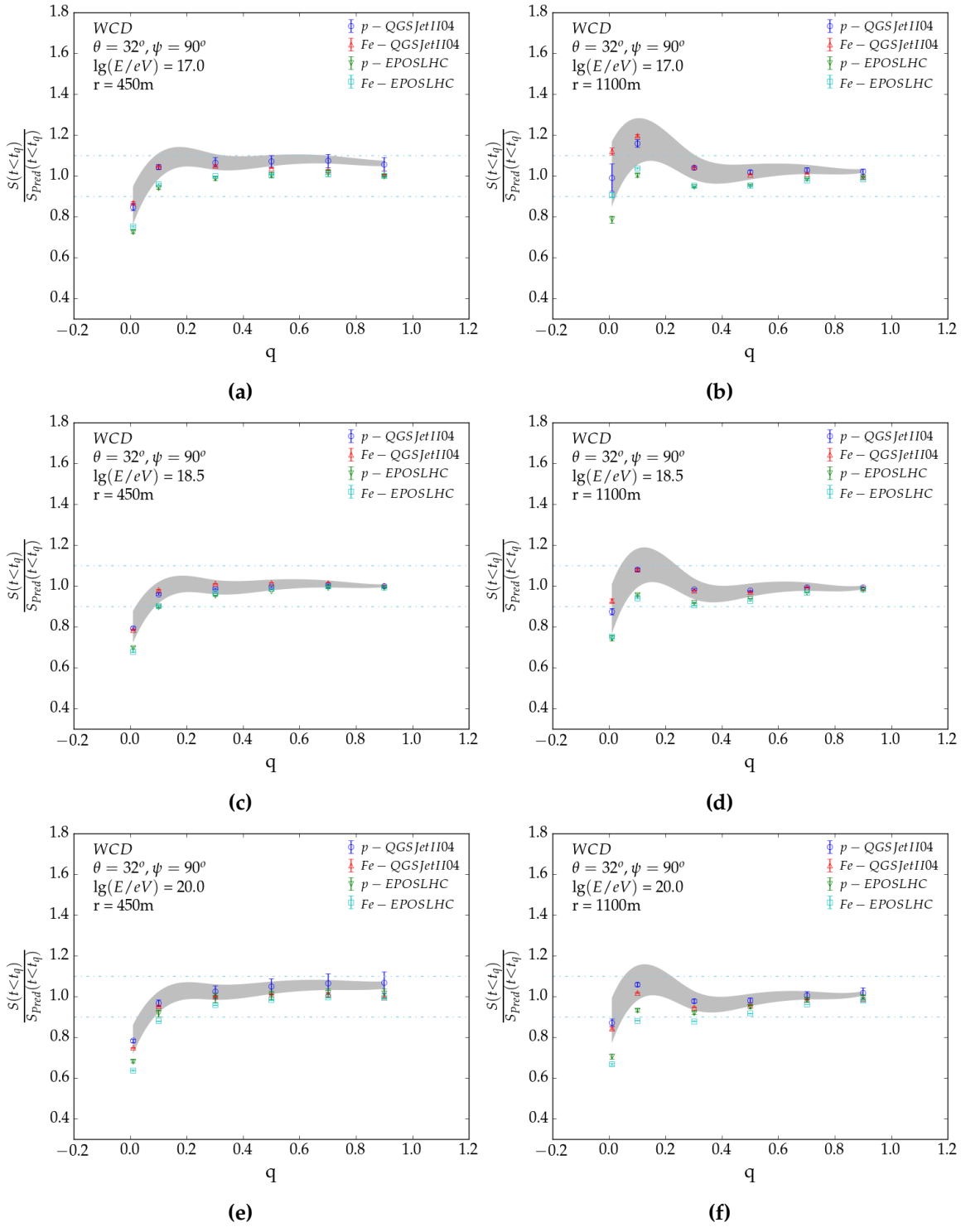

Figure 5.8: Ratio between the MC simulated and model predicted cumulative distribution of the signal trace. Signals at quantile q are those integrated up to t_q. They are depicted for the total trace of all particle components in the WCD at **left)** 450 m and **right)** 1100 m. The grey band represents the change in *cdf* (or trace shape) due to an $X_{\max}$ difference of up to $\pm 25\,\mathrm{g\,cm^{-2}}$. Comparisons for different hadronic models and primaries are shown. Error bars are the variance of 120 showers for the configuration depicted in the figure.

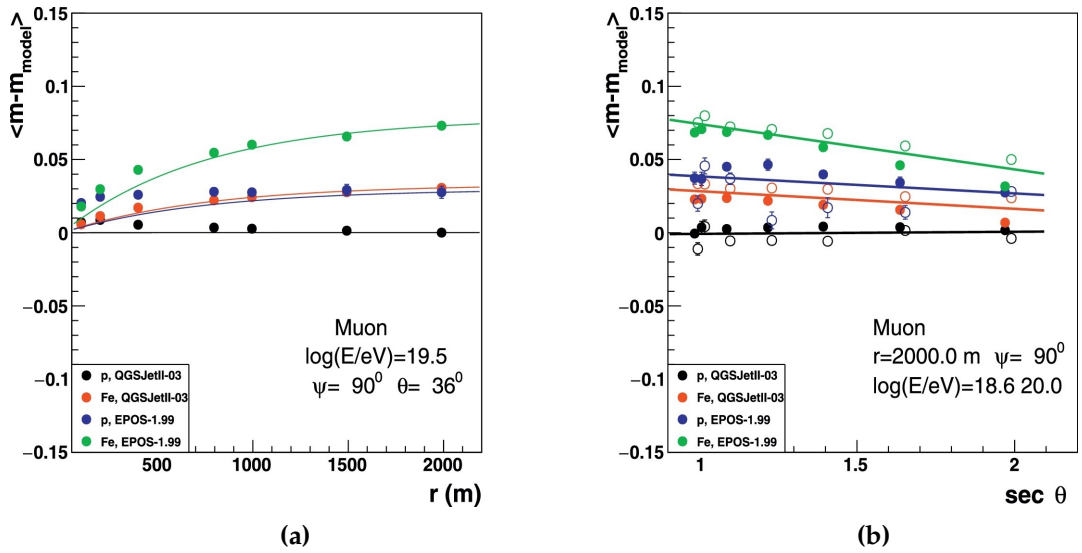

Figure 5.9: Residuals of m for different primaries and hadronic models. m_{model} refers to the reference model of proton QGSJETII-03. Results are depicted for the muonic component in the WCD from the time model discussed in reference [80]. **a)** Radial and **b)** zenith dependencies are illustrated.

As in reference [80], the individual component traces for muons and electromagnetic particles from muons differ between hadronic models. In reference [83], the pion to air elasticity differs as much as 10 %. It also decreases with larger center of mass energies, generating more low-energetic particles, mostly muons, during the early stages of the shower development. Low-energetic muons can decay just before reaching the detector, explaining the differences found here.

The figures in 5.9 show how this is addressed with a model dependent correction for m; $\Delta m(r, \theta)$. For the muonic trace component in WCD of showers at $10^{19.5}$ eV and $\theta = 36°$. The figures show radial (5.9a) and zenith (5.9b) dependencies up to 0.07 (below 1 % in m) for iron primaries from EPOS-1.99 (the predecessor to EPOS-LHC).

This correction implies a non-Universal time model. However, by using hybrid data from the FD and WCD any offsets in m and s can be calibrated for, minimizing hadronic model biases (similar to references [44, 65, 81]). It is therefore not further addressed during model development in this work.

Similarly to the WCD, the time models for the MD become more sensitive to X^{μ}_{max} with increasing trace information -depicted by the narrowing band for larger quantiles in figure 5.10. The time model for the 1-bit counting strategy predicts its early trace stage better than the integrator. Also, it is more sensitive to X^{μ}_{max} fluctuations, depicted by the larger grey band in figures 5.10a, 5.10c, and 5.10e. This feature is a product of the quasi-real approach to the 1-bit counting strategy. Due to the absence of a counting strategy, time bins in the 1-bit do not contain the intended "0"/"1" but rather the average muon number (see section 4.1.2 for more). Timing information is therefore more refined, yielding a better sensitivity to changes in X^{μ}_{max}. The inhibition window[20] in the 1-bit counting strategy is larger than the bin width for the integrator and will thus shift the X^{μ}_{max} sensitivity in favor of the integrator strategy.

[20] Currently, not determined for the SiPM.

For the highest energies at 450 m, the integrator time model introduces less biases in trace shape. Nevertheless, they are both within 25 g cm^{-2} of the MC muon production depth. It is also found that the MD time model is best used for traces with at least 30 % of the trace information (10 % for energies below $10^{18.5}$ eV). Following the same argumentation as for the WCD, an upper limit at the 70$^{\text{th}}$-percentile is set for MD time reconstructions (in chapter 6). The increased trace information becomes especially relevant for the 1-bit counting strategy when MD detectors have a low muon count.

Time biases for the 1-bit counting strategy increases for the highest energies at 1100 m (see figures B.13), favoring the integrator strategy. At larger distances, the X^{μ}_{max} sensitivity improves for either muon counting strategy. This results from the increased trace width, recognized in the figures 5.11. At 450 m, more than 90 % of the trace is within 250 ns. It increases to 550 ns at 1100 m, effectively reducing the relative time error from the bin size. However, at larger distances the trace shape also deteriorates due to fewer arriving particles. This suggests that the quality of a time reconstruction improves with increasing primary energy[21].

Primaries and hadronic models are within the 25 g cm^{-2}-level; with iron primaries from EPOS-LHC deviating most. They do not exhibit the same hadronic model dependencies previously seen in the WCD, suggesting that it is derived from the low energetic muons (below $\approx$ 1 GeV[22]). Corrections, as shown in figures 5.9a and 5.9b, are unnecessary within simulations. Regardless, they become pertinent for data driven X^{μ}_{max} reconstructions. Here, the FD cannot provide a direct measurement of the muon production depth as the longitudinal profile is dominated by electromagnetic particles. A novel calibration will become necessary where the X^{μ}_{max} is alternatively derived through direct detection. In reference [84], the timing information of muons in WCDs is exploited to derive the *apparent* muon production depth. Only detectors far from the core are taken into the analyses (where the electromagnetic particle contribution is negligible). This condition is not necessary with the MD and can thus be used as a novel X^{μ}_{max} calibration method. Note, the *apparent* X^{μ}_{max} differs with respect to the *true* X^{μ}_{max}. Neither the calibration method nor difference between the apparent and true X^{μ}_{max} were studied in this work. However, they are strongly recommended for data driven results (more to it in chapter 6).

In figures 5.11 and 5.12 average shower traces are overlaid with those predicted from the time model in this work (time corrections have been accounted for). They visualize the good agreement between simulations and prediction. Time bins for the WCD are 2 ns, whereas the 1-bit and integrator strategy in the MD are 3.125 ns and 6.25 ns here. The solid line represents the MC simulated detector response with the dashed line indicating the model prediction from this work. For illustrative purposes, the upper limit of the time axis in figure 5.11 is set at t^{ADC}_{95} of the integrator trace. Similarly, the upper limit of the time axis for the WCD in figure 5.12 is set at t^{all}_{95} for the total trace. Sample showers were selected at $\theta = 32°$. Traces at $\psi = 90°$ are selected at energies of 10^{17} eV, $10^{18.5}$ eV and 10^{20} eV and radial distances of 450 m and 1100 m (equivalent configurations as in figures 5.8, 5.10, and B.13). All traces are normalized with respect to the total trace of all particle components in the detector. The relative contribution of all particle components has already been derived for the signal model in section 4.2.5 and will is used for the time model.

[21] Disregarding the increased number of detectors.
[22] Soil shielding.

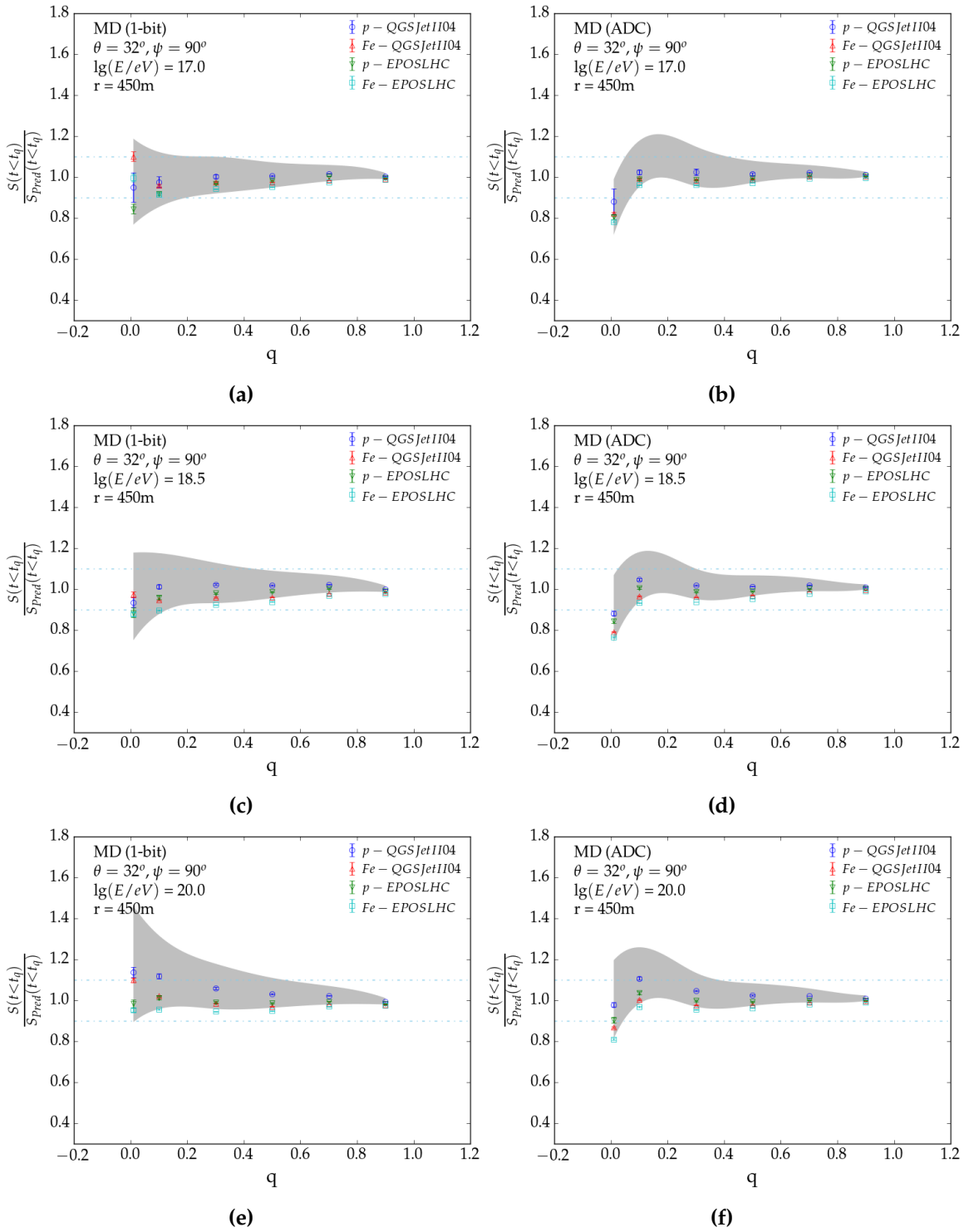

Figure 5.10: Ratio between the MC simulated and model predicted cumulative distribution of the signal trace. Signals at quantile q are those integrated up to t_q. They are depicted for the **left)** 1-bit and **right)** integrator counting strategy in the MD at 450 m. The grey band represents the change in *cdf* (or trace shape) due to an $X^{\mu}_{\max}$ difference of up to ±25 g cm^{-2}. Comparisons for different hadronic models and primaries are shown. Error bars are the variances of 120 showers for the configuration depicted in the figure.

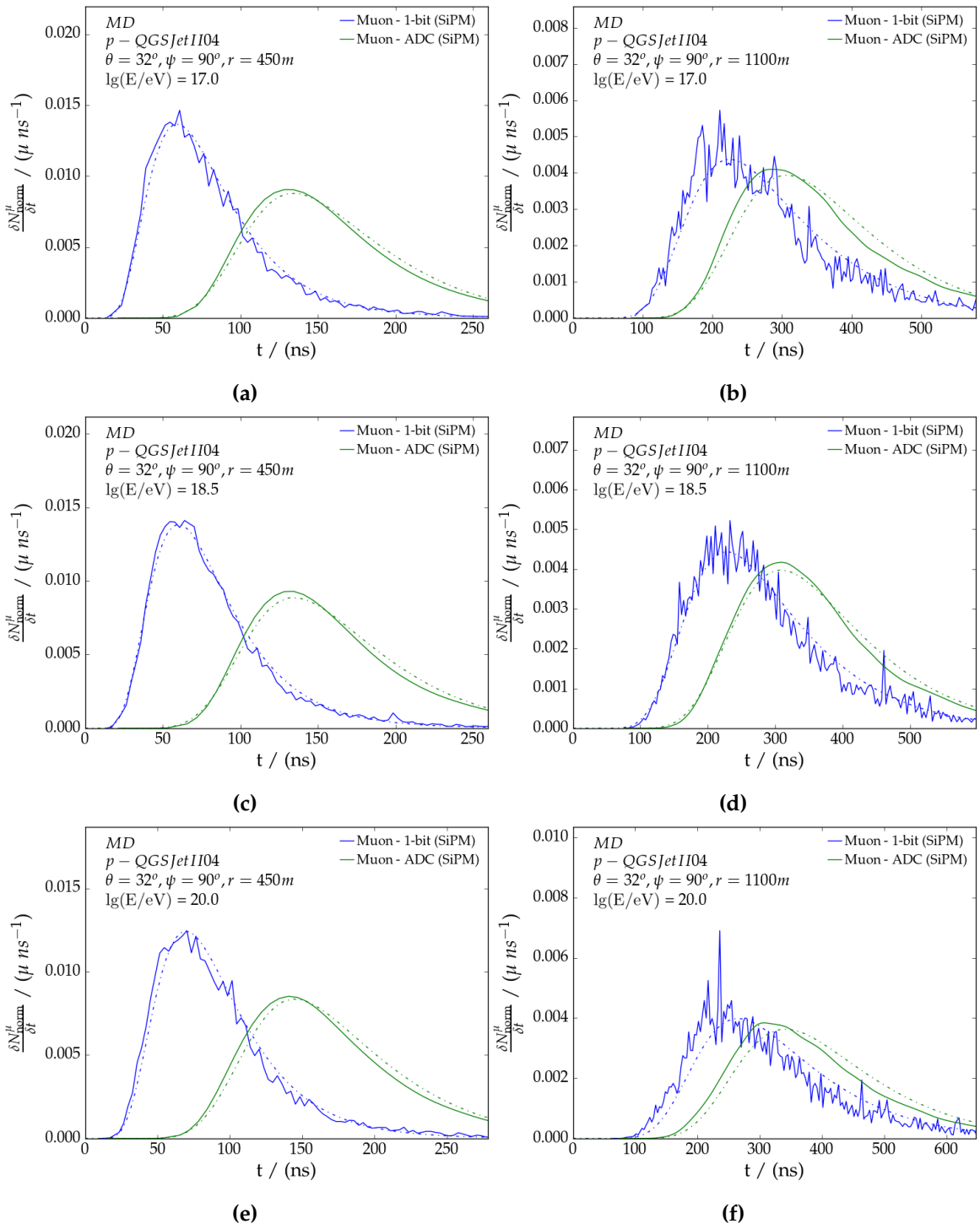

Figure 5.11: Average time dependent signal trace in a MD for the 1-bit and integrator counting strategy at **left)** 450 m and **right)** 1100 m. Time model predictions (dashed) overlay the MC simulated traces (solid). Select showers are shown for energies of **a-b)** 10^{17} eV, **c-d)** $10^{18.5}$ eV and **e-f)** 10^{20} eV.

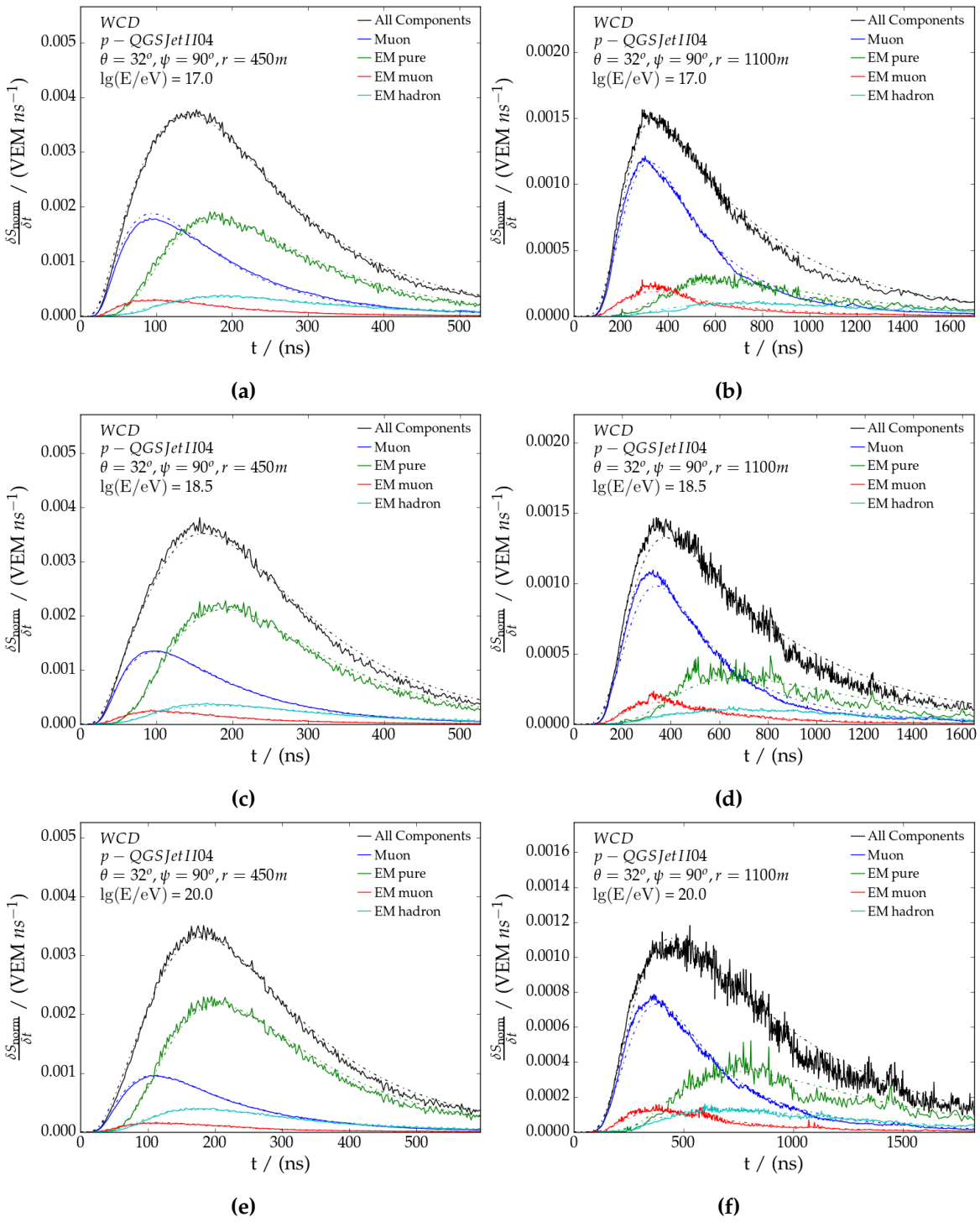

Figure 5.12: Average time dependent signal trace in a WCD at **left)** 450 m and **right)** 1100 m. Average traces are obtained from through all particles in the sampling area. Time model predictions (dashed) overlay the MC simulated traces (solid) for all individual particle components and the total signal. Select showers are shown for energies of **a-b)** 10^{17} eV, **c-d)** $10^{18.5}$ eV and **e-f)** 10^{20} eV.

CHAPTER 6

Universality Reconstruction

The universality reconstruction is an analysis tool developed to exploit detector information more deeply. It is based on the signal and time model discussed in section 4 and 5 respectively. In comparison to the standard reconstruction (briefly discussed in section 2.1 and more extensively in reference [44, 81]), detector information is exploited more deeply, providing better insight into the mass of the primary particle. The standard reconstruction algorithm for WCD and MD, implemented in $\overline{\text{Off}}\underline{\text{line}}$, is based on an NKG-type lateral distribution function to describe its lateral shape. A spherical shower front is used to describe its arrival time at the individual detectors. Shower parameters are the slope and normalization of the lateral distribution and the curvature of shower front. However, for the WCD, they are intrinsically poor parameters to infer the mass and properties of hadronic interactions at the highest energies. They also depend on the detector design. With the MD, the muon density at 450 m is a good estimator for mass composition discrimination.

The parameters used in the universality models developed in previous chapters are directly linked to the nature of the primary particle and properties of high energy hadronic interactions. These are the electromagnetic shower maximum X_{max}, maximum muon production depth X^{μ}_{max} and muon content R_{μ}. The former two are shower parameters, whereas R_{μ} is a global mass composition sensitive parameter. It is equivalent for all possible detector types (previously seen in figure 4.23). The universality reconstruction is therefore physically more fundamental and easily extendable with additional detector types (such as the SSD).

In this chapter, we describe a new reconstruction algorithm to accommodate the extended energy range in the WCD and for the addition of the MD. It has been tuned for detectors in the infilled array (750 m grid spacing). The reconstructions for the WCD and MD are first discussed independently, followed by the introduction of a novel hybrid reconstruction procedure. This provides the opportunity to study its strengths and limitations for mass composition analyses. The hybrid reconstruction is comprised of 10 parameters: *core position* $\vec{x}$, arrival direction (θ, ψ), energy E, electromagnetic shower maximum X_{max}, maximum muon production depth X^{μ}_{max}, relative core time t_{core} and muon content R_{μ}. For individual detector type reconstructions, it reduces to 9 parameters as WCD and MD are only sensitive to X_{max} and X^{μ}_{max} respectively. R_{μ} is relative to the average muonic signal of a proton-induced air shower simulated with QGSJETII-04 at the reference energy of 10^{18} eV. Depending on the detector type and reconstruction method, parameters may be fixed or freed during the

minimization of the likelihood.

Tools from the universality framework were previously used to generate the average signal response (i.e. a *pdf*) in each detector in a dense ring (for further elaboration see section 4.1). These tools are also used to simulate realistic detector responses, thus accounting for the Poisson nature of particle fluctuations seen in air showers measurements. This is achieved by sampling N particles[1] from the average signal response. The core position is randomly distributed in an infilled-like array, after which all detector signals are simulated through the aforementioned procedure. We use the same CORSIKA air shower library as during the development of the signal and time model. Also, we omit using $\overline{\text{Off}}\underline{\text{line}}$. This allows for a self-consistent and more accurate analysis on the reconstruction performance and its systematics.

The reconstruction is composed of two aspects: a simultaneous fit of the lateral distribution of the total measured signals and the time traces. Its total log-likelihood can be formulated as

$$\mathcal{L} = \sum_{\text{idet}}^{\text{WCD,MD}} \sum_{\text{stations}} \mathcal{L}_{\text{signal}}^{\text{idet,station}} + \mathcal{L}_{\text{time}}^{\text{idet,station}}, \tag{6.1}$$

where *idet* and *station* refer to all detector types and stations in the array respectively. Additional terms can be included to constrain the reconstruction. As equation (6.1) demonstrates, this can be easily expanded with the addition of e.g. the SSD. Individual likelihood contributions are explained in the following sections.

6.1 Fit of detector signal

All stations are included into the signal component of the likelihood, provided the shower stage ΔX is positive[2]. As part of the AugerPrime upgrade, the WCD will be equipped with a small PMT, increasing the dynamic range from 650 VEM to 20,000 VEM [85]. This corresponds to a saturation limit of about 600 VEM per 25 ns time bin [86]. Stations up to a radial distance of 250 m can therefore be used in the reconstruction procedure for showers at 10^{19} eV.

In reference [87] a signal recovery method was introduced by estimating the signal in the saturated time bins with a Moyal distribution from the remaining unsaturated time bins. The strategy allows for saturated stations to be recovered above 60 m. Due to time constraints, this strategy could not be included as part of this work. However, it is recommended to improve the reconstruction quality of the lateral distribution function. In this work, a conservative saturation limit is set at 500 VEM per time bin to qualitatively balance between the current detector electronics, its upgrade and possible signal recovery.

MDs are triggered by the WCD and are thus simultaneously included into the likelihood. The 1-Bit and integrator counting strategy provide two separate muon counts. Using the 1-Bit muon count strategy, a maximum of 192 muons can be identified (discussed in section 2.3.2). However, it quickly saturates due to a pile-up of muons in the scintillator

[1] N is derived by counting all particles in a sampling area and then scale it with respect to the detection area of WCD/MD (see section 4.1).

[2] ΔX is *positive* if the shower maximum is smaller with the respect to the integrated atmospheric overburden along the shower axis to the detector. Simplified, ΔX is *negative* for most detectors if the shower maximum is underground.

bars, therefore underestimating the muon count [88]. As a result, a generalized muon pile-up correction was introduced in reference [89]. Principally, the correction describes the probability distribution of a given number of muons hitting a segmented detector with a multinomial distribution. This changes the formalism of the likelihood compared to the WCD. In this work, MD signals could only be simulated with infinite segmentation. We therefore introduce (for a first order analysis) an artificial saturation limit at 90 muons per inhibition window (taken from [89]). The inhibition window is set at 25 ns or 8×3.125 ns bins.

The integrator strategy depends on the total charge measured (similar to the WCD). Its saturation limit is at roughly 800 muons. The muon signal response is typically 100 ns long, corresponding to an average saturation limit level of about 50 muons per 6.25 ns bin. The integrator saturation limit is higher for the integrator than it is for the 1-Bit counting strategy. This introduces three scenarios: (i) the 1-Bit counter and integrator are unsaturated, (ii) only the 1-Bit counter is saturated and (iii) the 1-Bit counter and integrator are saturated. As *one* detector can only give a unique muon count, their muon count is averaged for scenario (i). In scenario (ii), only the integrator signal is used. Finally, in scenario (iii), whichever saturated signal is highest will be used as a lower limit in the likelihood. This is a first order ("ad hoc") approach, as it does not properly account for overlapping regions and background noise. A more appropriate strategy would be a novel likelihood which accounts for the statistical properties of the two measurement techniques by introducing an estimator based on the arriving photon number (detailed in reference [90]). This strategy has not been developed for the MD and therefore could not be implemented during the scope of this work but is recommended to improve the overall likelihood function. In subsequent analysis, we use the simplified approach for scenarios (i), (ii) and (iii).

Only stations below 60 m are rejected from the reconstruction as it is outside the phase-space of the universality model. Signals until a radial distance of 1500 m from the shower core have been validated during model development. Including stations beyond the design limit could therefore introduce biases. Preliminary reconstructions did not show any inconsistencies. The model is therefore classified as *accurate* up to 1500 m and *stable* up to 2000 m. Stations with signals above the stable limit are rejected. This primarily affects extensive air showers of the highest energies of which the infilled array is expected only to see 10 events per year [50].

Accounting for all the aforementioned model and detector conditions, the signal contribution to the likelihood can be summarized (irrespective of detector type) as

$$\begin{aligned}\mathcal{L}^{idet}_{signal} &= f_S(R_\mu, E, \Delta X, \theta, r, \psi) \\ &= \sum_{\text{stations}}^{\text{sat.}} \ln(F_{\text{sat.}}(n_{st.}, \mu_{st.})) + \sum_{\text{stations}}^{\text{signal}} \ln(F_{\text{signal}}(n_{st.}, \mu_{st.})) + \sum_{\text{stations}}^{\text{silent}} \ln(F_{\text{silent}}(n_{st.}, \mu_{st.})),\end{aligned} \tag{6.2}$$

where n_{st} and μ_{st} are the measured and model prediction of the detector (*idet*) signal. *Saturated* signals, $F_{\text{sat.}}$, are included as lower limits to the likelihood. *Non-saturated* signals, F_{signal}, follow Poisson statistics through $F_{\text{signal}} = \mu_{st.}^{n_{st.}} exp(-\mu_{st.})/(n_{st.}!)$. For signals above 30 VEM (or 30 μ for the MD) the Poisson distribution is nearly identical to a Guassian distribution and thus replaced to accelerate numerical calculations. Single stations need roughly 3 VEM to be triggered. *Silent* stations, F_{silent}, are thus included by summing up Poissonian probabilities below the threshold.

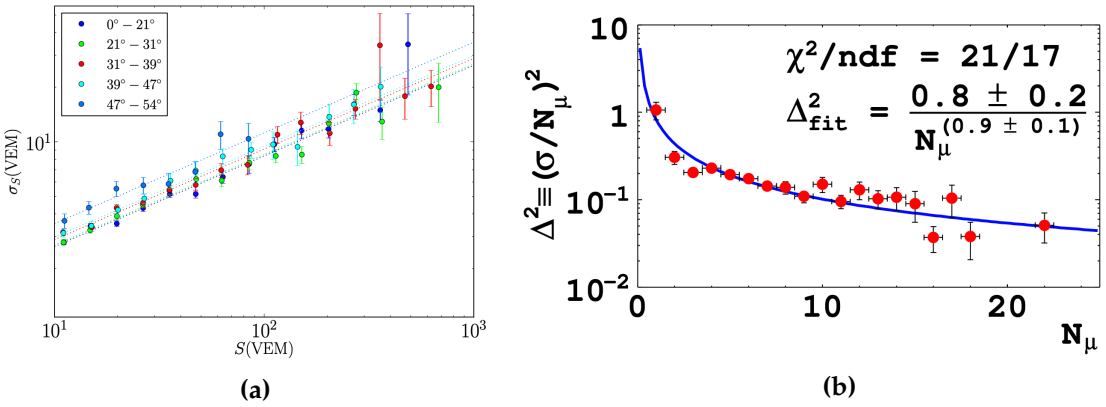

(a) **(b)**

Figure 6.1: a) Signal and **b)** muon uncertainty model for the WCD (from reference [93]) and MD (from reference [94]) respectively.

Sampling of the particle content with the WCD undergo statistical fluctuations. This affects the reconstruction of the physical parameters. Incorrectly estimating these fluctuations introduces systematic errors of these shower parameters. These fluctuations decrease with increasing energy and scale with $1/\sqrt{S}$, reflecting the underlying Poissonian nature of counting particles. Additional contributing fluctuations include detector stability, quality of calibration and possible unknown factors [91]. An end-to-end uncertainty is estimated from signal variations of stations situated at roughly the same location of the shower [92]. The stations are referred to as multiplets and are placed at various positions in the infilled array (750 m grid spacing). A zenith dependent signal variance structure is found due to the increased muons fraction with respect to the total signal (muons fluctuate more than electromagnetic particles do). This is illustrated in figure 6.1a.

The signal uncertainty is described as

$$\sigma_{\mathrm{WCD}}(S, \theta) = \sqrt{S} \cdot [0.865(1 + 0.593(\sec(\theta) - 1.22))], \tag{6.3}$$

where θ is the zenith of the shower axis. We include this in any subsequent WCD-related reconstruction. With a Poisson factor signals are converted into effective particle numbers.

A similar study was performed in the engineering array (Unitary Cell) of AMIGA. At one of the stations, twin MD detectors are positioned with the same 2×5 m^2 and 2×10 m^2 layout (i.e. 2×30 m^2). The twin detectors are equipped with PMTs (not SiPMs) and spaced approximately 20 m apart. As a result, muon measurements obtained closer to 200 m from the shower core are removed to guarantee that both detectors sample from the same muon density. Furthermore, events with at least 3 muons are used for the analysis [94]. As figure 6.1b reveals, muon fluctuations are within 1σ from a pure Poisson distribution. An equivalent analysis with the SiPMs is still pending. Considering the near exact Poisson structure, it is anticipated to differ little from the results seen in [94]. We therefore characterize the muon uncertainty as

$$\sigma_{\mathrm{MD}}(N_\mu) = \sqrt{N_\mu}. \tag{6.4}$$

We include this in any following MD-related reconstruction.

6.2 Fit of time distribution

WCD traces are only included into $\mathcal{L}_{\text{time}}$ if 5 or more bins (each 25 ns) are above 0.7 VEM/bin. This is a qualitative compromise between resolution and reconstruction accuracy[3]. For the MD, the same limit is used for the integrator strategy, whereas it is set at 1 μ/(inhibition window) for the 1-Bit counting strategy (each 25 ns). In addition, the WCD and MD detectors are expected to have a minimum signal size of 10 VEM/μ to be included into the shape fit. The per-bin constraint effectively rejects stations very close to the core, those which could be fully contained in e.g 100 ns. This is relevant for the WCD and 1-Bit counter in the MD, where 100 ns equates to 4 bins. The constraint also rejects stations far from the core, where the signal size is low. The second constraint (10 VEM/μ) is a more explicit limit to improve the shape of the time structure seen. This is a useful constraint for the 1-Bit counting strategy in the MD, where 5 muons may be measured in 5 independent bins without a clear shape.

The time likelihood compares the signal in bin i to the universality prediction (integrating from the start time of the bin to its end), obtained from the combination of the time and signal response for the four particle components. The time model is based on a normalized distribution and is thus scaled with respect to the total signal in the detector. We define the bin time t_i at the center of the bin. Each bin signal is included equally as in the signal likelihood. In other words, the time likelihood can be summarized as

$$\begin{aligned}\mathcal{L}_{time}^{idet} &= f_T(E, X_{\max}^{(\mu)}, \theta, r, \psi) \\ &= \sum_{\text{stations}} \Big(\sum_{\text{i}}^{\text{sat.}} \ln(F_{\text{sat.}}(n_i, \mu_i)) + \sum_{\text{i}}^{\text{signal}} \ln(F_{\text{signal}}(n_i, \mu_i)) + \sum_{\text{i}}^{\text{silent}} \ln(F_{\text{silent}}(n_i, \mu_i)) \Big),\end{aligned} \tag{6.5}$$

where $X_{\max}^{(\mu)}$ refers to the electromagnetic shower maximum ($X_{\max}$) used in the WCD or maximum muon production depth ($X_{\max}^{\mu}$) used in the MD[4]. Saturated bins are not entirely removed form the reconstruction but provide a lower limit.

The likelihood in equation (6.5) implies that stations used for the time likelihood are counted twice in the total likelihood. This reduces the contribution of far-lying stations to the total likelihood, introducing a bias to the energy and muon content R_μ. We correct this by subtracting the likelihood contribution of the signal size from $\mathcal{L}_{time}^{idet}$. This can be formulated as

$$\mathcal{L}'_{time} = \mathcal{L}_{time} - \mathcal{L}_{signal}^{used}, \tag{6.6}$$

where $\mathcal{L}_{signal}^{used}$ refers to the likelihood contribution of the signal size for stations *used* in the time reconstruction. It is computed with equation (6.2).

The time correction introduced in section 5.3 allows us to use the trace information up to its 90^{th} percentile. However, MC results for the late part are unreliable. Particles arriving late can have large thinning weights, introducing a biased accumulated delay. Furthermore, the rise of the trace is most sensitive to $X_{\max}$, whereas the tail is dominated by the diffusion of electromagnetic particles. These particles do not arrive in the MD. The MD is only sensitive to the muonic time structure, which diffuses less than electromagnetic particles. This provides the opportunity to use the trace shape, linked to the shower development, for studies on the

[3] The reconstruction of the trace depends on the quality of the *shape* of the trace.

[4] same notation as in chapter 4 and 5

first interaction and cross section σ_{p-air} (following a similar strategy as in reference [82]). As a compromise between these effects, we use trace information up to its 70^{th} percentile for reconstructions with the WCD and MD. This can be altered in future analyses to e.g. 50% in the WCD and 70% in the MD to emphasize the reconstruction quality of the shower maximum or the cross section of the primary particle.

Signals in the WCD reflect multiple times prior to arriving to the photo-multipliers. After the initial peak, the muon signal decays exponentially with a decay time of 50 ns to 70 ns [95]. Assuming a particle injection from a Poisson distribution, the bin-to-bin signal variance is derived from the convolution of a Poisson and exponential distribution. This also depends on the relative contribution between the muonic and electromagnetic signal component (due to their respective track length and energy deposit). No data driven analysis was performed to study this. As a result, in this work, we use the signal variance model (equation (6.3)) for each bin. This overestimates the signal variance in the bin, limiting the contribution of low signal stations in the likelihood. In other words, the time likelihood will bias towards stations close to the core.

The integrator signal of a muon in the MD has a decay length of about 40 ns. A per bin variance model is also missing but could be obtained through a similar analysis as in reference [94]. The muon tail is less significant for the 1-Bit counting strategy as the muon signals are below[5] the signal threshold after passing through the first 8 bins (equivalent to a 25 ns inhibition window). Consequently, the variance model derived for the total signal (equation 6.4) is a good first approach. It is also used for the integrator signal and thus introduces the same bias towards close stations as the WCD.

These signal variance models for the time bins (or inhibition windows) should be used with caution. Not only are detector effects on the time structure not accounted for but also the temporal delay due to particle fluctuations. Studies in reference [96] show that for the muonic component in the WCD the time dependent signal variance is approximately characterized as

$$\sigma_\mu(t) \cong \sqrt{\frac{\Delta t}{2\tau_{tank}}}\sqrt{\frac{S_\mu(t)}{\mathrm{VEM}}}\mathrm{VEM}, \tag{6.7}$$

whereas it is

$$\sigma_{\mathrm{EM}}(t) \cong \sqrt{\frac{\Delta t}{2\tau_{tank}}}\sqrt{\frac{< E^2(r,t) >}{E_c < E(r,t) >}}\sqrt{\frac{S_{\mathrm{EM}}(t)}{\mathrm{VEM}}}\mathrm{VEM} \tag{6.8}$$

for the combined electromagnetic signal component. Δt refers to the bin width in the detector, τ_{tank} the decay time in the tank at ≈ 60 ns, $< E(r,t) >$ the mean time dependent particle energy with respect to the shower and $S_i(t)$ the time dependent signal in continuous form. The analysis considered only vertical showers. Equations (6.7) and (6.8) already indicate that the signal variances are overestimated, sensitive to the geometry and particle energy spectrum. A similar study for the MD was not found but is expected to have a similar structure as seen in equation (6.7).

[5] This depends on the distance between the impact point of the muon on the scintillator strip.

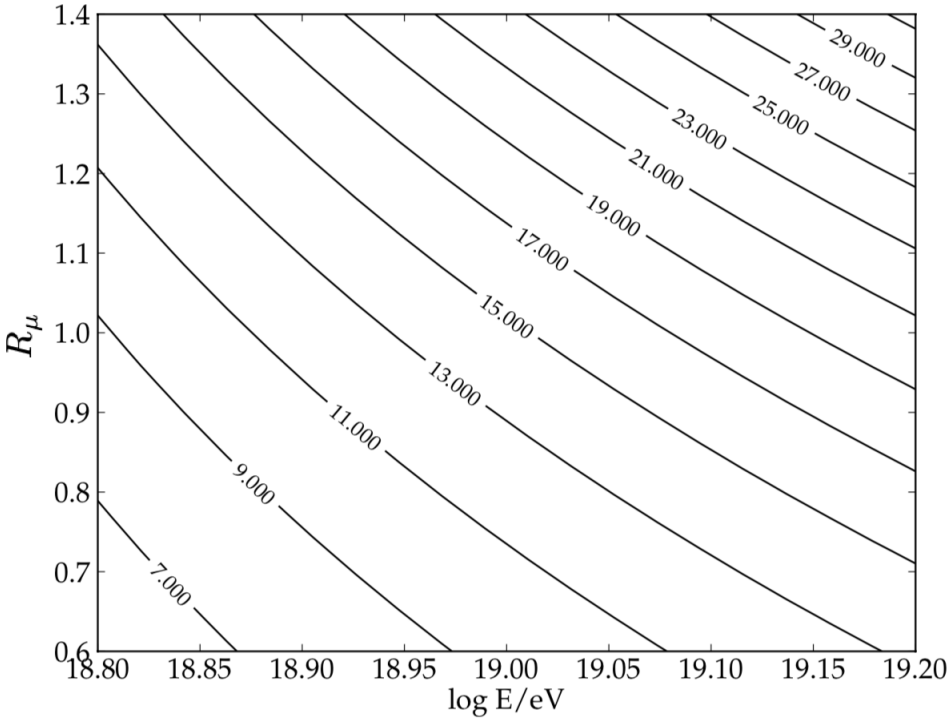

Figure 6.2: R_μ and E are correlated because the WCD does not measure the muonic and electromagnetic components separately [65]. The contour lines refer to the R_μ-E combination where the muon signal is the same.

The results obtained in reference [96] are incomplete for universality reconstructions[6]. Nevertheless, this demonstrates the need for a dedicated study on the signal variance for trace bins in the WCD and MD, providing a better estimate of the shower parameters; especially for X_{max} and X^{μ}_{max}.

6.3 Correlation between Shower Parameters

Studies for the WCD in references [44, 59, 65, 80, 81] have shown strong correlations between the shower parameters E, X_{max}, X^{μ}_{max} and R_μ[7]. This ambiguity is anticipated as WCDs cannot separate between the muonic and electromagnetic particle component. This is in part illustrated in figure 6.2. It shows that for a given subset of energies and R_μ (contour line) the muon signal at 1000 m remains unchanged. For example, the total muon signal in the WCD can be obtained by lowering the total energy and simultaneously increase the muon fraction. X_{max}, which can only be obtained by using the time model, reduces this ambiguity as it is directly linked to the electromagnetic contribution of the shower. The degeneracy is further reduced by stations positioned far from the shower core because the electromagnetic to muonic signal decreases.

Assuming a standalone reconstruction with the MD, the ambiguity is significantly less. However, the degeneracy arises from an incorrect estimate of X^{μ}_{max} for reconstructions using

[6] The four particle component and zenith angle need to be included into the analysis. Additionally, the analysis should be performed for MD purposes.

[7] , effectively resulting in an *initial value problem*

only the signal size. An increased maximum muon production depth with a low energy (indicative of a proton) yields a similar muon content as a small maximum muon production depth with a higher energy (indicative of an iron). With the addition of time information, the ambiguity is constrained[8].

The ambiguities can be minimized two-fold: (i) introduce a $R_\mu(E, X^{(\mu)}_{\max}, \theta)$ and $X^{(\mu)}_{\max}(E)$ estimator or (ii) combine the detector information of the WCD and MD (i.e. a hybrid reconstruction). Note, the estimators suggested in (i) are derived from simulated air showers for this work. However, they are also required to be derived through data-driven analyses. The $X^{(\mu)}_{\max}(E)$ estimator is characterized by

$$\langle X^{(\mu)}_{\max}(E)\rangle|_{primary,model} = \alpha_1 + (\lg(E/\mathrm{eV}) - 18.) \cdot \alpha_2, \tag{6.9}$$

where α_1 and α_2 are obtained from simulations for each primary and hadronic model. This poses a problem, as the primary particle is an unknown variable (we aim to find the composition of the primary particle). Information from the time distribution resolves this. However, the strict conditions imposed on stations for the reconstructions with time information (discussed in section 6.2) reduce the total number of events, especially those at low energies. Using information from the FD on the maximum shower depth and energy, an estimate on the proton fraction is derived. Equation (6.9) is then used to characterize $X^{(\mu)}_{\max}(E)$ as

$$\langle X_{\max}(E)\rangle|_{model} = f_p \cdot \langle X_{\max}(E)\rangle_p + (1 - f_p) \cdot \langle X_{\max}(E)\rangle_{Fe}, \tag{6.10}$$

where f_p denotes the proton fraction for a sample mixture composed solely of protons and iron particles[9]. Early work in [44] showed a successful application of this analysis for data.

The same procedure is also applied to derive a $X^{\mu}_{\max}(E)$ for the MD. The FD does not provide information on the maximum muon production depth[10]. To resolve this handicap, data from the *apparent* maximum muon production depth can be potentially used. Studies in reference [97] show that the production point of a muon along the shower axis can be obtained from its geometry and its arrival time with respect to the shower plane. The results in [97] are currently incompatible to obtain $X^{\mu}_{\max}(E)$ (and thus Universality reconstructions) because the former discusses the *apparent* maximum muon production depth, whereas this work assumes the *true* maximum muon production depth. The work in reference [97] was performed with WCD detectors located more than 2000 m from the shower core to minimize the signal fraction from the electromagnetic particles. Low energy muons can decay before they arrive, introducing an offset between the true and apparent $X^{\mu}_{\max}$. Repeating the studies in [97] for the MD will greatly benefit the search for a data-driven $X^{\mu}_{\max}(E)$ estimator. With MDs, detectors closer to the core can be used. This reduces the fraction of decayed muons with respect to muons arriving to the detector, which in turn reduces the offset between the true and apparent maximum muon production depth. Currently, deriving the maximum muon production depth through other means than with the time model in Universality (chapter 5) are still in development. We therefore use the characterization obtained from simulations in subsequent analysis. The proton fraction f_p in equation (6.10) remains unchanged.

[8] This feature has not been thoroughly analyzed during the course of this work.

[9] We understand this is an incomplete picture. Nevertheless, it provides a useful first-order analysis.

[10] Note, the fluorescence light produced in the longitudinal profile is dominated (more than 90%) by the electromagnetic particles.

The characterization for the R_μ estimator combines information from the FD and surface detectors. In data, events measured by both detector types are referred to as the *golden hybrid* events. Assuming only a WCD-FD scenario, R_μ is derived from universality reconstructions, whereas the energy and maximum shower depth are obtained from FD reconstruction. The latter shower parameters are fixed during the universality reconstruction. Its functional form (derived in reference [59]) is

$$R_\mu(\theta, E, X_{\max}) = R_\mu(\theta, E)\frac{1 + 0.5 \cdot \text{atan}(\frac{X_{\max} - <X_{\max}>}{40\text{g cm}^{-2}})/\pi}{1 + 0.5 \cdot \text{atan}(\frac{X_{\max}(E) - <X_{\max}>}{40\text{g cm}^{-2}})/\pi}, \tag{6.11}$$

where $< X_{\max} >$ is the average shower depth of a 50%-50% proton-iron composition and $\langle X_{\max}(E)\rangle$ the energy dependent estimator described in equation (6.10). $R_\mu(\theta, E)$ is the mean muon content, characterized as

$$R_\mu(\theta, E)|_{primary,model} = \alpha_1 + \alpha_2 \cdot (1/\cos\theta - 2.) + \alpha_3 \cdot (\lg(E/\text{eV}) - 18.), \tag{6.12}$$

where α_i is obtained from simulations for each primary and hadronic model.

Note that the R_μ estimator in equation (6.11) is only valid for universality reconstructions with WCD. It cannot be applied to the MD as the FD cannot measure $< X^\mu_{\max} >$. However, figures 4.22 in chapter 4 proved that R_μ is a detector independent variable. In other words, the R_μ estimator derived from WCD and FD can be applied for the MD. Alternatively, the maximum muon production depth obtained through methods such as in reference [97] can be used to fix the MD universality reconstruction. This procedure is subject to more systematics compared to data from the FD. As a result, we also apply the procedure in equation (6.11) for the MD. They are tuned for simulated events.

The estimators in (6.10) and (6.11) minimize the biases in $X^{(\mu)}_{\max}$ and R_μ. However, as a consequence, their variance increases. Results of the hybrid reconstruction will reveal this feature in subsequent sections.

In previous paragraphs, we have evaluated the estimators for the WCD and MD independently. Shared shower parameters in the hybrid reconstructions are the energy, muon scale and geometry. The estimators for $X^{(\mu)}_{\max}$ are equivalent to those for the WCD/MD reconstruction[11]. The shared muon content R_μ is defined as

$$R_\mu = \frac{R^{\text{WCD}}_\mu + R^{\text{MD}}_\mu}{2}, \tag{6.13}$$

where R^{WCD}_μ and R^{MD}_μ are the muon content estimators of the WCD and MD respectively. Equivalently, the *hybrid* R_μ estimator is computed as in equation (6.13). On average, using R^{WCD}_μ would be sufficient (as they are unitary). However, through equation (6.13) a better estimate on the muon content is obtained as particle fluctuations are minimized. With additional analysis a better description could be derived, e.g. a weighted R_μ, to account for the particle fluctuations seen at the detectors.

[11] with the exceptions the additional condition that $X^\mu_{\max} < X_{\max}$

6.4 Reconstruction Strategies

Preferably a global reconstruction, where all parameters are free, should reveal the shower parameters. Due to the ambiguities and correlation between shower parameters (discussed previously in section 6.3), an iterative reconstruction method was developed to improve the resolution of the parameters. Studies in reference [81] show it is a suitable strategy for WCD-only reconstructions, tuned for energies above $10^{18.5}$ eV. More extensive analysis in reference [44] improved the strategy and understanding of the reconstruction performance. Due to the extension of universality for low energy events in the WCD, addition of MD and introduction of a hybrid reconstruction, a new iterative reconstruction method is developed. It has been tuned to be used for events in the infilled array. Starting values for the reconstruction are taken from MC.

The subsequent universality reconstruction steps of the iterative procedure for a WCD-only or MD-only reconstruction are as follows:

1. Core position and energy are freed while $X^{\mu}_{\max}$, $X_{\max}$ and R_{μ} are set to their estimators. All other shower parameters are fixed to the MC true values. The reconstruction is performed without time information (i.e. only $\mathcal{L}_{signal}$) and only uses information from WCD (also for MD reconstructions).

2. Core position is freed wile $X^{\mu}_{\max}$, $X_{\max}$ and R_{μ} are set to their estimators. The energy is fixed to its previous fit result. The remaining shower parameters are fixed to the MC true values. The reconstruction uses only information on the signal size (i.e. only $\mathcal{L}_{signal}$). - This step is redundant when applied to the WCD. It is designed to benefit MD reconstructions.

3. The core position and energy are fixed to their previous fit results. $X^{\mu}_{\max}$ and R_{μ} are set to their respective estimators. $X_{\max}$ and core time t_{core} are free. The combined information of signal size and time distribution is used for the reconstruction.

4. The core position, energy and $X_{\max}$ are fixed to their previous fit results. R_{μ} is set to its respective estimator. $X^{\mu}_{\max}$ and core time t_{core} are free. The combined information of signal size and time distribution are used for the reconstruction.

5. The core position and energy are fixed and R_{μ} is set to its estimator. $X_{\max}$, $X^{\mu}_{\max}$ and core time t_{core} are free (their 'initial values' are those from the previous fit). The signal size and time distribution are used for the reconstruction.

6. All parameters are fixed to their previous fit results with exception of R_{μ}, which is freed. The minimization is applied with signal and time information.

7. All parameters are fixed to their previous fit results with exception of energy E, which is freed. The minimization is applied with signal and time information. All parameters are fixed to their previous fit results with exception of R_{μ}, which is freed. The minimization is applied with signal and time information.

In all reconstruction steps the axis is constrained[12] within 2σ ($\approx 1°$). This has proven to benefit the overall reconstruction [44]. It's full potential has not been studied within the scope of this work. The reconstruction steps for the hybrid setup follows a similar iterative procedure. They differ at step 2. to address the ambiguity seen in R_{μ}. The steps are equivalent with exception of:

[12] to the MC true values or those obtained from the standard Auger reconstruction

2. The core position and R_μ are freed while the energy is fixed to its previous fit result. $X^\mu_{\max}$ and $X_{\max}$ are set to their estimators. All other shower parameters are fixed to the MC true values. The reconstruction is performed without time information.

3.-5. R_μ is now fixed to the previous fit value (as opposed to the estimator).

Note, the iterative procedure developed in this work serves as a prototype and can be further optimized. Subsequent reconstruction results apply this iterative procedure. The minimization is performed with the Minuit package [98] in ROOT [99] and apply the MIGRAD option for the minimization procedure. A reconstruction is considered *successful* if the minimizer converged successfully.

6.5 Reconstruction Example

To visualize the results of the reconstruction, a simulated proton shower with energy $10^{19.5}$ eV at $\theta = 48°$ was chosen. We illustrate the results of a hybrid reconstruction where signal and time information are used. To simplify the complexity of the fit, the lateral distribution of the signal is shown in figure 6.3. The offset seen close to the shower core is due to detector saturation. Note, universality accounts for azimuthal effects introduced by the particle interaction with the atmosphere. As a result, for illustrative purposes, the detector signals are scaled to be projected to an LDF at $\psi = 90\,°$. This is formulated as

$$S(\psi = 90\,°, \vec{p}) = \frac{S(\psi, \vec{p}) \cdot f(\psi = 90\,°, \vec{p})}{f(\psi, \vec{p})}, \tag{6.14}$$

where $\vec{p}$ refers to the other shower parameters, whereas $f(\psi, \vec{p})$ provides the total azimuthal correction from universality (particle spectrum, atmospheric effects, geometry and detector projection). Figure 6.3 illustrates the LDF of the WCD (red line), MD (blue line) and their reconstruction. It also illustrates the expected muon signal in the WCD (green line). Differences between the lateral shape of the MD and predicted muon component in the WCD can be attributed to shielding of low energy muons. In figure 6.4, the LDF for all particle components in the WCD are shown.

Figures 6.5 and 6.6 show sample traces of the selected air shower for the WCD and MD respectively. Detectors at 413 m, 649 m, 1000 m and 1269 m are selected to emphasize features such as saturation or low signal detectors (and their overestimated variances). Each figure provides the integrated signal size of the trace and the reconstructed shower depth (with the MC value in brackets). In figure 6.5, we see the total signal (black line) is in good agreement to the measured detector signal. The coloured lines reflect the expected particle component signal. In figure 6.6, we recognize the 1-Bit and integrator traces and their respective reconstruction. The reconstruction is mostly in good agreement with the trace. However, it is apparent that the inhibition window of the 1-Bit counting strategy reduces the quality of the shape. Figure 6.6a is a good example to indicate the saturation of a trace. Differing muon counts between the integrator and 1-Bit trace are attributed to either detector saturation (as in figure 6.6a) or location at which the muon impinges (as in figure 6.6c).

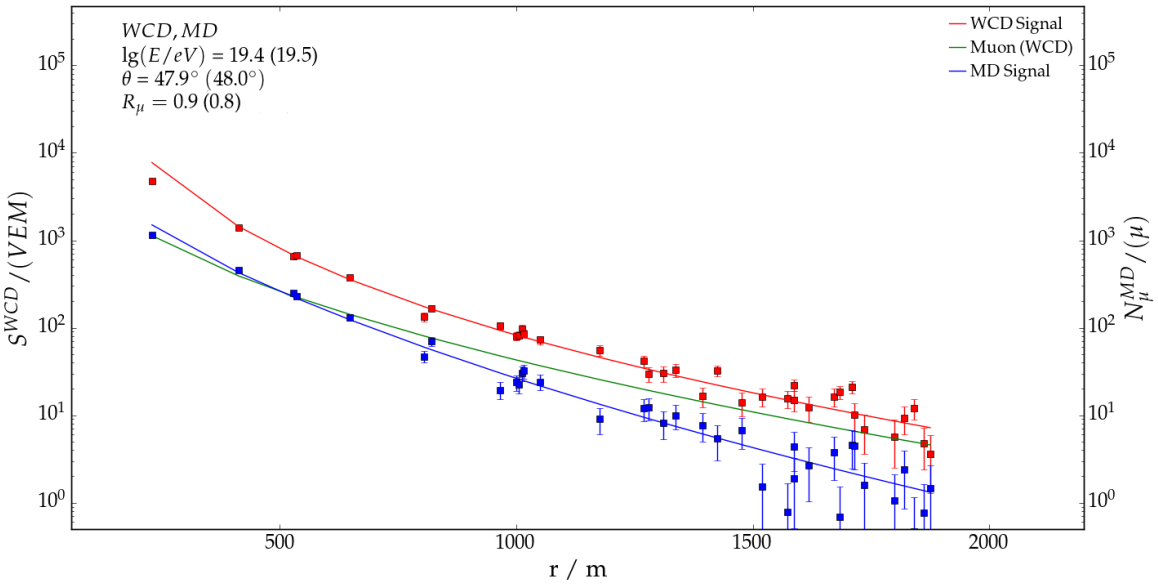

Figure 6.3: LDF of a simulated proton air shower with an energy $10^{19.5}$ eV at $\theta = 48°$. The hybrid reconstruction procedure was applied. The red and blue markers refer to the total signal in the WCD and MD detector respectively. Their line indicate the model prediction of Universality. The green line refers to the predicted muonic signal component in the WCD.

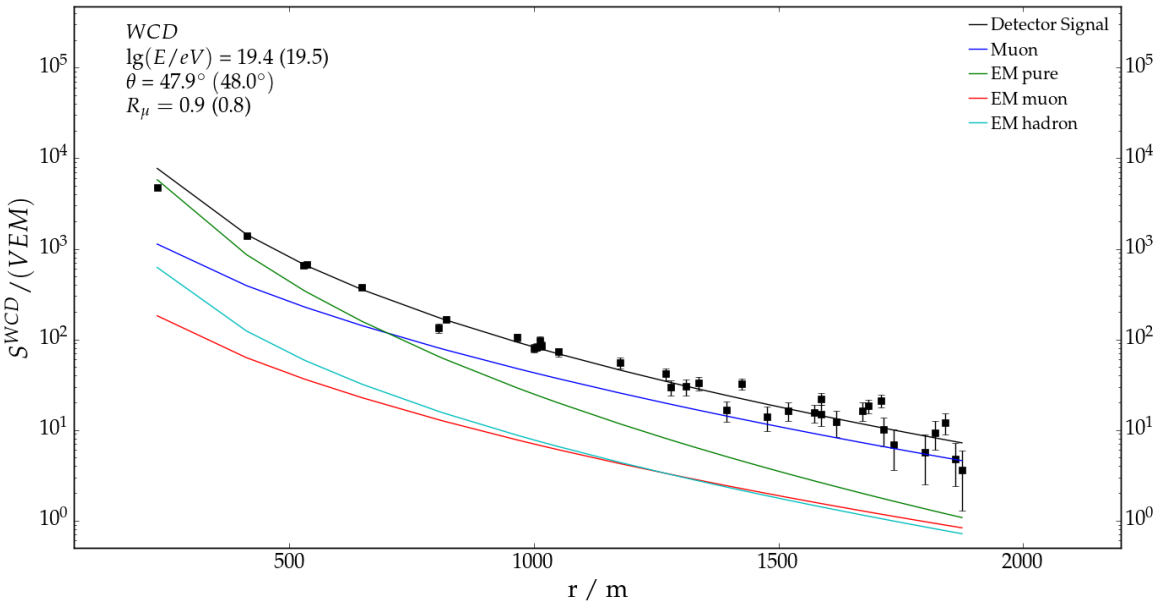

Figure 6.4: LDF of a simulated proton air shower with an energy $10^{19.5}$ eV at $\theta = 48°$. The hybrid reconstruction procedure was applied.

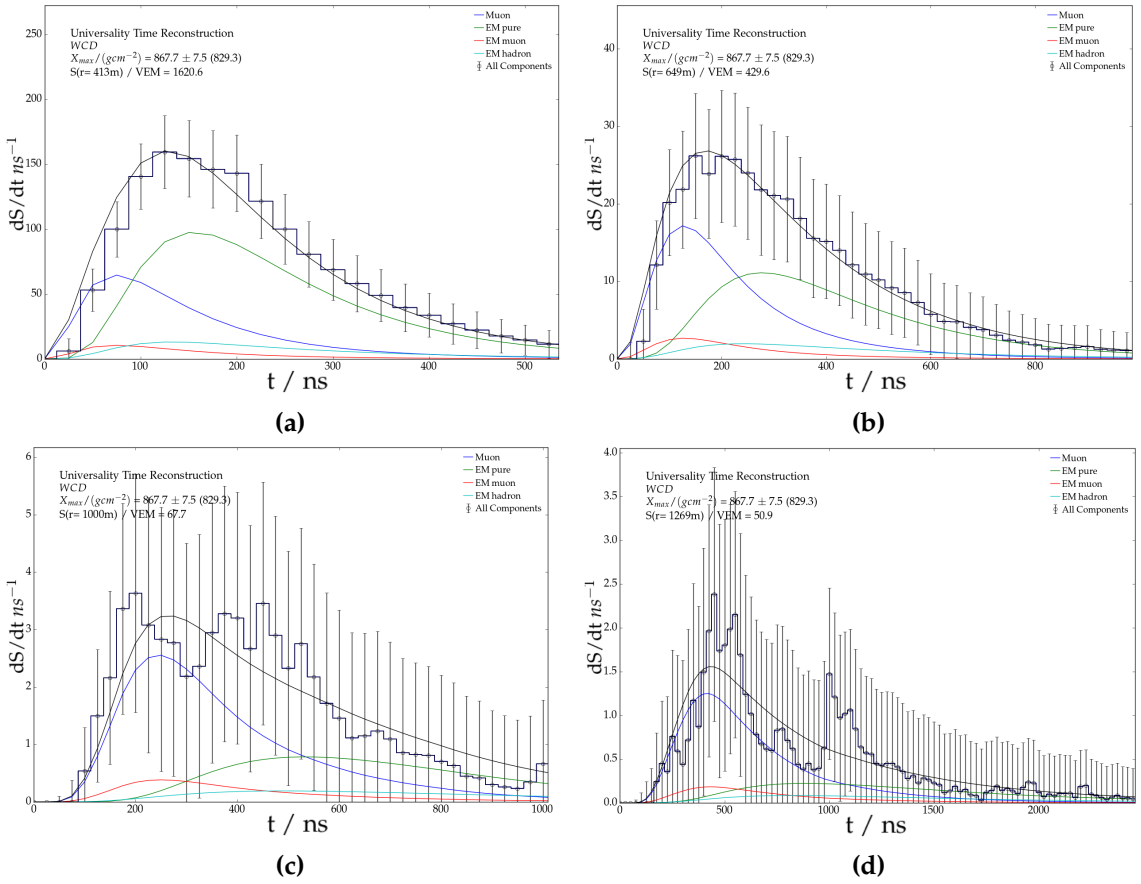

Figure 6.5: WCD sample traces of a proton air shower with an energy $10^{19.5}$ eV at $\theta = 48°$ and different radial distances to the shower core. The colored lines reflect the relative contributions of the particle components. The time axis is chosen to contain 95% of the total trace.

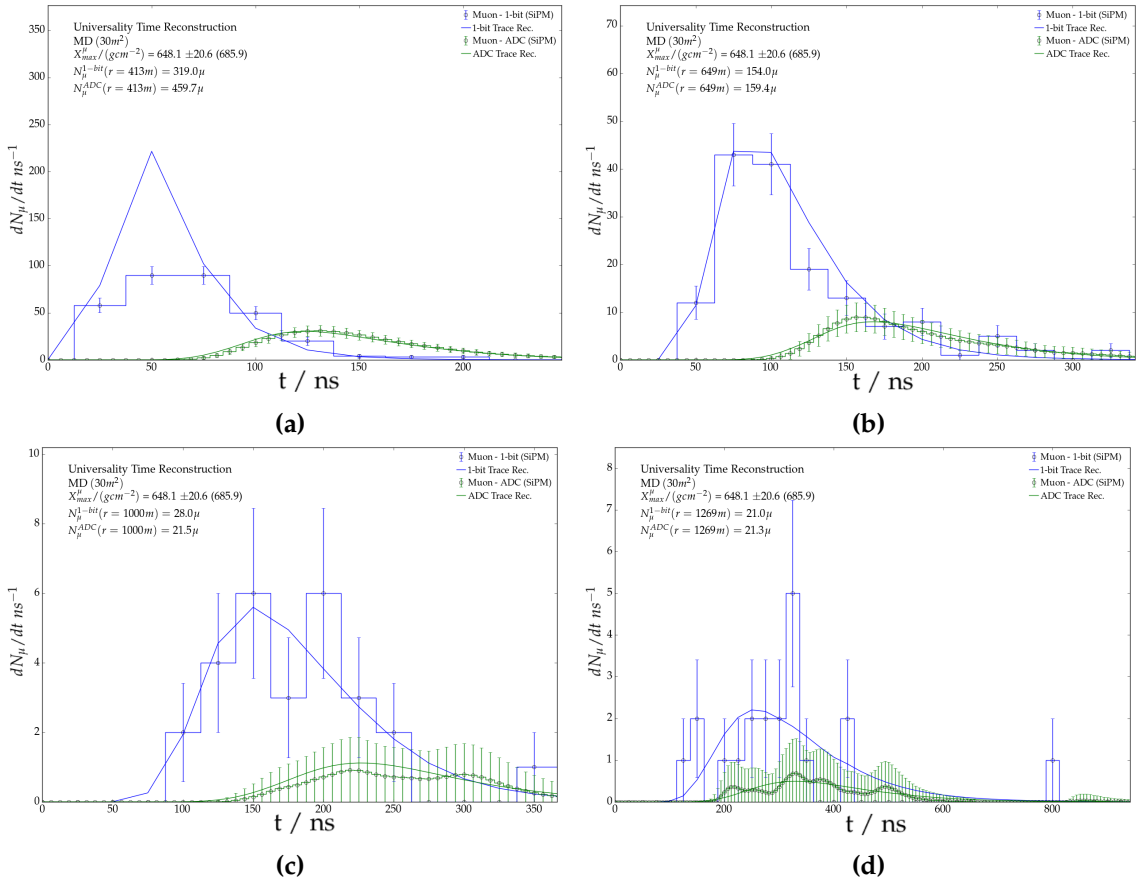

Figure 6.6: MD sample traces of a proton air shower with an energy $10^{19.5}$ eV at $\theta = 48°$ and different radial distances to the shower core. The colored lines reflect the 1-Bit (blue) or integrator (green) counting strategy. The time axis is chosen to contain 95% of the total trace.

CHAPTER 7

Reconstruction Performance

In this chapter we present the results of the Universality reconstruction for different primaries and high energy hadronic models. The CORSIKA air shower library used during model development is used here. The universality reconstruction can be divided into 6 *modes*: (i) WCD with signal information, (ii) WCD with signal and time information, (iii) MD with signal information, (iv) MD with signal and time information, (v) hybrid (WCD+MD) with signal information and (vi) hybrid with signal and time information. The reconstructions for the WCD and MD are first discussed independently, followed by the introduction of a novel hybrid reconstruction procedure. This provides the opportunity to study its strengths and limitations for mass composition analyses. We emphasize the performance of the hybrid reconstruction and compare relevant shower parameters for mass composition purposes. The reconstruction has been *tuned*[1] to mimic the procedure done for future data analysis (see chapter 6.3). Biases between hadronic models can be easily corrected for.

Note, the studies are based for an infilled array. About 12500, 990, 90 and 10 events are expected to be annually measured above $10^{17.5}$ eV, 10^{18} eV, $10^{18.5}$ eV and $10^{19.5}$ eV respectively [50]. Also, in this analysis, we do not distinguish between *saturated*[2] and *un-saturated* events. This results from the higher stations density in the infilled array with respect to the standard array, where more than 50% of all events are considered saturated above $10^{18.5}$ eV (more than 30% above 10^{18} eV). This is indicated in figure C.1 of Appendix C. Appendix C also includes addition figures discussed in this chapter.

7.1 WCD Reconstruction

7.1.1 Signal Model

Successful reconstructions (i.e. reconstructions which have converged successfully) are shown through their efficiency in figures 7.1a, 7.1b and C.2. Here, the efficiency ϵ_{rec} is defined as the number of converged reconstructions, for every E-θ bin (120 showers), after completing the second step in the iterative reconstruction procedure (found in section 6.4). The error bars are obtained from a binomial distribution. The general trend of the reconstruction efficiencies are in agreement with the 3-TOT trigger efficiency shown in figure 7.1c. The

[1] often referred to as *Universality calibration*

[2] An event where at least one station is saturated

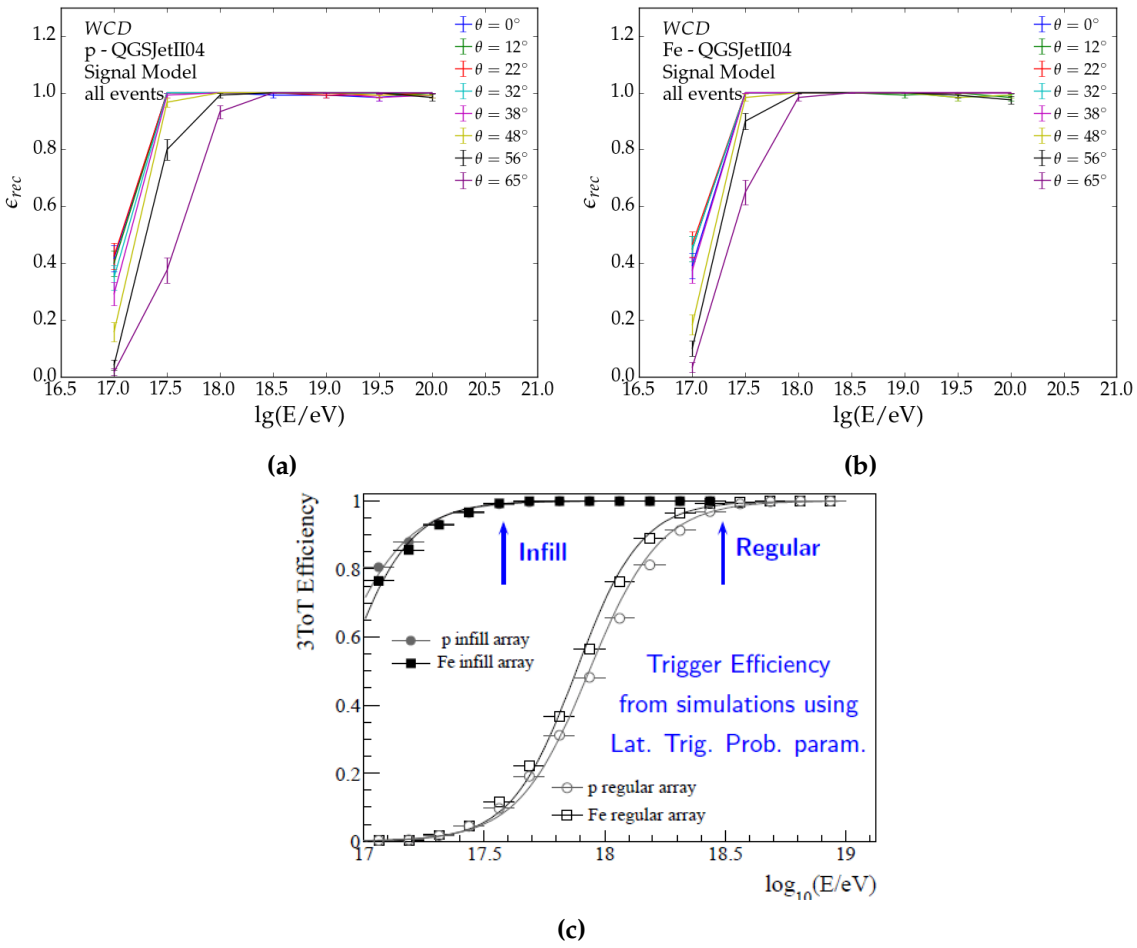

Figure 7.1: Fit efficiency for successful WCD-only reconstructions of **a)** proton and **b)** iron induced air showers. Each energy-zenith bin accounts for 120 air showers. **c)** The 3TOT efficiency for the infilled and standard array, derived from simulations [100].

3-TOT is a local trigger condition where 3 neighbouring stations form a triangle. 3-TOT is fully efficient for shower energies above $10^{17.5}$ eV ($10^{18.5}$ eV for the standard array) and zenith $\theta < 55°$. Universality is expected to reconstruct all events within the phase-space of full 3-TOT efficiency, which is reflected in figure 7.1. No primary or hadronic model differences are found for $\theta \leq 48°$. Iron induced showers are more likely to be reconstructed successfully at inclined angles, as can be seen above 56°. Electromagnetic particle are more attenuated by inclined showers, resulting in a lower signal size and thus a lower probability for a station to sample a particle. The increased muon content in iron showers is barely affected by the inclination, providing more signal information for inclined low energy showers.
Subsequent results will only include energy and zenith showers for which the reconstruction efficiency is above 90%. Figures illustrated with respect to energy yield the average for all showers in the zenith range. Similarly, figures depicted with respect to zenith account for showers in the relevant energy range.

Biases in the zenith and azimuth are below 0.2 ° for all shower zenith and energy above $10^{17.5}$ eV. Accounting for all showers between 0 ° and 65 °, we find that σ_θ is nearly constant at 0.65 ° for energies above $10^{18.5}$ eV. It increases to approximately 1 ° at $10^{17.5}$ eV. Primary and hadronic model differences are negligible (as seen in figures C.3a and C.3b). The standard deviation of the azimuth σ_ψ is smallest for inclined showers. It is 0.3 ° at $\theta = 65$ °, increasing

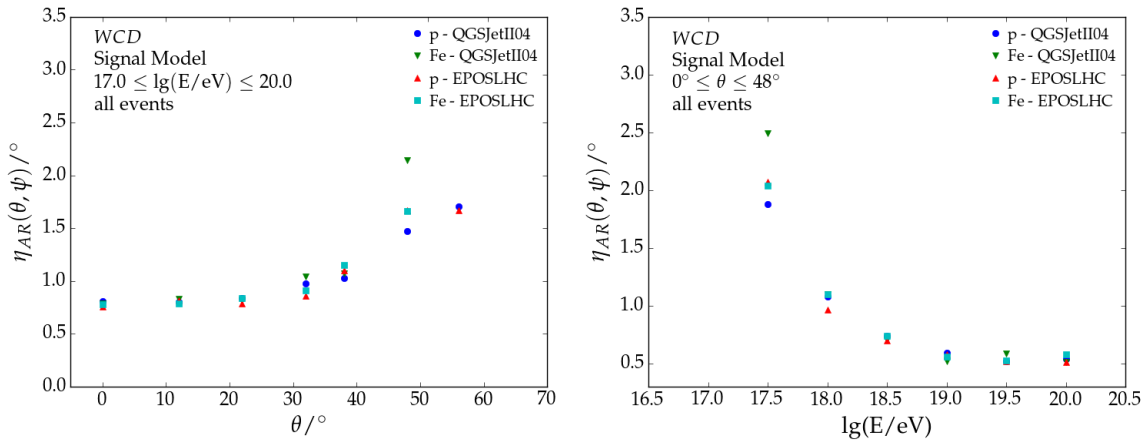

(a) **(b)**

Figure 7.2: Angular resolution $\eta_{AR}(\theta, \psi)$ of reconstructed showers with different primaries and hadronic models. Only the information on the signal size in the WCD is used in the reconstruction.

for more vertical showers. This feature is expected as the shower is symmetric in ψ at $\theta = 0\,°$. Furthermore, vertical showers trigger fewer stations. The latter also results from low energy showers, which can be seen in figure C.3d.

The combined contribution of σ_θ and σ_ψ is reflected in the angular resolution of the shower axis $\eta_{AR}(\theta, \psi)$. It is defined as the angular radius, containing 68% of the showers[3]. The resulting angular distribution can be fitted to a Rayleigh distribution with mode σ_{Rayleigh}. η_{AR} is then computed through

$$\eta_{AR} = \sqrt{-2\ln(1-0.68)}\sigma_{\text{Rayleigh}}. \tag{7.1}$$

Profile figures of angular resolutions derived through equation (7.1)[4] can be seen in 7.2a and 7.2b. Markers in figure 7.2a are the combined resolution for energies between 10^{17} eV and 10^{20} eV, provided reconstruction efficiency is above 90%. Similarly, in figure 7.2b, the markers are the combined resolution for zenith angles between 0 ° and 65 °. The figures show that the reconstruction performs poorly above $\theta = 50\,°$ and below 10^{18} eV. We find that the angular resolution is in agreement with previous studies in reference [81] (E>10^{19} eV and $\theta < 50\,°$); 0.5° in this work with respect to 0.6° in [81]. We also find it to be better than the angular resolution of the standard reconstruction seen in reference [102]. Limiting universality reconstructions to showers below 50 ° reduces the exposure by almost a factor of 2. This could be recovered by fixing the axis to the standard reconstruction, which has an angular resolution below 2 ° (lower for higher energies). This approach was not further investigated. In this work, we limit ourselves to events below 50 °.

The core position is unbiased for all primaries and hadronic models, not exceeding more than 2 m. A low bias is expected as universality accounts for the azimuthal effects of particle propagation in the atmosphere, which is carried into the LDF fit. The core resolution is calculated with the *mean absolute deviation* (MAD[5]) and yields a resolution of 10 m for vertical and high energy showers (in agreement with reference [81]). It (depicted in figure 7.3) does

[3]The angle between shower axes is obtained by considering them as vectors and compute their dot product through $\cos(\theta) = \vec{v}_{Univ} \cdot \vec{v}_{\text{MC}}$

[4]The definition in equation (7.1) is adopted by the Pierre Auger Collaboration. [101]

[5]The mean absolute deviation is a robust estimator of the unbiased standard deviation of a sample [103].

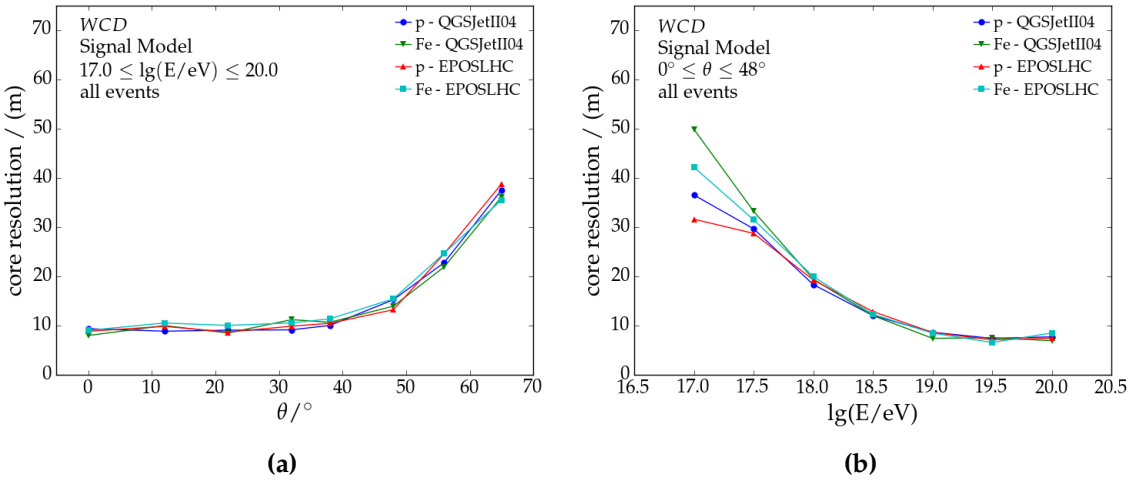

Figure 7.3: The resolution of the reconstructed core position as a function of **a)** energy and **b)** zenith.

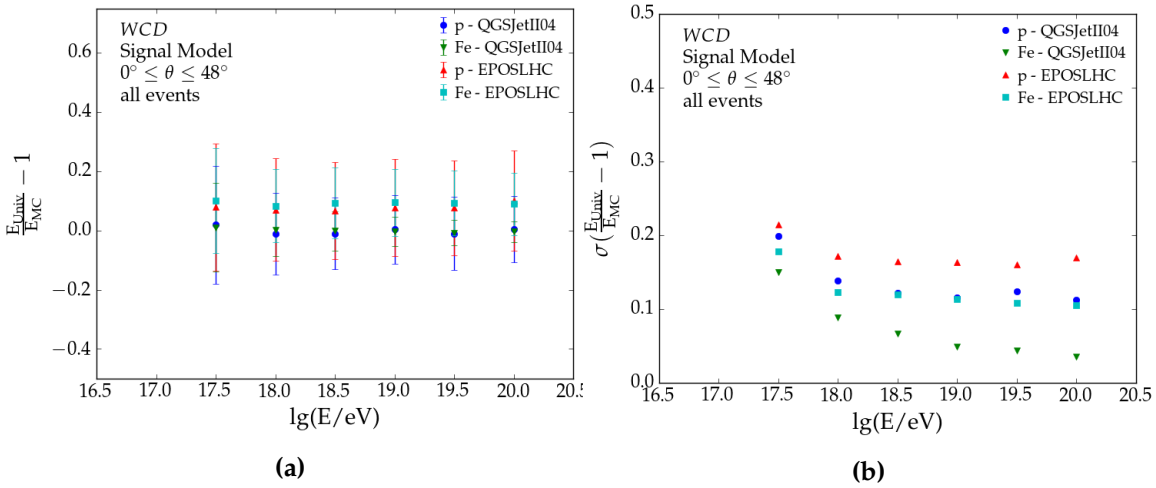

Figure 7.4: a) Energy bias and **b)** resolution with respect to true shower energy for different primary and hadronic models. The error markers denote the resolution seen in **b)**.

not exceed 40 m with exception in the lowest energy bin. Also, it is independent of mass composition and hadronic model.

As figures 7.4a and C.4a depict, energy biases are below 1% for air showers from QGSJeTII-04 (reference hadronic model). It is 10% for showers from EPOS-LHC, irrespective of primary, shower energy or zenith. The bias results from intrinsic differences in the hadronic model and can be corrected through methods discussed in section 6.3. Energy resolutions in figures 7.4b and C.4b are below 20%. In comparison, the energy resolution of the standard reconstruction in the infilled array (based on 8 years of data) is 13% [104]. Averaging over proton and iron showers, simulated with QGSJeTII-04, we find the energy resolution to be below 11% above 10^{18} eV (7% at 10^{20} eV). The average resolution of air showers simulated with EPOS-LHC are nearly constant at 13% for energies above 10^{18} eV. These results are an improvement with respect to the previous iteration of the universality model, where energy resolutions are about 15% at $10^{18.5}$ eV. A distinct feature in figure 7.4b is the difference between mass composition. Its origin is not fully understood and is not present in earlier work. It may be attributed to the differences in the high energy hadronic model -the previous Universality

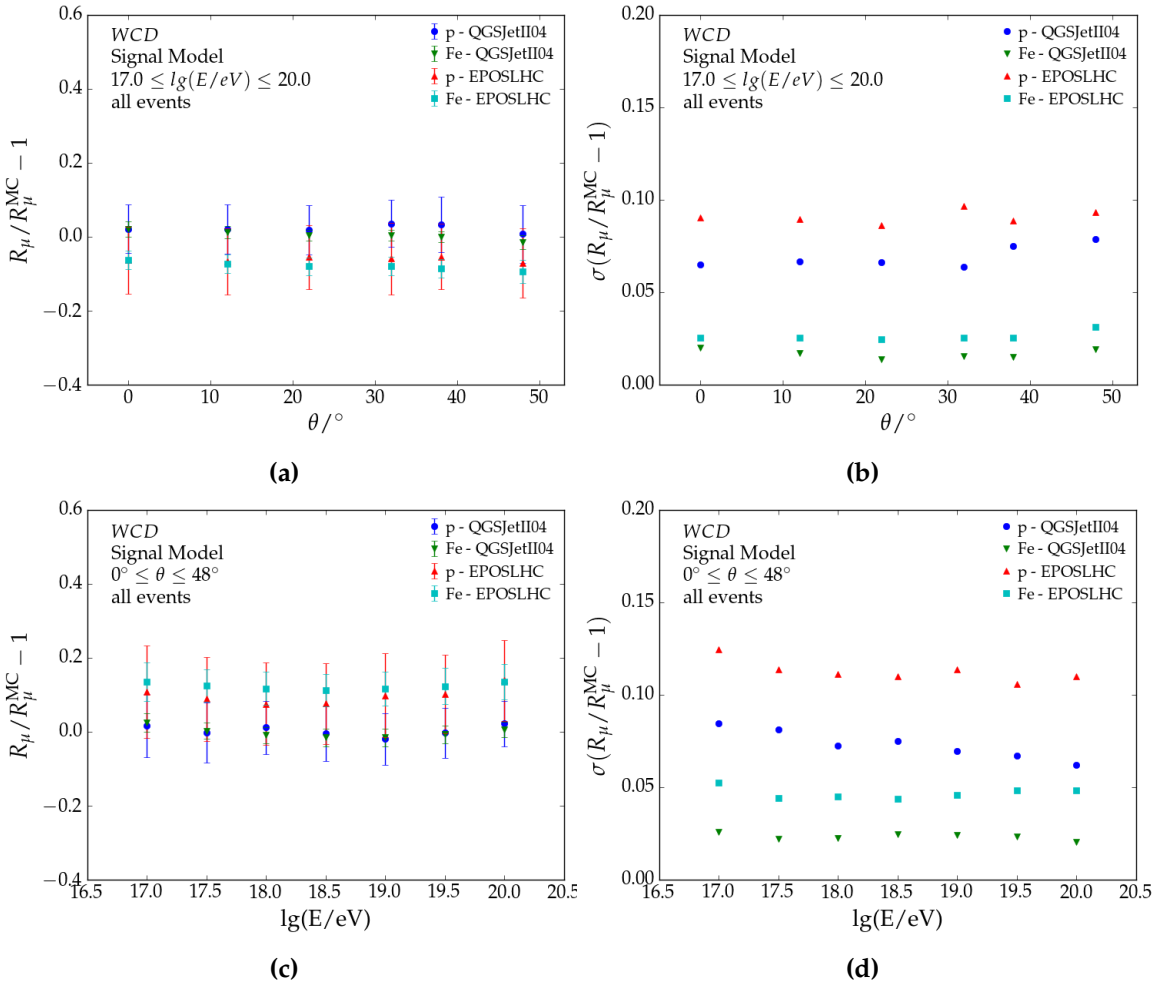

Figure 7.5: *Top:* R_μ **a)** bias and **b)** resolution with respect to shower zenith. *Bottom:* R_μ **c)** bias and **d)** resolution with respect to energy.

model used QGSJETII-03, differing in its muon content. Alternatively, the R_μ estimator can propagate the shower to shower fluctuations in the muon content to the reconstructed energy.

For R_μ to be classified as *good*, the resolution must be below 20% ($\langle R_\mu^p \rangle = 1$ and $\langle R_\mu^{Fe} \rangle \approx 1.4$. Differences between primary biases should also not exceed 40%. These limits apply to a mass composition discrimination between proton and iron. Lower resolutions allow for better mass discrimination with respect to e.g. nitrogen or oxygen. Note, R_μ is obtained through the estimator in equation (6.11), which depends on the reconstructed energy, zenith and estimated $X_{\max}(E)$. Figures 7.5a and 7.5c indicate no bias for QGSJETII-04 shower, whereas it is 10% for showers from EPOS-LHC. The bias does not depend on energy or zenith. These bias features are expected, as the R_μ estimator is tuned for QGSJETII-04 showers (discussed in section 6.3). R_μ are below 10% with exception of proton showers simulated with EPOS-LHC (seen in figure 7.5d). They are also calculated with the MAD-approach. Figures 7.5b and 7.5d shows the limitation of the estimator, as shower to shower fluctuations are not fully accounted for. Nevertheless, results presented in figures 7.5 are in agreement with studies in [81]. Detailed figures on the bias and resolution can be found in C.5 and C.6.

7.1.2 Signal and Time Model

Including time information to the reconstruction reduces the reconstruction efficiency for energies below 10^{18} eV. This results from the strict constraints imposed on the station selection (discussed in 6.2). Also note, reconstructions with time information only follow after a successful reconstruction of the signal size. Figures 7.6a and 7.6b indicate the same mass composition dependencies for low energetic showers, favoring iron induced air showers. This results from the larger signal produced by muons, fulfilling the necessary shape and signal size criteria.

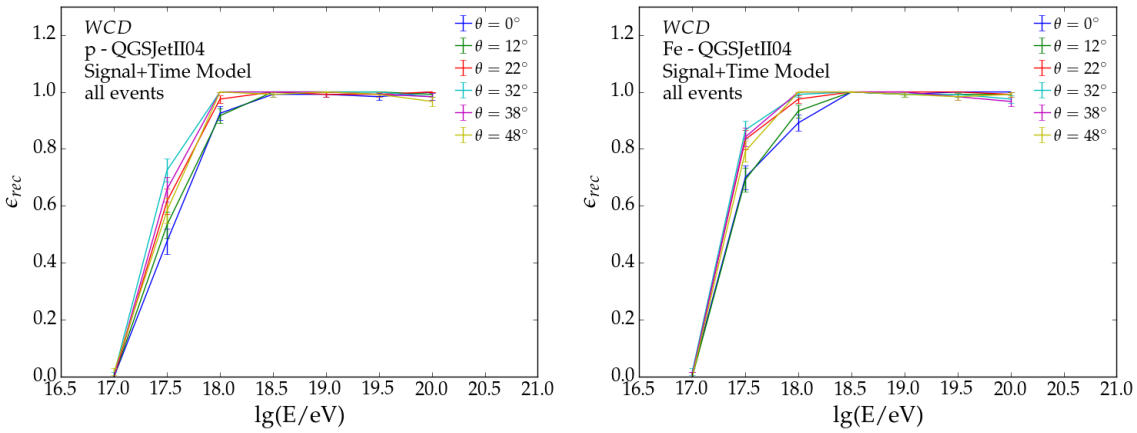

(a) **(b)**

Figure 7.6: Fit efficiency for successful WCD-only reconstructions of **a)** proton and **b)** iron induced air showers. Each energy-zenith bin accounts for 120 air showers. Signal and time information is used in the reconstruction.

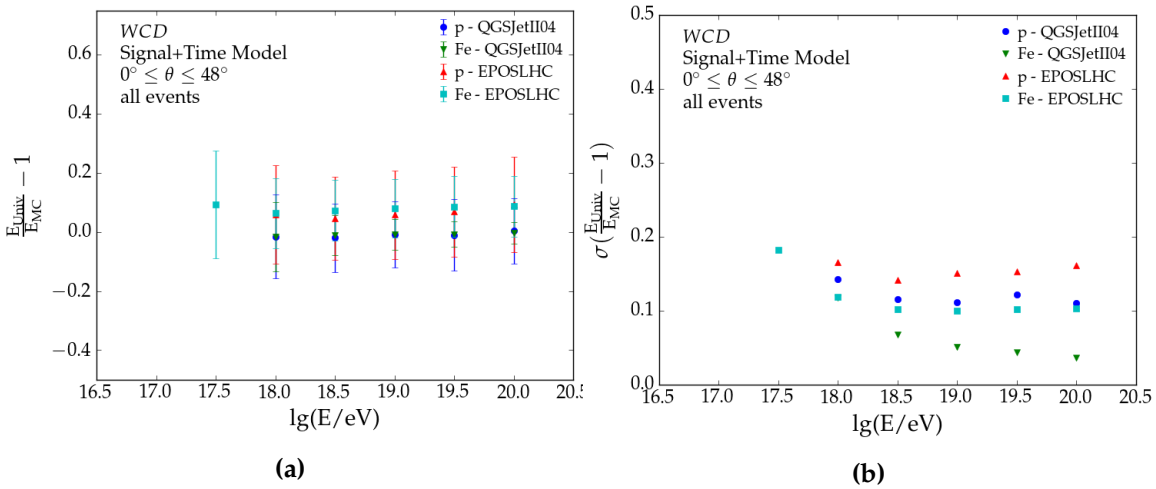

(a) **(b)**

Figure 7.7: a) Energy bias and **b)** resolution with respect to true shower energy for different primary and hadronic models. Signal and time information are used during the reconstruction. The error markers denote the resolution seen in **b)**.

The addition of time information has not improved the angular resolution and core resolution shown in figures 7.2 and 7.3 respectively. Also, energy biases (figure 7.7a)are equivalent to those seen in 7.4a. The energy resolution remains largely the same with two minor features. First, the iron resolution of QGSJETII-04 showers has increased from 10%

to 12%. Second, the overall energy resolution is minimal at $10^{18.5}$ eV for all proton showers from EPOS-LHC showers.

As the iterative reconstruction procedure shows, R_μ is freed after the shower maximum had been determined. This provides a more realistic description of the bias and resolution of the muon content. R_μ differs as much as 0.1 between proton and iron (figure 7.8a). The muon content in QGSJETII-04 showers is overestimated by 10%, whereas it is underestimated by 10% for EPOS-LHC showers. This can be corrected, reducing the composition biases to 5%. In figure 7.8b, we find that the separation between protons and irons from EPOS-LHC showers is about 20%. This implies, assuming it represents the *true* hadronic model, that no composition analysis can be performed with R_μ below 10^{18} eV. This is supported by the resolution seen in figure 7.8d. Nevertheless, current findings are an improvement with respect to studies in reference [44], shown in figure 7.8e. Detailed figures on the biases and variances can be seen in Appendix C.7 and C.8.

To exploit $X_{\max}$ for mass composition purposes, biases and resolutions must be below 50 gcm^{-2}[6]. Differences between proton and iron are about 30 gcm^{-2} for vertical showers, reducing to 10 gcm^{-2} at $\theta = 48°$ (see figure 7.9a). Figure 7.9c shows that proton and iron showers differ by 20 gcm^{-2}, irrespective of energy. Unlike the bias, the resolution does not change with respect to zenith and remains at 40 gcm^{-2} for all energies. Looking at figure 7.9d, we find that the $X_{\max}$ resolution improves from 50 gcm^{-2} at 10^{18} eV to 20 gcm^{-2} at 10^{20} eV. This is also an improvement with respect to analysis in reference [44], shown in 7.9e. It indicates a successful extension down to energies of 10^{18} eV. Figures C.9 and C.10 indicate the bias and resolution of the shower maximum for every energy-zenith bin. $\sigma(X_{\max})$ is only competitive to the FD at the highest energies. With additional information from the SSD the resolution from universality reconstructions may improve.

[6]The shower depth between proton and iron showers is approximately 100 gcm^{-2}.

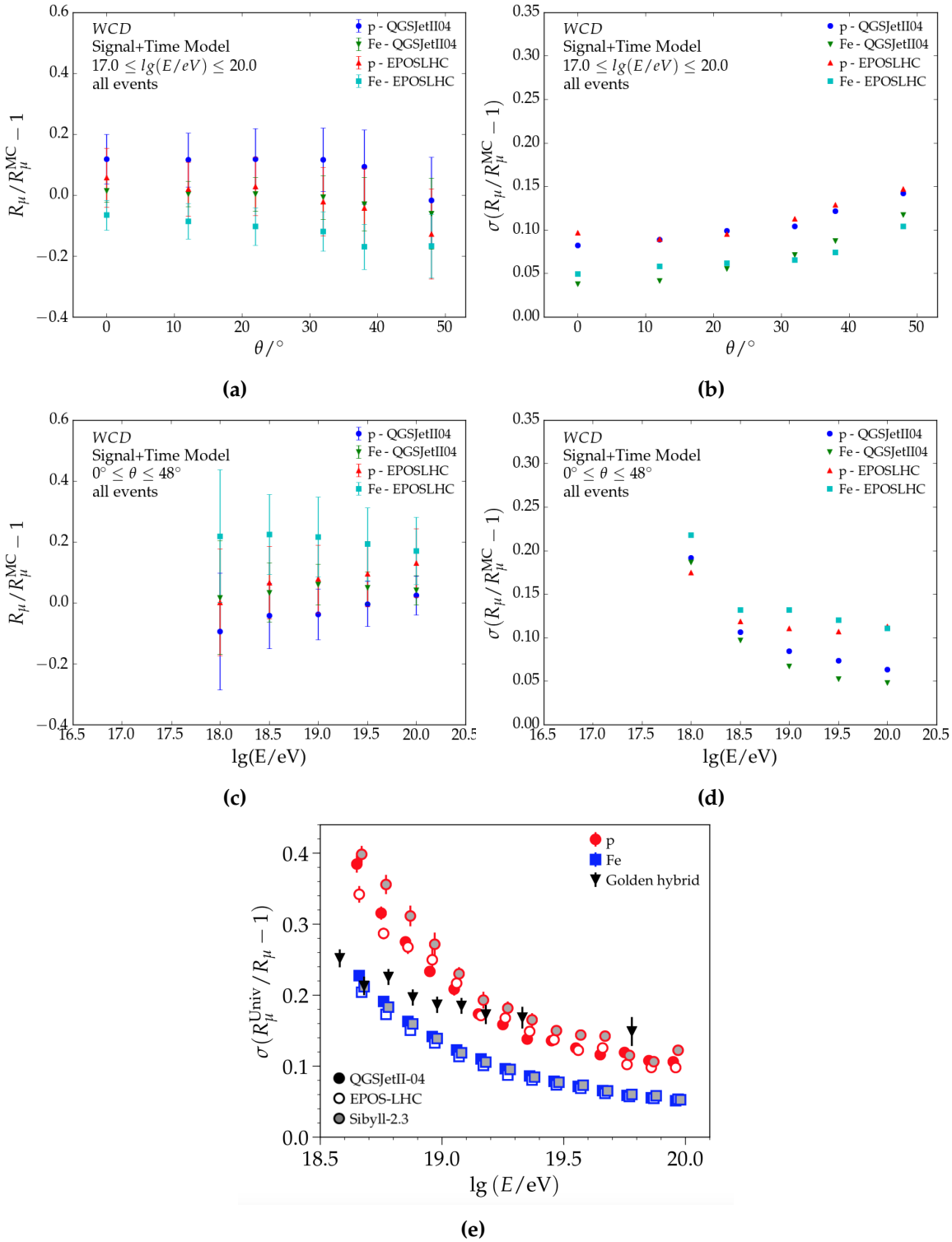

Figure 7.8: *Top:* R_μ **a)** bias and **b)** resolution with respect to shower zenith. *Bottom:* R_μ **c)** bias and **d)** resolution with respect to energy. **e** Muon content resolution for the standard array data with respect to energy [44].

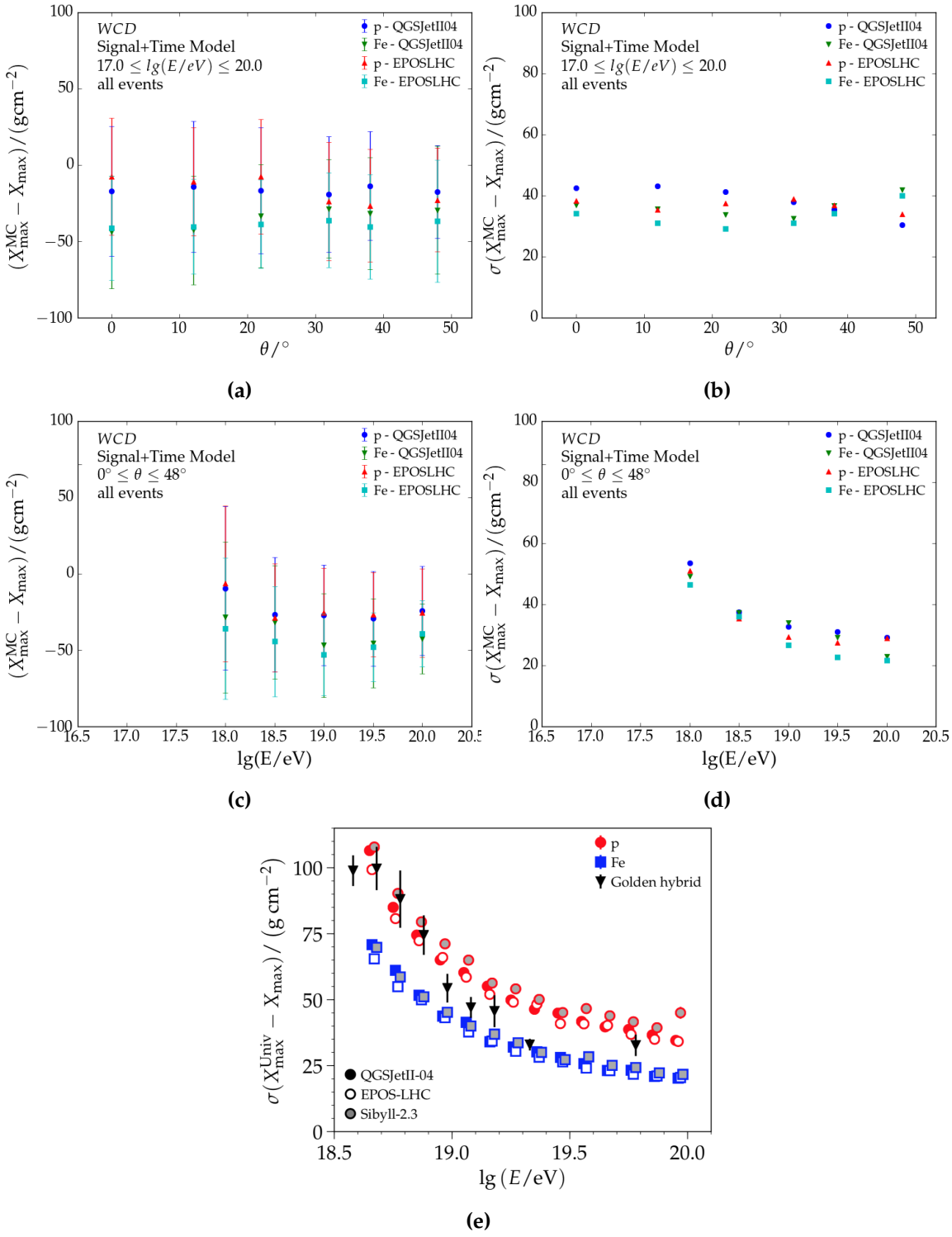

Figure 7.9: *Top:* X_{max} **a)** bias and **b)** resolution with respect to shower zenith. *Bottom:* X_{max} **c)** bias and **d)** resolution with respect to energy. **e)** Maximum shower depth resolution for the standard array data with respect to energy [44].

7.2 MD Reconstruction

Although the MD is triggered by the WCD, its signal and time information can be reconstructed independently to the WCD. This provides the opportunity to study universality-based air shower reconstructions with scintillator detectors (beneficial to similar detectors as the SSD). Most importantly, it enhances our understanding of its limitations, necessary for the analysis of hybrid reconstructions. It was found that the MD has an energy resolution above 20%, resulting from the combined effect of detector saturation (see figures C.1a and C.1b) and low number of detectors registering a muon. As a result, the energy estimator of the LDF fit is often underestimated for the highest energies. Between 10^{18} eV and $10^{18.5}$ eV the energy resolution is minimal. To minimize the effect of the energy bias, it is fixed to the energy obtained from the WCD reconstruction (accounting only information on the signal size - $\mathcal{L}_{signal}$).

In subsequent results, we only include energy and zenith showers for which the reconstruction efficiency is above 90%. Profile figures illustrated with respect to energy account for all showers in the zenith range with the desired minimum efficiency. Similarly, figures depicted with respect to zenith account for showers in the energy range with the desired minimum efficiency.

7.2.1 Signal Model

MD reconstructions, accounting only for the signal size in the detector, are fully efficient above $10^{17.5}$ eV for iron showers below 48° (seen in figure 7.10a and 7.10b). We find it to be also fully efficient at 56° above 10^{18} eV. This is expected as the effective detector area has almost decreased by a factor 2, necessitating high energy showers to sample more particles. Interestingly, proton showers are reconstructed less efficiently at the highest energies (see figure 7.10a). This may be attributed to the production height of muons between proton and iron showers. $X^{\mu}_{\max}$ is larger for proton showers compared to iron showers. Assuming muons produced at the height of the maximum muon production depth (subtended to an equivalent angle to the shower axis), it is apparent that the lateral spread of iron showers is larger than for protons. In other words, fewer MD stations measure muons. Combined with a large fraction of saturated detectors (for vertical showers), the reconstruction becomes unstable. This feature is also found for air showers from EPOS-LHC, shown in figure C.11. No hadronic model dependencies are found.

Biases in the zenith and azimuth are smaller compared to those from WCD reconstructions (see figures in C.12). This is largely attributed to the angular limitations of the MD. MDs are designed to be used for showers up to 45° (discussed in 2.3) and thus we limit ourselves to events below 48°. Increased biases in the WCD result from showers at 65°. The angular resolutions η_{AR} shown in figures 7.11a and 7.11b are nearly equivalent to those of the WCD in figures 7.2a and 7.2b. This result is beneficial for the hybrid reconstruction, as it shows that the addition of the MD should not reduce the angular resolution.

Core biases in the MD are below 2 m for all hadronic models and primaries. As figure 7.12a shows, the core resolution is around 10 m below 40°. It increases up to 25 m for showers at 56°, a similar structure as seen for the WCD. Similarly to figure 7.3b, the core resolution for the MD reconstruction deteriorates for low energy showers (seen in 7.12b). Above 10^{18} eV, differences between the MD and WCD core resolution are negligible. Below 10^{18} eV, it is found that MD core resolutions are better with an average core resolution of about 27 m and

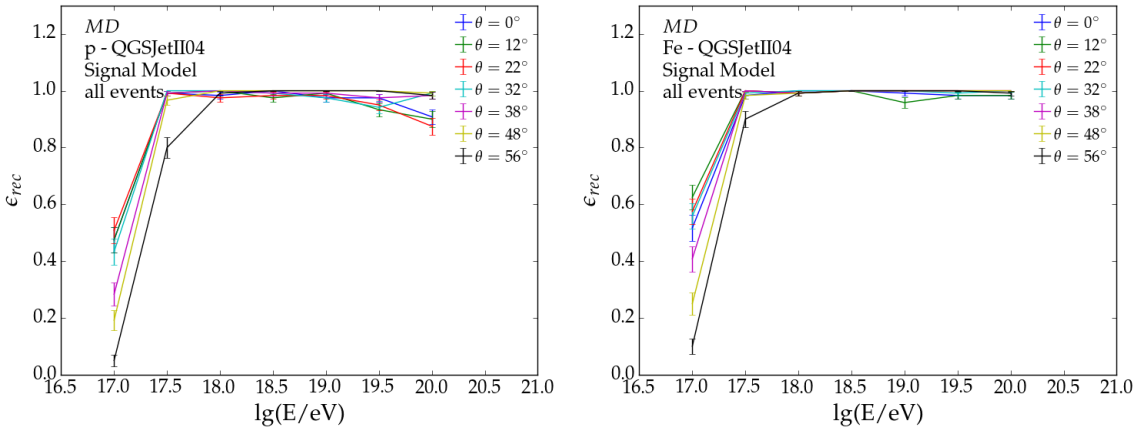

(a) **(b)**

Figure 7.10: Fit efficiency for successful MD-only reconstructions of **a)** proton and **b)** iron induced air showers. Each energy-zenith bin accounts for 120 air showers.

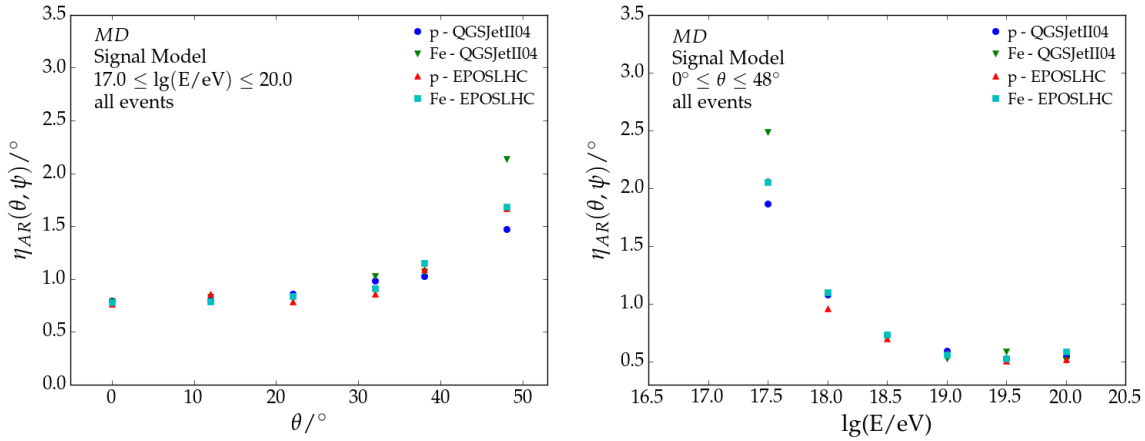

(a) **(b)**

Figure 7.11: Angular resolution $\eta_{AR}(\theta, \psi)$ of reconstructed showers with different primaries and hadronic models. Only the information on the signal size in the MD is used in the reconstruction.

35 m in the MD and WCD respectively. Clear primary dependencies are only found in the lowest energy bin 10^{17} eV.

Figure 7.13a and 7.13b reveal that the energy bias and resolution for MD-only reconstructions are significantly worse compared to those from the WCD. Iron showers present a bias of 25% at $10^{17.5}$ eV, decreasing for highest energies. Proton showers show an interesting structure, as their biases are largest at $10^{17.5}$ eV and 10^{20} eV with a minimum at $10^{18.5}$ eV. No zenith dependencies are found for iron showers, whereas proton showers show a bias of about 40% at $\theta = 0°$. The origin of the bias is not fully understood, considering that it occurs with proton showers. Incidentally, mass composition differences arise in the same parameter-space where the reconstruction efficiency is not fully efficient (figure 7.10).

Mass composition differences are further emphasized in the energy resolutions seen in figures 7.13b and 7.13d. In figure 7.13b, the energy resolution shows the same distinct minimum at $10^{18.5}$ eV for proton showers, whereas iron showers improve with increasing energy. The latter indicates an energy resolution of 10% for the highest energies. However,

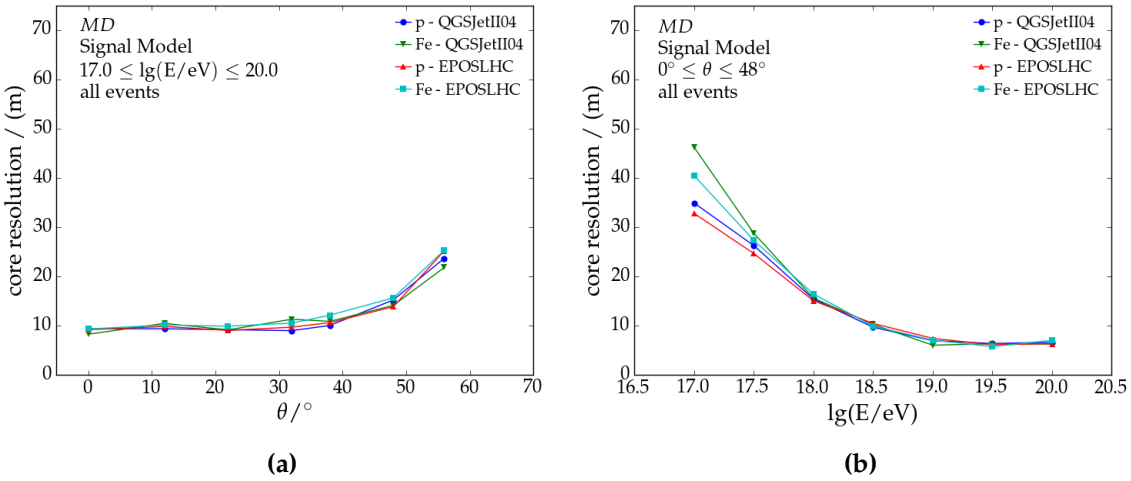

Figure 7.12: The resolution of the reconstructed core position as a function of **a)** energy and **b)** zenith.

exceeds 20% below 10^{18} eV. At the minimum of proton showers, the energy resolution is 30%. No zenith dependencies were found for proton showers. Contrary (as with the bias), the energy resolution of proton showers worsens for vertical showers; 60% at 0°.

The origins of these features are not fully understood but are assumed to be a limitation due to detector saturation and number of MD with muon signals. No hadronic model dependencies were found. Although outside the scope of this work, reanalyzing the reconstruction without any saturation limits would improve our understanding of this feature. Regardless, it is clear that the MD cannot reconstruct the energy independently[7] and will likely reduce the quality in a hybrid reconstruction. As a result, hybrid reconstructions reconstruct the energy exclusively with WCD information.

As for the WCD, the muon content R_μ is obtained with its estimator from equation (6.11). Figures 7.14a and 7.14c reveal that primary biases are below 5% without any primary dependencies. This is an improvement compared to the WCD in figure 7.5. The improved bias results from the correlation between R_μ and the signal from other particle components. As equation (4.53) proved for the MD, R_μ is a direct indicator to the muon content and thus its total signal. For the WCD, equation (4.52) showed that uncertainties depend on the underlying model of the four particle components and their correlation to the muon content (addressed in section 4.2.5). Biases for the reference model and primary were below 2%, irrespective of detector type. However, intrinsic differences between QGSJETII-04 and EPOS-LHC are more apparent with the WCD. Following the same reasoning, the R_μ resolutions in the MD are expected to outperform those from the WCD. In figures 7.14b and 7.14d resolutions are mostly below 10%, suitable for mass composition analysis. As with the WCD, the mass composition differences are present. Comparing to the WCD, it is apparent that the resolution of the muon content from EPOS-LHC showers (proton and iron) is better with MD-only reconstructions. This implies a secondary effect, likely introduced by intrinsic differences in the muon energy spectrum between EPOS-LHC and QGSJETII-04, more specifically with low energy muons $< 1\,\mathrm{GeV}/\cos\theta_\mu$[8]. A more detailed analysis would introduce more clarity to the origin of the improved R_μ resolution. If the muon shielding reduced hadronic model differences, future universality reconstructions could rely only on

[7] Energy resolutions must be competitive with respect to the standard resolution. These are below 20%.
[8] representing the energy cut introduced due to soil shielding

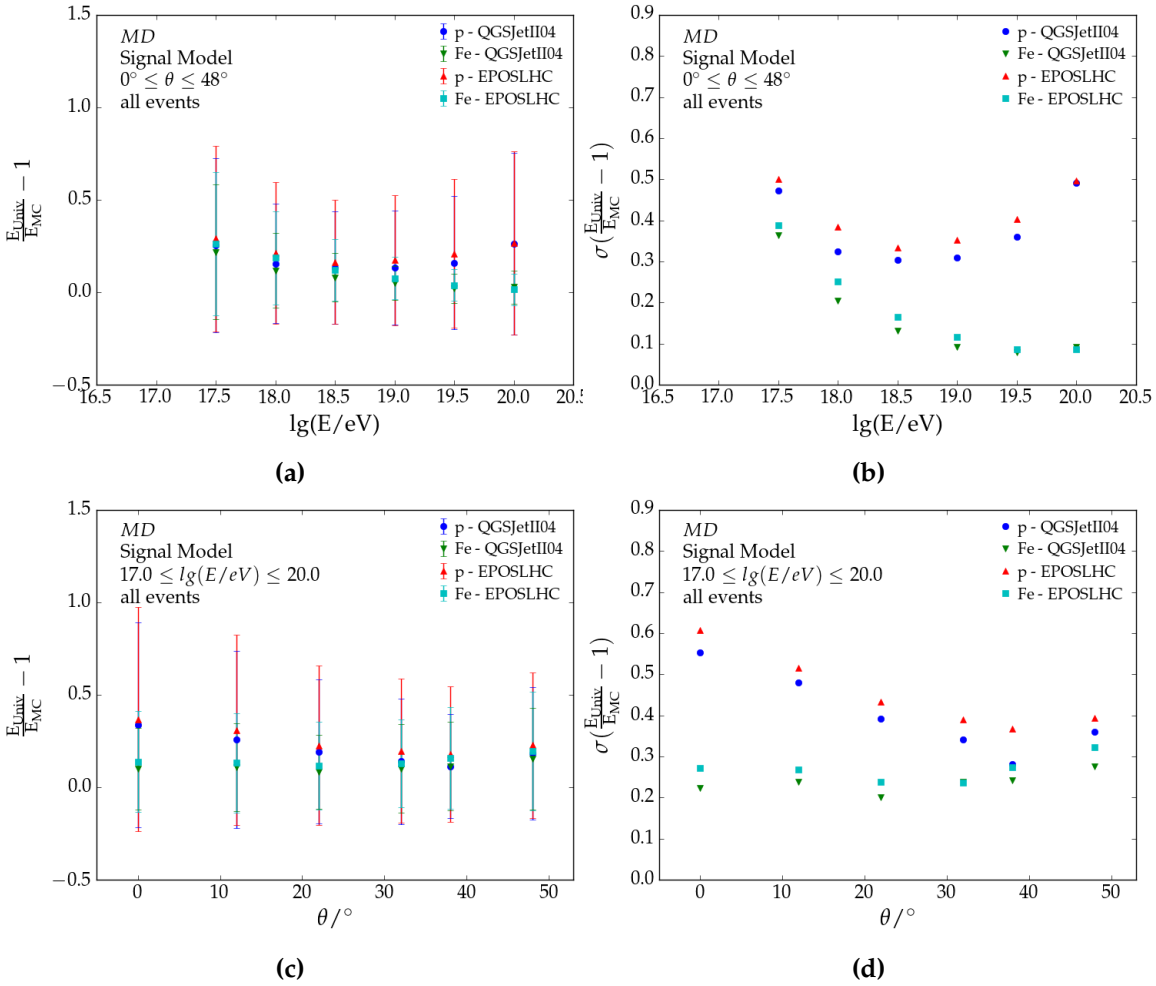

Figure 7.13: a) Energy bias and **b)** resolution with respect to true shower energy (top) and shower inclination (bottom) for different primary and hadronic models. Only signal information is used during the reconstruction. The error markers seen in **a)** denote the resolution seen in **b)**, the same for **c)** and **d)**.

MD information to extract R_μ. Detailed figures on the bias and resolution can be found for every energy-zenith bin in Appendix C.13 and C.14.

7.2.2 Signal and Time Model

Results on MD reconstructions using signal size and time information are limited to showers up to $\theta = 38°$ for qualitative trace shapes. Figures 7.15a and 7.15b do not show any unexpected features. At lower energies (≤ 17.5 eV), the efficiency is below 90% -in agreement with results from the WCD seen in figure 7.6. Above 18.5 eV, proton showers reduce in efficiency as in figure 7.10. These results imply that the time reconstruction is nearly 100% efficient after a successful LDF reconstruction. No hadronic model dependencies were identified (see figure C.15).

Marginal improvements in core and angular resolution (and their respective biases) are seen with respect to figure 7.11 and 7.12. It further highlights that reconstructions with time information has its peak performance at high energies and vertical showers. No significant

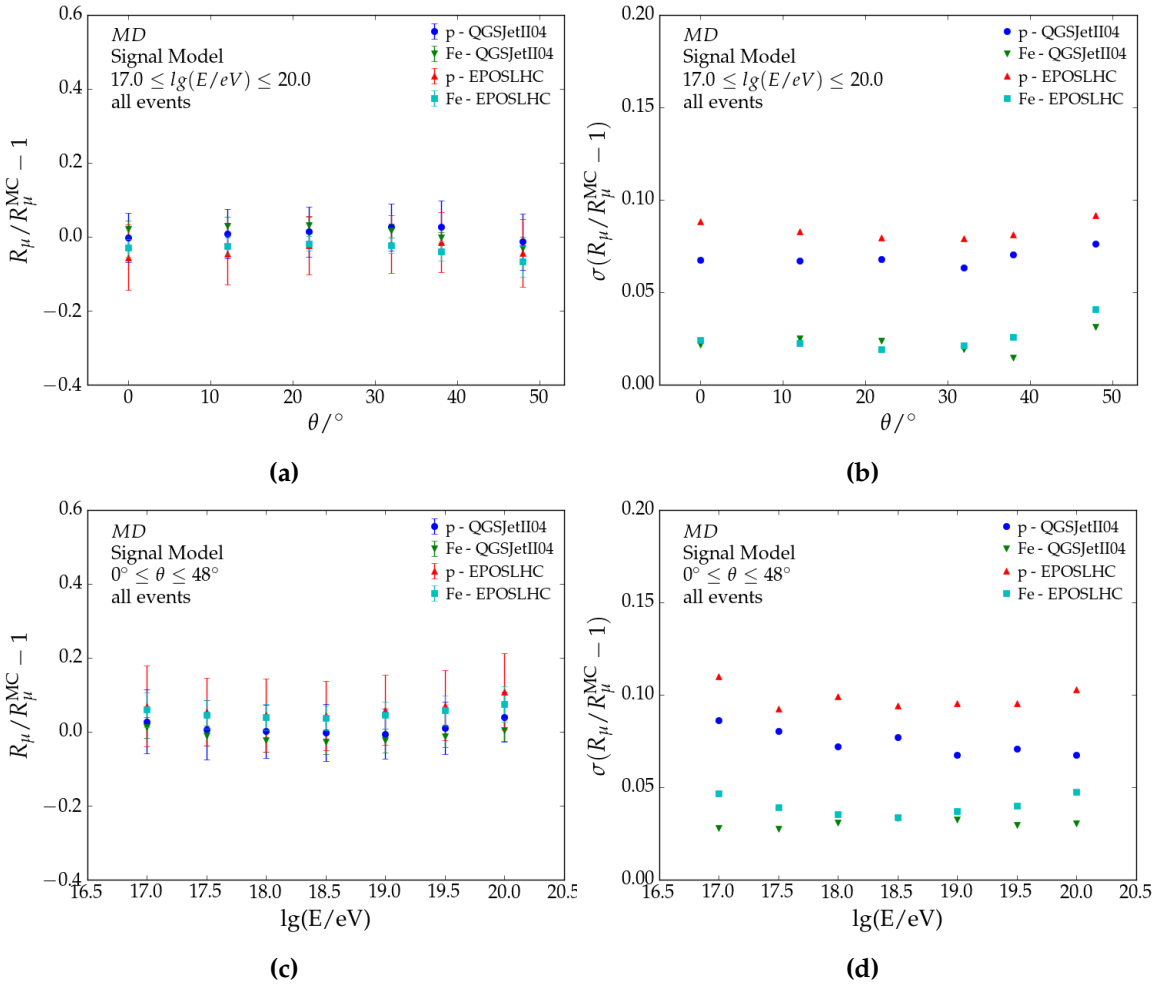

Figure 7.14: *Top:* R_μ **a)** bias and **b)** resolution with respect to shower zenith. *Bottom:* R_μ **c)** bias and **d)** resolution with respect to energy. The error bars seen in **a)** and **c)** denote the resolution seen in **b)** and **d)** respectively.

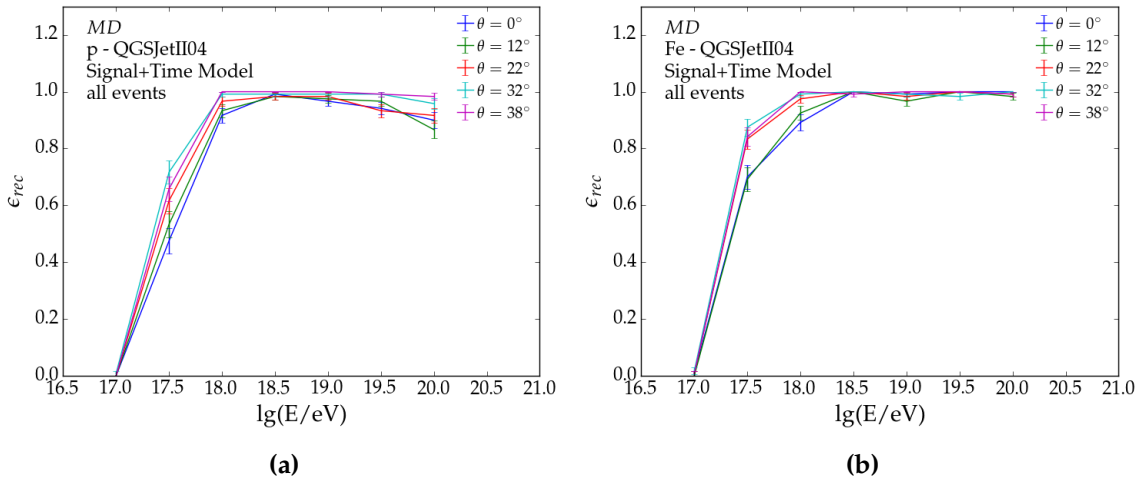

Figure 7.15: Fit efficiency for successful MD-only reconstructions of **a)** proton and **b)** iron induced air showers. Each energy-zenith bin accounts for 120 air showers. Signal and time information is used in the reconstruction.

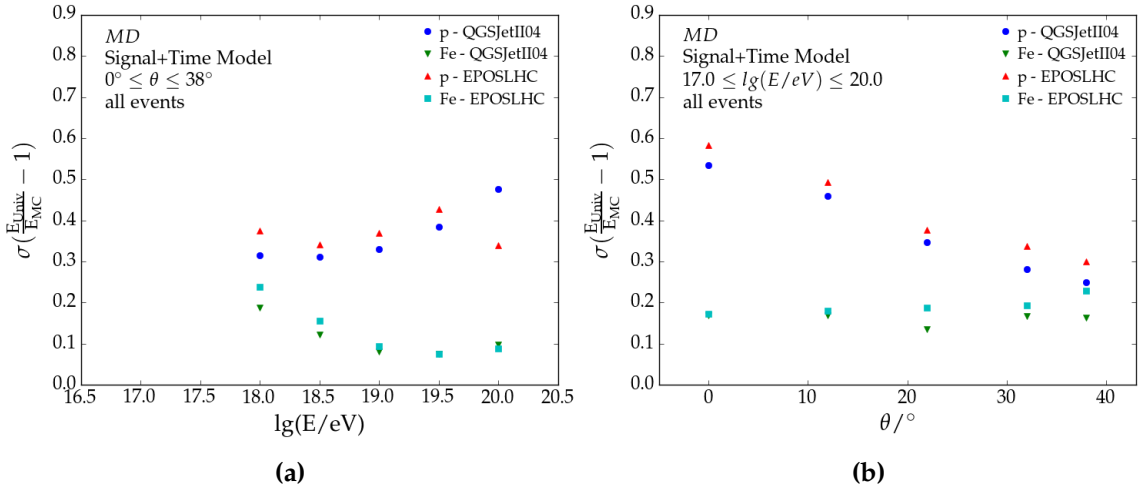

(a) **(b)**

Figure 7.16: Energy resolution with respect to true shower **a)** energy and **b)** zenith. Signal and time information is used during the reconstruction.

change was found in the energy bias. However, the energy resolution has improved. Without time information, the energy resolution for iron showers (averaged over all energies) are between 25% and 35%. As figure 7.16b indicates, it has reduced to 17% and 24% (still above the preferred 20% limit). The energy dependent structure seen in figure 7.16a could not be resolved. Note, only unsaturated trace bins are included into the time reconstruction. This suggests that the energy is more sensitive to the LDF fit than it is to the shape fit. EPOS-LHC and QGSJETII-04 are mostly in agreement with the latter outperforming the former by 5%.

From figure 7.17a, it is apparent that biases in R_μ are smaller compared to the WCD. Hadronic model and primary biases are largest for vertical showers, reducing with more inclined showers. At $\theta = 0°$, the hadronic model bias is 11% and 7% for QGSJETII-04 and EPOS-LHC. Their respective offset is 7% at $\theta = 38°$. Irrespective of hadronic model, primary differences in R_μ are 0.14 and 0.25 at $\theta = 0°$ and $\theta = 38°$ respectively. The reduced difference in mass composition is expected to result from the increased number of stations with muon information. Figure 7.17c shows a clear energy dependent bias for iron showers. They increase from 5% to 30% between 10^{18} eV and 10^{20} eV respectively. These biases are introduced from high energetic vertical showers (seen in figure C.16). Within this phase-space, proton showers have a lower reconstruction efficiency (figure 7.15). These biases may be introduced through *bad fits*, necessitating a detailed study on quality cuts (analogous to reference [44]) or an alternative reconstruction procedure.

The resolution of the muon content is $\approx$ 10% for proton showers, averaged over the zenith range (seen in 7.17d). The resolution for iron showers is 5% at 10^{18} eV, increasing to 13% at 10^{20} eV. Its decrease in resolution is correlated to the bias found in figure 7.17d and could be resolved with the quality cut (or new reconstruction procedure). In figure 7.17b, iron showers improve their resolution from 14% to 6% between 0° and 38°, whereas proton showers remain constant between 8% and 10%. Hadronic model differences are less than 2%. In comparison with WCD, proton showers are equivalent, whereas iron showers under-perform by about 8%. Contrary to WCD, the resolution of R_μ of MD reconstructions improves with inclined showers. A combined reconstruction could therefore benefit from

their respective performance[9].

In figures 7.18, novel $X^{\mu}_{\max}$ results through MD universality reconstructions are presented for energies above 10^{18} eV (i.e. above 90% reconstruction efficiency). Figure 7.18c shows different energy dependent biases between proton and iron showers. Above 10^{18} eV, iron showers yield an offset of $-50\,\mathrm{gcm}^{-2}$, whereas proton showers gradually reduce from $0\,\mathrm{gcm}^{-2}$ to $-50\ \mathrm{gcm}^{-2}$ with decreasing energy. This may be associated to the increased trace width of iron induced showers, benefiting the shape fit (by including more bins into the fit). Figure 7.18a illustrate a stronger zenith dependency for proton showers compared to iron showers. Most notably, proton and iron showers differ as much as $75\ \mathrm{gcm}^{-2}$ for inclined showers, indicating that the maximum muon production depth from MD becomes less reliable. Note, however, $X^{\mu}_{\max}$ is obtained from the time information of the 1-Bit and integrator counting strategy. A detailed analysis for their respective $X^{\mu}_{\max}$ resolution would greatly benefit the understanding of the biases seen here. In comparison, the maximum muon production depth obtained from WCD data (see figure 7.18e and reference [105]) yields an average bias of about $20\ \mathrm{gcm}^{-2}$ with primary and hadronic model differences. In this work, no hadronic model differences are present.

In figure 7.18b, the $X^{\mu}_{\max}$ resolution increases moderately with increasing inclination from $35\,\mathrm{gcm}^{-2}$ to $55\,\mathrm{gcm}^{-2}$. Hadronic model and primary dependencies are within $5\,\mathrm{gcm}^{-2}$. Below $10^{18.5}$ eV, the resolution exceeds the $50\,\mathrm{gcm}^{-2}$ limit. Nevertheless, the resolution seen in figure 7.18d exceeds those seen through alternative analyses (reference [105]) in 7.18f. Nevertheless, $X^{\mu}_{\max}$ resolutions do not outperform those seen by the WCD for $X_{\max}$. This is expected as the concept of universality holds more validity for the electromagnetic longitudinal profile (the muonic profile is quasi-universal - see chapter 3). More detailed figures on the energy-zenith bin of showers are presented in C.19 and C.18.

[9]Note, as previously discussed, the quality of the *shape* improves with vertical showers, whereas R_{μ} improves for inclined showers.

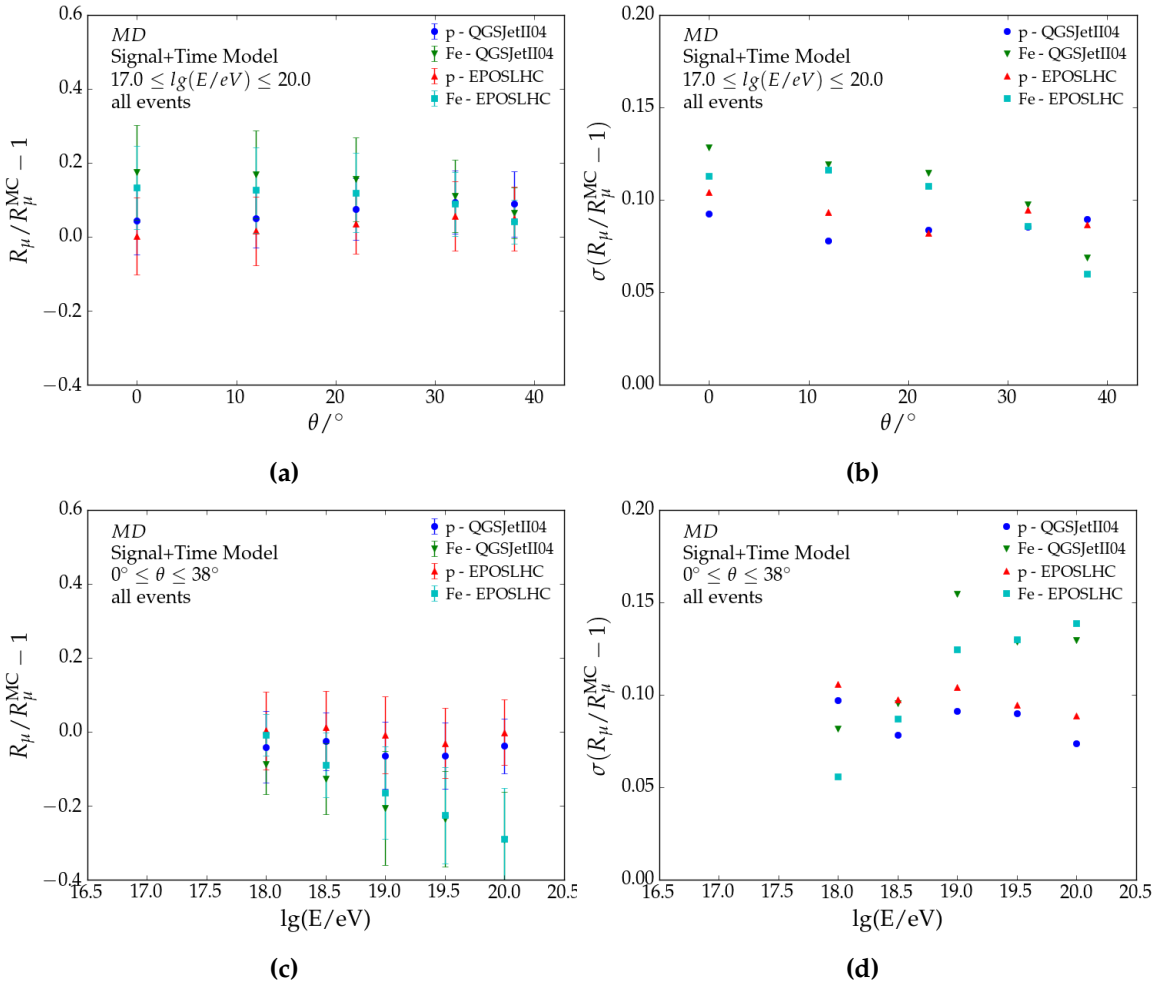

Figure 7.17: *Top:* R_μ **a)** bias and **b)** resolution with respect to shower zenith. *Bottom:* R_μ **c)** bias and **d)** resolution with respect to energy.

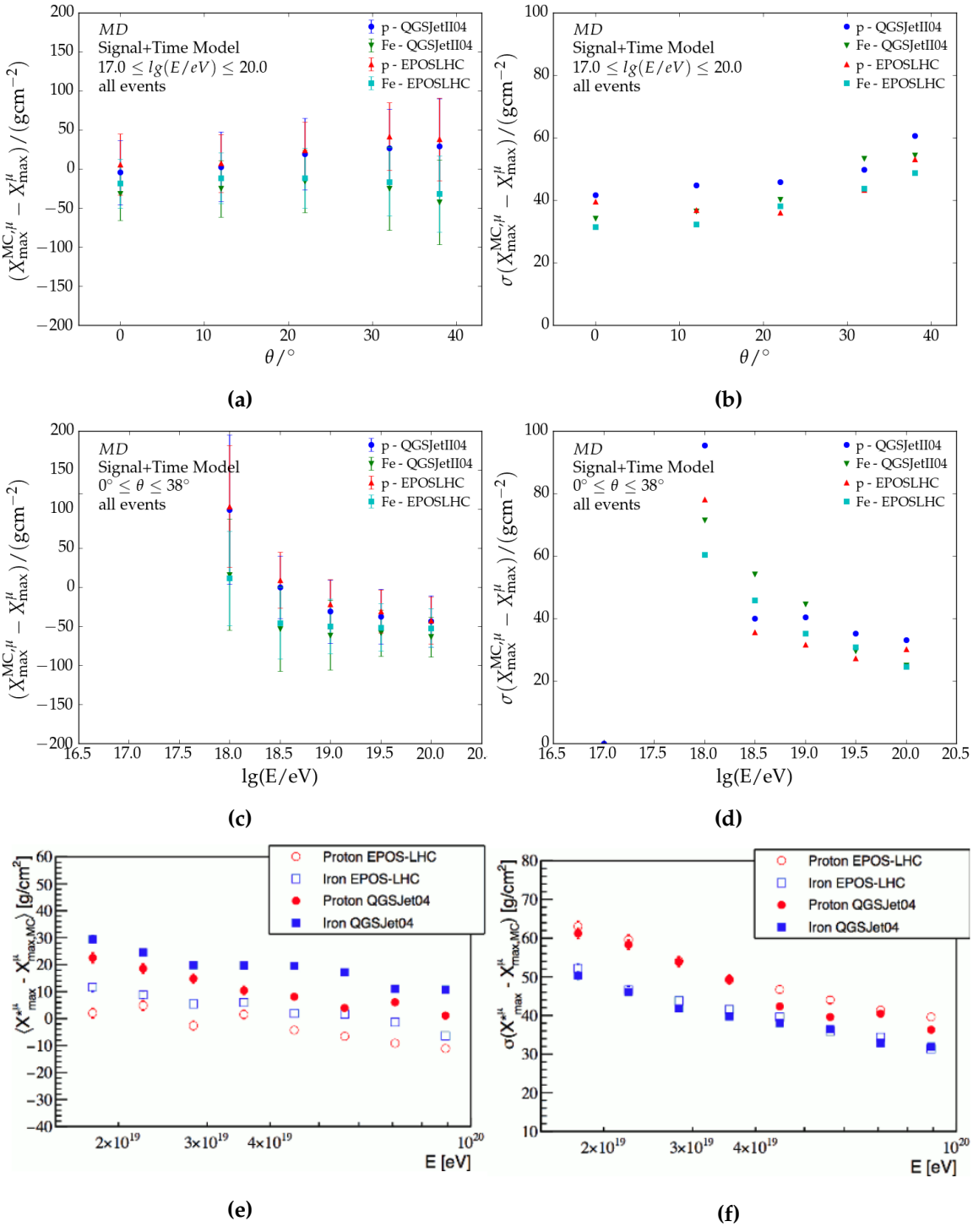

Figure 7.18: *Top:* $X^{\mu}_{\max}$ **a)** bias and **b)** resolution with respect to shower zenith. *Middle:* $X^{\mu}_{\max}$ **c)** bias and **d)** resolution with respect to energy. *Bottom:* $X^{\mu}_{\max}$ **e)** bias and **e)** resolution with respect to energy from *MPD reconstructions* with WCD data [105].

7.3 Hybrid Reconstruction

The performance of the hybrid reconstruction is limited by the performance of its weakest link. Here, the limitations imposed by the MD. Hybrid reconstructions are not capable of reconstructing showers above $\theta = 56°$. As in section 7.2, we limit ourselves to events below 48° for reconstructions using only signal size information (38° for those including time information). The hybrid reconstruction procedure shown in 6.4 has been designed to account for the additional muon information and reduced energy resolution from MD. The results presented here include showers from energy-zenith bins where the reconstruction efficiency is above 90% (unless stated otherwise).

7.3.1 Signal Model

Figures 7.19a and 7.19c reiterate the better reconstruction efficiencies for iron showers (previously seen in figure 7.10), irrespective of hadronic model. Note, ϵ_{rec} is lower compared to those seen for MD-only reconstructions (>80% with respect to >60% here). The decreased efficiency implies (as was suggested in section 7.2) that many successful MD LDF fits reconstructed an incorrect energy E, caused by the relatively high saturated detectors. With WCD information, the reconstructed energy is in contradiction, resulting in an unsuccessful fit. In terms of mass composition, this introduces a bias towards heavier elements for 27% of all events. Alternative reconstruction procedures may improve the efficiency on a percentage level. However, since the structures in figure 7.19 originate from shower physics and detector limitations, it should be accounted for in subsequent mass composition or spectrum analyses.

Figure 7.20a provides an illustration on the spread of shower cores for different primaries and hadronic models. Their bias is below 2 m. The core resolution is very similar to the one obtained from WCD-only reconstruction. Figures 7.20c and 7.20d show results from the hybrid core resolution with respect to previous universality studies and standard reconstruction [81]. Between 10^{19} eV and 10^{20} eV, the core resolution obtained in this work is better by 5 m (60%) and 7 m (85%) for the old universality and standard reconstruction respectively. At $10^{18.5}$ eV, the core resolution in this work is almost better by a factor 2.

The energy dependency of the angular resolution could not be further improved with the hybrid setup, plateauing at 0.5° above 10^{19} eV (see figure 7.21b). The zenith dependency of the angular resolution is mostly consistent with results in figures 7.2a and 7.11a. However, below 20°, the angular resolution for proton showers increases from 0.8° to 1°. The increase is independent of hadronic model. It is related to the low reconstruction efficiency, ϵ_{rec}, previously shown in 7.19. No biases in θ or ψ were found.

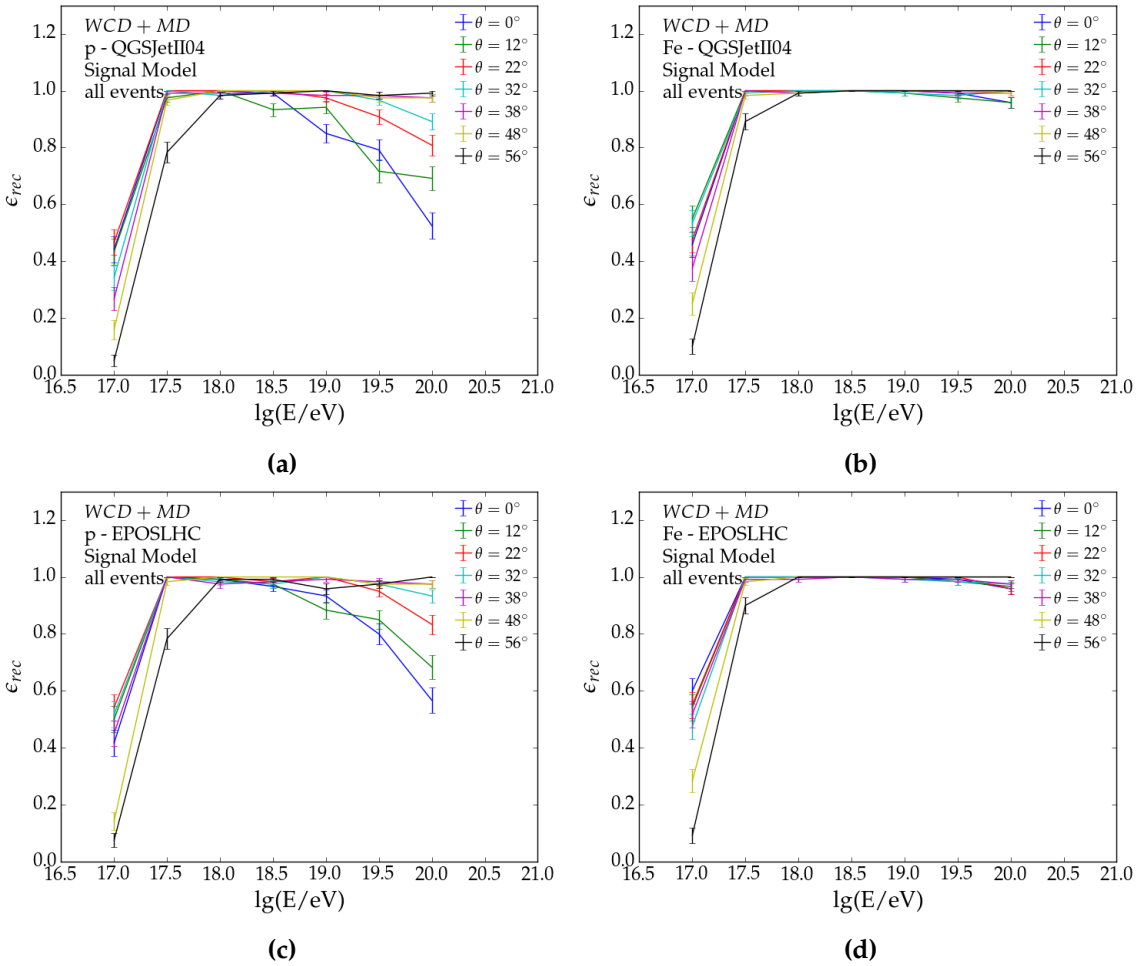

Figure 7.19: Fit efficiency for successful hybrid reconstructions of **a)** proton and **b)** iron induced air showers. Each energy-zenith bin accounts for 120 air showers. *Top*: QGSJETII-04 *Bottom*: EPOS-LHC.

By first limiting only to WCD for the energy reconstruction, its bias and resolution could be improved compared to results from the MD reconstruction. No primary biases are found, whereas hadronic model biases for EPOS-LHC are at the 10% level without any zenith dependencies (see figure 7.22a). Figure 7.22c shows that there is also no energy dependency. Again, EPOS-LHC is offset by 10% for all energies. These are encouraging results as the current reconstruction method minimizes energy biases previously seen in figures 7.13.

Energy resolutions from MD are as large as 40% (depending on shower energy and zenith). In the hybrid configuration, these have been reduced to below 20% (QGSJETII-04 iron showers are below 10% above 10^{18} eV). This is an expected improvement from the reconstruction procedure. A detailed comparison between figures 7.22c and 7.4a indicates that the energy resolution from WCD-only reconstruction is better by about 2 percentage points for proton induced air showers. Energy resolutions for iron showers are consistent with those from WCD-only reconstructions.

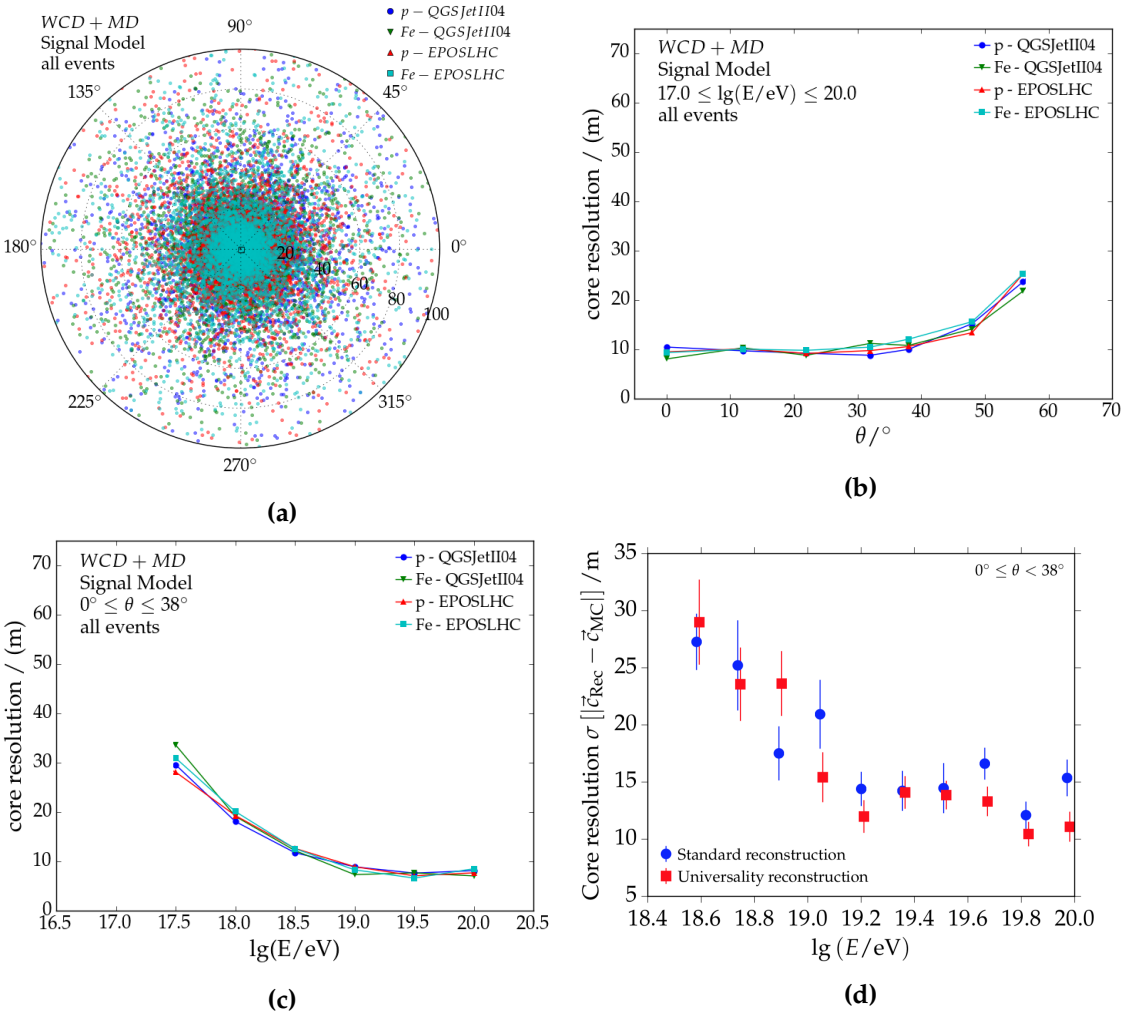

Figure 7.20: a) Distribution of the distance between the reconstructed core positions and its MC true value for all proton/iron showers from QGSJETII-04/EPOS-LHC. The resolution of the reconstructed core position as a function of **b)** energy and **c)** zenith. **d)** Core resolution from the standard and *old* universality reconstruction [81].

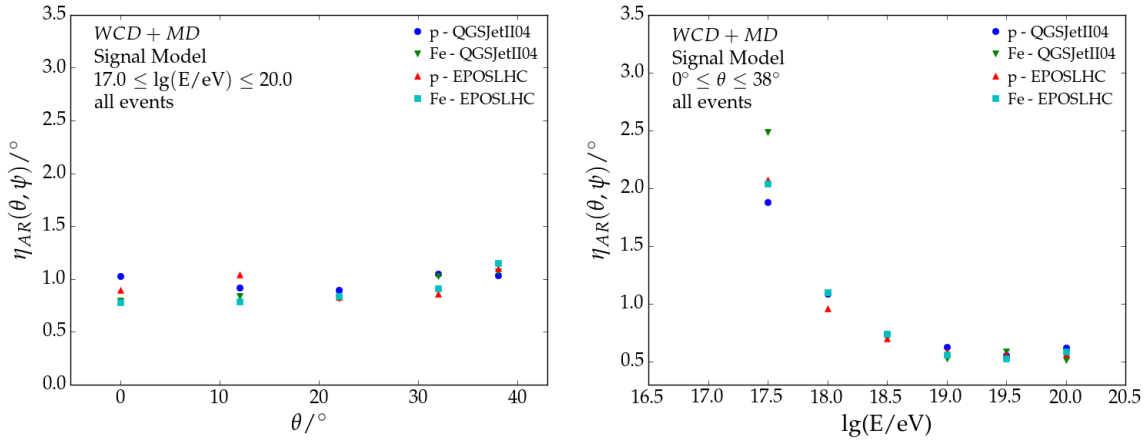

(a) **(b)**

Figure 7.21: Angular resolution $\eta_{AR}(\theta, \psi)$ of reconstructed showers with different primaries and hadronic models. Information on the signal size of the WCD and MD are used in the reconstruction.

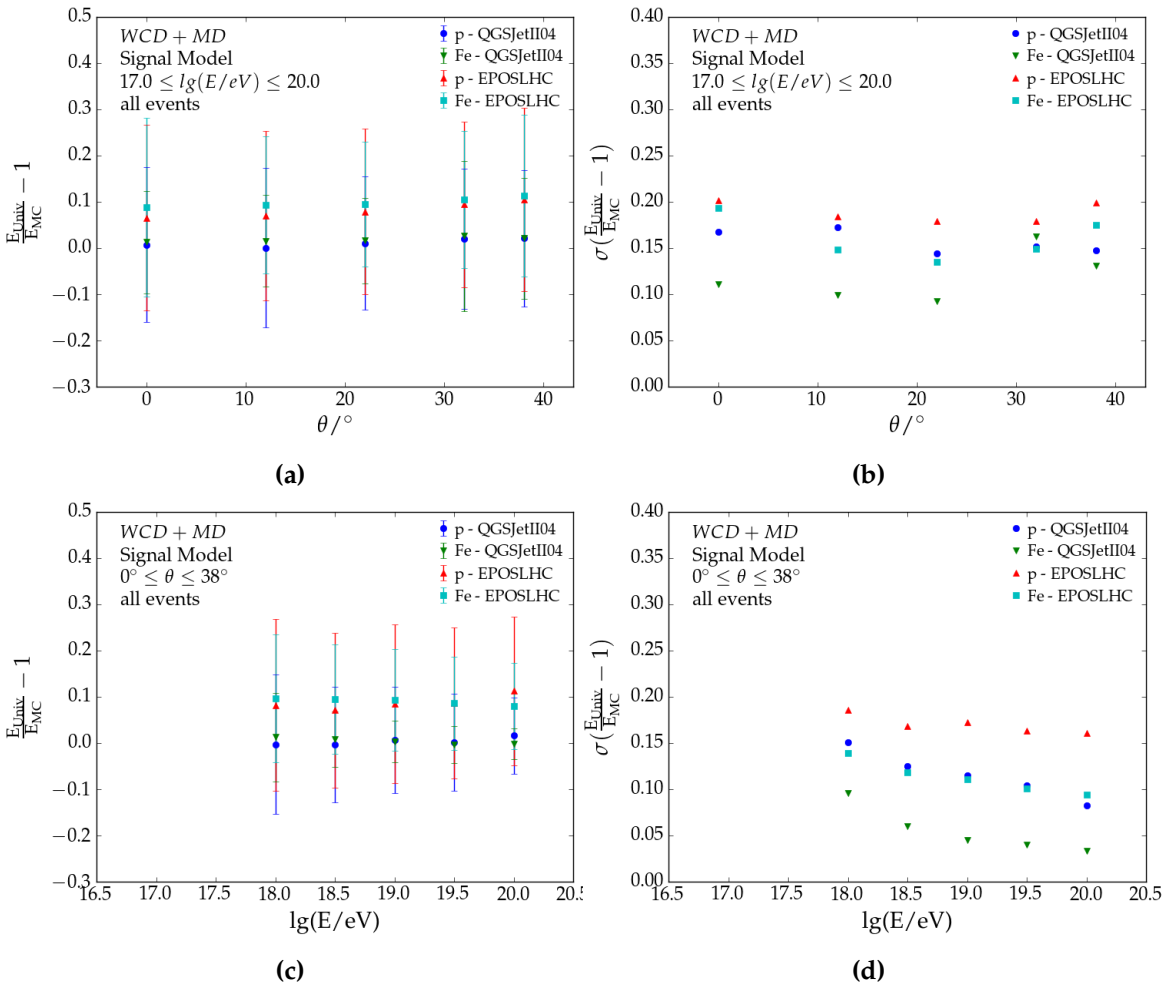

(a) **(b)**

(c) **(d)**

Figure 7.22: Energy bias (*Left*) and resolution (*Right*) with respect to true shower **Top)** zenith and **Bottom)** energy.

Figures 7.23a and 7.23c show that for QGSJETII-04, biases of R_μ are within the 2% level. Showers produced with EPOS-LHC are offset by 10%, which can be corrected for. The resolutions in figures 7.23b and 7.23d reveal an unprecedented result. Note, R_μ resolutions below 0.2 were classified as *good*. Analysis by [44], previously shown in figure 7.8e, exceeded 0.15 at $10^{19.4}$ eV and $10^{18.9}$ eV for proton and iron showers. The analysis in [44] also showed a decreasing resolution with increasing energy. These features are not present in this work. The absence of energy and zenith dependency (in figures 7.23b and 7.23d) implies that the current Universality models account the energy dependency in the shower development better. Resolutions are generally worse for EPOS-LHC showers and are attributed to intrinsic differences to QGSJETII-04. Nevertheless, it is also an improvement to [44]. Findings in figure 7.23 also resolve the long-standing problem of the degeneracy seen in R_μ (discussed in section 6.3 and [44, 59, 65, 81]). Finally, in terms of mass composition, R_μ has become a more sensitive parameter with a merit factor of 3.4 at $10^{18.5}$ eV[10].

The figures in 7.24 provide a detailed picture on the bias and resolution for every energy-zenith bin. The x-y axis reflect the CORSIKA shower library. Each colored circle reveals its respective bias or resolution of ideally 120 showers. Energy-zenith bins below the 90% reconstruction efficiency are included but shaded with dashed lines. The benefit of these figures is that is provides a two dimensional illustration on the R_μ, revealing pattern which are generally washed away in profile plots such as in 7.23. Results in 7.24 apply to showers from QGSJETII-04. Those for EPOS-LHC are included in the Appendix C.20.

Biases for iron showers depicted in figure 7.24c yield small energy or zenith dependencies. Proton showers (figure 7.24a) are less independent, indicating an underestimation of vertical high energy proton showers and overestimation for inclined lower energy showers. These biases are mostly within the 5%. Resolutions shown in figures 7.24b and 7.24d, show no energy or zenith dependencies for proton showers. For iron showers, a minor zenith dependency is present at the 3% level. As these biases and resolutions are small, they do not need to be further addressed in subsequent analyses.

[10] without taking the energy uncertainty into account

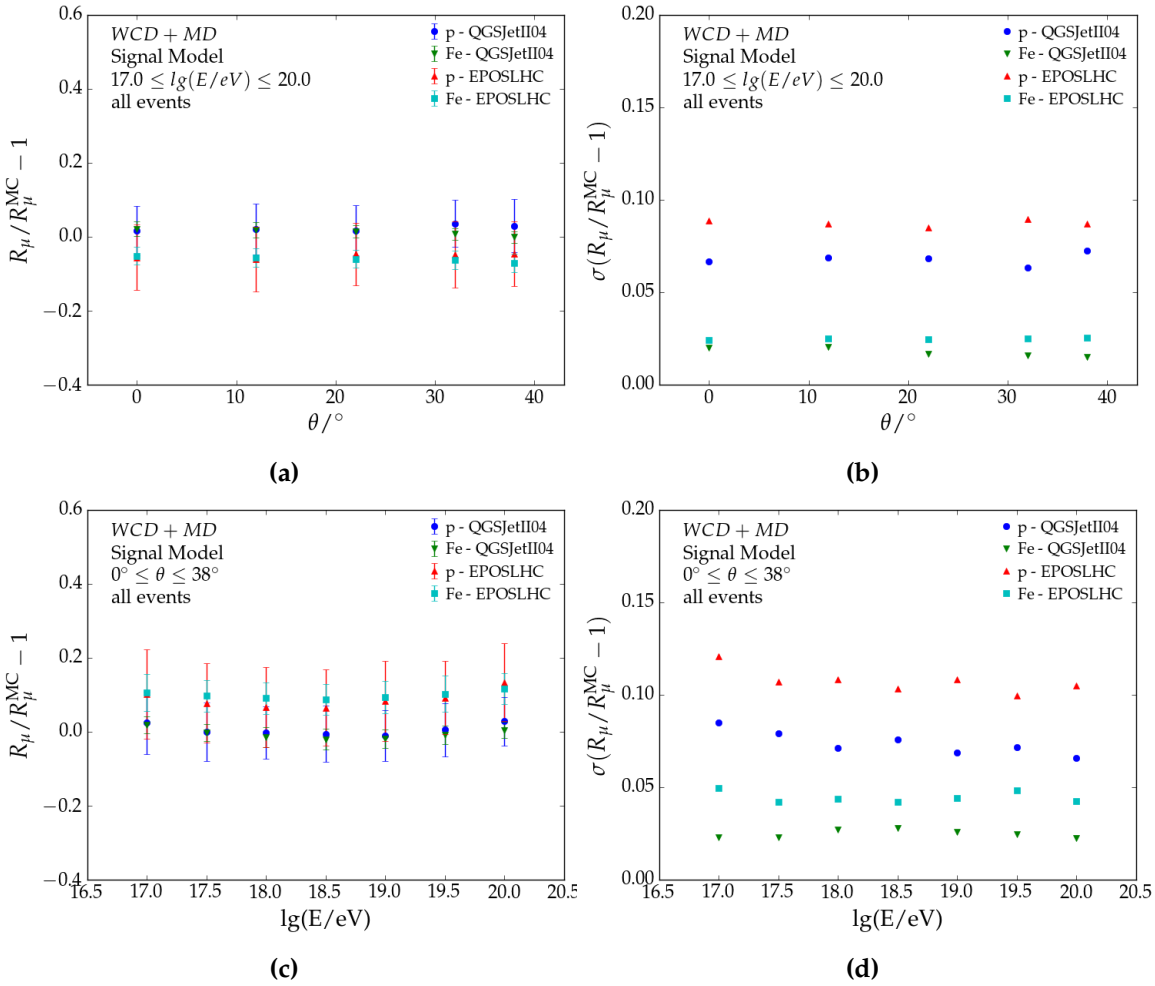

Figure 7.23: *Top:* R_μ **a)** bias and **b)** resolution with respect to shower zenith. *Bottom:* R_μ **c)** bias and **d)** resolution with respect to energy.

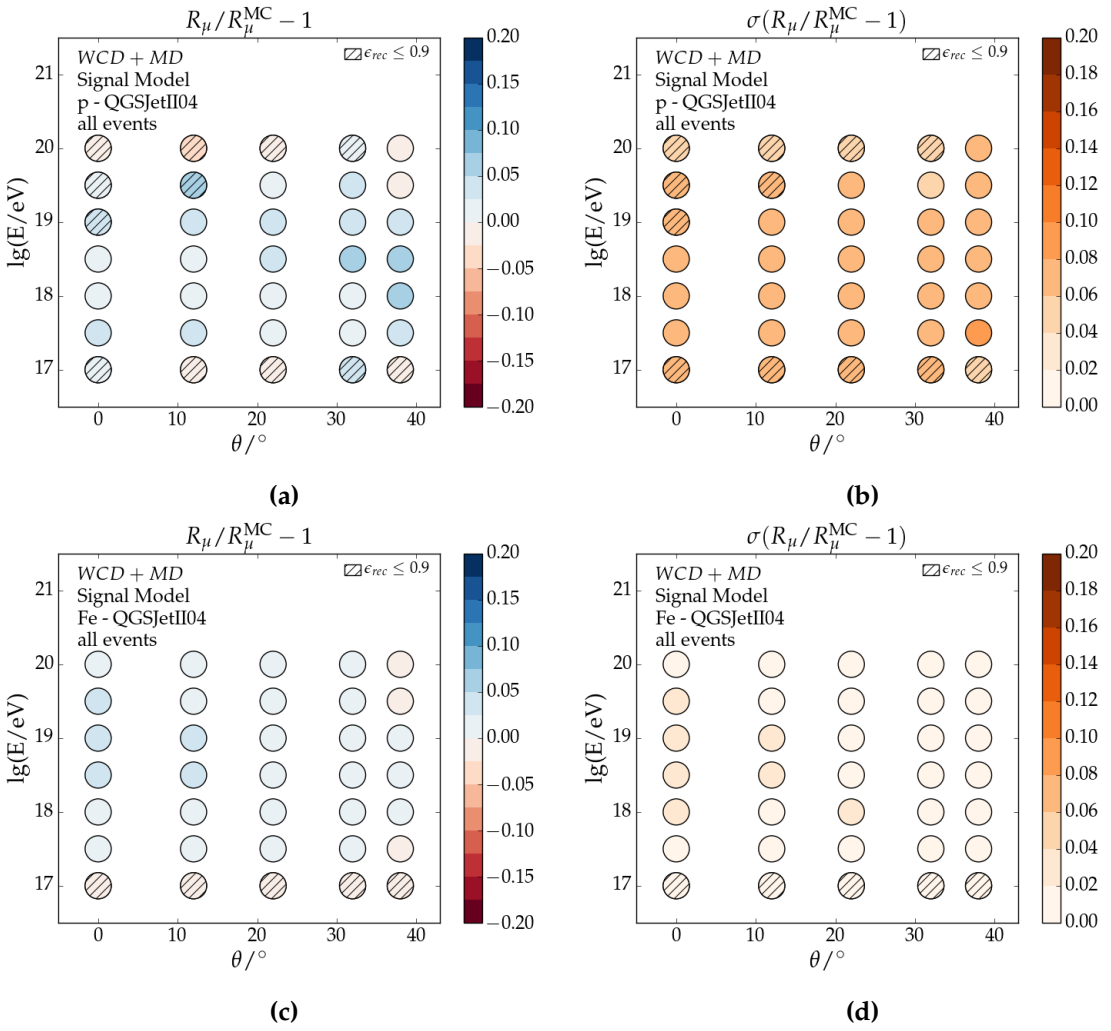

Figure 7.24: *Top:* R_μ **a)** bias and **b)** resolution for every energy-zenith bin of proton showers. *Bottom:* R_μ **c)** bias and **d)** resolution for energy-zenith bins of iron showers. Showers are simulated with QGSJETII-04. Striped circles indicate a fit reconstruction efficiency below 90%.

7.3.2 Signal and Time Model

Hybrid reconstructions using time and signal size information are limited by the phase space of MDs. Results are therefore limited to showers with zenith below $\theta = 38°$. For more inclined showers, only information from the WCD can be employed.
The reconstruction efficiencies are nearly equivalent to those seen in figure 7.19. This implies that the time reconstruction is almost fully efficient after a successful LDF fit. A notable difference between figures 7.19 and 7.25 is the small decrease in the efficiency for iron showers at 10^{20} eV. They are expected to derive biases seen in MD-only reconstructions (figure 7.17c). Nevertheless, their efficiencies are above 95%.

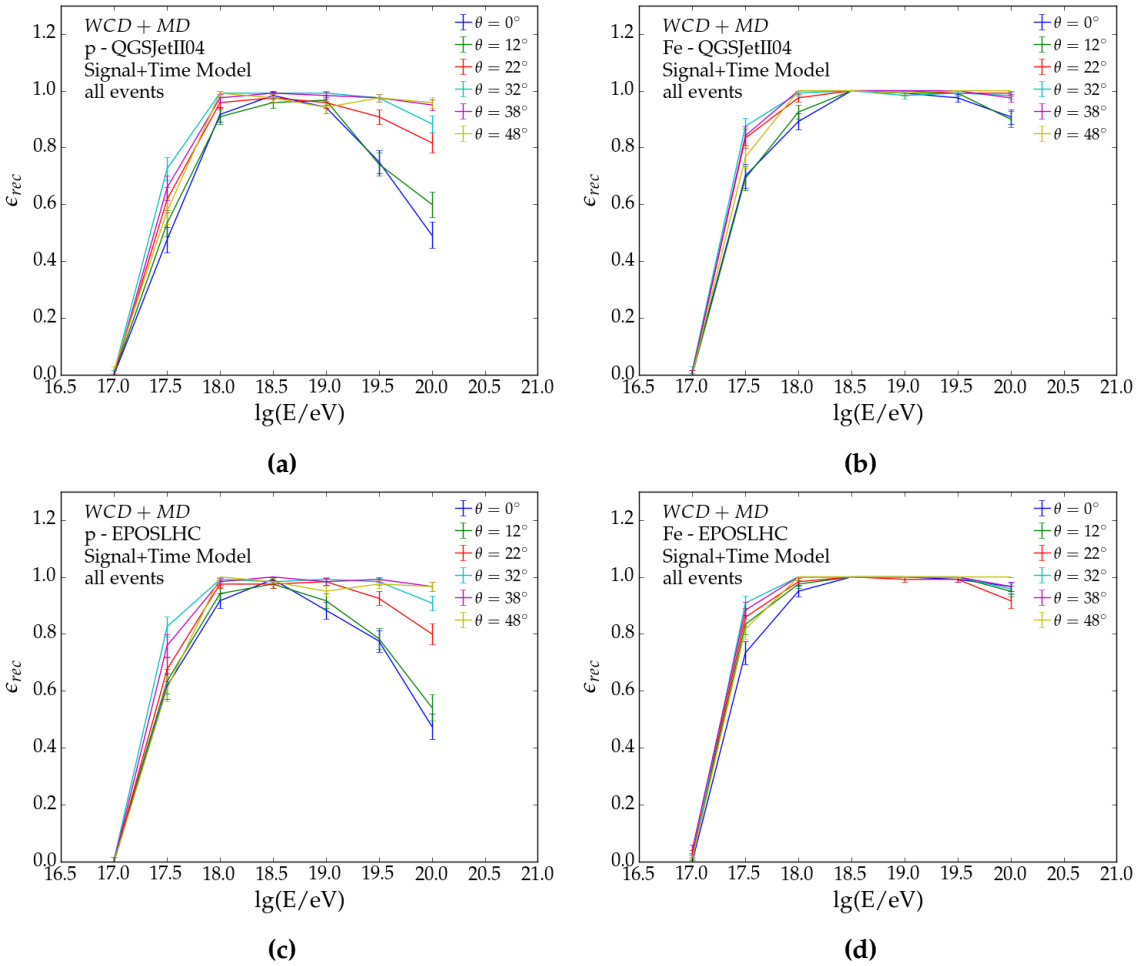

Figure 7.25: Fit efficiency for successful hybrid reconstructions of **a)** proton and **b)** iron induced air showers using signal size and time information in the detector. Each energy-zenith bin accounts for 120 air showers. *Top*: QGSJETII-04 *Bottom*: EPOS-LHC.

Reconstructions have shown an improved bias and core resolution with respect to WCD-only and MD-only reconstructions. Core biases are all below 1 m. Compared to resolutions seen in figure 7.20d, they have improved by a factor 2. They are 5 m for the highest energies, increasing to 7 m and 12 m at $10^{18.5}$ eV and 10^{18} eV respectively. Note, the core resolution seen at 10^{18} eV is better than the lowest resolution seen in 7.20d. The improved core resolution is partially attributed to the increased station number in the infilled grid. However, this contribution is limited by their signal variances (equations (6.3) and (6.4)) - i.e. the quality of the signal. At its best, the resolution in this work is 5 m, whereas it is 12 m in reference [81]. This suggests that the shower geometry in this work is described more refined.

Biases in θ and ψ remain unchanged. However, the angular resolution has improved significantly with the addition of time information. The profile figures in 7.27 show the average angular resolution to be about $\approx 0.6°$ ($\approx 1°$ before), irrespective of shower zenith. The angular resolution is 0.5° above 10^{19} eV and increases to 1° at 10^{18} eV. This is in agreement with angular resolutions previously seen by WCD-only reconstructions.

A notable improvement with the energy parameter is the 2% decrease in resolution for all primaries and hadronic models. A comparison between figure C.21 and 7.7b shows that the most significant feature is the smaller difference between hadronic models. Due to the

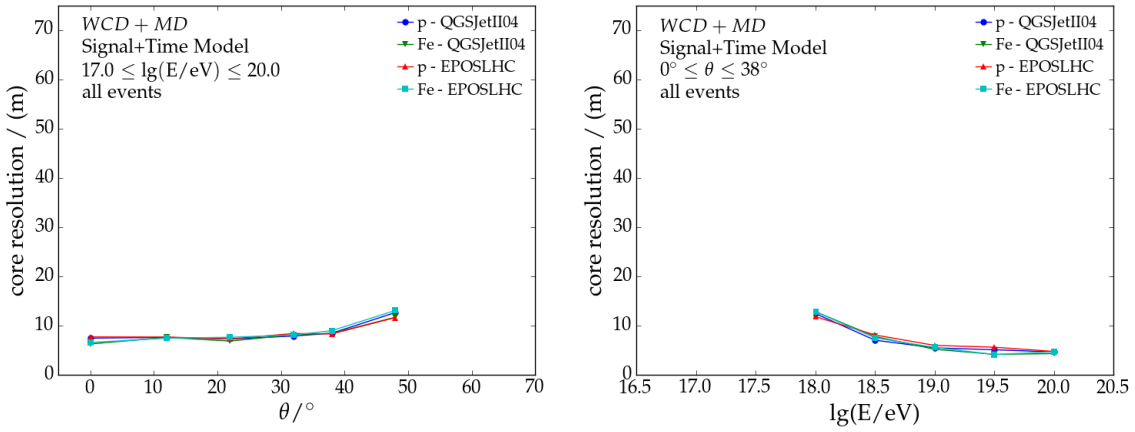

(a) **(b)**

Figure 7.26: The resolution of the reconstructed core position as a function of **a)** energy and **b)** zenith. Information on the signal size and time structure of the WCD and MD are used in the reconstruction.

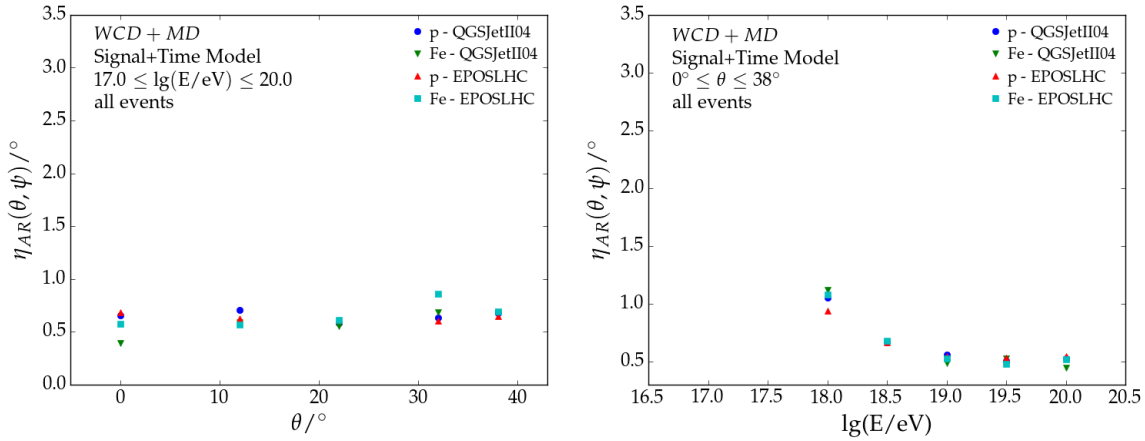

(a) **(b)**

Figure 7.27: Angular resolution $\eta_{AR}(\theta, \psi)$ of reconstructed showers with different primaries and hadronic models. Information on the signal size and time structure of the WCD and MD are used in the reconstruction.

complexity of the reconstruction, this feature could not be fully understood.

In figures 7.23 only hadronic model biases were found without any primary dependencies. This has changed in figures 7.28a and 7.28c where QGSJETII-04 and EPOS-LHC are found to be offset by 10% and 7% (averaged over all energies). No zenith dependencies are seen. However, as figure 7.28c indicates, the muon content is underestimated with decreasing energy. Differences in R_μ between proton and iron showers are about 0.1 and do not change with respect to energy or zenith. The structures found in the biases can be corrected for. However, the increased proton-iron difference reduces the mass discrimination power of R_μ. In terms of merit factor, it reduces from 3.4 to 2.5 (assuming no further changes to its resolution). This results from the $X_{\max}$ reconstruction[11]. Hybrid reconstructions account-

[11] $X_{\max}$ changes yield a different perceived shower stage at the detector, which alters the expected particle number (assuming the energy remains constant).

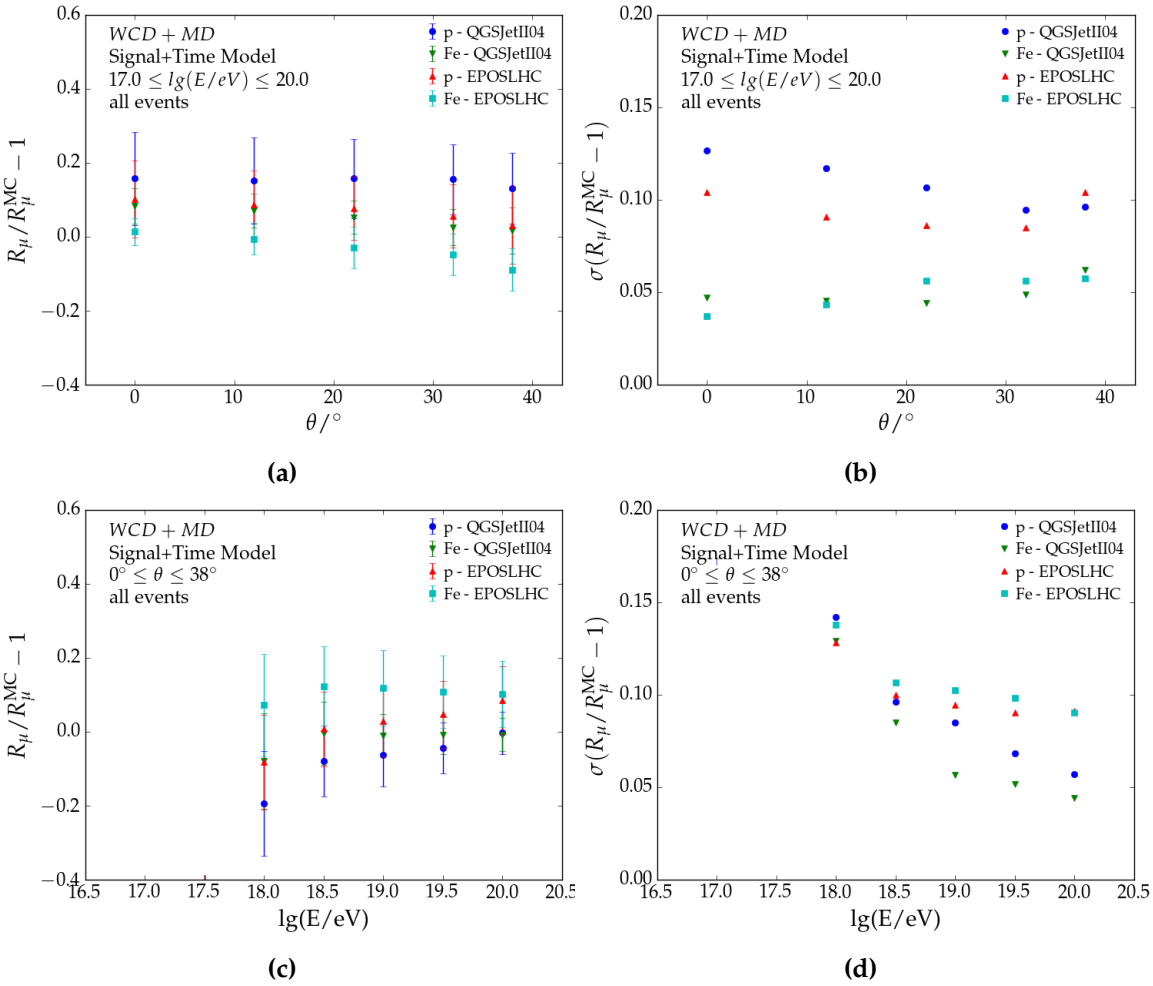

Figure 7.28: *Top:* R_μ **a)** bias and **b)** resolution with respect to shower zenith. *Bottom:* R_μ **c)** bias and **d)** resolution with respect to energy.

ing only the signal size use the $X_{\max}$ estimator, yielding an energy and zenith independent R_μ.

The resolution of the muon content in figures 7.28b and 7.28d also performs poorly compared to those seen in 7.23. Most notably, now, the muon content resolution increases with increasing energy (as in figure 7.8e). Furthermore, a minor zenith dependency is seen. Muon content resolutions worsen for iron showers (from 0.04 to 0.06), whereas they improve for proton showers (from 0.12 to 0.1). These structures also arise due to the $X_{\max}$ reconstruction from the time model. Regardless, $\sigma(R_\mu)$ remains below the 0.20 limit and can thus be used for mass composition purposes. Accounting for the biases and resolutions, the merit factor has decreased from 3.4 to 2.2 at $10^{18.5}$ eV. More elaborate results for every energy-zenith bin are shown in figure C.22 and C.23.

The core time t_{core}, maximum electromagnetic shower depth ($X_{\max}$) and maximum muon production depth ($X^{\mu}_{\max}$) are first reconstructed with WCD-only and MD-only detector information. They are subsequently reconstructed together to account for correlations between $X_{\max}$-$X^{\mu}_{\max}$ and their shared core time. As the figures in 7.29 show, hadronic model differences are below 5 gcm^{-2} for $X_{\max}$. Averaging over all zenith angles (figure 7.29c), primary differences are 25 gcm^{-2} for energies above $10^{18.5}$ eV with a sudden increase to 50 gcm^{-2} at 10^{18} eV. Figure 7.30a and 7.30c reveal this to be caused by a general overestimation (about

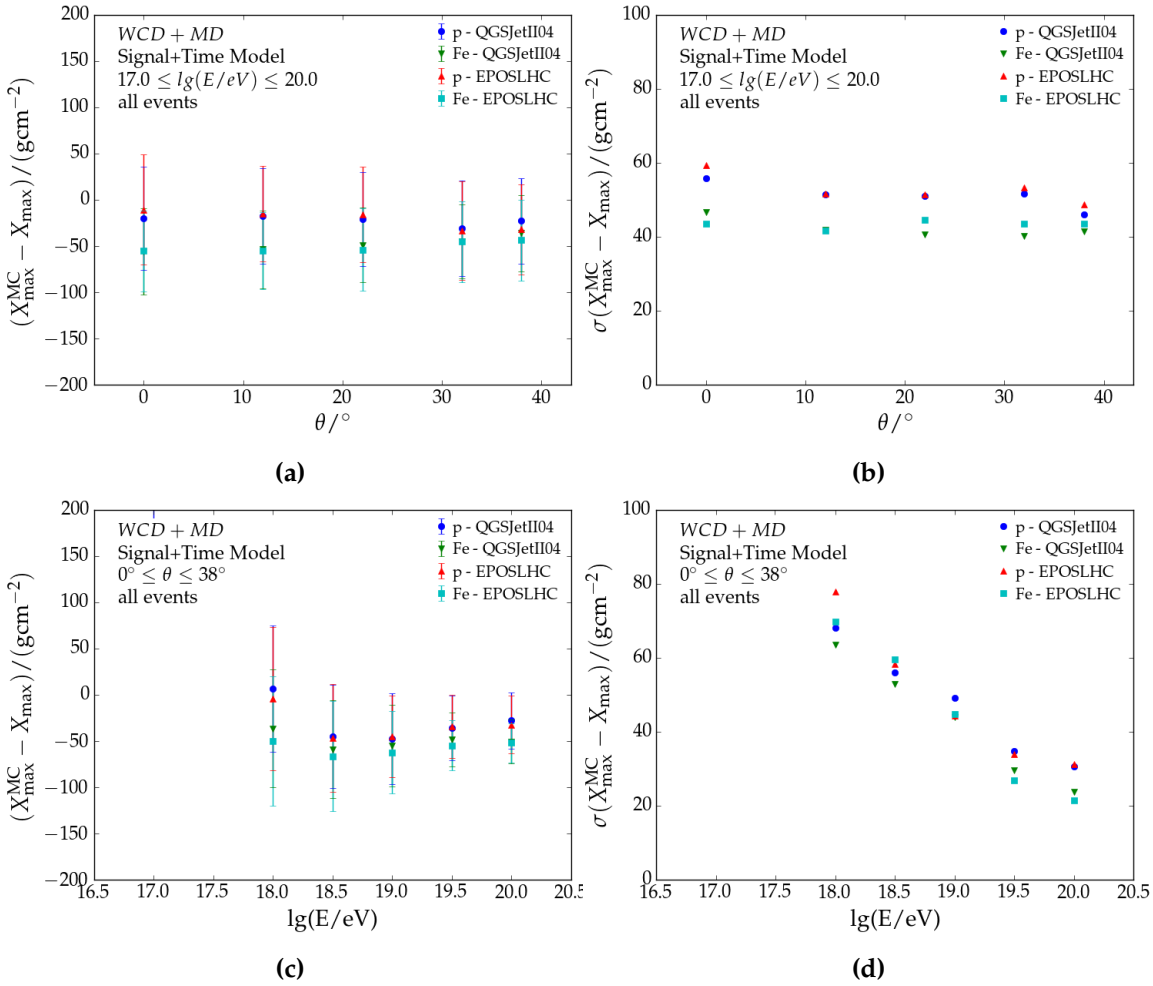

Figure 7.29: *Top:* $X_{\max}$ **a)** bias and **b)** resolution with respect to shower zenith. *Bottom:* $X_{\max}$ **c)** bias and **d)** resolution with respect to energy.

25 gcm^{-2}) of $X_{\max}$ in proton showers below $10^{18.5}$ eV. This is attributed to fewer saturated stations. The bias shows no zenith dependencies (figure 7.29a), whereas it reduces with increasing energy (figure 7.29c). Furthermore, the bias is minimal for QGSJETII-04 proton showers at 10^{18} eV, corresponding to the reference model and energy used in chapter 5. This may imply the need for more detailed time corrections.

The resolution of $X_{\max}$ is in agreement with respect to results from [44], seen in figure 7.9e. In figure 7.29d, the resolution exceeds 50 gcm^{-2} below $10^{18.7}$ eV, rending it useless for mass composition discrimination at low energies. In comparison to WCD-only reconstructions, the resolution has also increased from 50 gcm^{-2} to 70 gcm^{-2}. This is expected to originate form the combined fit of $X_{\max}$, $X^{\mu}_{\max}$ and t_{core}. More specifically, the reconstruction of the core time. A more refined study should facilitate a better understanding between $t^{\text{WCD+MD}}_{core}$ and $t^{\text{WCD/MD}}_{core}$, possibly revealing the origin to the poor resolution found in $X_{\max}$. Note, the poor resolution seen in figure 7.29d also correlates to the poor R_{μ} resolution seen in figure 7.28d.

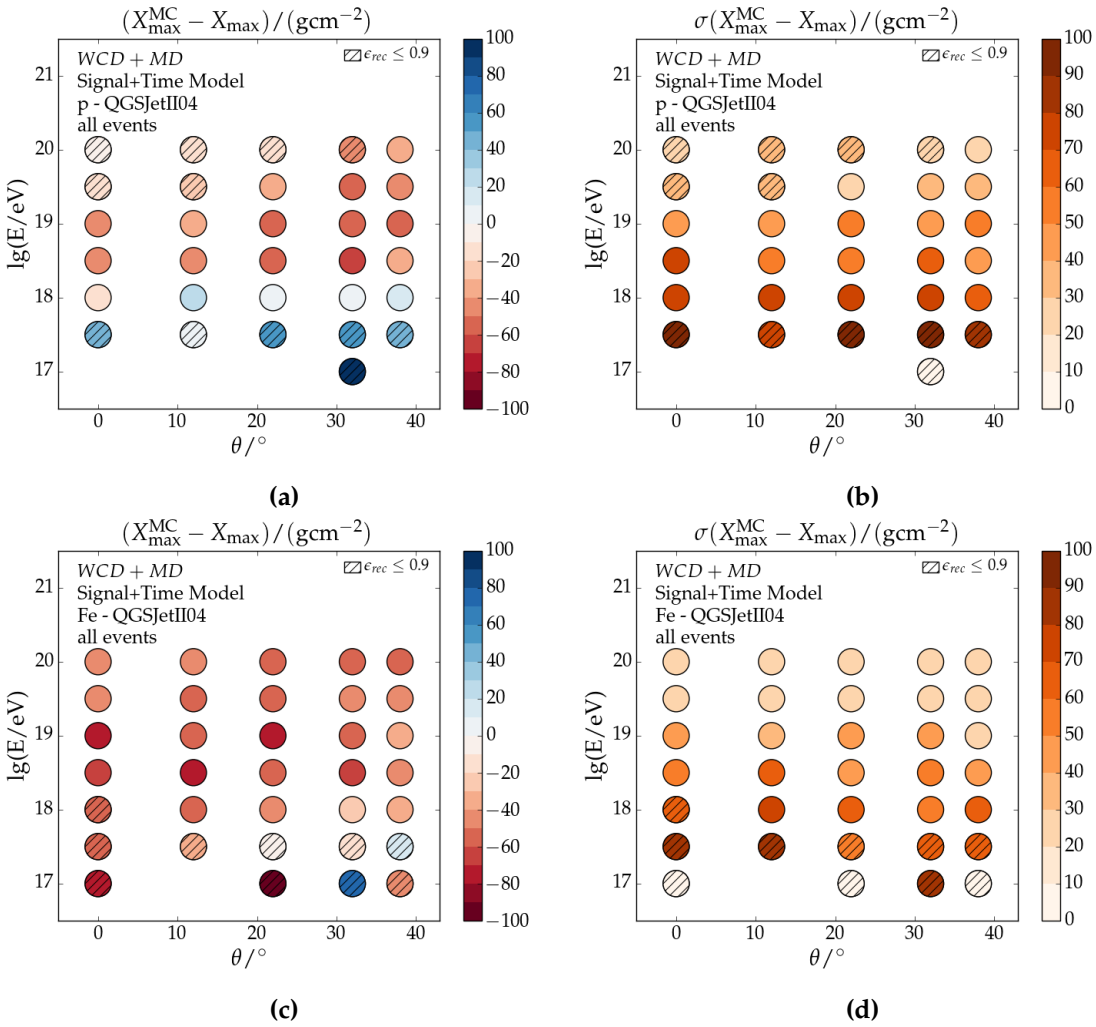

Figure 7.30: *Top:* X_{max} **a)** bias and **b)** resolution for every energy-zenith bin of proton showers. *Bottom:* X_{max} **c)** bias and **d)** resolution for energy-zenith bins of iron showers. Showers are simulated with QGSJETII-04. Striped circles indicate a fit reconstruction efficiency below 90%. Equivalent figures for EPOS-LHC are in C.24.

In comparison to MD-only reconstructions, the X^{μ}_{max} bias for proton showers with respect to zenith (figure 7.31a) has shifted by 25 gcm^{-2}, whereas no changes are seen for iron showers. This is also reflected in figure 7.31c. This can be attributed to the saturation levels between WCD and MD. Above $10^{18.5}$ eV, saturated events are more likely to occur with MDs than WCD. Through the hybrid reconstruction a better description of t_{core} could be obtained, subsequently improving the bias for proton showers. This effect expected to be suppressed for iron showers, saturating more events at lower energies (see figures in C.1).

Figures 7.32a and 7.32c provide a detailed description of the bias for every energy-zenith bin. It shows a gradual decrease of the bias with increasing energy without strong zenith dependencies. Iron showers indicate a much steeper decrease as well as a stronger zenith dependency. They are most biased at 38°. This unique feature is not fully understood but is expected to originate from MD detector limitations.

The resolution seen in figures 7.31b and 7.31d are nearly equivalent to MD-only reconstructions. The most distinct feature is a larger X^{μ}_{max} resolution for proton showers -between 5 gcm^{-2} and 10 gcm^{-2}. The resolution is smallest for the highest energies, exceeding 50 gcm^{-2}

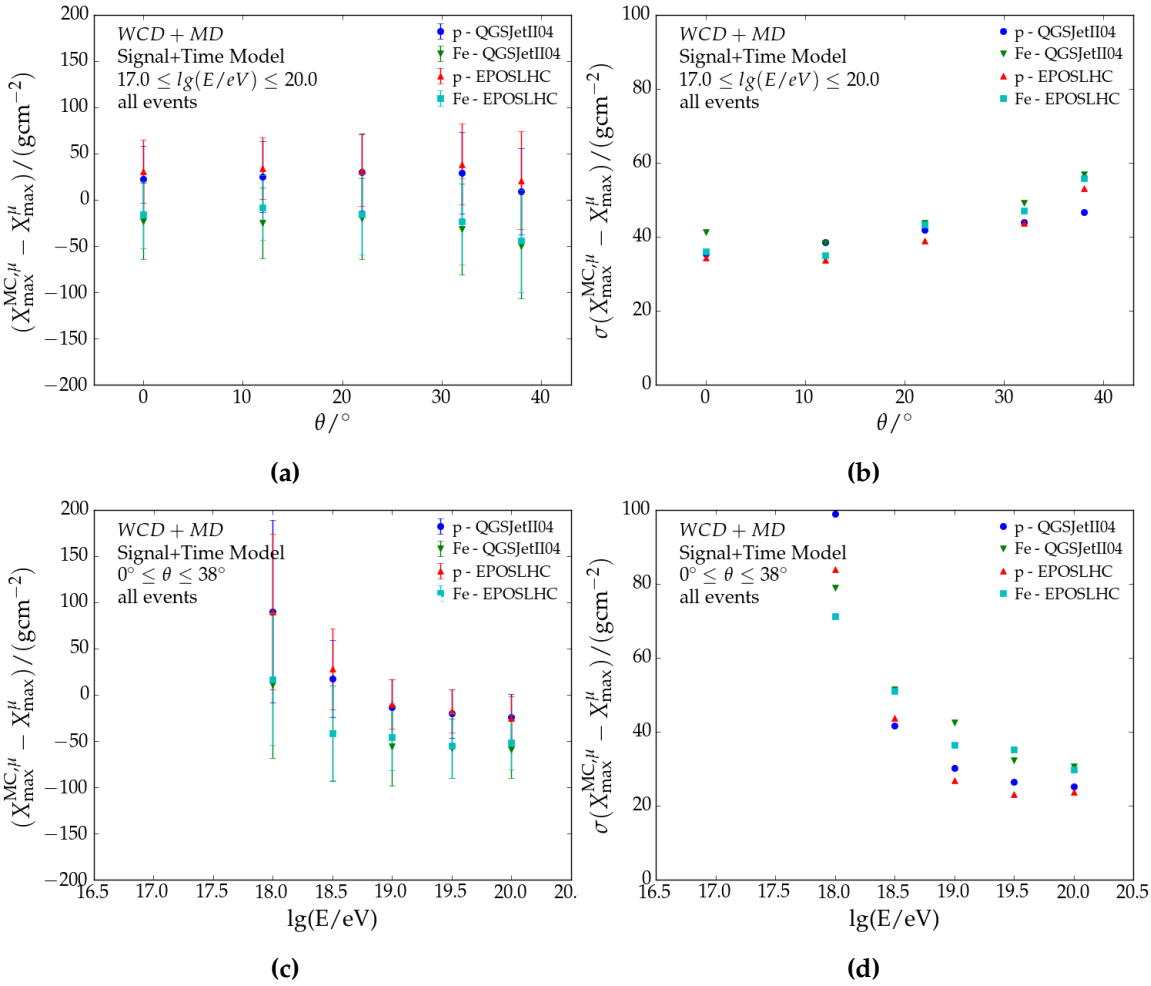

Figure 7.31: *Top:* X^{μ}_{max} **a)** bias and **b)** resolution with respect to shower zenith. *Bottom:* X^{μ}_{max} **c)** bias and **d)** resolution with respect to energy.

below $10^{18.5}$ eV.

Figures 7.32b and 7.32d show that the most dominant feature is the decreasing resolution with energy. A second order feature is the poor resolution for low energy showers (most emphasized by iron showers). This results from the decreased quality of the trace shape - an expected feature for low energy inclined showers.

The near equivalent performance for X^{μ}_{max}, yet decrease in X_{max} may suggest a bias towards the MD-part in the hybrid reconstruction. Note, the MD includes the 1-Bit and integrator counting strategy; i.e. more data points to include in the minimization. Also, the signal variance for each time bin is a first order estimate (as well as for the WCD). As discussed in chapter 6, a more detailed study on the likelihood and their variances should resolve this. Alternatively, the iterative reconstruction procedure could be modified by removing the combined X_{max}-X^{μ}_{max} fit (step 5 in 6.4).

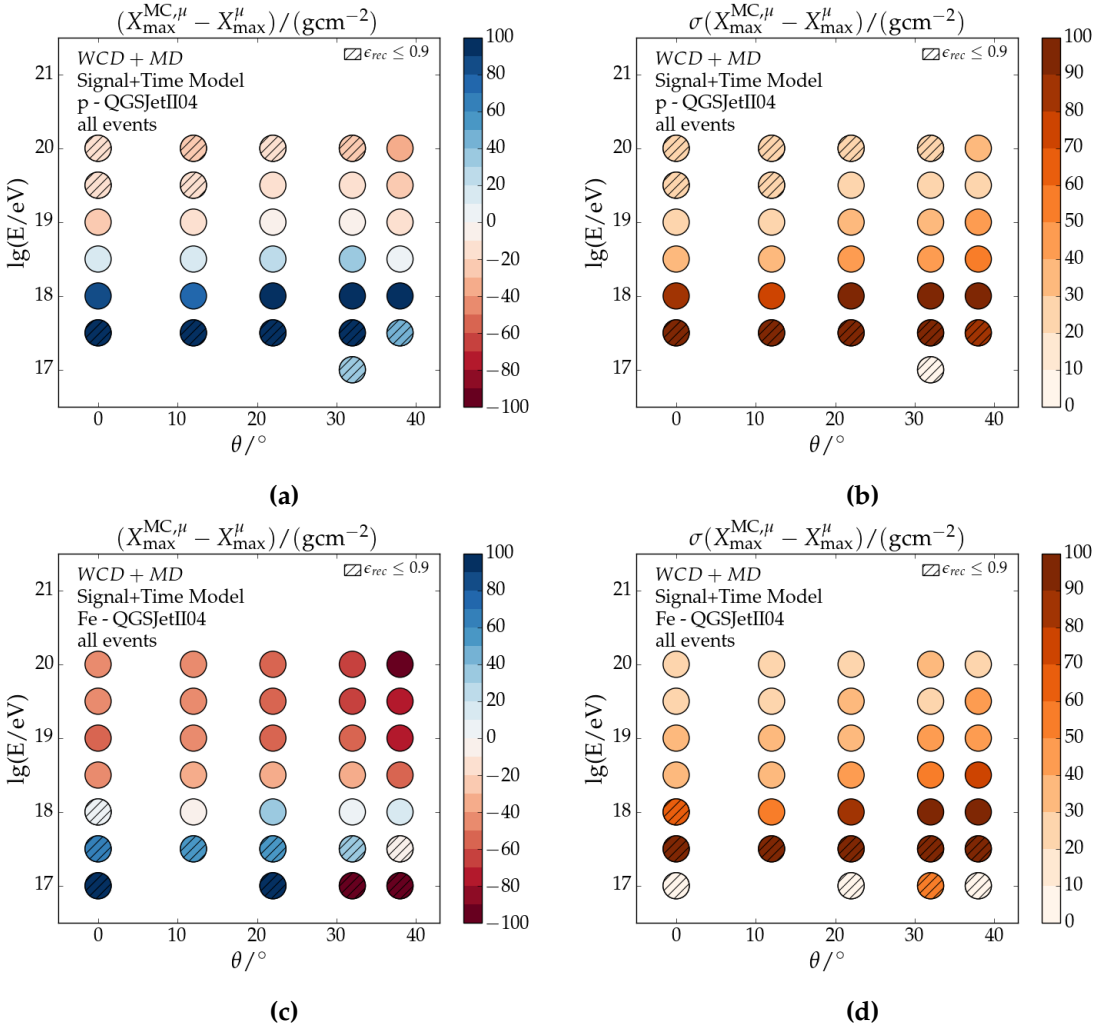

Figure 7.32: *Top:* X^{μ}_{max} **a)** bias and **b)** resolution for every energy-zenith bin of proton showers. *Bottom:* X^{μ}_{max} **c)** bias and **d)** resolution for energy-zenith bins of iron showers. Showers are simulated with QGSJETII-04. Striped circles indicate a fit reconstruction efficiency below 90%. Equivalent figures for EPOS-LHC are in C.25.

7.4 Mass Composition

The shower parameters R_μ, X_{max} and X^{μ}_{max} are assessed with the *merit factor* (MF) to quantify their strength for mass composition purposes (here between proton and iron). It also serves as a first order analysis to quantify the implications of the biases and resolutions seen in previous sections for mass discrimination purposes. The merit factor (MF) is defined as

$$MF = \frac{|\mu_p - \mu_{Fe}|}{\sqrt{\sigma_p^2 + \sigma_{Fe}^2}}, \tag{7.2}$$

where μ_i refers to the mean of the parameter distribution and σ_i its resolution. A large merit factor indicates a strong separation power.

As the figures in 7.33 indicate, the merit factor is always higher for QGSJETII-04 (solid lines) than for EPOS-LHC (dashed lines). R_μ is most sensitive to mass composition with MFs above 3. Its separation power is also significantly higher compared to $N_\mu(600)$ from

reference [89], where the merit factor is 2 at 10^{18} eV. Figures 7.33a and 7.33b illustrate how the hybrid signal reconstruction outperforms the WCD-only and MD-only reconstruction. They also highlight the decreased performance of the hybrid reconstruction when signal and time information are used (discussed in 7.3).

The MF for $X_{\max}$ could only be obtained from WCD-only and hybrid reconstruction (accounting for signal and time). Figure 7.33c, as well as figure 7.33d, yield merit factors below 2. Furthermore, their MF is below 1 for energies below $10^{18.3}$ eV and $10^{18.8}$ eV for the hybrid and WCD-only reconstructions. This implies a poor discrimination power from $X_{\max}$ for the intended energy range of infilled array. Notably, the MF improves with increasing energy (due to the improved resolution).

X^{μ}_{max} has the poorest mass discriminating power, only exceeding 1 above $10^{19.5}$ eV. As with the WCD, its MD-only reconstruction outperforms the hybrid. It also improves with energy (as seen in figure 7.33e). Despite the poor merit factor, the result is promising as figures 7.33e and 7.33f also imply that the reconstruction performance is sensitive to how detector signal or timing information is used. Studies in [44] proved this to require an extensive analysis, which is anticipated to be performed in future work. Upon further optimizing the reconstruction method, a multi-variate shower parameter analysis will enhance the mass composition discrimination for universality reconstructions on a shower to shower basis.

7.5 Review and Outlook

In this chapter, six different universality reconstructions were performed. The aim is the development of a novel hybrid reconstruction combining WCD and MD data. A prototype iterative reconstruction method was developed to maximize the reconstruction efficiency and optimal information usage to derive the shower parameters. We briefly review the findings in this work and recommendations for future analyses.

WCD-only reconstructions have proven to be ineffective to extract R_{μ} without the aid of an estimator (section 6.3). The estimator is effective for fit stability. However, introduces large $\sigma_{R_{\mu}}$ resolutions. This also applies to $X_{\max}$ for signal-only reconstructions. No reconstruction strategy can resolve this bottleneck. Only through the addition of an another detector[12], such as the MD or the SSD, can R_{μ} be extracted on a shower to shower basis. This was accomplished through the hybrid reconstruction (section 7.3). MDs are significantly better than WCD in reconstructing R_{μ} as they provide direct insight into the muon content of the shower. The combined reconstruction yielded an even better mass discrimination power from R_{μ}.

Form reference [38], muons produced in simulations are underestimated with respect to data. This introduces a bias towards heavier elements in R_{μ}. Following the principles of universality, a muon deficit is only reflected in the scaling of the muon longitudinal profile and not its overall shape[13]. In terms of R_{μ}, only a *constant* shift is expected for all energies and zenith. The muon deficit can therefore be resolved by calibrating R^{hybrid}_{μ} with FD data around $\approx 10^{18.3}$ eV, where the composition is found to be very proton-like [106]. Events measured

[12] with a different signal response to the particle components
[13] This implies a break in the paradigm of Universality.

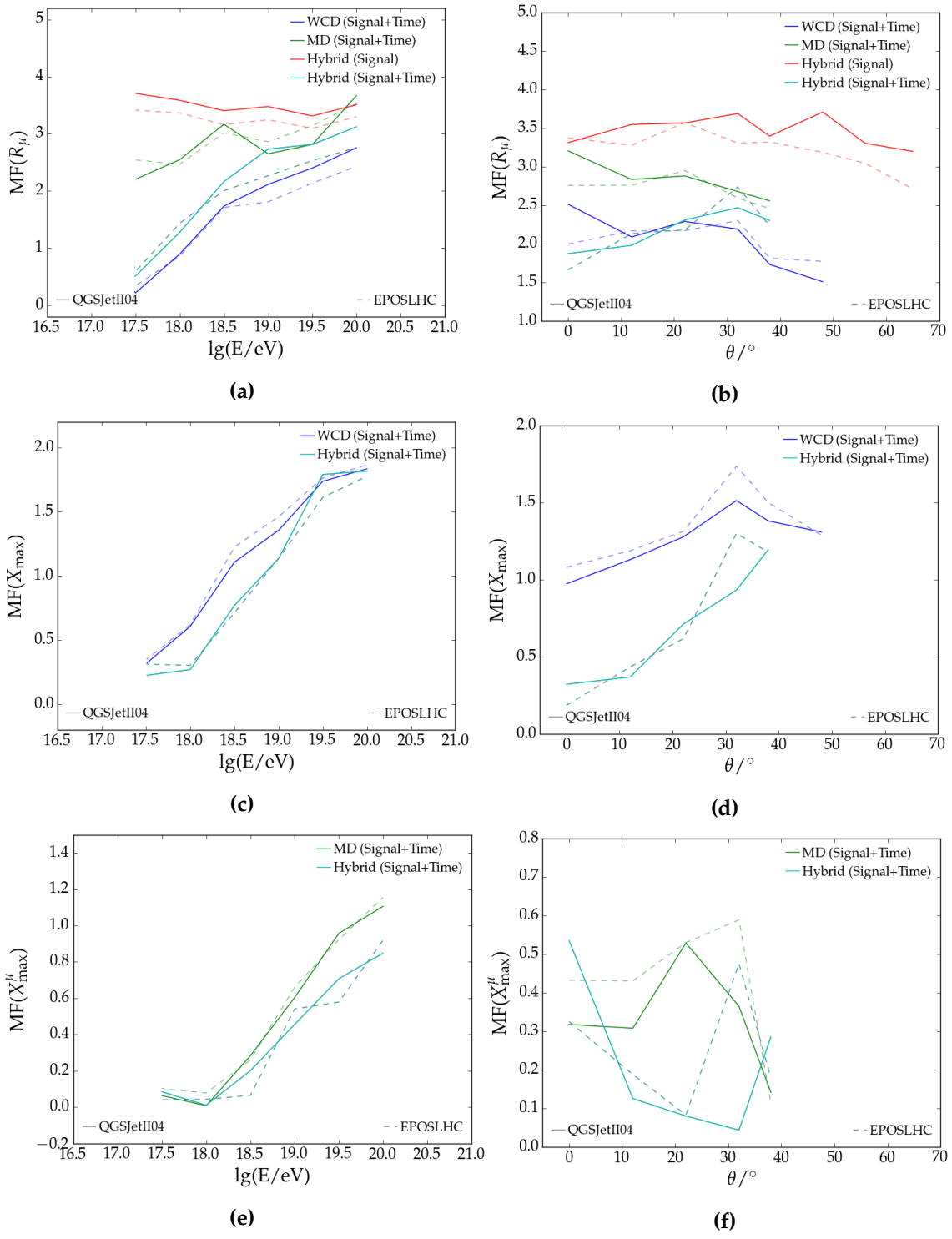

Figure 7.33: Merit Factor of R_μ (*top*), $X_{\max}$ (*middle*) and $X^\mu_{\max}$ (*bottom*) with respect to energy (*left*) and shower zenith (*right*). Performances of QGSJETII-04 showers (solid lines) and EPOS-LHC (dashed lines) showers are shown.

by FD, WCD and MD are referred to as *golden trinity*.

X_{max} yielded an improved result to previous analyses in references [44, 65, 81]. However, its resolution exceeds 50 gcm^{-2} for energies below 10^{18} eV. This is not from the limitation of the time model (see section B.4) but from the information feeded into the time reconstruction. Caveats in the current reconstruction are (i) the bin size of the WCD (set at 25 ns) and (ii) first order signal time variance and thus incorrectly estimating the variance between early and late arriving particles. Upgrades to the WCD electronics will resolve the former, greatly enhancing the sampling size (120 MHz instead of 40 MHz) and thus the precision of the trace shape. Only a dedicated study, similar to the development of the time model, provides an accurate understanding of the signal time variance. Currently, a signal and time model is being developed for the SSD. A hybrid WCD-SSD time reconstruction would greatly enhance the resolution of X_{max}. Both detectors are subjected to electromagnetic particles from the air shower.

Reconstruction of the maximum muon production depth has proven to be more difficult compared to X_{max}. Caveats in the MD are (i) the large bin width in the 1-Bit counter (set at 25 ns), (ii) signal time variance and (iii) information selection (1-Bit, integrator or both). As with the WCD, the large bin width of the 1-Bit counting strategy reduces the shape quality. Its upgrade is the parallel integrator strategy with a bin width of 6.25 ns. This raises the question on how the information should be treated for optimal time reconstructions. In this work, 1-Bit and integrator strategy time information were used for the reconstruction. This has yielded a resolution below 50 gcm^{-2} above $10^{18.5}$ eV (albeit with mass composition biases at 40 gcm^{-2}). Nevertheless, this is the first successful demonstration to obtain the maximum muon production depth through universality (through the most conservative approaches). Its reconstruction strategy allows for many possible improvements not yet explored in this work.

Finally, we have demonstrated through the altering iterative reconstruction method (between WCD, MD and Hybrid) that select shower information benefit shower parameters differently. This was demonstrated for R_{μ}, E, X_{max} and X^{μ}_{max}. Future work will follow the first steps introduced in this work and optimize upon it (as was done for the WCD in [44]). This will not only benefit the 'WCD+MD' reconstruction but also the 'WCD+SSD' and 'WCD+MD+SSD' reconstruction strategy as the MD and SSD are similar detector types.

CHAPTER 8

Summary and Conclusion

The focus of this thesis is the development of a reconstruction algorithm for extensive air showers to ultimately determine the mass composition of ultra-high cosmic rays. The reconstruction follows the principles of air shower universality, which allows one to describe the complex process of extensive air showers by few macroscopic variables: X_{max}, X^{μ}_{max}, R_{μ}, E and geometry. It is tuned for the WCD and MD, which sample the air shower differently. The algorithm encompasses signal and time information seen in the detectors for primary energies between 10^{17} eV and 10^{20} eV. Furthermore, novel reconstruction methods were developed to obtain the results seen in this work. These include reconstruction procedures for the WCD or MD independently, as well as a novel approach for hybrid analyses.

Main achievements include:

- A dedicated **GEANT4 look-up table** with WCD detector signals was created to significantly increase the computation speed to process simulated air showers, allowing for more efficient analyses. In this work, a new table was developed for the MD, accounting for the latest detector features (partially discussed in [48, 68]). These dedicated simulation files account for time delays due to soil depth, where the particle impinges and the response of the electronics.

- The development of a new **signal model for the WCD**. Proton-induced air showers were simulated with CORSIKA for energies between 10^{17} eV and 10^{20} eV and high energy hadronic interaction model QGSJETII-04. The new model significantly expands the phase-space compared to [59]. It has a more refined description for the energy dependency. Furthermore, it more accurately accounts for the muon production seen in air showers. The resulting model is a modified Gaisser-Hillas function and an NKG-like lateral distribution function. It depends on X_{max}, R_{μ}, E and geometry. As figure 8.1a shows, the model differs less than 5% from the MC simulated detector signals.

- A novel **signal model** was developed for the **MD**. It shares the same phase-space as the model developed for the WCD. The Gaisser-Hillas function was significantly modified to account for the higher tail seen for muons. As the MD are only exposed to muons, it was possible to develop a model which depends on the muon production depth X^{μ}_{max} for primary energies between 10^{17} eV and 10^{20} eV. This was previously not attempted. The signal model depends on X^{μ}_{max}, R_{μ}, E and geometry. Figure 8.1b shows that model differences are within the 5% level.

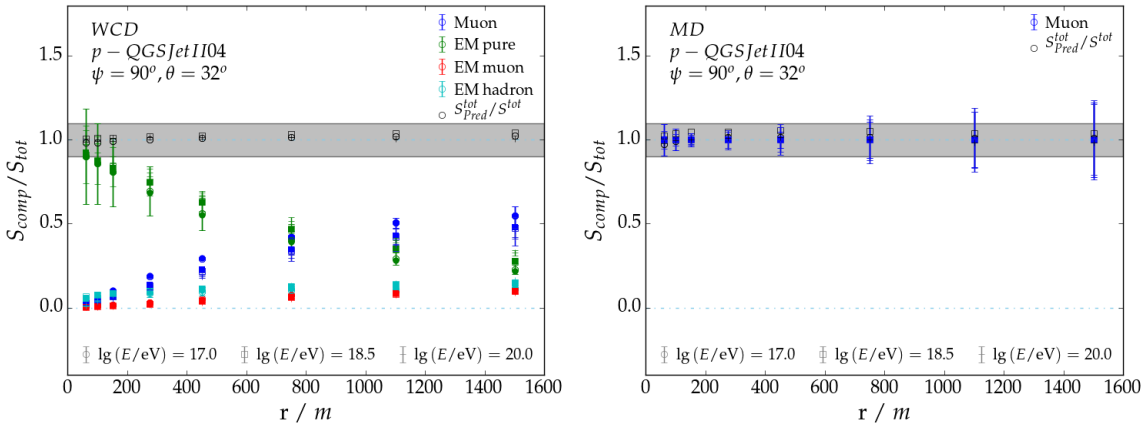

(a) **(b)**

Figure 8.1: Normalized particle component signal in the **a)** WCD and **b)** MD for different energies and radial distances. The predicted particle component fraction is overlaid with MC simulations. Bias of the total signal is also shown. Error bars refer to the particle component variance.

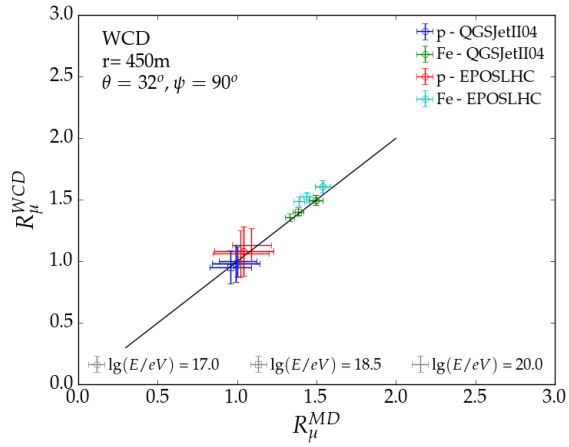

Figure 8.2: Normalization factors R_μ^{MD} and R_μ^{WCD} are compared for different primaries and hadronic models. The solid black line is the identity line.

- First results were presented on the relation between the muon content in the WCD and MD. Their unitary behavior (in figure 8.2) proves that $\boldsymbol{R_\mu}$ **is a global shower variable**, the validity of the signal model and conservation of the principles of shower Universality[1]. On a reconstruction level, this emphasizes the highly modular nature of Universality reconstructions, allowing for easily expandable reconstruction procedures.

- A complex analytical **time model for WCD** was derived from normalized average time distributions in simulations. The time model is a mixture of physics-motivated and empirical functions. The primary ansatz is the log-normal function, whose geometric and shower parameter dependencies are found through in-depth analyses - notably the shower maximum X_{max}. Note, trace information up to t_{90} is used to derive the parameterization. For unsaturated detectors, the prediction of the time distribution is within the 3% level between 275 m and 1500 m from the shower core. Uncertainties are at the 10% level for radial distances between 60 m and 275 m. Minor primary and

[1] no primary and hadronic model dependencies were found

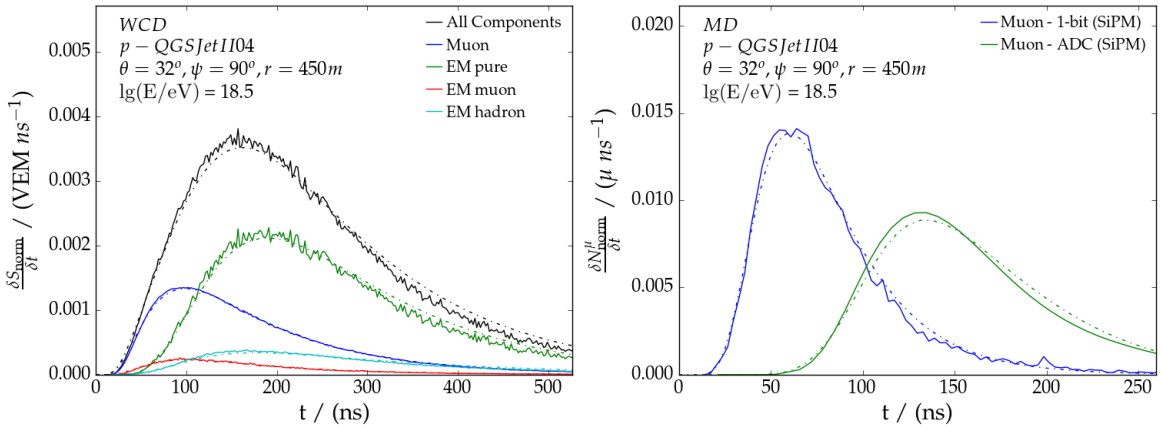

(a) **(b)**

Figure 8.3: Average time dependent signal trace for a sample $10^{18.5}$ eV proton shower in a **a)** WCD and **b)** MD (1-bit and integrator counting strategy) at 450 m. Time model predictions (dashed) overlay the MC simulated traces (solid).

hadronic model differences were found and are addressed in this work. A sample trace (solid) is overlaid by the model prediction (dashed) in figure 8.3a.

- Two novel and independent **time models** were designed **for the 1-Bit and integrator counting strategy of the MD**. The development strategy is similar to the WCD. The most notable difference is that it accounts for the maximum muon production depth $X^{\mu}_{\max}$. Their validation has revealed primary and hadronic model differences to be mostly within the 3% level (or within 25 gcm^{-2}). A sample trace is shown in figure 8.3b. The solid line indicates the simulated trace, whereas the dashed line represents its model prediction.

- Two **reconstruction procedures** were introduced for independent use of the **MD and WCD**. They are based on the iterative reconstruction procedure, optimized for a faster and robust shower reconstruction. Their respective limitations were addressed and later compared to the hybrid reconstruction. Limitations of WCD-only reconstructions are ambiguities between R_{μ} and E (due to the addition of the electromagnetic content). Saturation effects in the MD greatly limit accuracy of the energy, reducing the overall quality of the shower reconstruction. For the WCD, the energy resolution is below 20%, whereas the resolution for R_{μ} is below the desired 20% limit. $X_{\max}$ is approximately $\approx 40\,\mathrm{gcm}^{-2}$. These are significant improvements compared to early studies in [44, 59, 81]. With the MD, the resolution for R_{μ} is 15%, whereas energy resolutions range from 10% to 40% depending on primary mass. Finally, it was demonstrated that the maximum muon production depth could be obtained from MD time information. Currently, the maximum muon production depth reconstruction through MD information and Universality remain unrivalled. First results have yielded a resolution of ≈ 50 gcm^{-2}.

- First results on **hybrid universality reconstructions** were presented within this work. For its purpose, a novel reconstruction method was introduced. Due to the inherent design of the signal and time models of the WCD and MD, $X_{\max}$ and $X^{\mu}_{\max}$ could not be further improved with respect to their 'WCD-only' and 'MD-only' reconstruction counterparts. However, the combined information significantly improves the resolution of R_{μ} to 10%. These results are unprecedented and encourage further analysis.

- The **merit factor** is found to be best for R_μ. It is highest (>3) for hybrid reconstructions. The separation power between proton and iron primaries is less for $X_{\max}$ and $X^{\mu}_{\max}$.
- Knowledge gained through this work has led towards the **development of a new framework** (*Universality-v2*), currently used to develop a signal model for the SSD.

Recommended improvements with the current detector design are:

- Analysis of a novel calibration for MD time reconstructions. Recommendations are addressed in this work.
- The development of signal time variance for the WCD and MD. The current variance model overestimates the uncertainty for each time bin in the trace.
- Changing the form of the log-likelihood to simultaneously account for 1-Bit and integrator signal.
- Extension of the algorithm to include signal and time information far from the shower core.
- Further analysis into the reconstruction procedure for MD and hybrid reconstruction.

It is anticipated these improvements will benefit the general performance of the reconstruction, as well as set the platform for first data-based hybrid universality reconstructions. The latter can be achieved through a novel calibration method for MD time reconstructions, outlined in chapter 6. A dedicated signal time variance will correctly account for detector effects and particle fluctuations between the early and late part of the trace. This effectively emphasizes qualitatively important features in the trace for $X_{\max}$ and $X^{\mu}_{\max}$ reconstruction. Finally, by further optimizing the reconstruction procedure, the ambiguities between shower parameters can be further minimized. As discussed, the combined information of MD and WCD has greatly improved R_μ. As a result, we also expect significant improvements in $X_{\max}$ through the development of a SSD universality model.

APPENDIX A

Signal Model

A.1 A_{rad}

For every radial distance and shower zenith, the functional shape of (4.14) is fitted ($A_{rad}|_{r,\theta}$). It is then characterized for its radial dependency with

$$A_{rad}(\theta, r) = \alpha_0(\theta) + \frac{\alpha_1(\theta) - \alpha_0(\theta)}{e^{-\alpha_2(\theta)} - 1} \cdot e^{-\alpha_2(\theta) r} \tag{A.1}$$

where $\alpha_i(\theta)$ are the fit parameters for each shower zenith. For the WCD, all parameters, irrespective of particle component, are described with a linear function

$$\alpha_i = p_0 + p_1 cos(\theta) \tag{A.2}$$

For the MD they are similarly described as

$$\begin{aligned} \alpha_{i\neq 1} &= p_0 + p_1 cos(\theta) \\ \alpha_1 &= p_0 + p_1 cos(\theta) + p_2 cos(\theta)^2 \end{aligned} \tag{A.3}$$

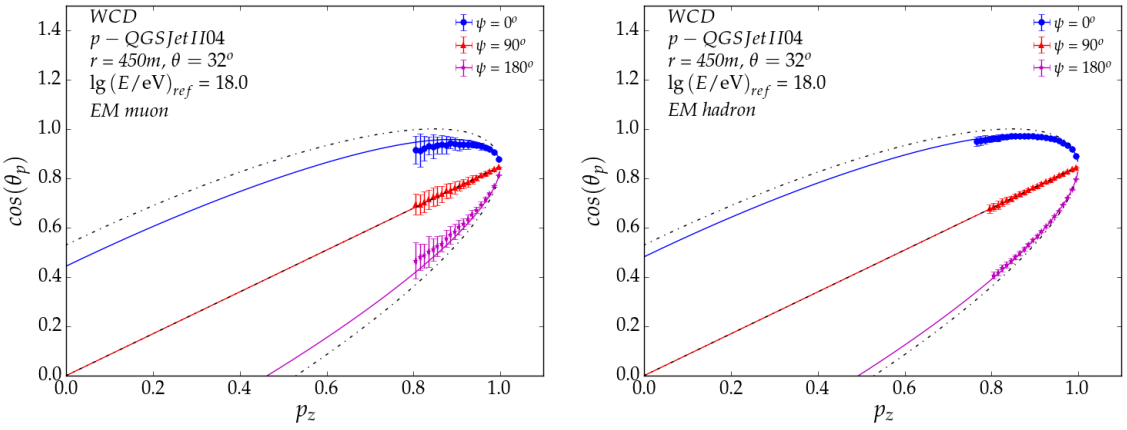

(a) **(b)**

Figure A.1

A.2 $\frac{\delta S}{\delta p_z}$

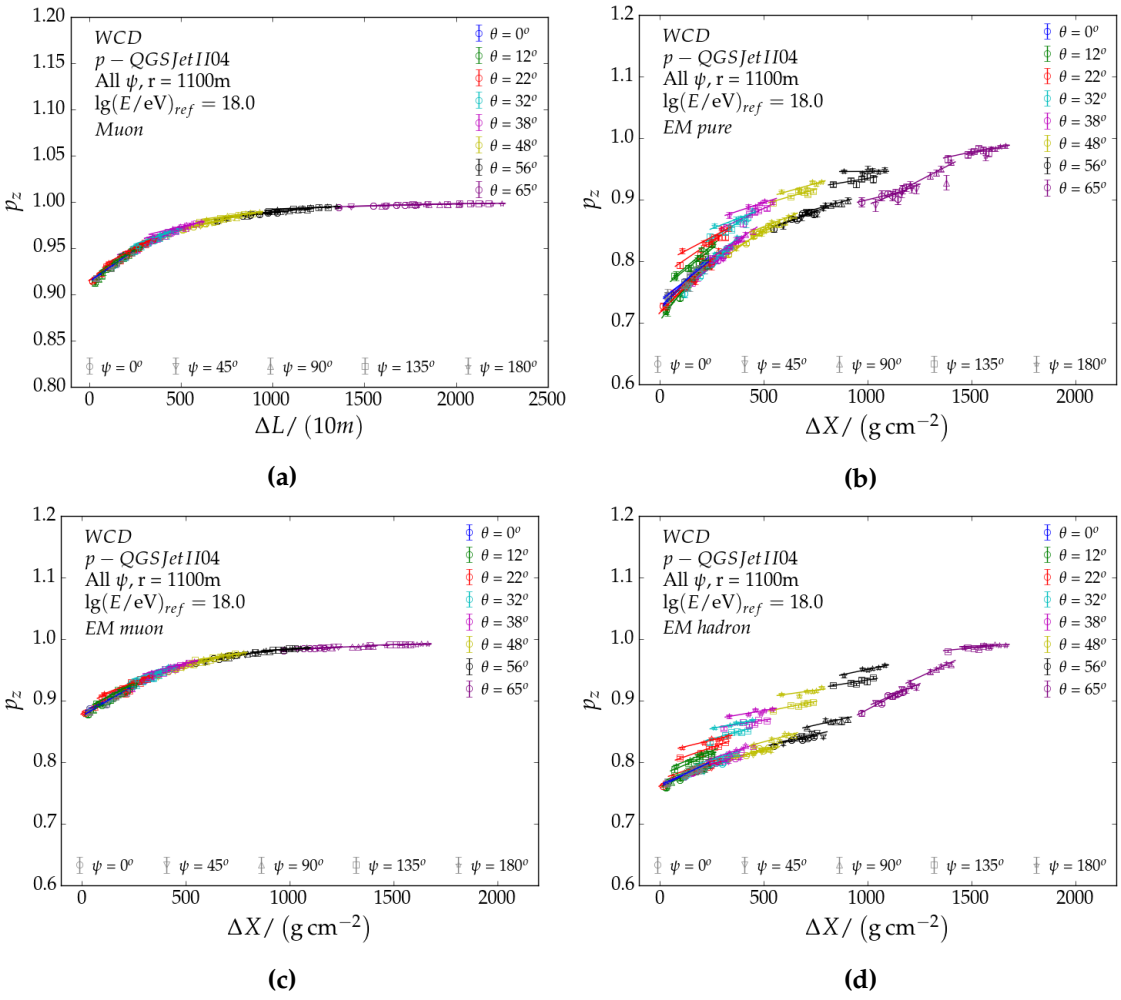

Figure A.2

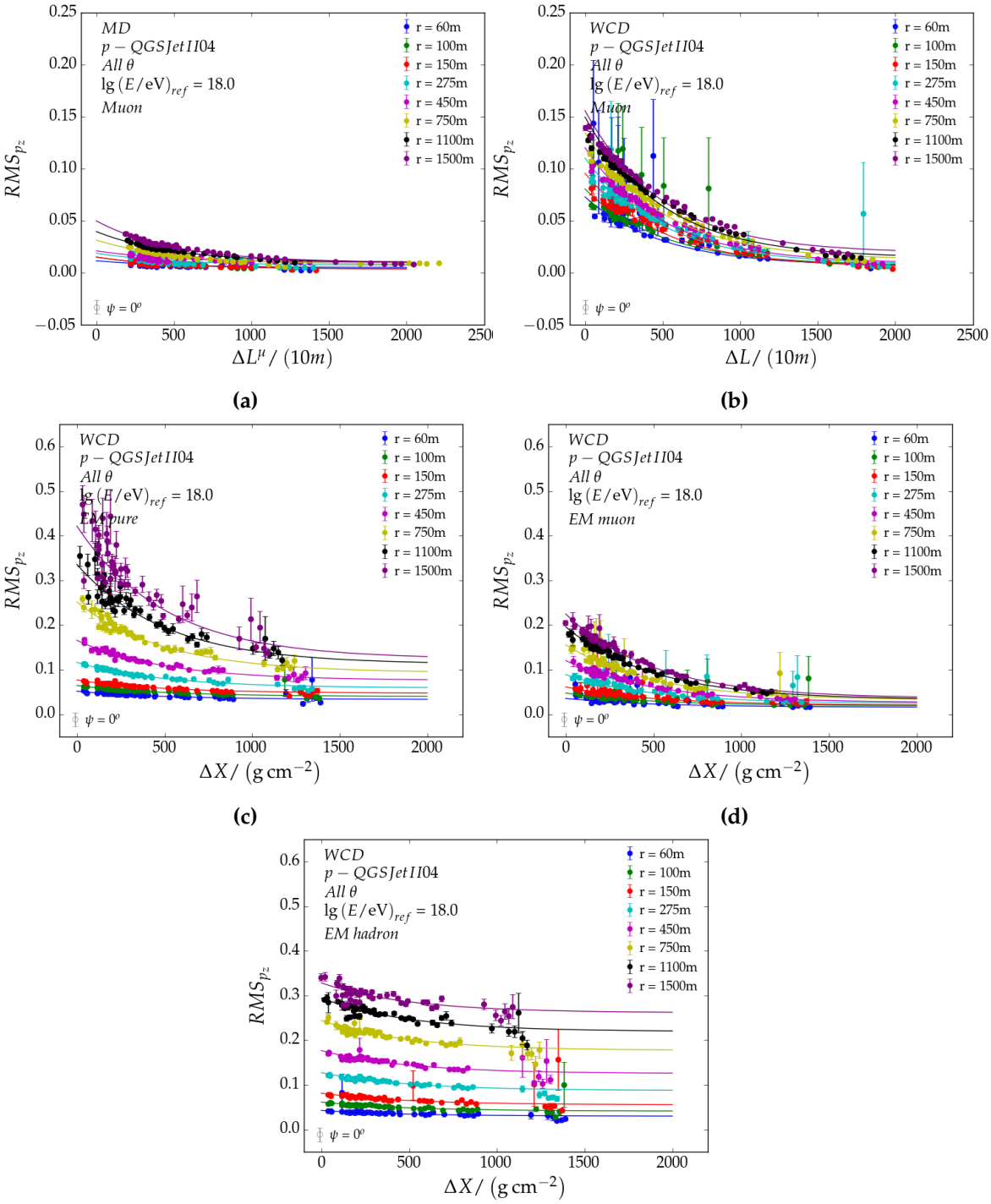
MD
p − QGSJetII04
All θ
lg(E/eV)ref = 18.0
Muon
r = 60m
r = 100m
r = 150m
r = 275m
r = 450m
r = 750m
r = 1100m
r = 1500m
ψ = 0°
RMSpz
ΔLμ / (10m)
(a)
WCD
p − QGSJetII04
All θ
lg(E/eV)ref = 18.0
Muon
ΔL / (10m)
(b)
WCD
p − QGSJetII04
All θ
lg(E/eV)ref = 18.0
EM pure
ΔX / (g cm−2)
(c)
WCD
p − QGSJetII04
All θ
lg(E/eV)ref = 18.0
EM muon
ΔX / (g cm−2)
(d)
WCD
p − QGSJetII04
All θ
lg(E/eV)ref = 18.0
EM hadron
ΔX / (g cm−2)
(e)

Figure A.3

A.3 $A_{\mathrm{mod}}T_{\mathrm{mod}}$

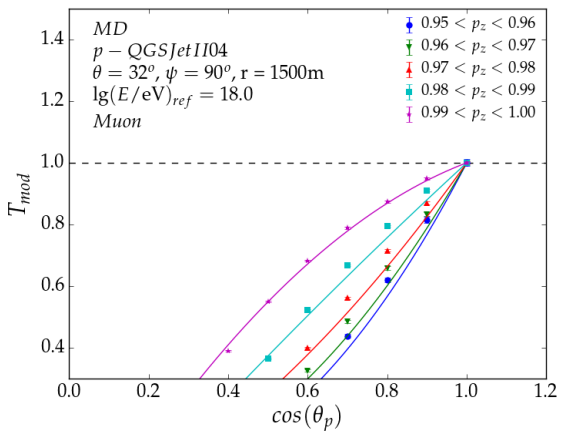

(a)

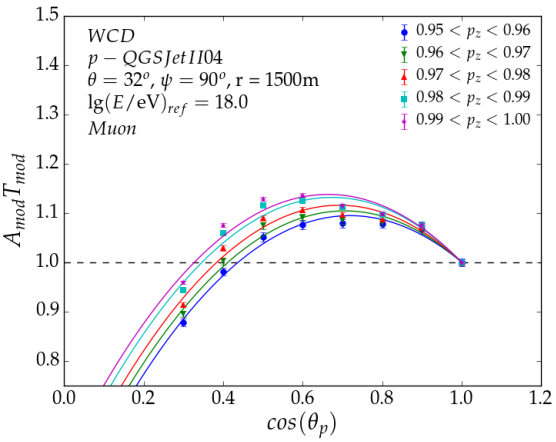

(b)

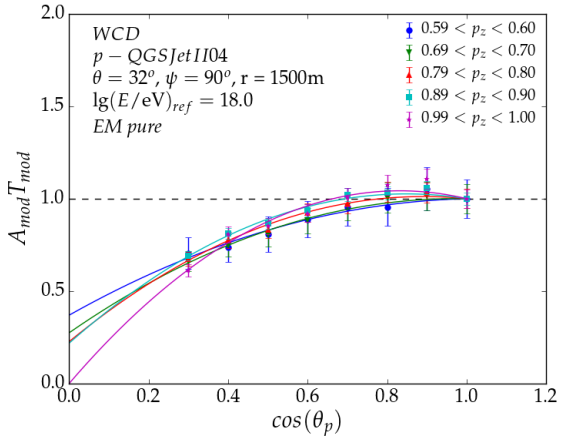

(c)

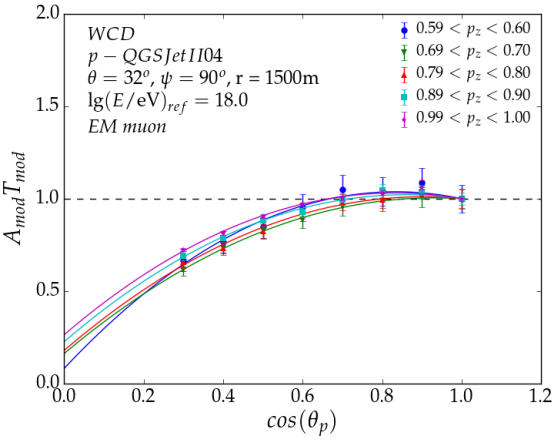

(d)

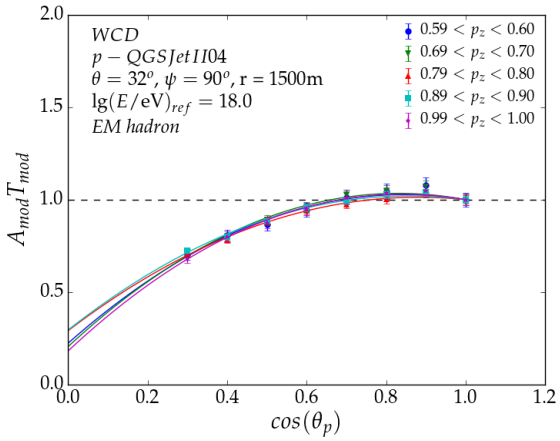

(e)

Figure A.4

A.4 S_{real} with respect to shower stage $\Delta X/\Delta L^{(\mu)}$

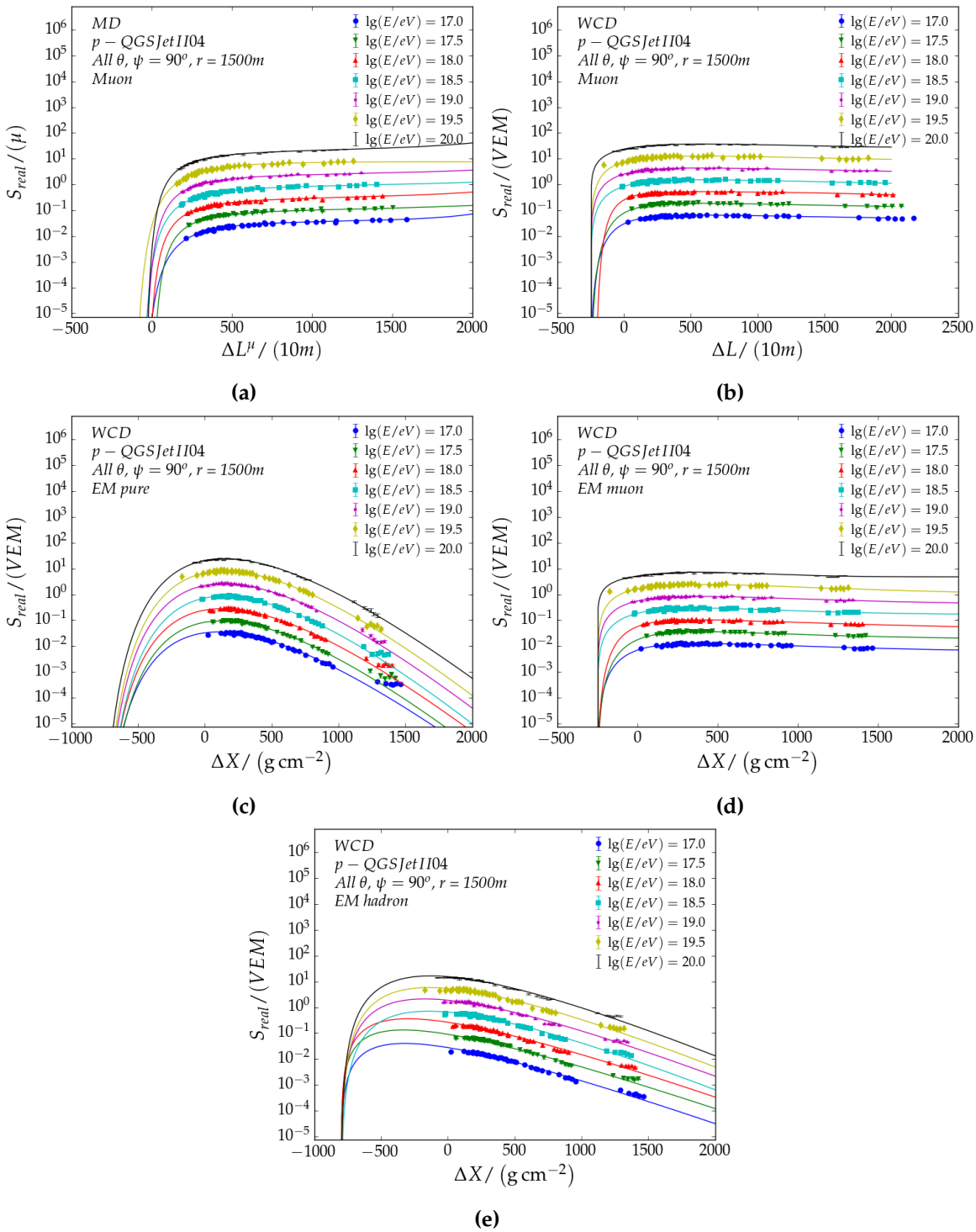

Figure A.5

A.5 Atmospheric densities

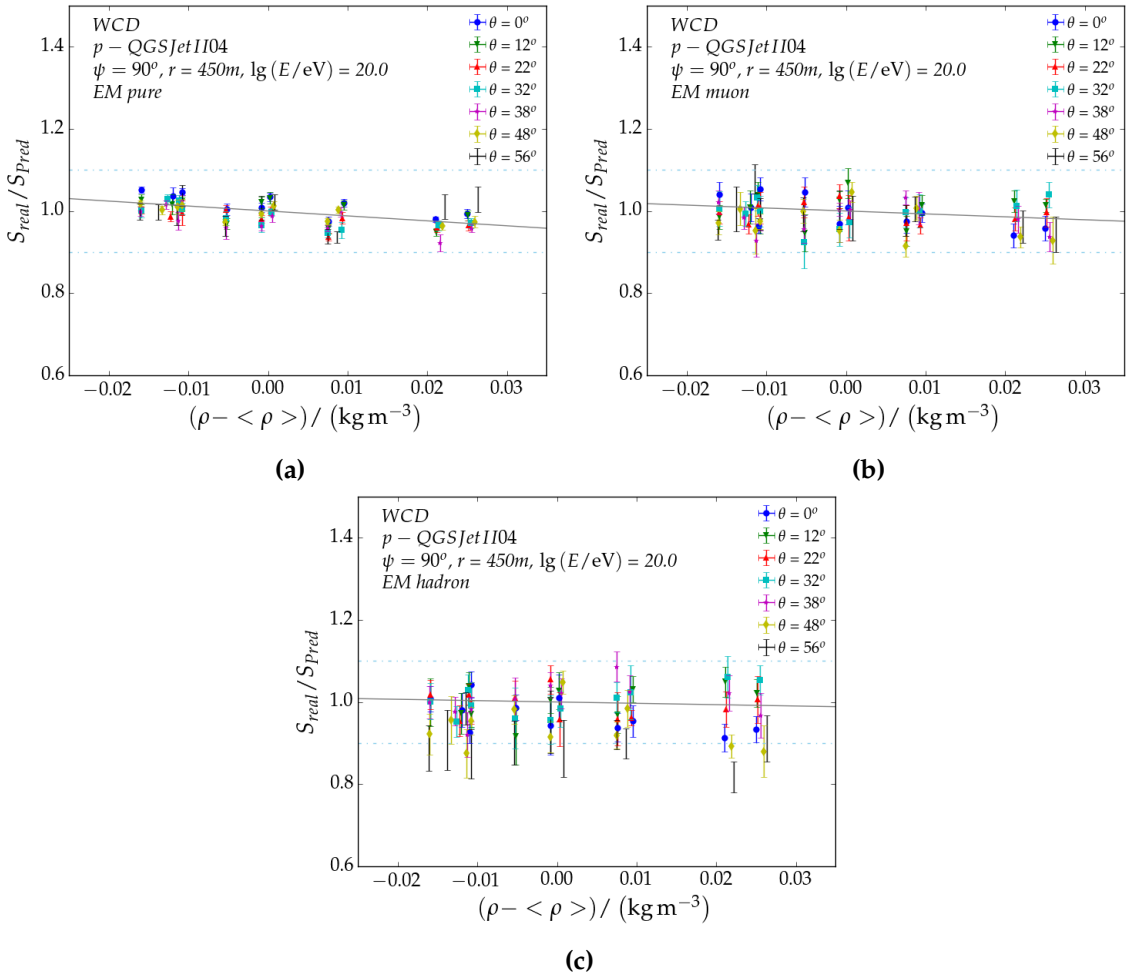

Figure A.6

A.6 Azimuth asymmetries

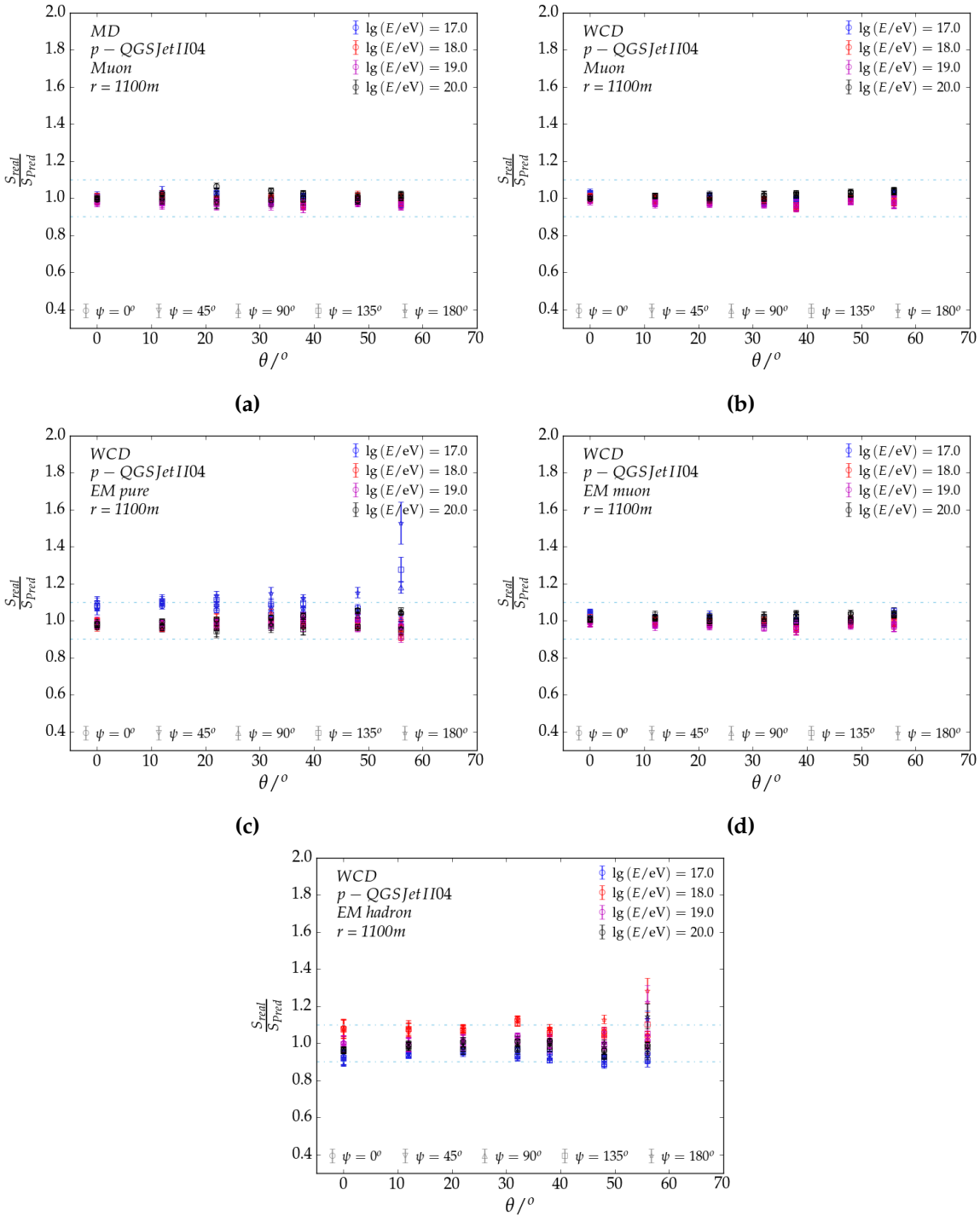

Figure A.7

A.7 Gaisser-Hillas Characterization

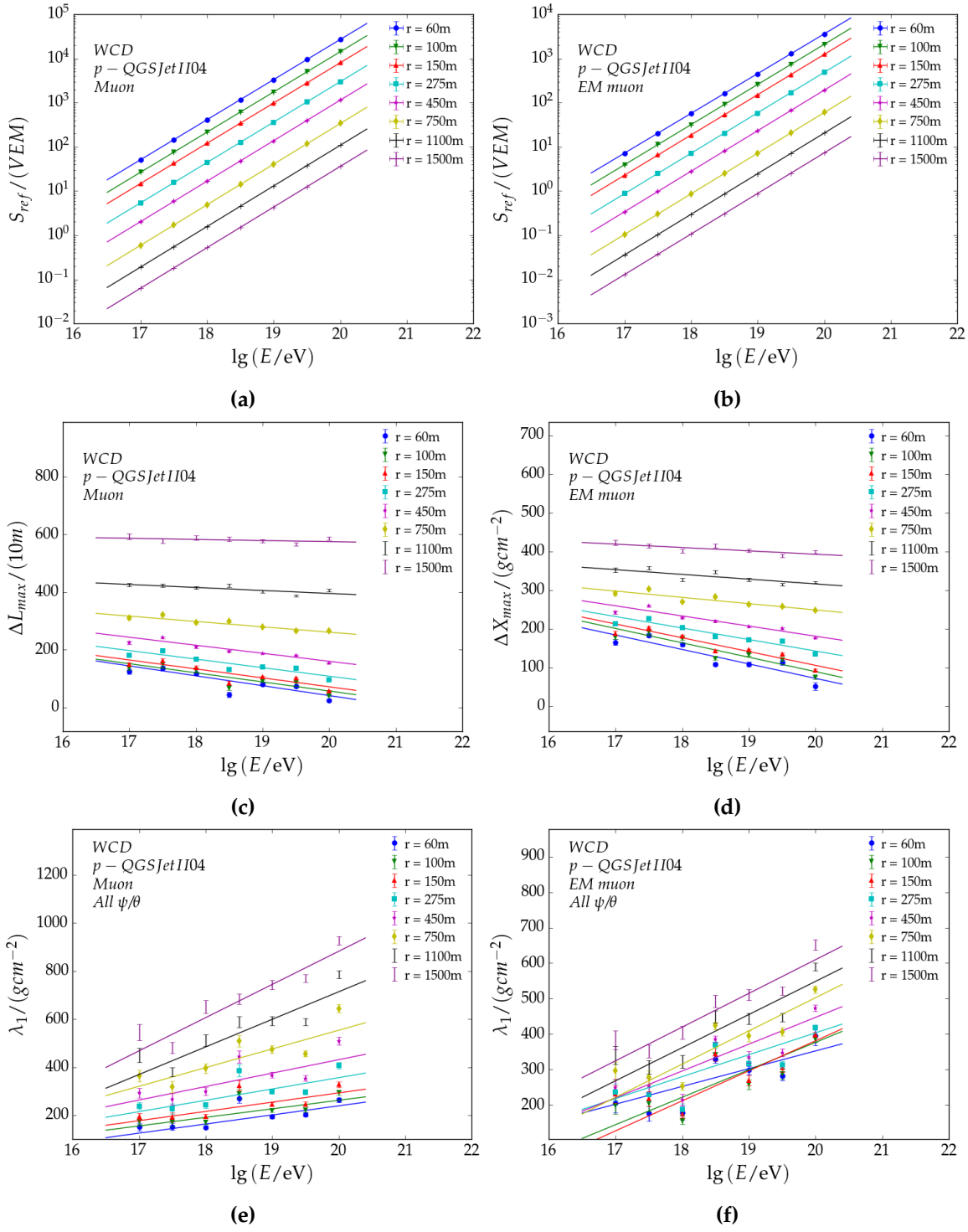

Figure A.8

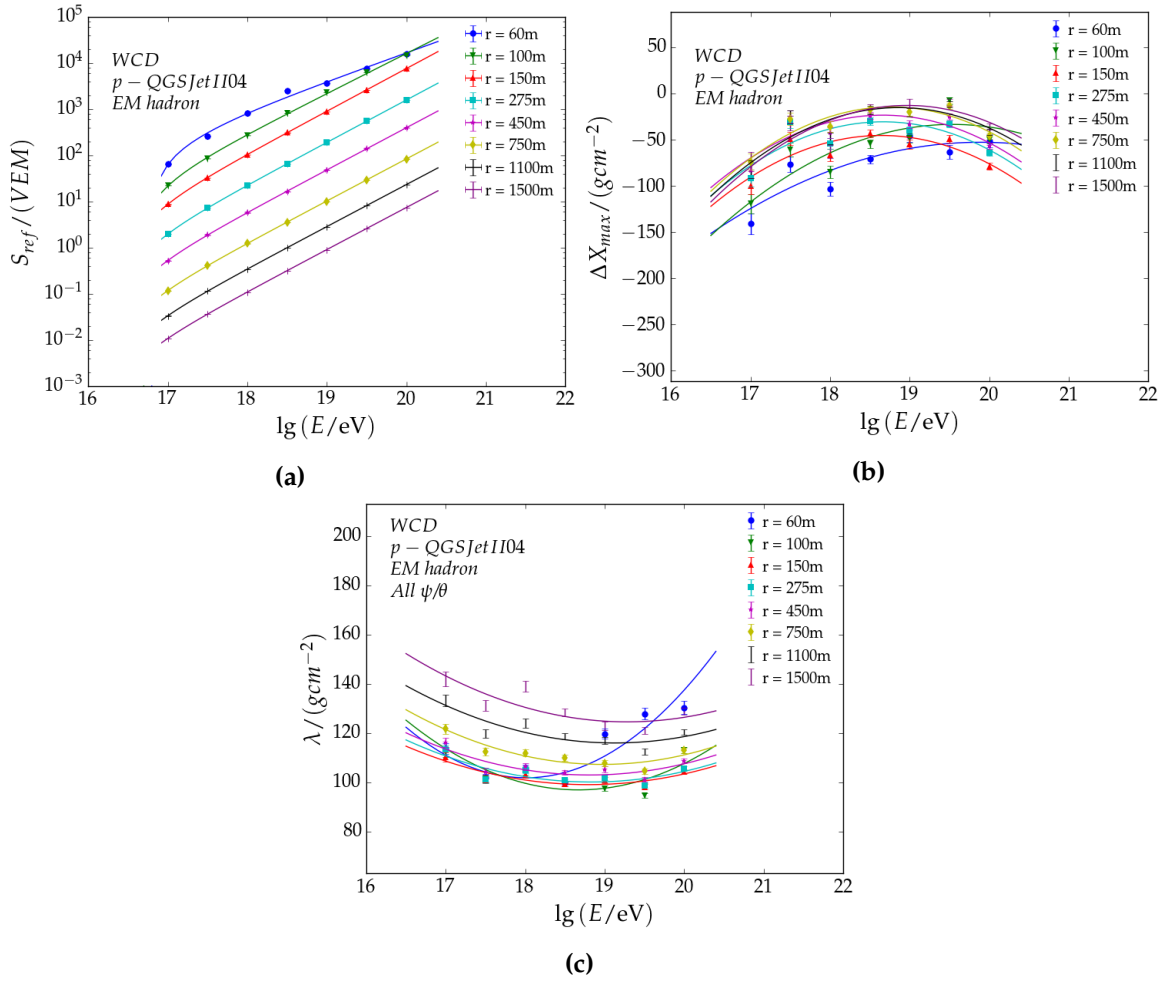

Figure A.9

A.7.1 Radial Characterization

Here all radial characterizations are listed for the Gaisser-Hillas function discussed in chapter 4.39. Due to the vast number of parameters, the parameter values p_i are not shown. These can be found in [69]. The characterizations (however no the parameter values) between the MD and WCD are considered equivalent unless stated otherwise.

Muon

For the muon component, the power-law for the energy scale $\gamma(r)$ introduced in equation (4.41) is characterized by

$$\begin{aligned}\gamma^{\mathrm{MD}}(r) &= p_0 + p_1 r + p_2 r^2 \\ \gamma^{\mathrm{WCD}}(r) &= p_0 + p_1 e^{-\frac{r}{p_2}}\end{aligned} \tag{A.4}$$

The parameters for the shower stage $\Delta L^{(\mu)}_{\mathrm{max}}$ at which the signal is maximal (equation (4.45)) are

$$\begin{aligned}
\alpha_0(r) &= p_0 + p_1 e^{\frac{p_2 r}{1000\,\mathrm{m}}} \\
\alpha_1^{\mathrm{MD}}(r) &= p_0(1 + p_1 r) \\
\alpha_1^{\mathrm{WCD}}(r) &= p_0(1 + \frac{r}{1000\,\mathrm{m}})^{p_1} + p_2
\end{aligned} \tag{A.5}$$

The parameters of $\lambda_i(r, E)$ (equation (4.46)) are described by

$$\left.\begin{aligned}
\alpha_0^{\mathrm{MD}}(r) &= p_0 + p_1 r + p_2 r^2 \\
\alpha_1^{\mathrm{MD}}(r) &= p_0(1 + p_1 r) \\
\alpha_0^{\mathrm{WCD}}(r) &= p_0(1 + p_1 r) \\
\alpha_1^{\mathrm{WCD}}(r) &= p_0 + p_1 r + p_2 r^2
\end{aligned}\right\} \lambda_1$$

$$\left.\begin{aligned}
\alpha_0(r) &= p_0 + p_1 r + p_2 r^2 \\
\alpha_1^{\mathrm{MD}}(r) &= p_0 e^{p_1 r} \\
\alpha_1^{\mathrm{WCD}}(r) &= p_0 + p_1 r
\end{aligned}\right\} \lambda_2 \tag{A.6}$$

$$\left.\begin{aligned}
\alpha_0^{\mathrm{MD}}(r) &= p_0 e^{p_1 r} \\
\alpha_1^{\mathrm{MD}}(r) &= p_0 e^{p_1 r} \\
\alpha_0^{\mathrm{WCD}}(r) &= p_0 r \\
\alpha_1^{\mathrm{WCD}}(r) &= p_0 + p_1 r
\end{aligned}\right\} \lambda_3$$

EM pure

The power-law for the energy scale $\gamma(r)$ of the pure electromagnetic particle component is characterized by

$$\gamma(r) = p_0(1 + \frac{r}{1000\,\mathrm{m}})^{p_1}(1 + \frac{r}{2000\,\mathrm{m}})^{p_2} \tag{A.7}$$

The parameters for the shower stage ΔX_{max} at which the signal is maximal are all described by

$$\begin{aligned}
\alpha_0(r) &= p_0(1 + r)^{p_1} e^{p_2 r} \\
\alpha_1(r) &= p_0 + p_1 e^{(}p_2 r) \\
\alpha_2(r) &= p_0 + p_1/r
\end{aligned} \tag{A.8}$$

The parameters of $\lambda(r, E)$ (equation (4.48)) are described by

$$\alpha_{0,1,2}(r) = p_0 + p_1 r + p_2 r^2 \tag{A.9}$$

EM from muons

The electromagnetic particles from muons, follow the same characterizations as the muonic component. The power-law for the energy scale $\gamma(r)$ introduced in equation (4.41) is characterized by

$$\gamma(r) = p_0 + p_1 r \tag{A.10}$$

The parameters for the shower stage $\Delta X_{\max}$ at which the signal is maximal are

$$\begin{aligned} \alpha_0(r) &= p_0 + p_1 e^{\frac{p_2 r}{1000\,\mathrm{m}}} \\ \alpha_1(r) &= p_0(1 + \frac{r}{1000\,\mathrm{m}})^{p_1} + p_2 \end{aligned} \tag{A.11}$$

The parameters of $\lambda_i(r, E)$ (equation (4.46)) are described by

$$\left.\begin{aligned} \alpha_0(r) &= p_0(1 + p_1 r) \\ \alpha_1(r) &= p_0 + p_1 r + p_2 r^2 \end{aligned}\right\} \lambda_1$$

$$\left.\begin{aligned} \alpha_0(r) &= p_0 + p_1 r + p_2 r^2 \\ \alpha_1(r) &= p_0 + p_1 r \end{aligned}\right\} \lambda_2 \tag{A.12}$$

$$\left.\begin{aligned} \alpha_0(r) &= p_0 + p_1 r + p_2 r^2 \\ \alpha_1(r) &= p_0 e^{p_1 r} \end{aligned}\right\} \lambda_3$$

EM from hadronic jets

The signal offset $S_{\text{offset}}(r)$ and power-law for the energy scale $\gamma(r)$ for the electromagnetic particles from hadronic jets are characterized by

$$S_{\text{offset}}(r) = \frac{p_0}{r^4} \tag{A.13}$$

and

$$\gamma(r) = p_0 + p_1 e^{p_2 r} \tag{A.14}$$

The characterization of $S_{\text{offset}}(r)$ already shows its more significant effect at larger distances. The parameters for the shower stage $\Delta X_{\max}$ at which the signal is maximal are all described by

$$\begin{aligned} \alpha_0(r) &= \frac{p_0}{r} + p_1 \\ \alpha_1(r) &= p_0 + p_1 e^{(}p_2 r) + p_3 r \\ \alpha_2(r) &= p_0 + p_1 e^{p_2 r} \end{aligned} \tag{A.15}$$

The parameters of $\lambda(r, E)$ (equation (4.48)) are described by

$$\begin{aligned} \alpha_0(r) &= p_0 + p_1 r + p_2 r^2 \\ \alpha_{1,2}(r) &= p_0 + p_1 r + \frac{p_2}{r} \end{aligned} \tag{A.16}$$

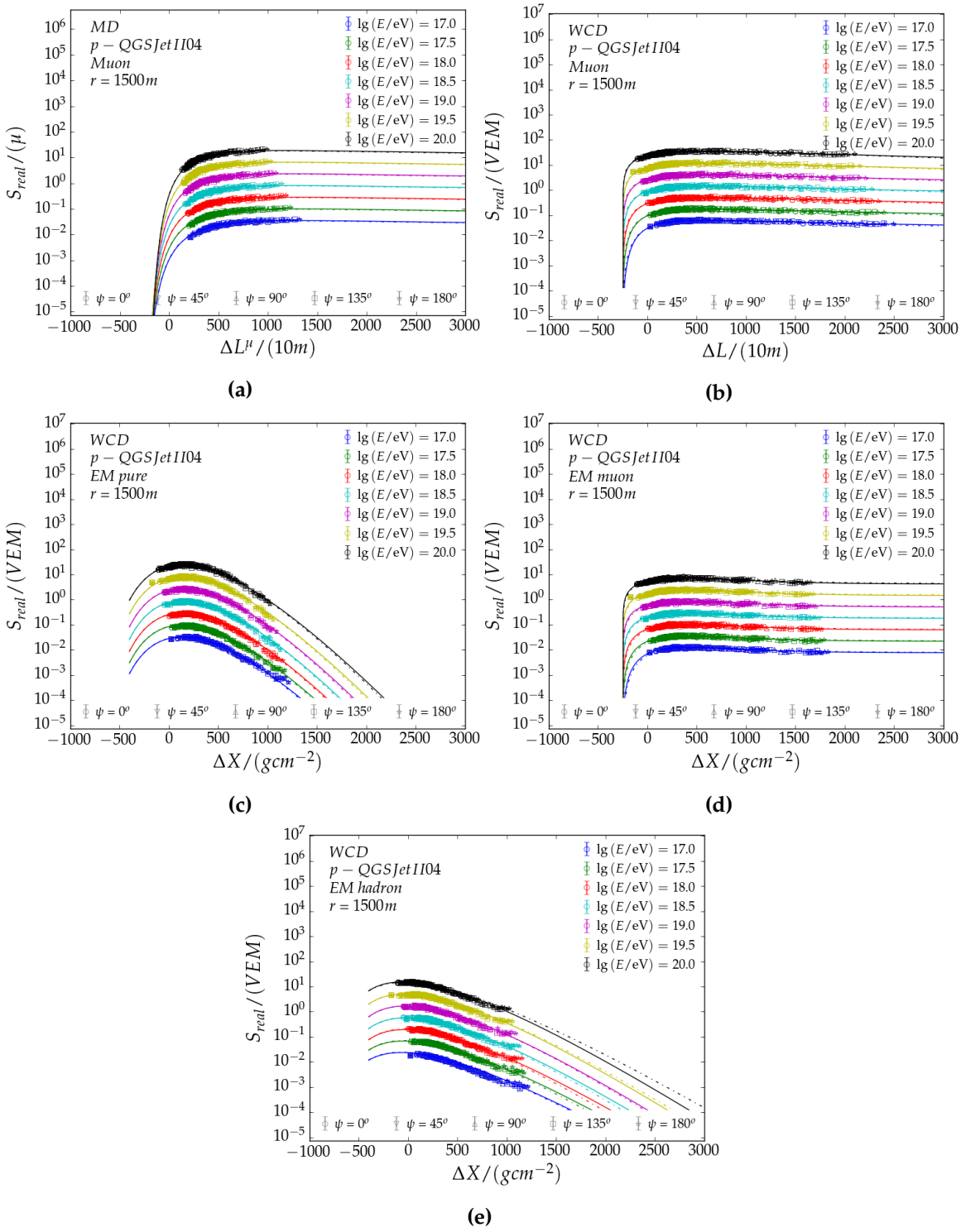

Figure A.10

Component Correlation

The characterization for $\alpha(r)$ and $\beta(r)$ in equation (4.50) are where $\alpha(r)$ and $\beta(r)$ are

$$\alpha_i(r) = p_0 + p_1/r + p_2 r\beta_i(r) = p_0 + p_1/r + p_2 r \tag{A.17}$$

For the hadronic jet component in (4.51), it is described as

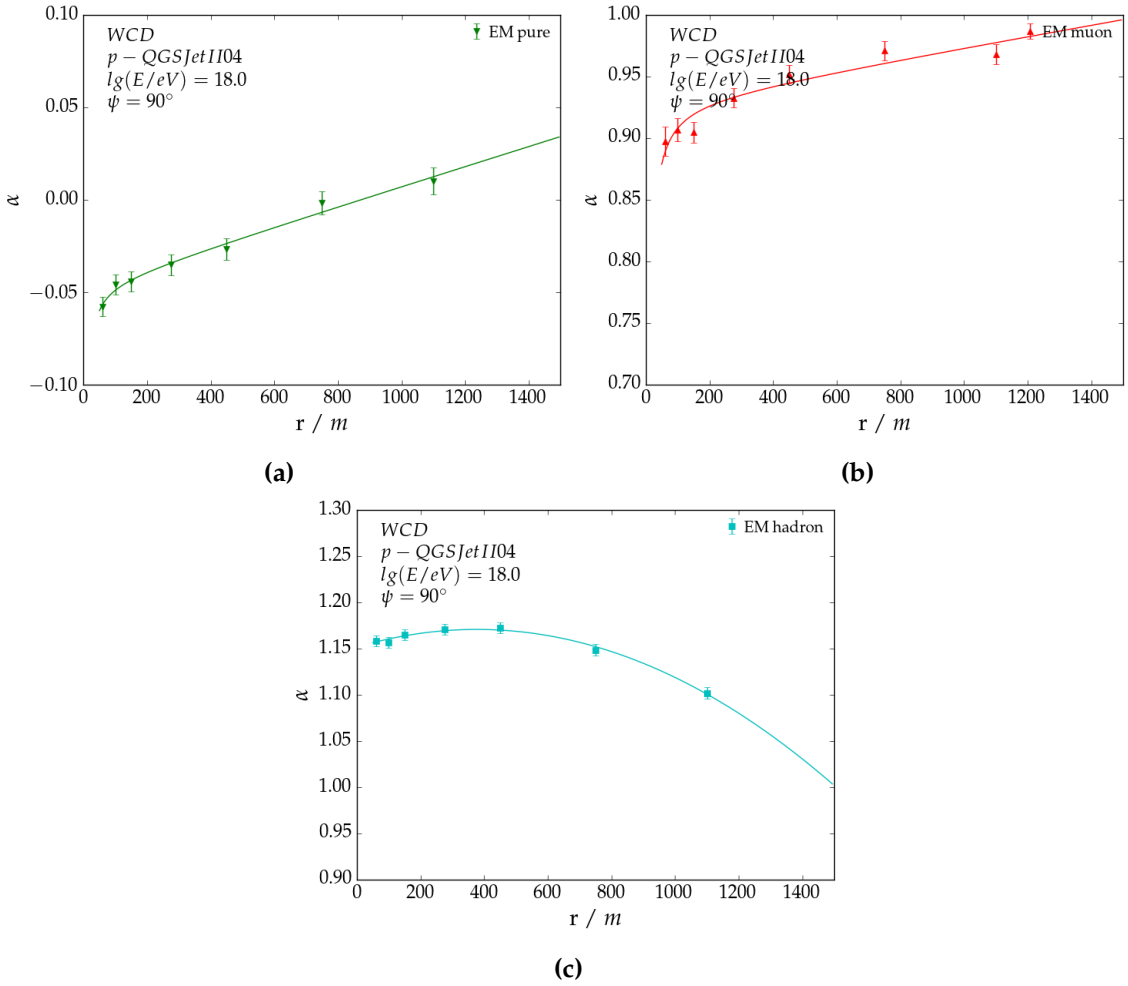

Figure A.11

$$\alpha_{\text{EM-hadron}}(r) = p_0 + p_1 r + p_2 r^2 \beta_{\text{EM-hadron}}(r) = p_0 + p_1 r \tag{A.18}$$

A.7.2 Validation

The figures in A.12 reveal the same horizontal structure for the muonic component and electromagnetic particles from muons. Pure electromagnetic particles and those from hadronic jets show biases up to 50% and 25% respectively. Considering the radial distance of 1500 m, the shower energies at which these biases occur (17 eV) and their signal fraction (18% and 9% respectively), it is safe to conclude that it will not affect the performance of the signal model. Also, as seen in figure A.5, the signal size is below 0.1 VEM and thus outside the intended scope of use for this model.

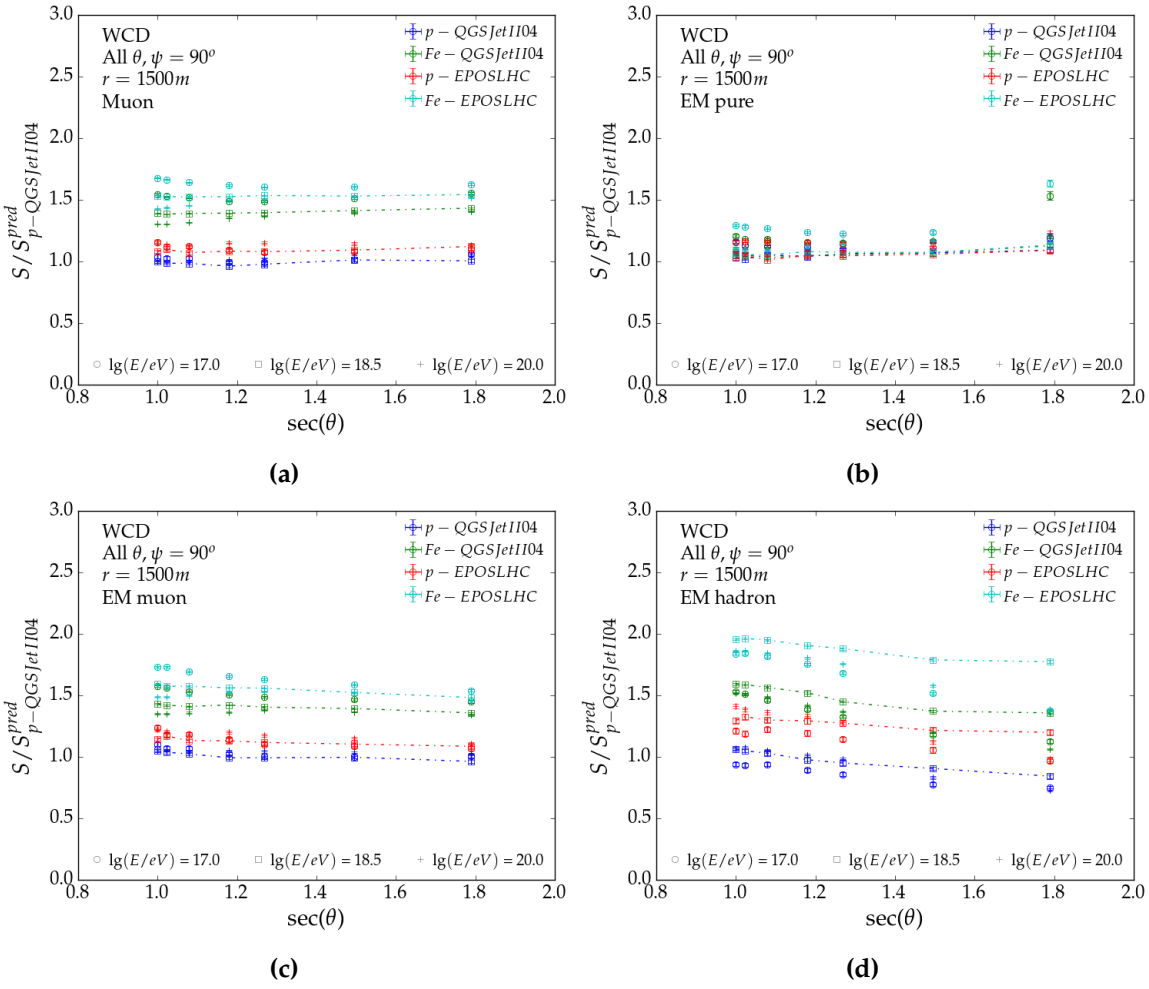
WCD
All $\theta, \psi = 90^o$
$r = 1500m$
Muon
$p - QGSJetII04$
$Fe - QGSJetII04$
$p - EPOSLHC$
$Fe - EPOSLHC$
$S/S^{pred}_{p-QGSJetII04}$
sec(θ)
$\lg(E/eV) = 17.0$
$\lg(E/eV) = 18.5$
$\lg(E/eV) = 20.0$
(a)
WCD
All $\theta, \psi = 90^o$
$r = 1500m$
EM pure
(b)
WCD
All $\theta, \psi = 90^o$
$r = 1500m$
EM muon
(c)
WCD
All $\theta, \psi = 90^o$
$r = 1500m$
EM hadron
(d)

Figure A.12

APPENDIX B

Time Model

B.1 Time Origin - t_0

The scale and slope parameters $\alpha_i(E, \theta)$ in equations (5.6) (MD) and (5.7) (WCD) are empirically characterized.

B.1.1 MD

1-Bit

$$\begin{aligned} \alpha_1(E,\theta) &= (p_0 + p_1(log_{10}(E) - 18.)) + (p_2 + p_3(log_{10}(E) - 18.)) \cdot (sec(\theta) - 1)^2 \\ \alpha_2(E,\theta) &= -(p_0 + p_1(log_{10}(E) - 18.)) \end{aligned} \tag{B.1}$$

Integrator

$$\alpha_1(E,\theta) = p_0 + p_1(log_{10}(E) - 18.) + p_2(sec(\theta) - 1 \tag{B.2}$$

B.1.2 WCD

Muon and EM-muon

$$\begin{aligned} \alpha_1(E,\theta) &= (p_0 + p_1(log_{10}(E) - 18.)) + (p_2 + p_3(log_{10}(E) - 18.)) \cdot (sec(\theta) - 1) \\ \alpha_2(E,\theta) &= -(p_0 + (p_1(log_{10}(E) - 18.) + p_2)sin(\theta)) \end{aligned} \tag{B.3}$$

EM-Pure

$$\begin{aligned} \alpha_1(E,\theta) &= (p_0 + p_1(log_{10}(E) - 18.)) + (p_2 + p_3(log_{10}(E) - 18.)) \cdot (sec(\theta) - 1) \\ \alpha_2(E,\theta) &= p_0 + p_1(log_{10}(E) - 18.) + p_2(sec(\theta) - 1) \end{aligned} \tag{B.4}$$

EM-Hadron

$$\begin{aligned} \alpha_1(E,\theta) &= (p_0 + p_1(log_{10}(E) - 18.)) + (p_2 + p_3(log_{10}(E) - 18.)) \cdot (sec(\theta) - 1)^2 \\ \alpha_2(E,\theta) &= p_0 + p_1(log_{10}(E) - 18.) + p_2(sec(\theta) - 1)^2 \end{aligned} \tag{B.5}$$

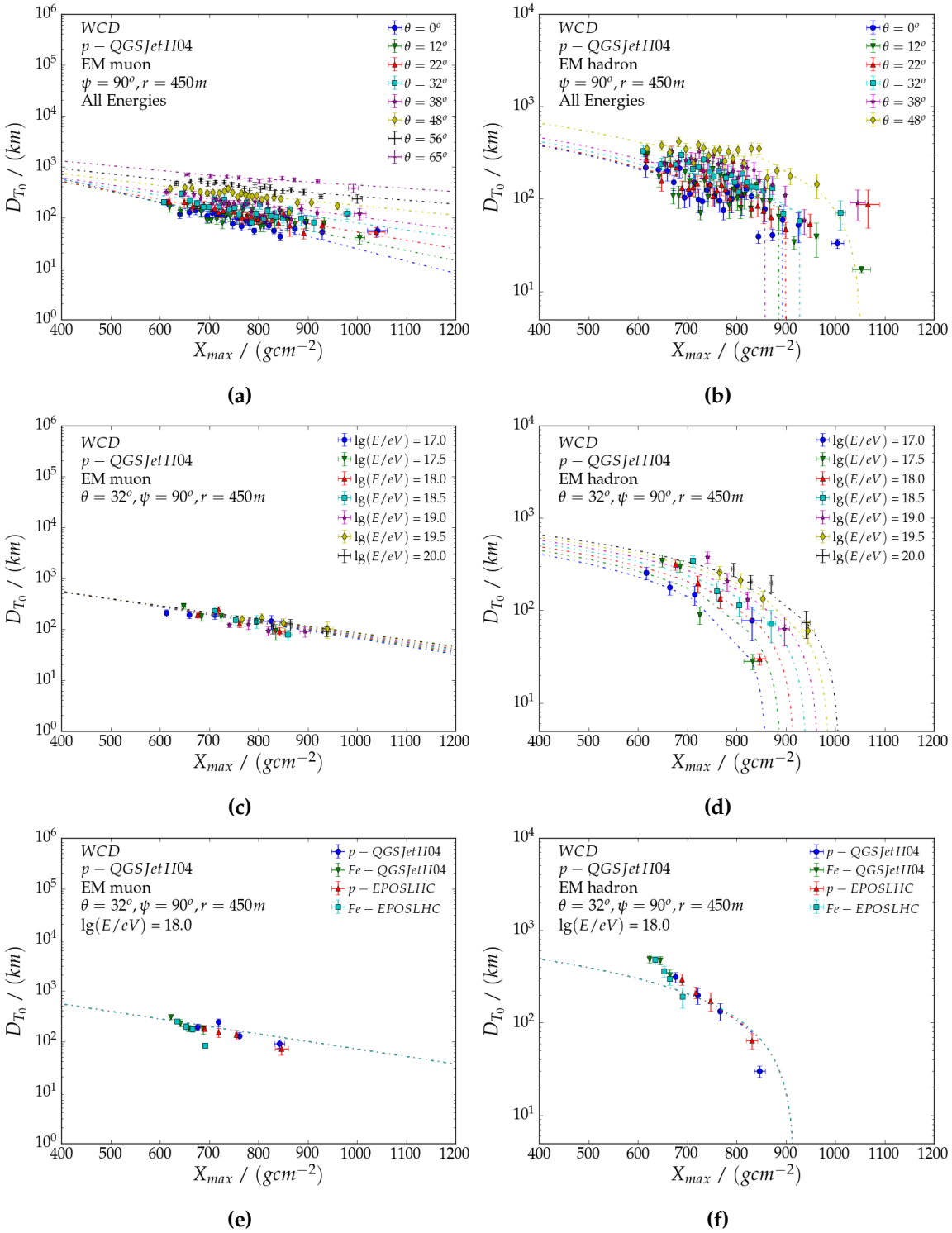
WCD
p − QGSJetII04
EM muon
ψ = 90°, r = 450m
All Energies
θ = 0°
θ = 12°
θ = 22°
θ = 32°
θ = 38°
θ = 48°
θ = 56°
θ = 65°
D_T0 / (km)
X_max / (gcm^-2)
(a)
WCD
p − QGSJetII04
EM hadron
ψ = 90°, r = 450m
All Energies
θ = 0°
θ = 12°
θ = 22°
θ = 32°
θ = 38°
θ = 48°
D_T0 / (km)
X_max / (gcm^-2)
(b)
WCD
p − QGSJetII04
EM muon
θ = 32°, ψ = 90°, r = 450m
lg(E/eV) = 17.0
lg(E/eV) = 17.5
lg(E/eV) = 18.0
lg(E/eV) = 18.5
lg(E/eV) = 19.0
lg(E/eV) = 19.5
lg(E/eV) = 20.0
D_T0 / (km)
X_max / (gcm^-2)
(c)
WCD
p − QGSJetII04
EM hadron
θ = 32°, ψ = 90°, r = 450m
lg(E/eV) = 17.0
lg(E/eV) = 17.5
lg(E/eV) = 18.0
lg(E/eV) = 18.5
lg(E/eV) = 19.0
lg(E/eV) = 19.5
lg(E/eV) = 20.0
D_T0 / (km)
X_max / (gcm^-2)
(d)
WCD
p − QGSJetII04
EM muon
θ = 32°, ψ = 90°, r = 450m
lg(E/eV) = 18.0
p − QGSJetII04
Fe − QGSJetII04
p − EPOSLHC
Fe − EPOSLHC
D_T0 / (km)
X_max / (gcm^-2)
(e)
WCD
p − QGSJetII04
EM hadron
θ = 32°, ψ = 90°, r = 450m
lg(E/eV) = 18.0
p − QGSJetII04
Fe − QGSJetII04
p − EPOSLHC
Fe − EPOSLHC
D_T0 / (km)
X_max / (gcm^-2)
(f)

Figure B.1

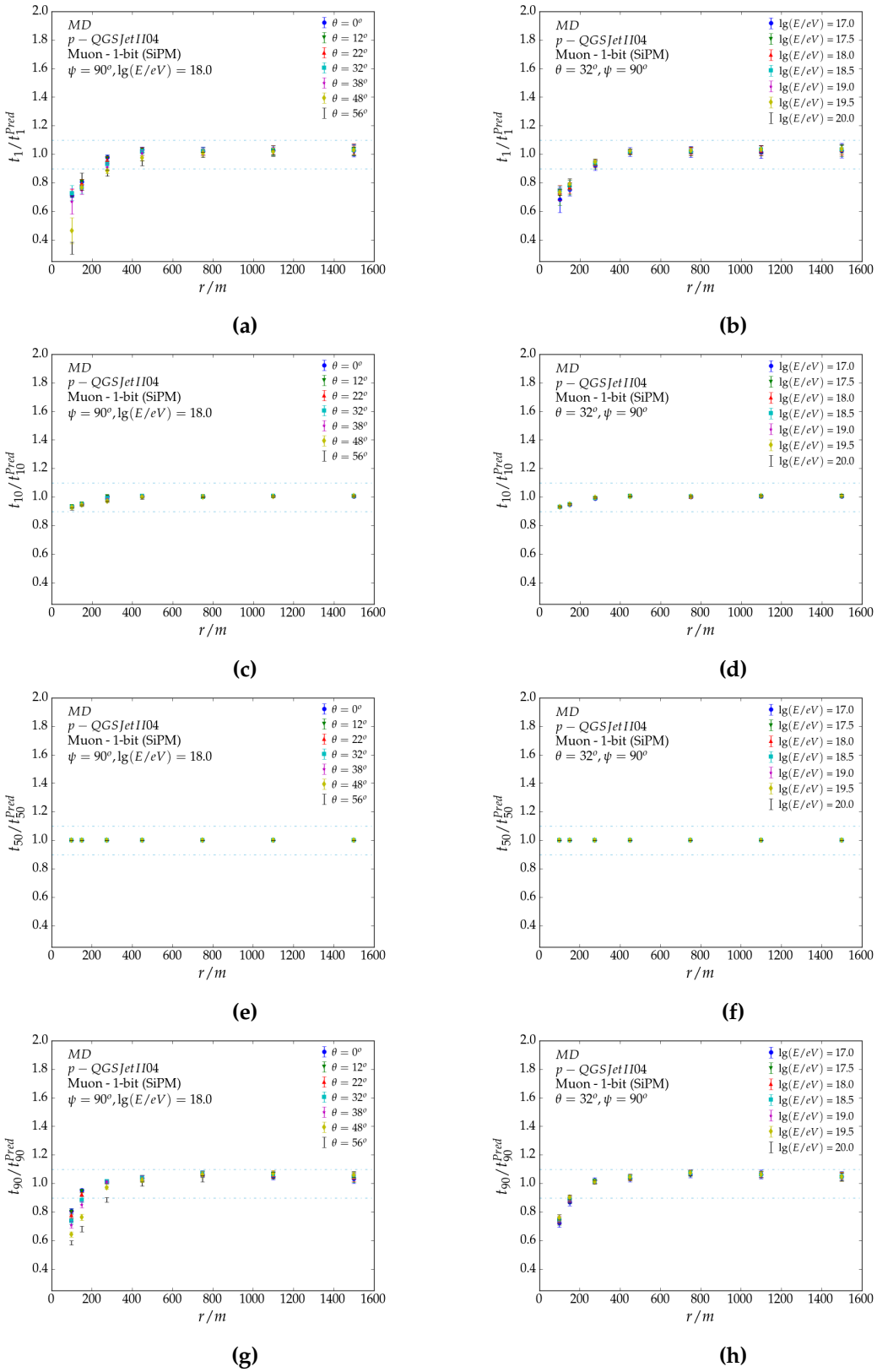
MD
p − QGSJetII04
Muon - 1-bit (SiPM)
ψ = 90°, lg(E/eV) = 18.0
θ = 0°
θ = 12°
θ = 22°
θ = 32°
θ = 38°
θ = 48°
θ = 56°
t1/t1Pred
t10/t10Pred
t50/t50Pred
t90/t90Pred
r/m
(a)
MD
p − QGSJetII04
Muon - 1-bit (SiPM)
θ = 32°, ψ = 90°
lg(E/eV) = 17.0
lg(E/eV) = 17.5
lg(E/eV) = 18.0
lg(E/eV) = 18.5
lg(E/eV) = 19.0
lg(E/eV) = 19.5
lg(E/eV) = 20.0
(b)
(c)
(d)
(e)
(f)
(g)
(h)

Figure B.2

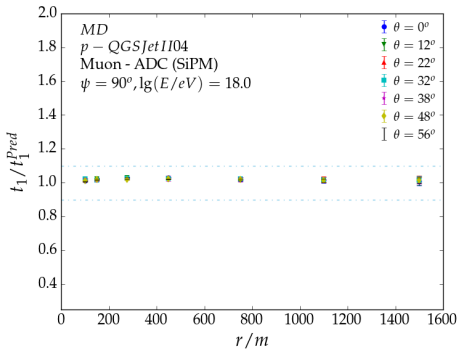

(a)

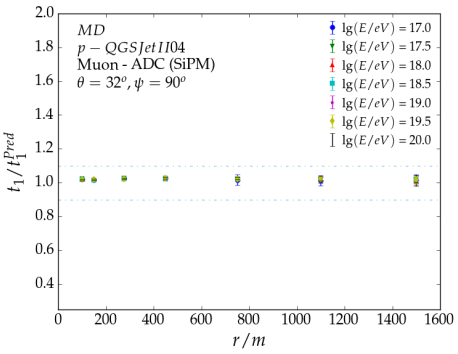

(b)

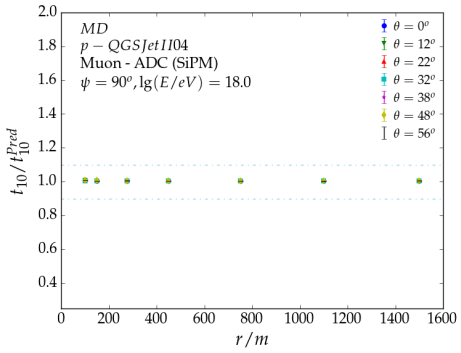

(c)

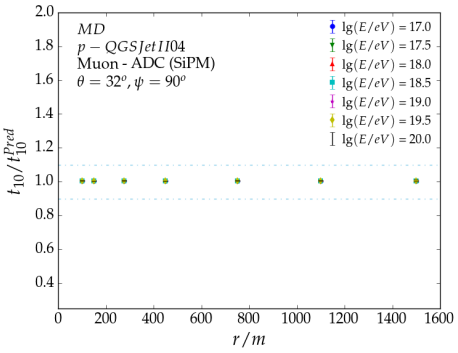

(d)

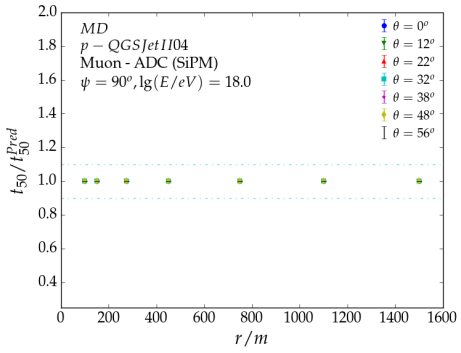

(e)

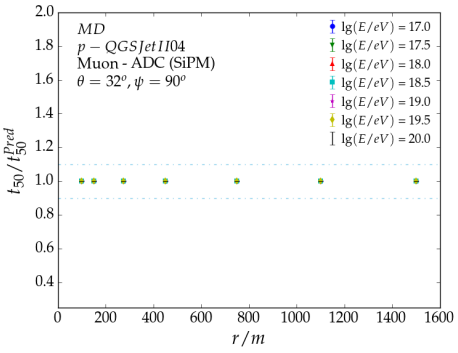

(f)

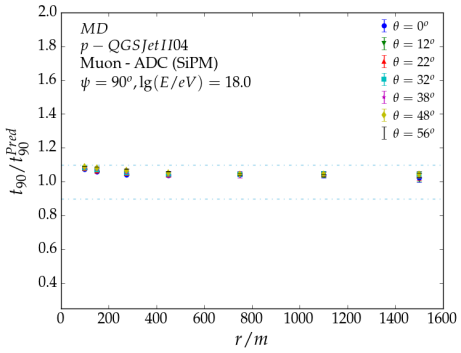

(g)

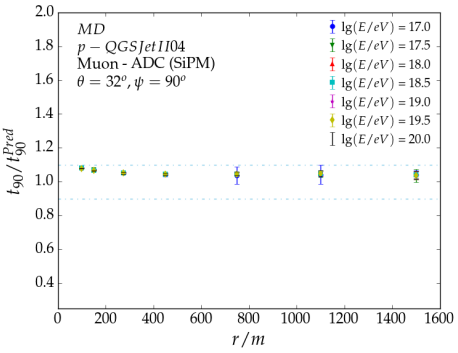

(h)

Figure B.3

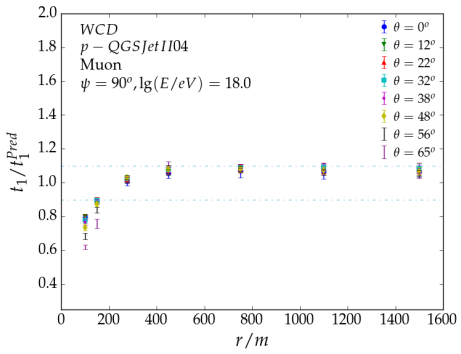

(a)

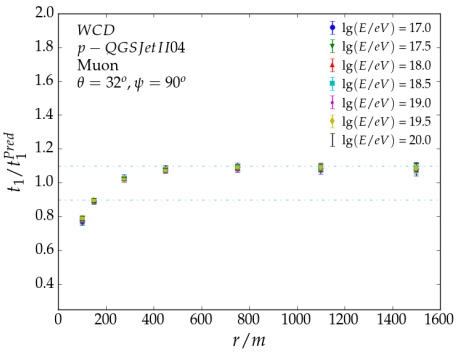

(b)

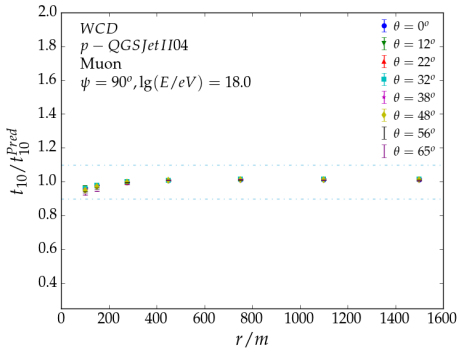

(c)

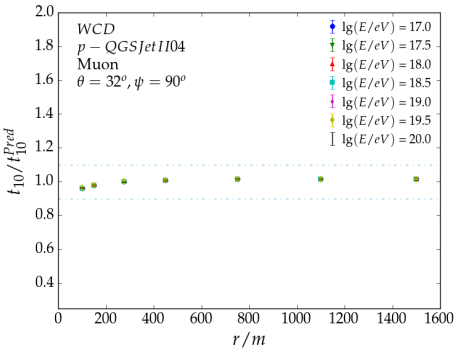

(d)

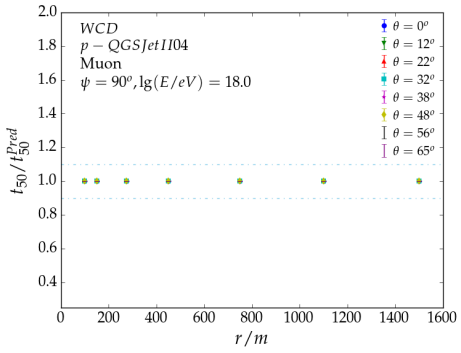

(e)

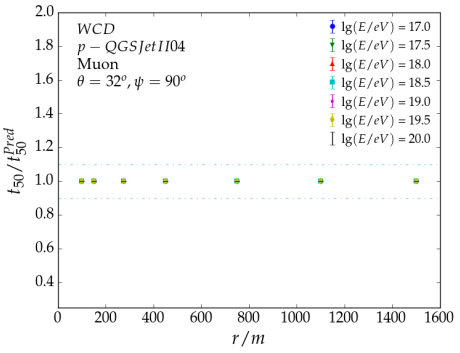

(f)

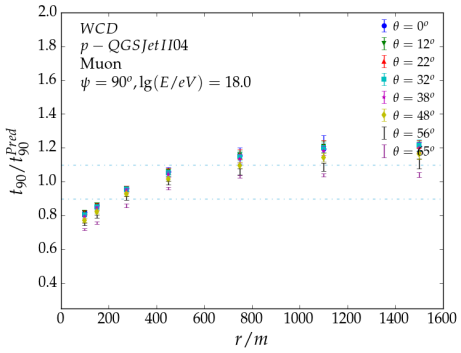

(g)

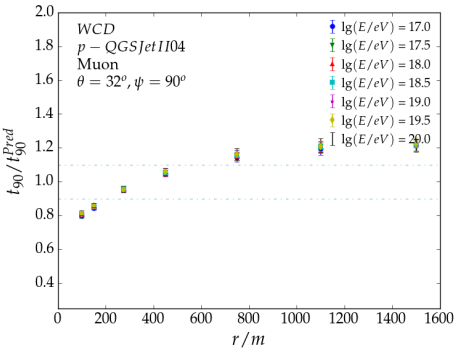

(h)

Figure B.4

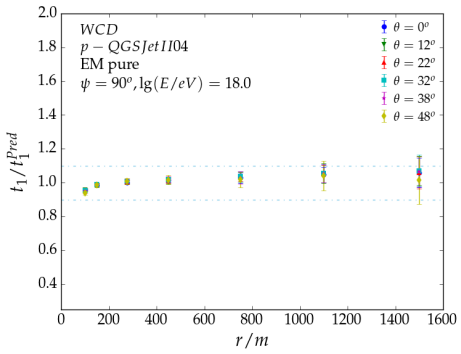

(a)

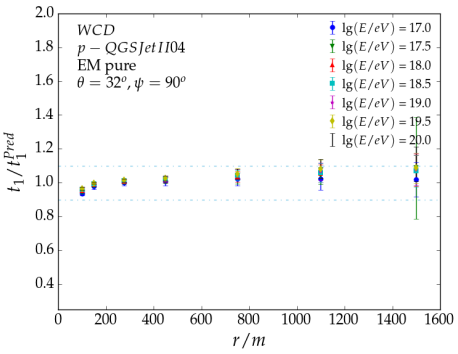

(b)

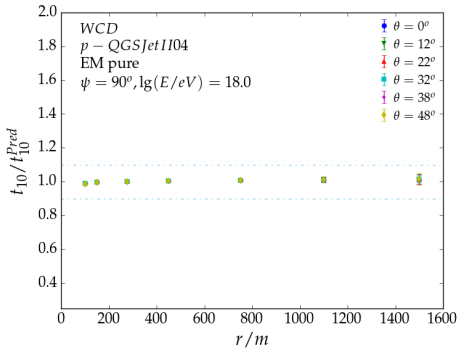

(c)

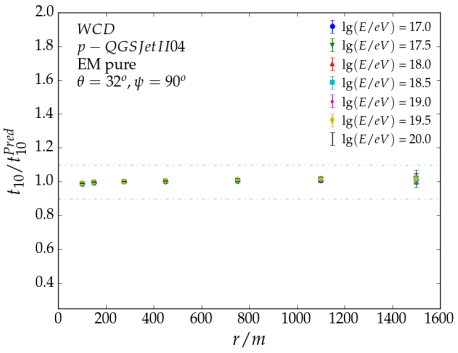

(d)

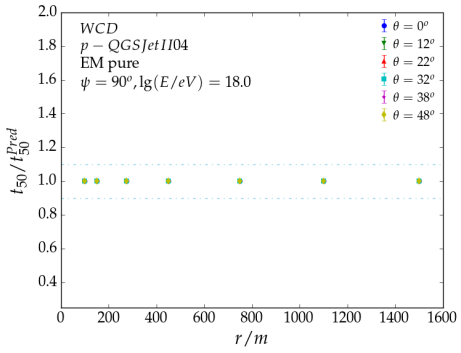

(e)

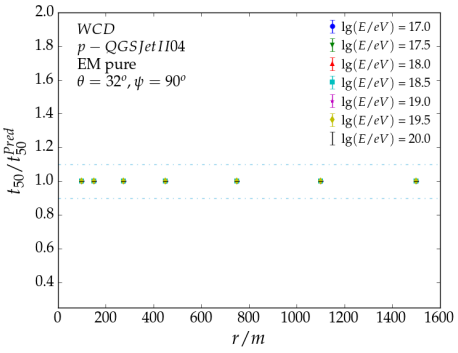

(f)

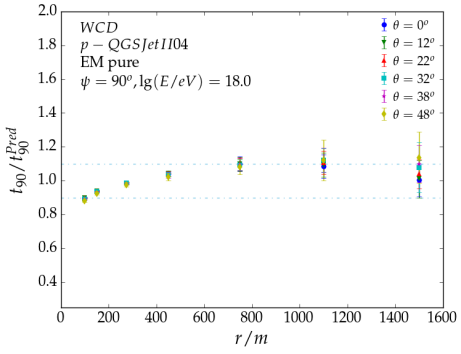

(g)

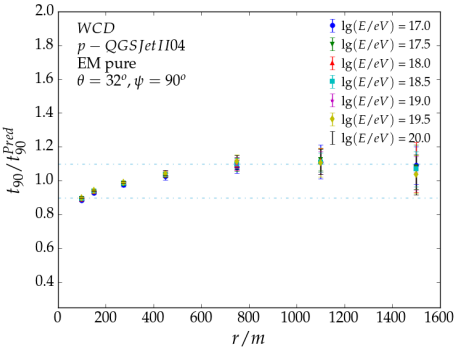

(h)

Figure B.5

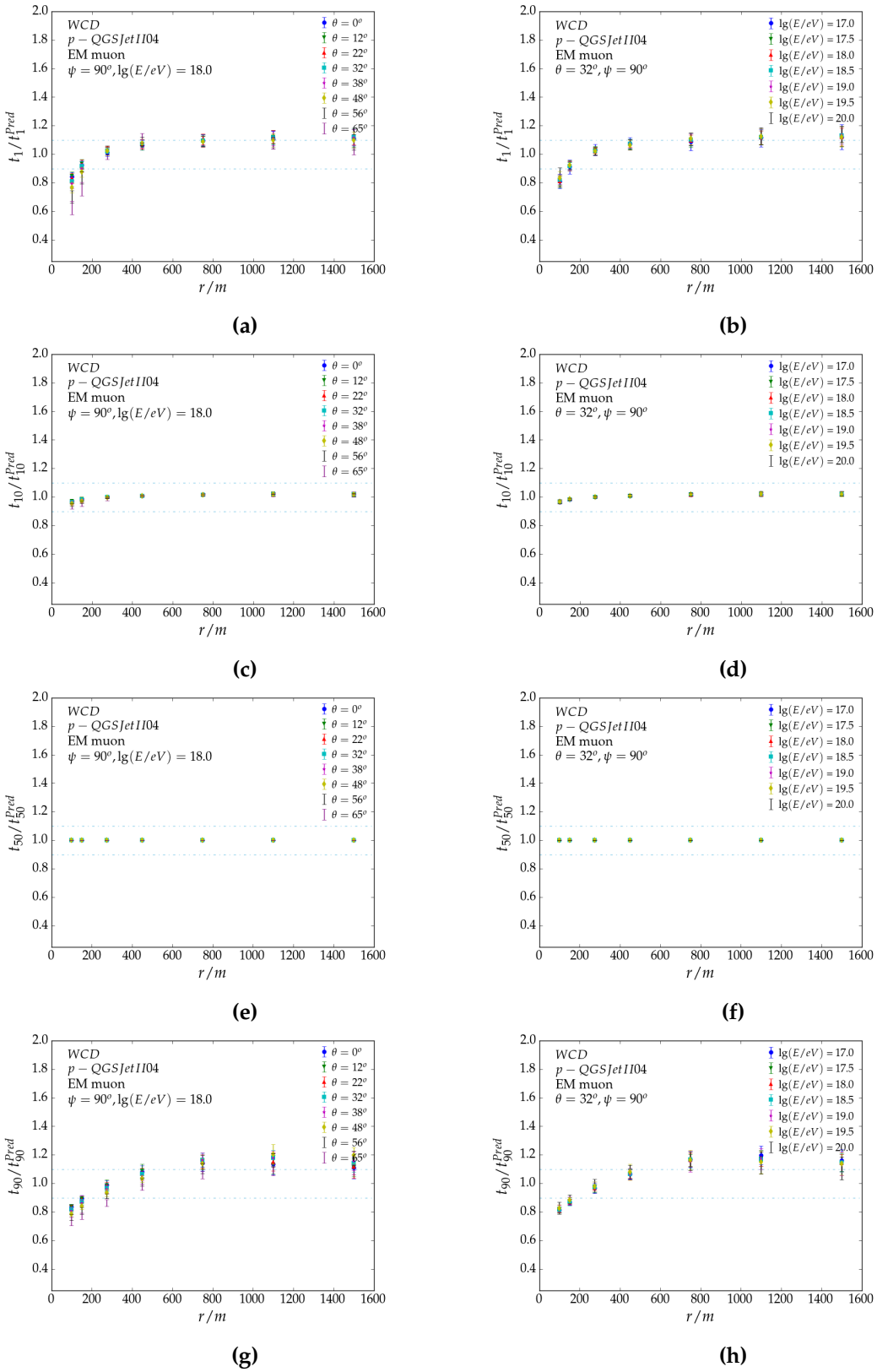
WCD
$p - QGSJetII04$
EM muon
$\psi = 90^o, \lg(E/eV) = 18.0$
$\theta = 0^o$
$\theta = 12^o$
$\theta = 22^o$
$\theta = 32^o$
$\theta = 38^o$
$\theta = 48^o$
$\theta = 56^o$
$\theta = 65^o$
t_1/t_1^{Pred}
r/m
(a)
WCD
$p - QGSJetII04$
EM muon
$\theta = 32^o, \psi = 90^o$
$\lg(E/eV) = 17.0$
$\lg(E/eV) = 17.5$
$\lg(E/eV) = 18.0$
$\lg(E/eV) = 18.5$
$\lg(E/eV) = 19.0$
$\lg(E/eV) = 19.5$
$\lg(E/eV) = 20.0$
t_1/t_1^{Pred}
r/m
(b)
t_{10}/t_{10}^{Pred}
(c)
(d)
t_{50}/t_{50}^{Pred}
(e)
(f)
t_{90}/t_{90}^{Pred}
(g)
(h)

Figure B.6

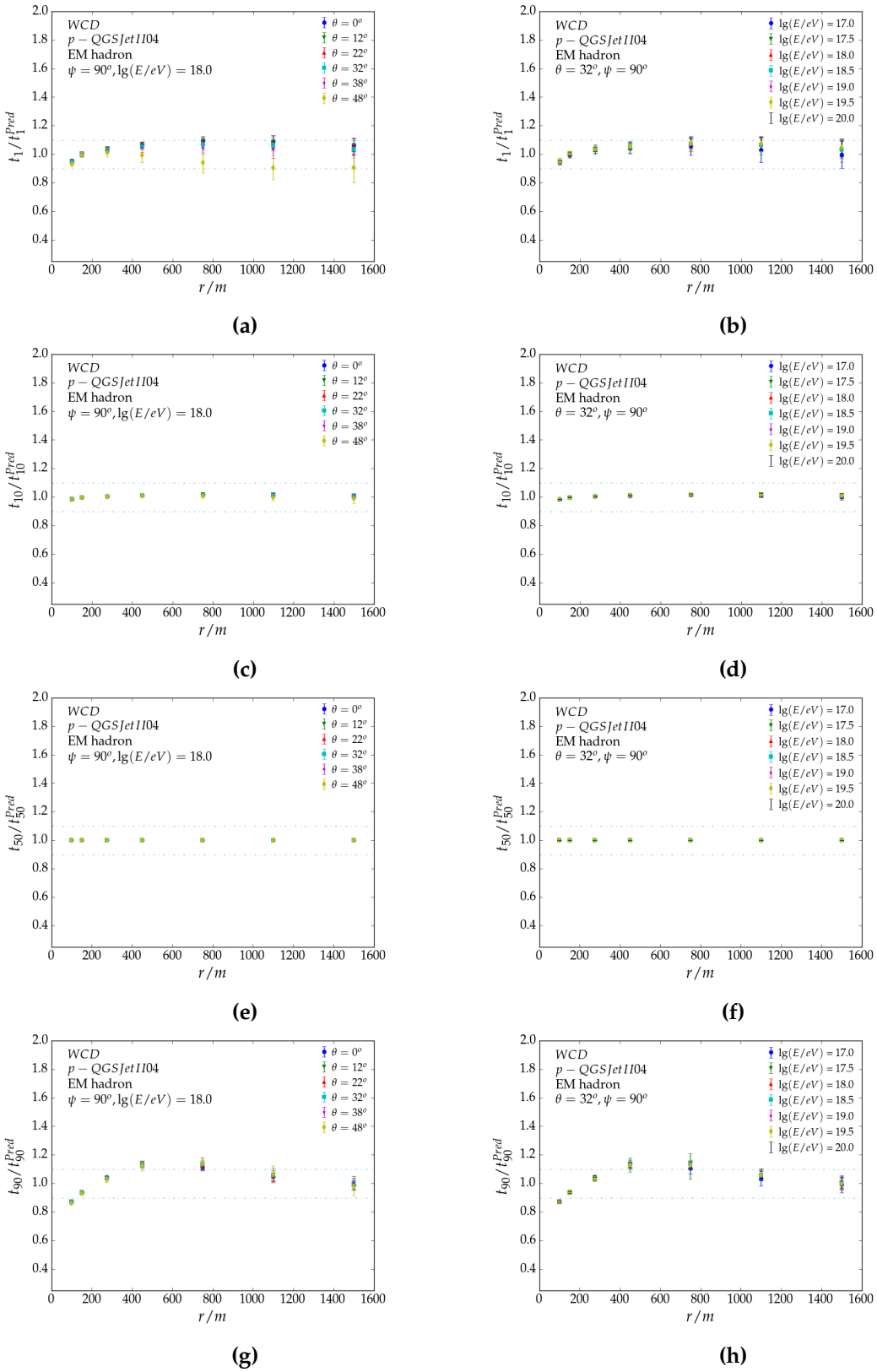
WCD
p − QGSJetII04
EM hadron
ψ = 90°, lg(E/eV) = 18.0
θ = 0°
θ = 12°
θ = 22°
θ = 32°
θ = 38°
θ = 48°
t1/t1Pred
t10/t10Pred
t50/t50Pred
t90/t90Pred
r/m
(a)
WCD
p − QGSJetII04
EM hadron
θ = 32°, ψ = 90°
lg(E/eV) = 17.0
lg(E/eV) = 17.5
lg(E/eV) = 18.0
lg(E/eV) = 18.5
lg(E/eV) = 19.0
lg(E/eV) = 19.5
lg(E/eV) = 20.0
(b)
(c)
(d)
(e)
(f)
(g)
(h)

Figure B.7

B.2 Shape Parameters - m, s

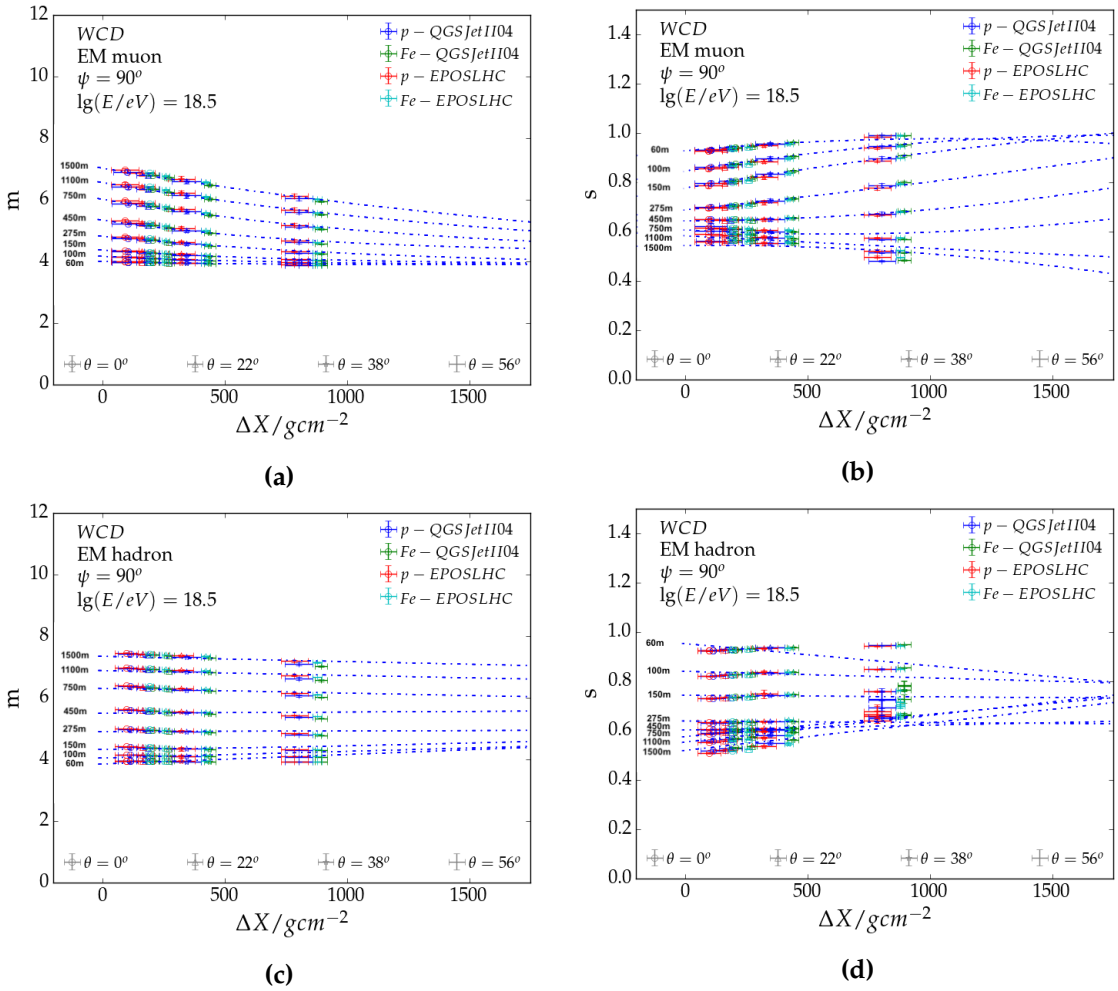

B.3 Time Correction

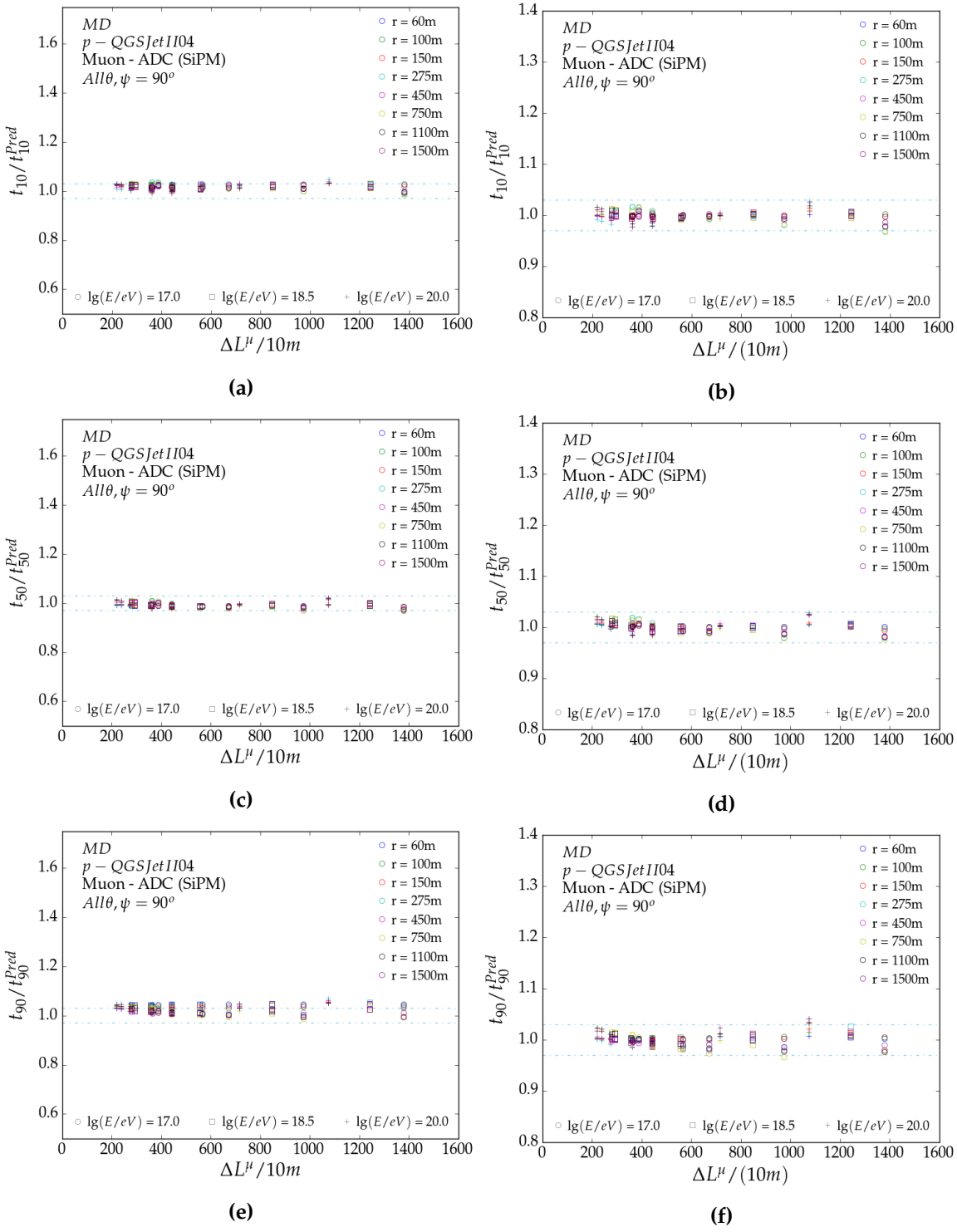

Figure B.9

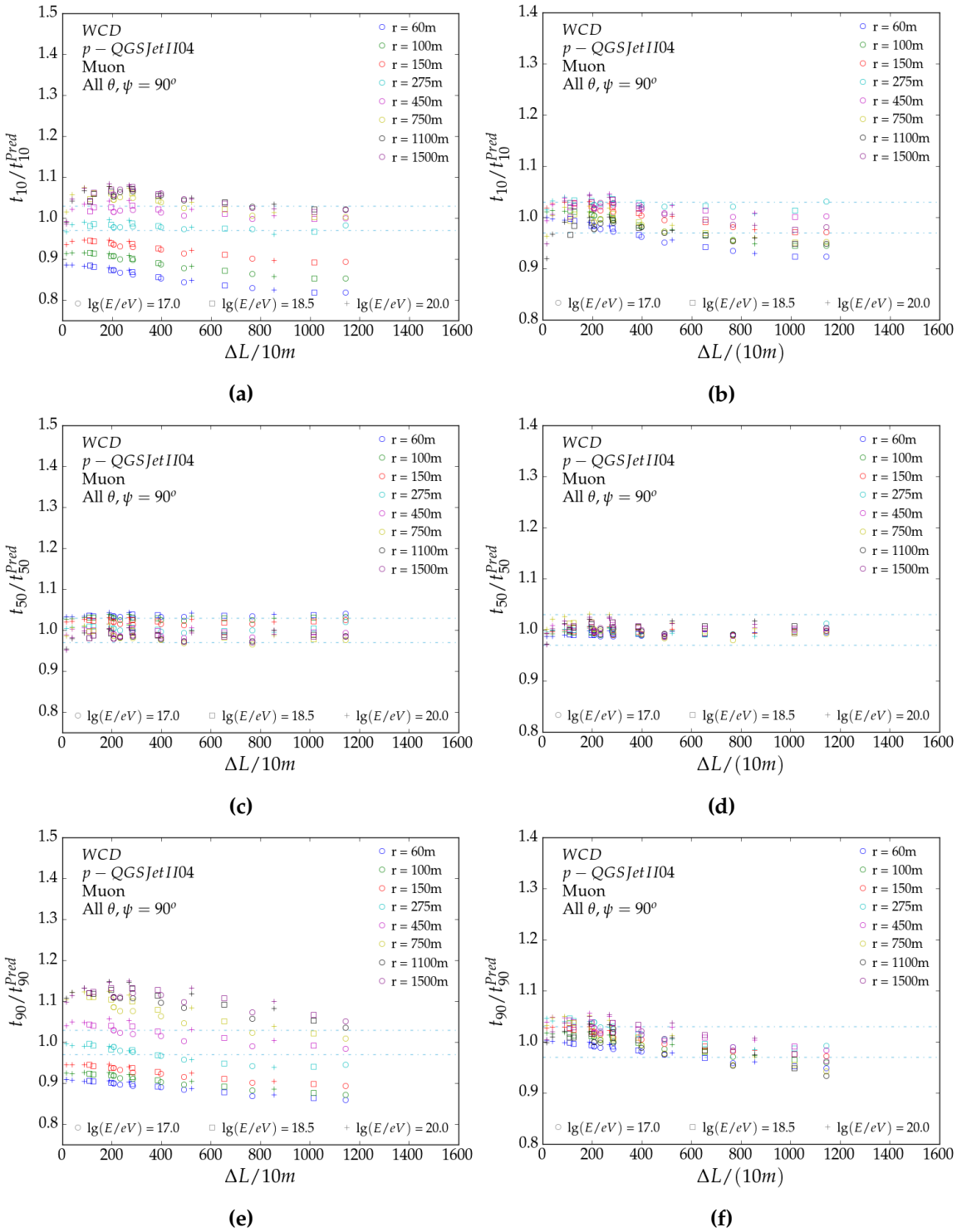
WCD
$p - QGSJetII04$
Muon
All $\theta, \psi = 90^o$
r = 60m
r = 100m
r = 150m
r = 275m
r = 450m
r = 750m
r = 1100m
r = 1500m
$\lg(E/eV) = 17.0$
$\lg(E/eV) = 18.5$
$\lg(E/eV) = 20.0$
t_{10}/t_{10}^{Pred}
t_{50}/t_{50}^{Pred}
t_{90}/t_{90}^{Pred}
$\Delta L/10m$
$\Delta L/(10m)$
(a)
(b)
(c)
(d)
(e)
(f)

Figure B.10

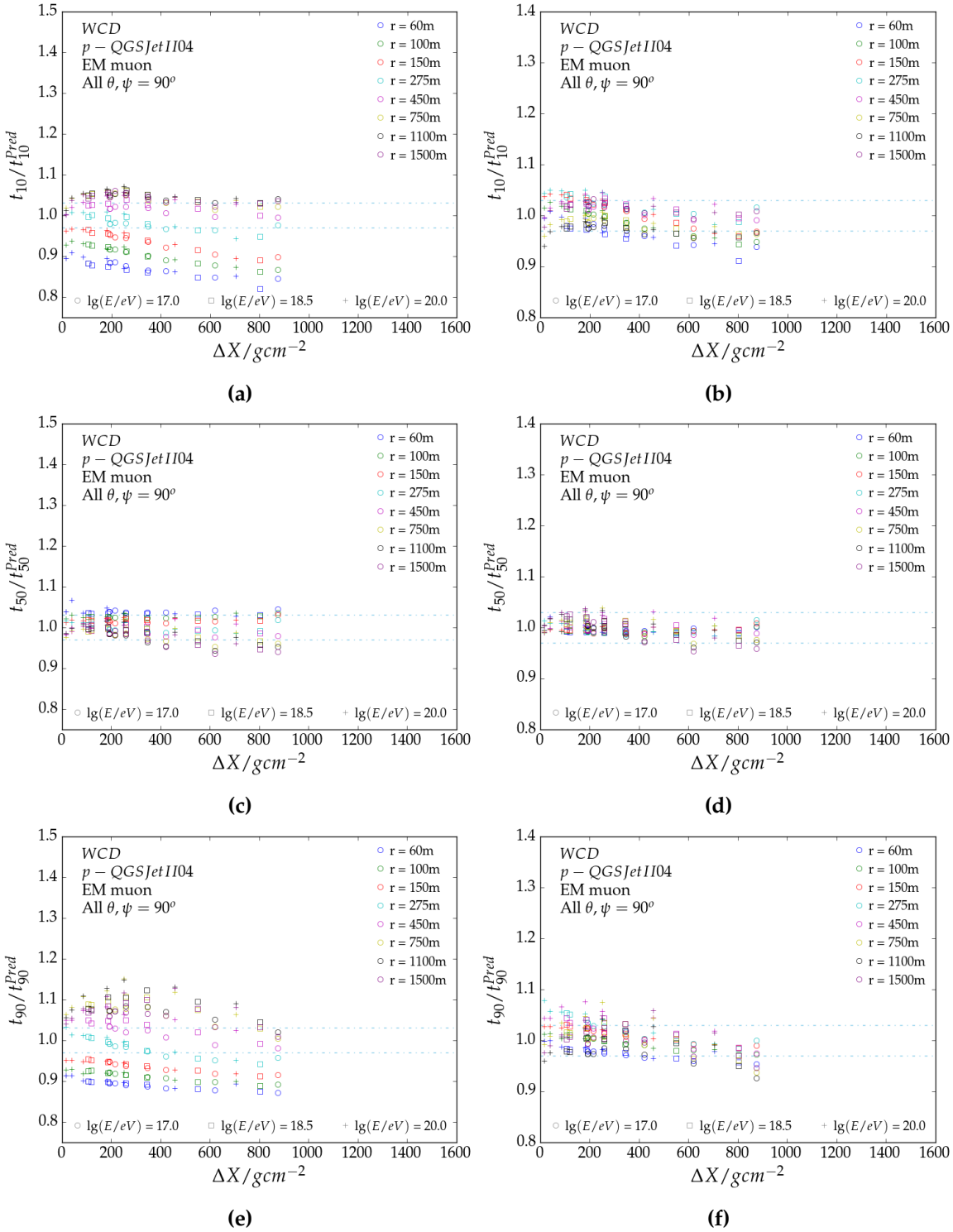
WCD
p − QGSJetII04
EM muon
All θ, ψ = 90°
r = 60m
r = 100m
r = 150m
r = 275m
r = 450m
r = 750m
r = 1100m
r = 1500m
lg(E/eV) = 17.0
lg(E/eV) = 18.5
lg(E/eV) = 20.0
t10/t10Pred
t50/t50Pred
t90/t90Pred
ΔX/gcm−2
(a)
(b)
(c)
(d)
(e)
(f)

Figure B.11

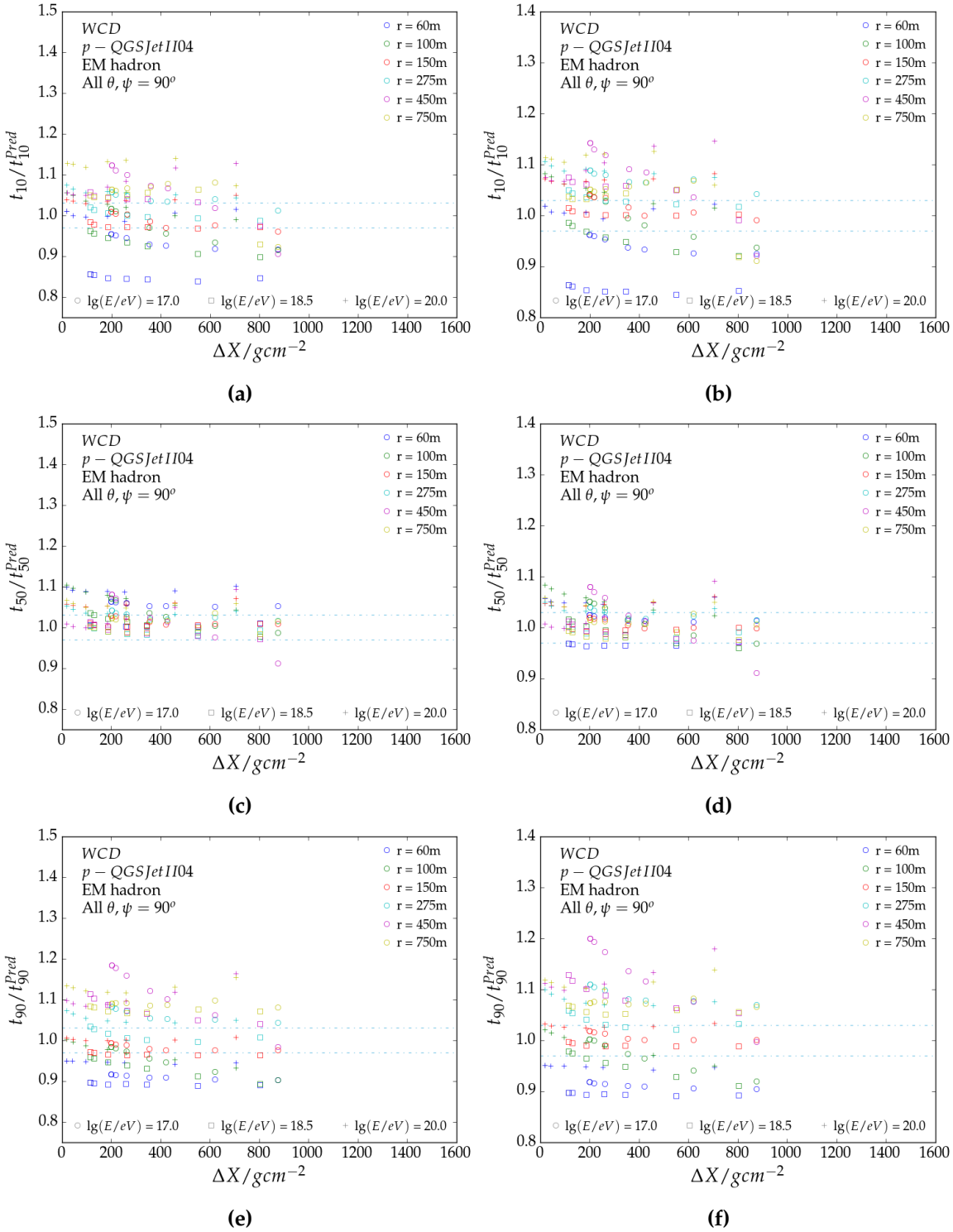
WCD
p − QGSJetII04
EM hadron
All θ, ψ = 90°
r = 60m
r = 100m
r = 150m
r = 275m
r = 450m
r = 750m
lg(E/eV) = 17.0
lg(E/eV) = 18.5
lg(E/eV) = 20.0
t10/t10Pred
t50/t50Pred
t90/t90Pred
ΔX/gcm−2
(a)
(b)
(c)
(d)
(e)
(f)

Figure B.12

B.4 Validation

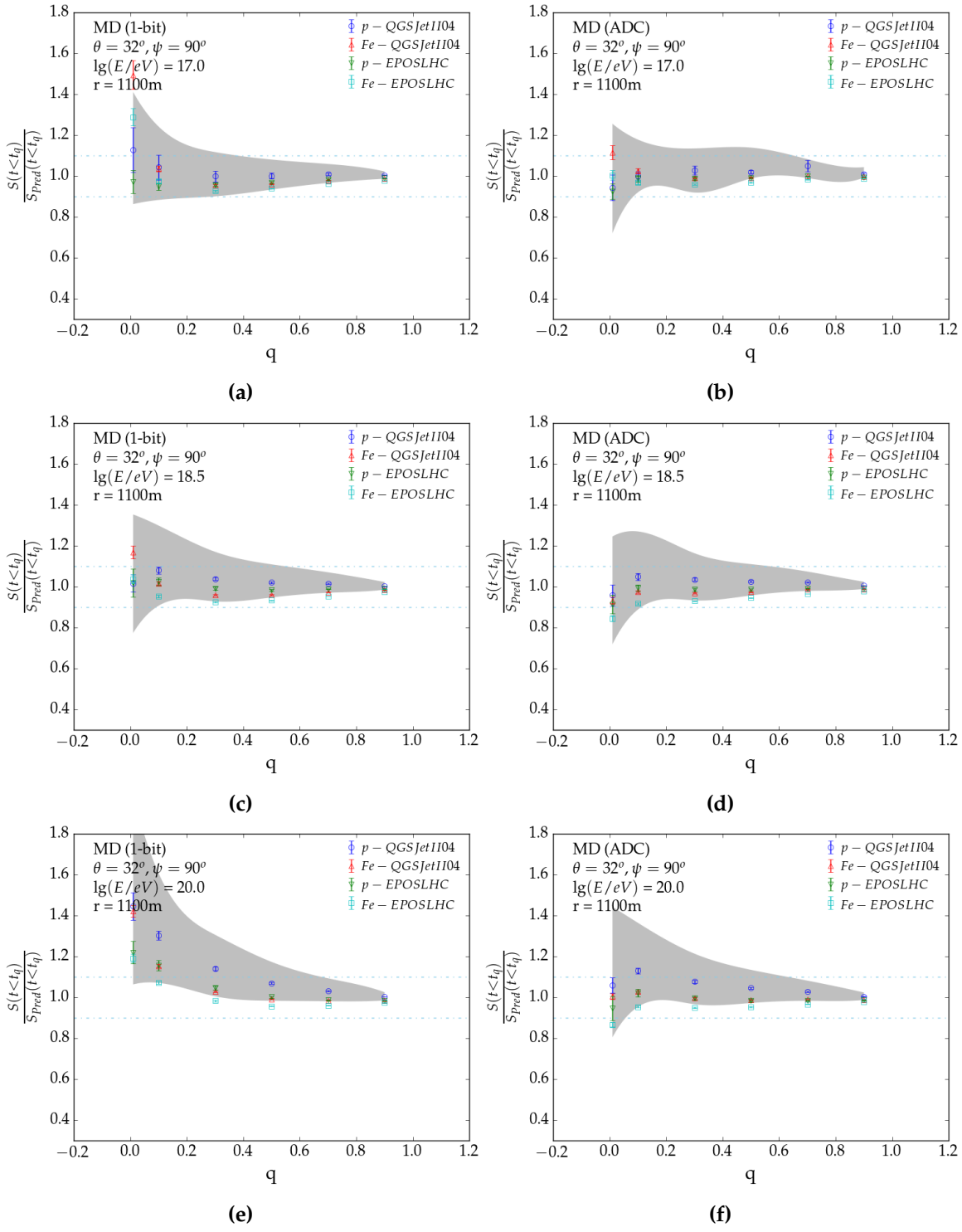

Figure B.13

APPENDIX C

Reconstruction

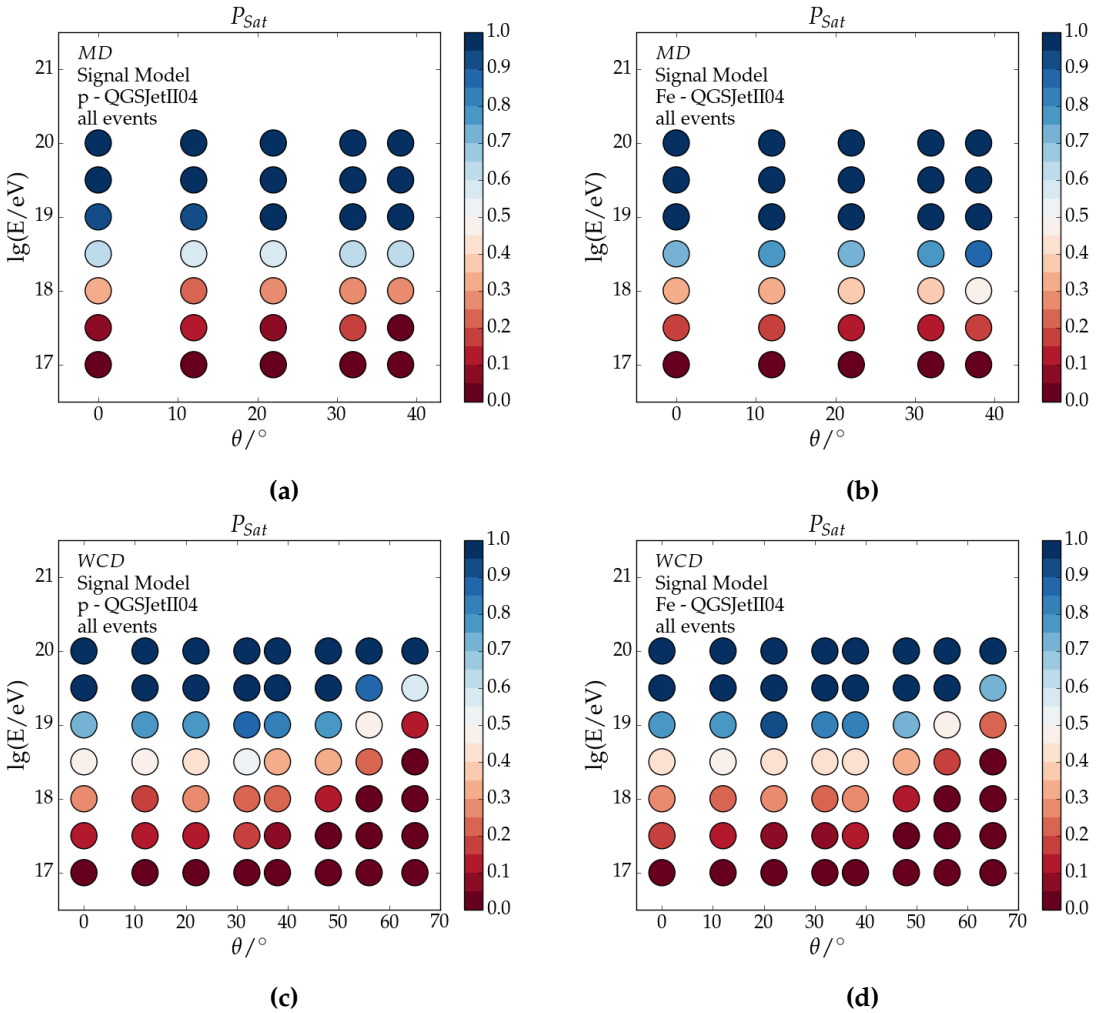

Figure C.1

C.1 WCD-only

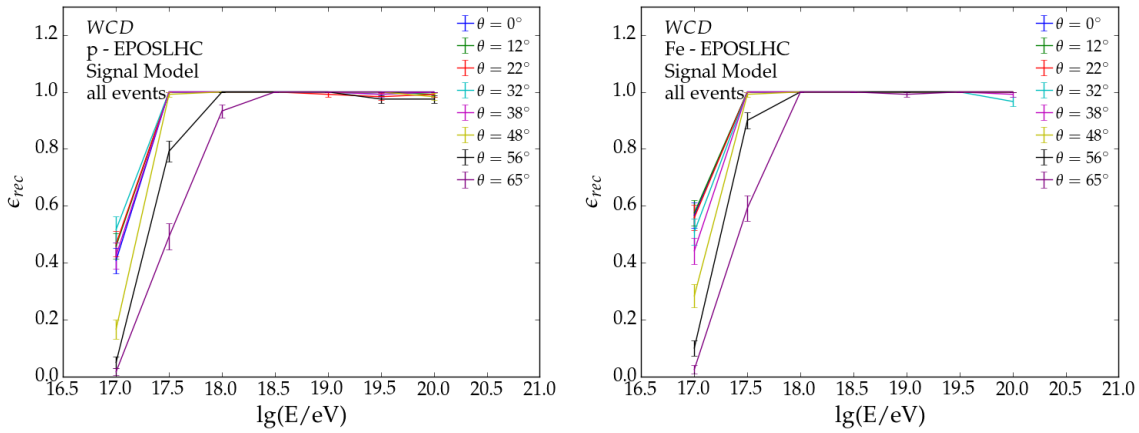

(a) **(b)**

Figure C.2

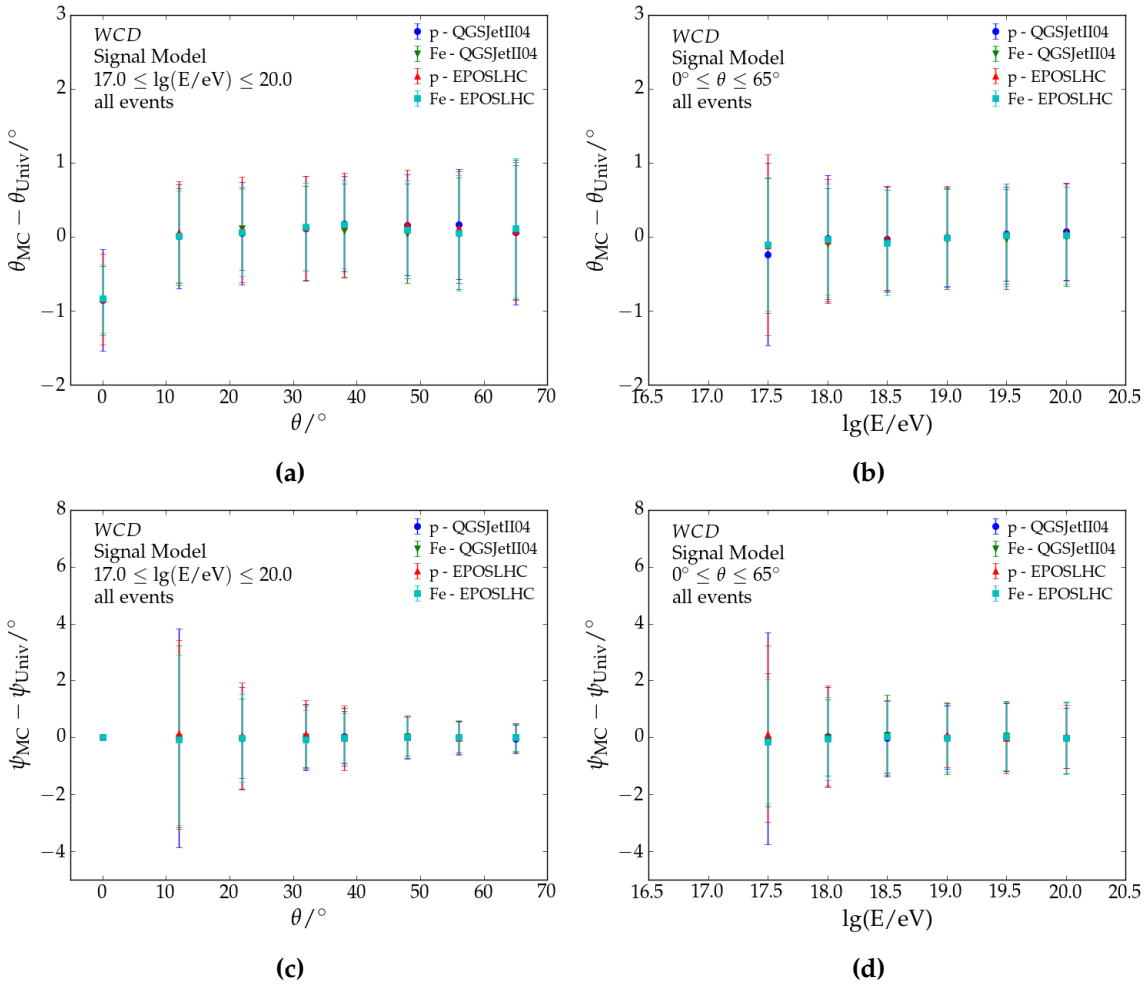

(a) **(b)**

(c) **(d)**

Figure C.3

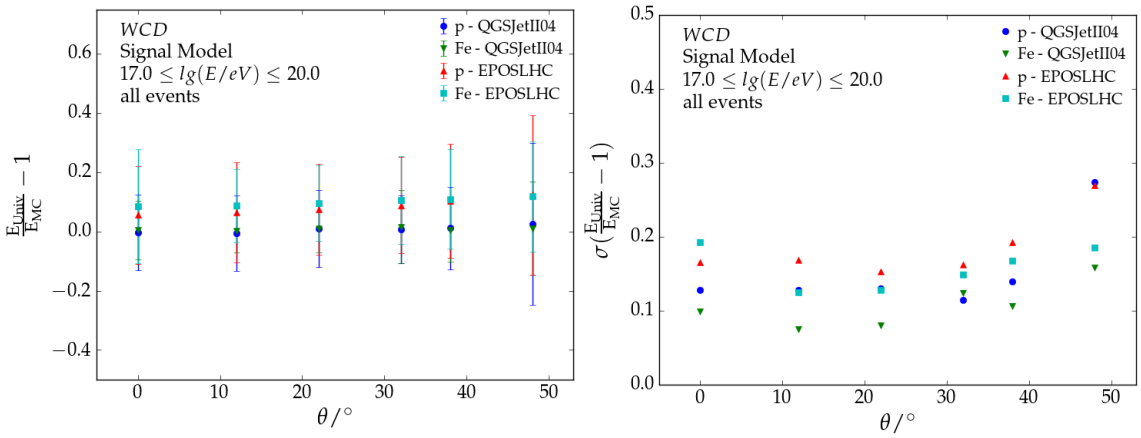

(a) **(b)**

Figure C.4

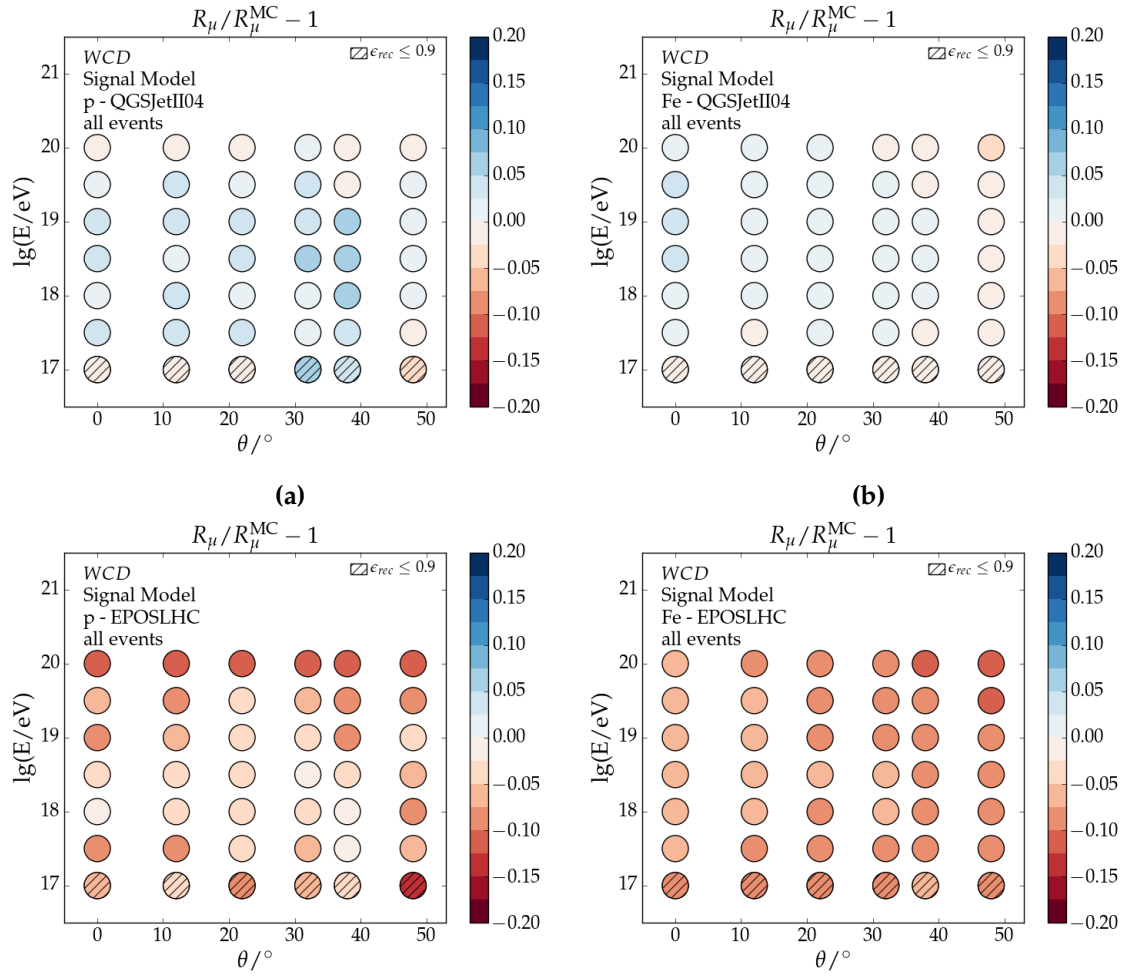

(a) **(b)**

(c) **(d)**

Figure C.5

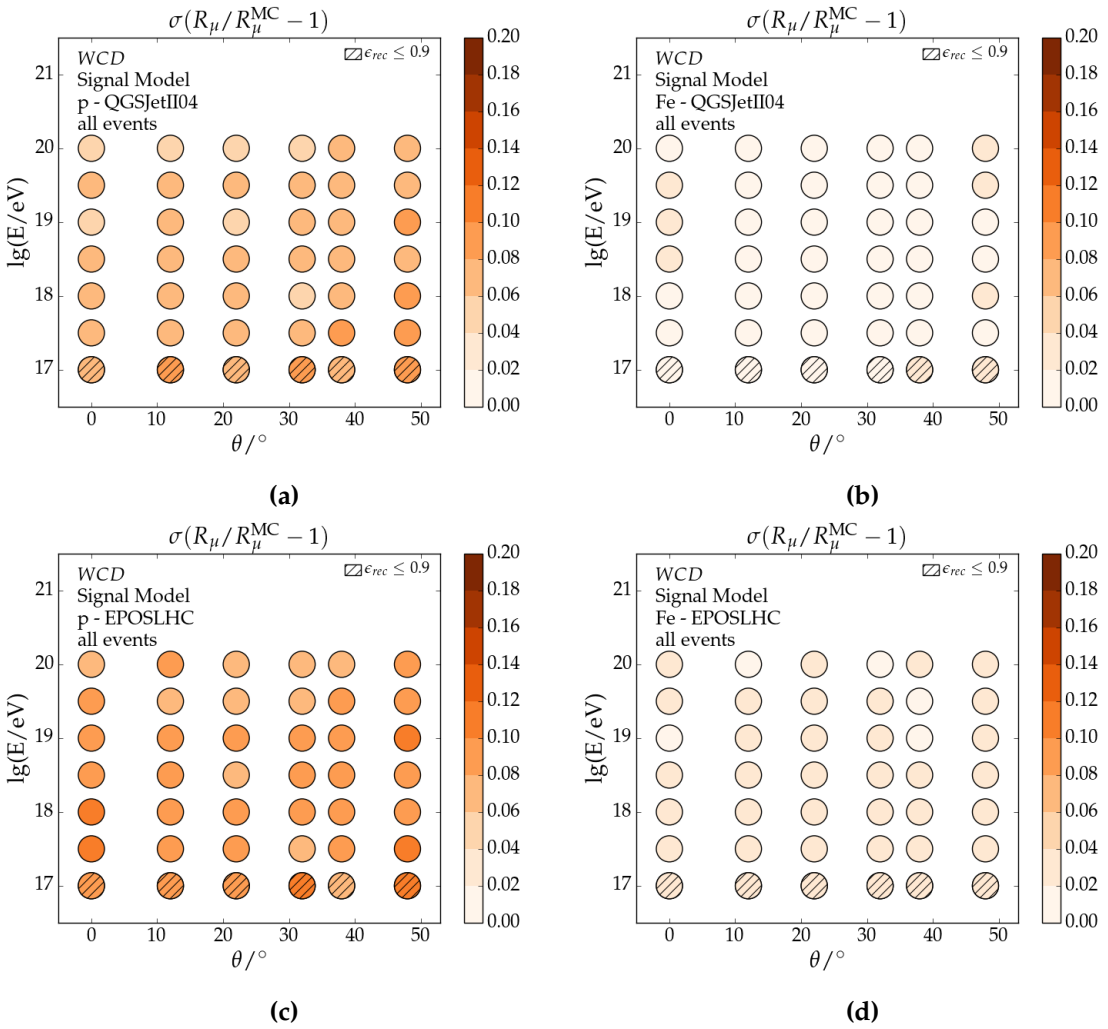
$\sigma(R_\mu/R_\mu^{MC}-1)$
WCD
Signal Model
p - QGSJetII04
all events
$\epsilon_{rec} \leq 0.9$
lg(E/eV)
$\theta/^\circ$
(a)
$\sigma(R_\mu/R_\mu^{MC}-1)$
WCD
Signal Model
Fe - QGSJetII04
all events
$\epsilon_{rec} \leq 0.9$
lg(E/eV)
$\theta/^\circ$
(b)
$\sigma(R_\mu/R_\mu^{MC}-1)$
WCD
Signal Model
p - EPOSLHC
all events
$\epsilon_{rec} \leq 0.9$
lg(E/eV)
$\theta/^\circ$
(c)
$\sigma(R_\mu/R_\mu^{MC}-1)$
WCD
Signal Model
Fe - EPOSLHC
all events
$\epsilon_{rec} \leq 0.9$
lg(E/eV)
$\theta/^\circ$
(d)

Figure C.6

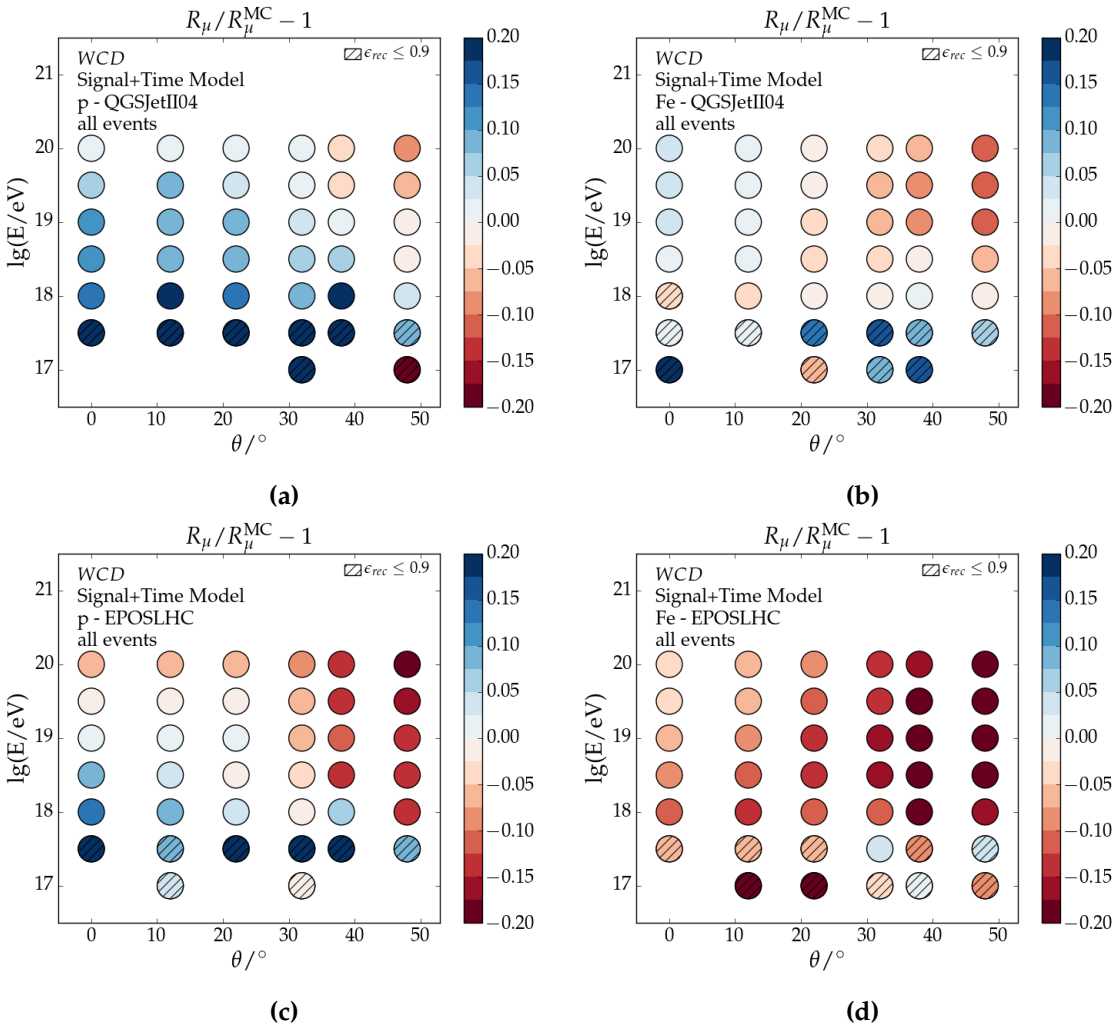
$R_\mu / R_\mu^{\mathrm{MC}} - 1$
WCD
Signal+Time Model
p - QGSJetII04
all events
$\epsilon_{rec} \leq 0.9$
lg(E/eV)
$\theta / ^\circ$
(a)
$R_\mu / R_\mu^{\mathrm{MC}} - 1$
WCD
Signal+Time Model
Fe - QGSJetII04
all events
$\epsilon_{rec} \leq 0.9$
lg(E/eV)
$\theta / ^\circ$
(b)
$R_\mu / R_\mu^{\mathrm{MC}} - 1$
WCD
Signal+Time Model
p - EPOSLHC
all events
$\epsilon_{rec} \leq 0.9$
lg(E/eV)
$\theta / ^\circ$
(c)
$R_\mu / R_\mu^{\mathrm{MC}} - 1$
WCD
Signal+Time Model
Fe - EPOSLHC
all events
$\epsilon_{rec} \leq 0.9$
lg(E/eV)
$\theta / ^\circ$
(d)

Figure C.7

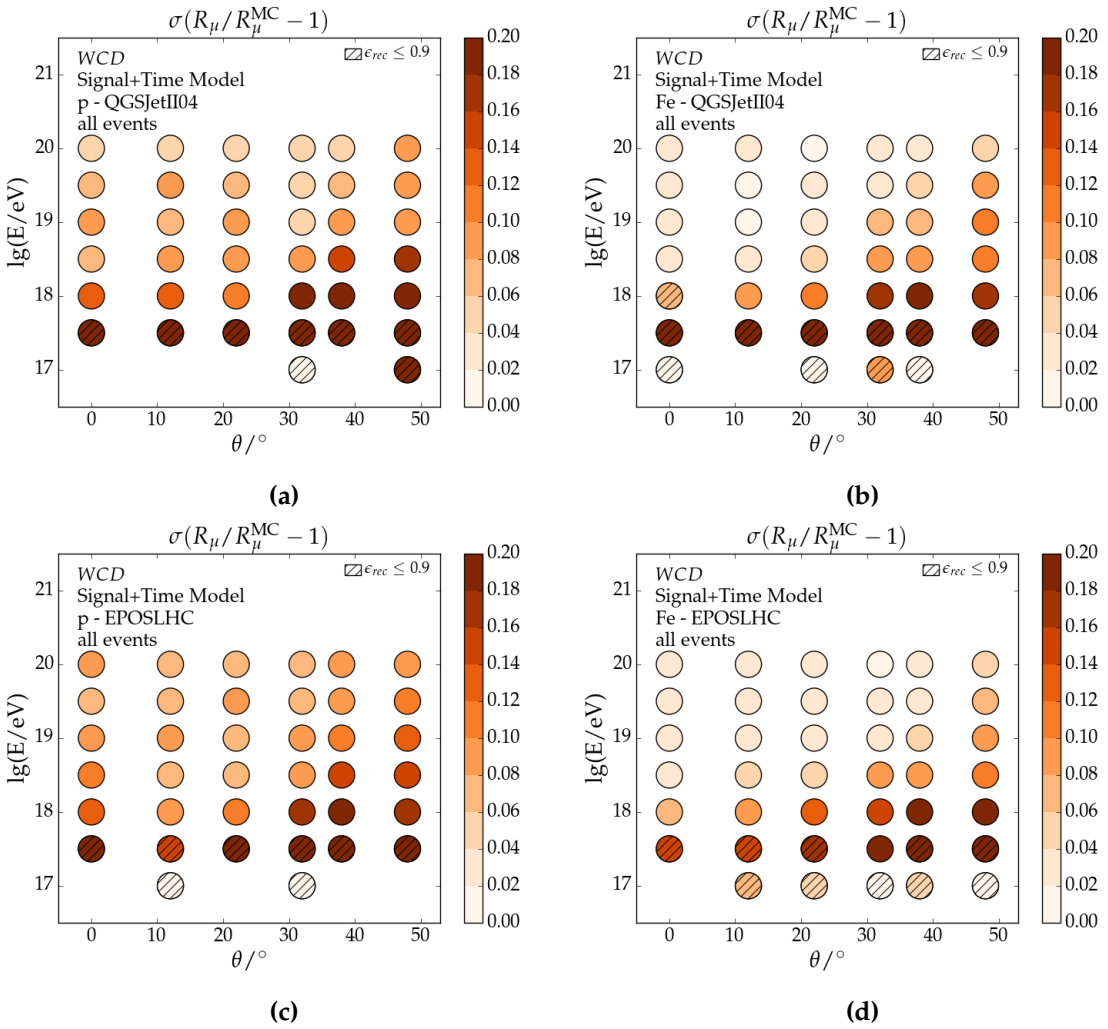
$\sigma(R_\mu/R_\mu^{MC}-1)$
WCD
Signal+Time Model
p - QGSJetII04
all events
$\epsilon_{rec} \leq 0.9$
lg(E/eV)
$\theta/^\circ$
(a)
$\sigma(R_\mu/R_\mu^{MC}-1)$
WCD
Signal+Time Model
Fe - QGSJetII04
all events
$\epsilon_{rec} \leq 0.9$
lg(E/eV)
$\theta/^\circ$
(b)
$\sigma(R_\mu/R_\mu^{MC}-1)$
WCD
Signal+Time Model
p - EPOSLHC
all events
$\epsilon_{rec} \leq 0.9$
lg(E/eV)
$\theta/^\circ$
(c)
$\sigma(R_\mu/R_\mu^{MC}-1)$
WCD
Signal+Time Model
Fe - EPOSLHC
all events
$\epsilon_{rec} \leq 0.9$
lg(E/eV)
$\theta/^\circ$
(d)

Figure C.8

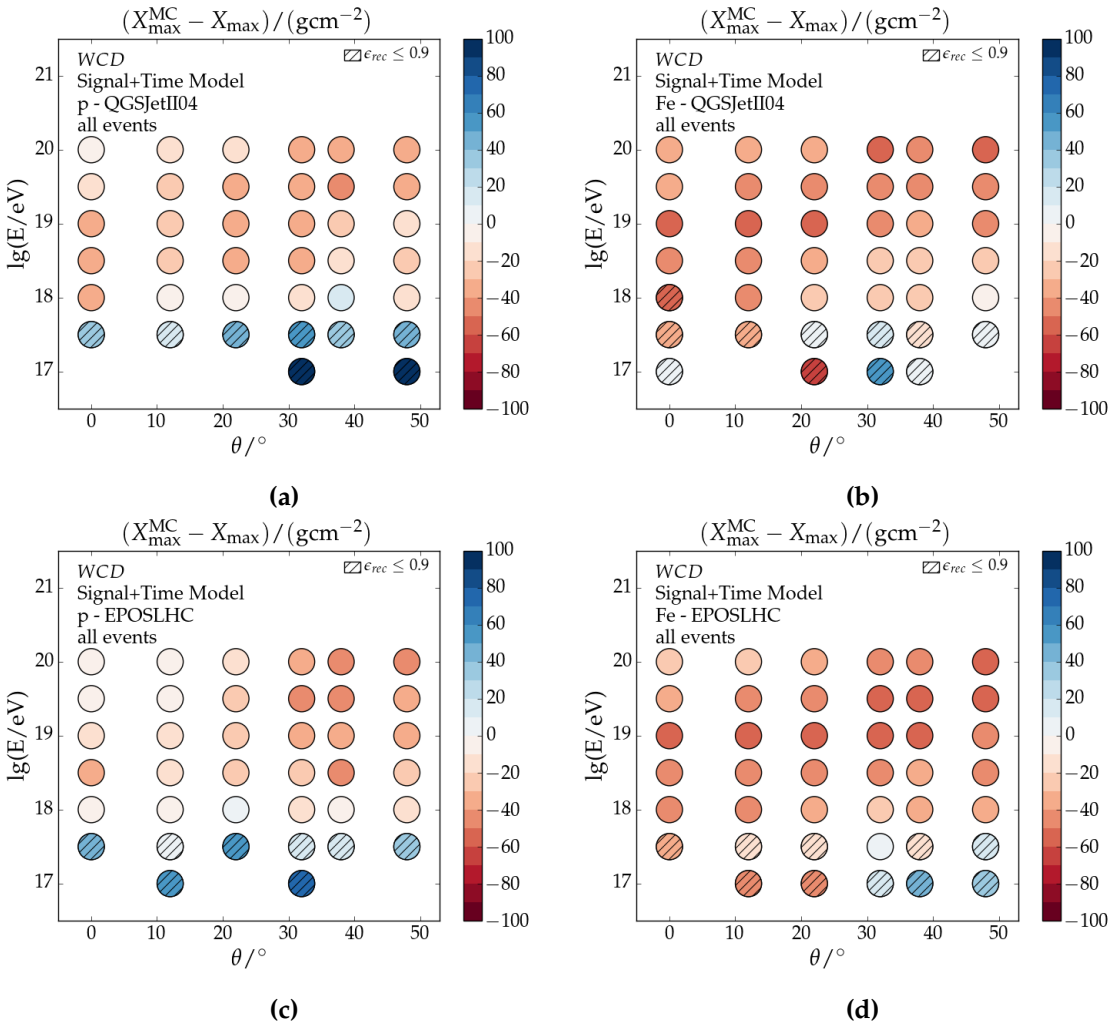
$(X^{MC}_{max} - X_{max})/(gcm^{-2})$
WCD
Signal+Time Model
p - QGSJetII04
all events
$\epsilon_{rec} \leq 0.9$
lg(E/eV)
$\theta/^\circ$
(a)
$(X^{MC}_{max} - X_{max})/(gcm^{-2})$
WCD
Signal+Time Model
Fe - QGSJetII04
all events
$\epsilon_{rec} \leq 0.9$
lg(E/eV)
$\theta/^\circ$
(b)
$(X^{MC}_{max} - X_{max})/(gcm^{-2})$
WCD
Signal+Time Model
p - EPOSLHC
all events
$\epsilon_{rec} \leq 0.9$
lg(E/eV)
$\theta/^\circ$
(c)
$(X^{MC}_{max} - X_{max})/(gcm^{-2})$
WCD
Signal+Time Model
Fe - EPOSLHC
all events
$\epsilon_{rec} \leq 0.9$
lg(E/eV)
$\theta/^\circ$
(d)

Figure C.9

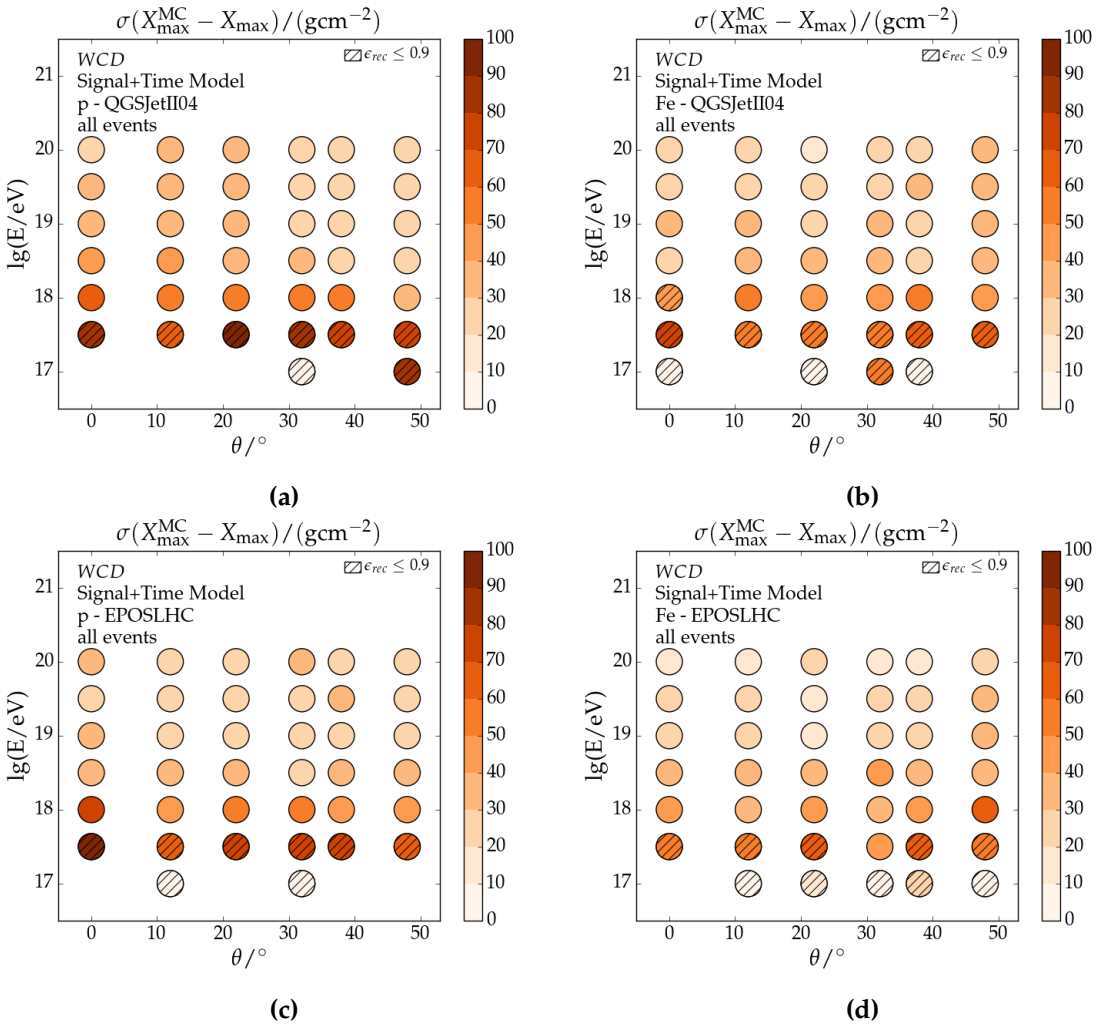

Figure C.10

C.2 MD-only

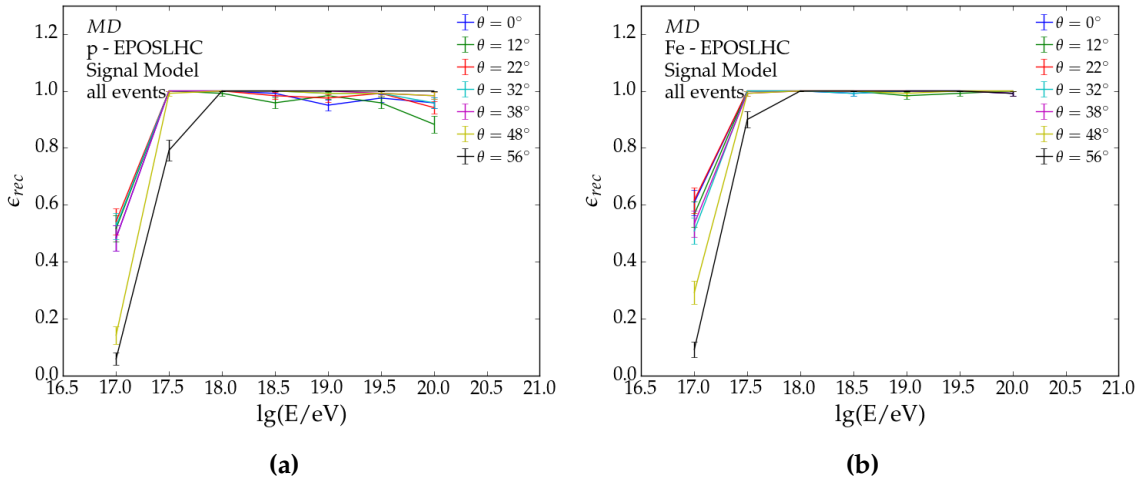

Figure C.11: Fit efficiency for successful MD-only reconstructions of **a)** proton and **b)** iron induced air showers. Each energy-zenith bin accounts for 120 air showers.

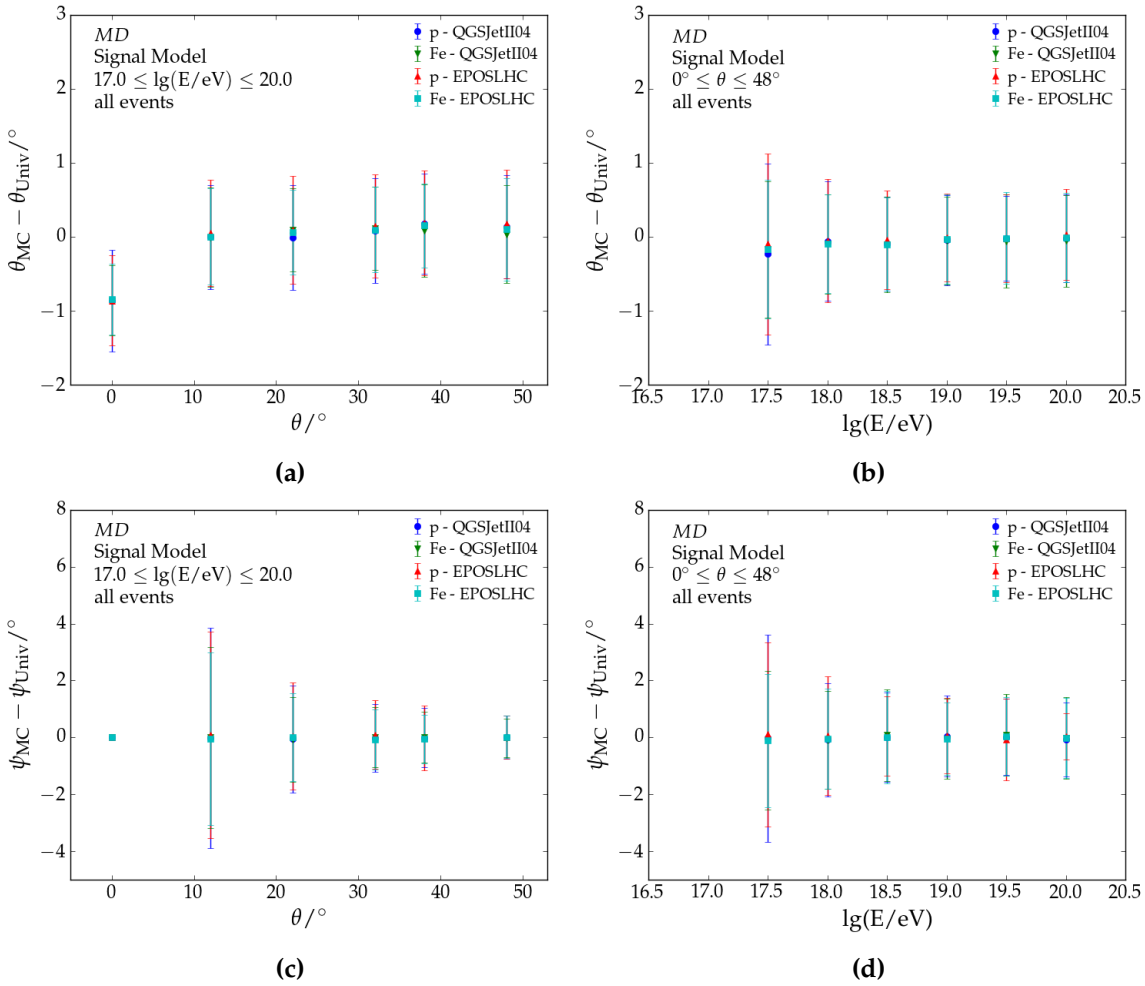
MD
Signal Model
17.0 ≤ lg(E/eV) ≤ 20.0
all events
p - QGSJetII04
Fe - QGSJetII04
p - EPOSLHC
Fe - EPOSLHC
θMC − θUniv / °
θ / °
(a)
MD
Signal Model
0° ≤ θ ≤ 48°
all events
p - QGSJetII04
Fe - QGSJetII04
p - EPOSLHC
Fe - EPOSLHC
θMC − θUniv / °
lg(E/eV)
(b)
MD
Signal Model
17.0 ≤ lg(E/eV) ≤ 20.0
all events
p - QGSJetII04
Fe - QGSJetII04
p - EPOSLHC
Fe - EPOSLHC
ψMC − ψUniv / °
θ / °
(c)
MD
Signal Model
0° ≤ θ ≤ 48°
all events
p - QGSJetII04
Fe - QGSJetII04
p - EPOSLHC
Fe - EPOSLHC
ψMC − ψUniv / °
lg(E/eV)
(d)

Figure C.12

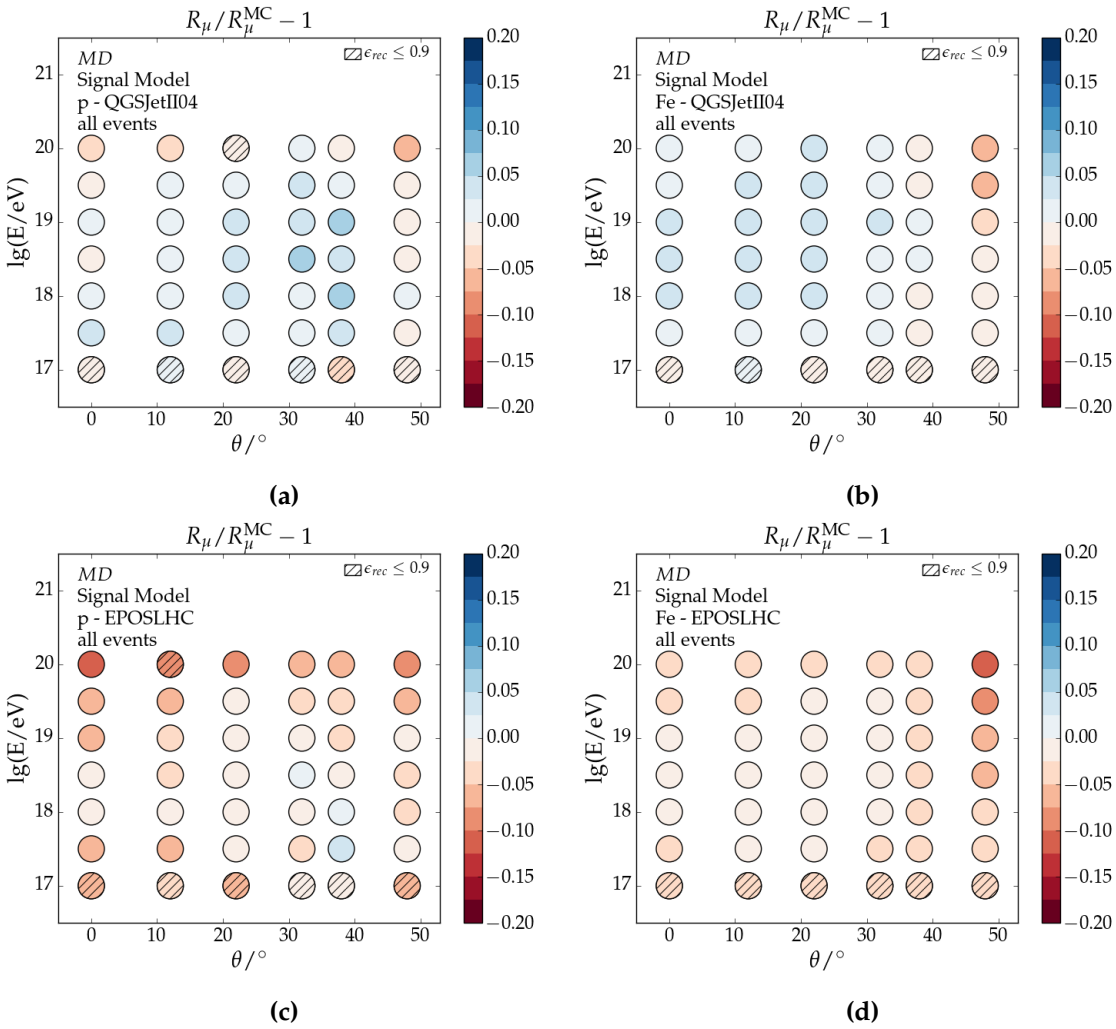
$R_\mu / R_\mu^{\mathrm{MC}} - 1$
MD
Signal Model
p - QGSJetII04
all events
$\epsilon_{rec} \leq 0.9$
lg(E/eV)
$\theta / ^\circ$
(a)
$R_\mu / R_\mu^{\mathrm{MC}} - 1$
MD
Signal Model
Fe - QGSJetII04
all events
$\epsilon_{rec} \leq 0.9$
lg(E/eV)
$\theta / ^\circ$
(b)
$R_\mu / R_\mu^{\mathrm{MC}} - 1$
MD
Signal Model
p - EPOSLHC
all events
$\epsilon_{rec} \leq 0.9$
lg(E/eV)
$\theta / ^\circ$
(c)
$R_\mu / R_\mu^{\mathrm{MC}} - 1$
MD
Signal Model
Fe - EPOSLHC
all events
$\epsilon_{rec} \leq 0.9$
lg(E/eV)
$\theta / ^\circ$
(d)

Figure C.13

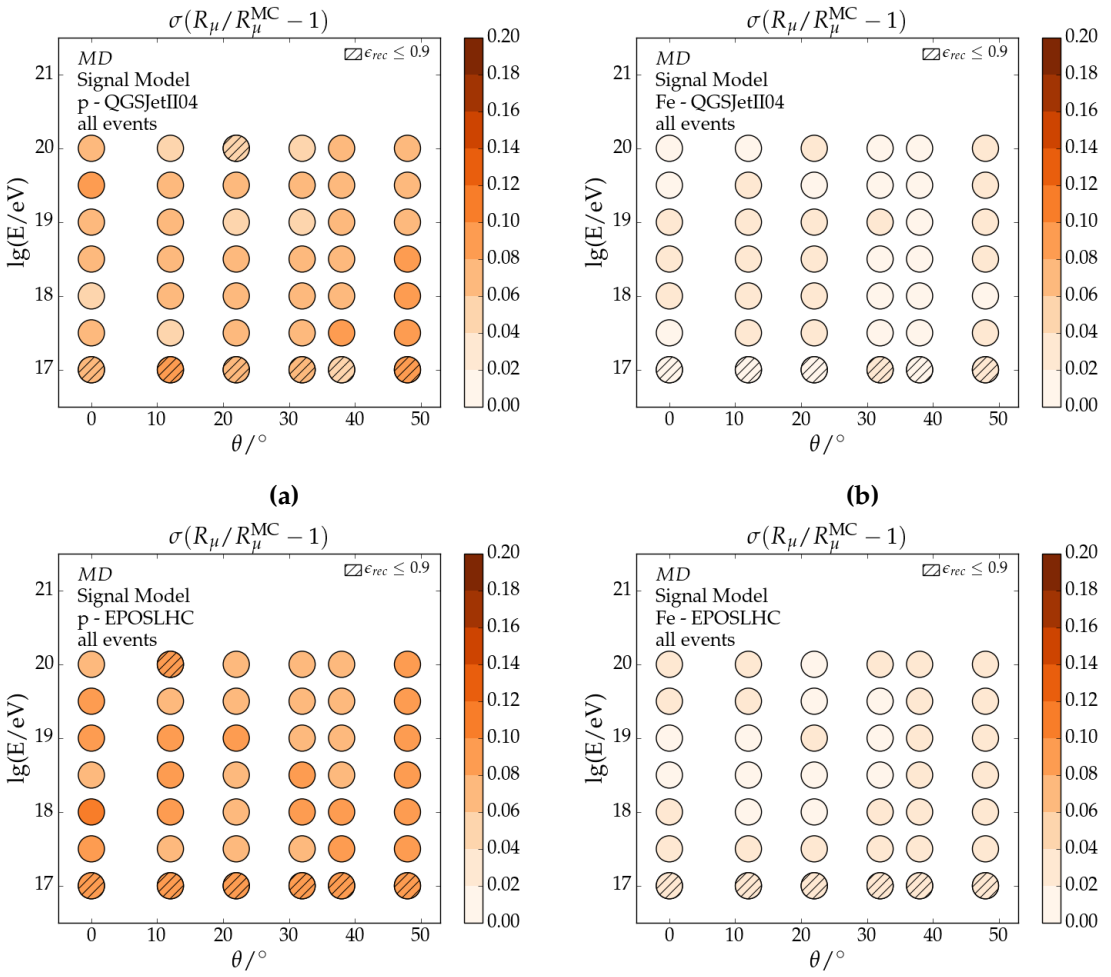

Figure C.14

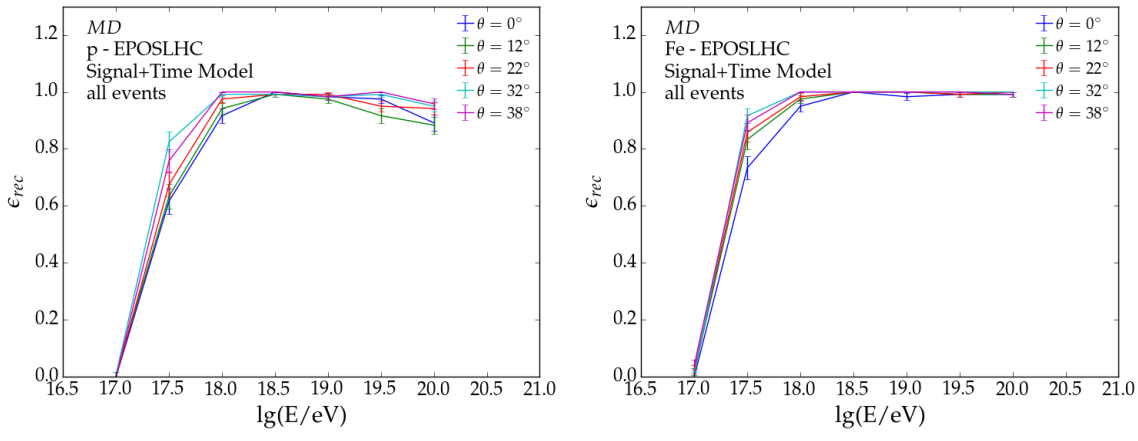

Figure C.15

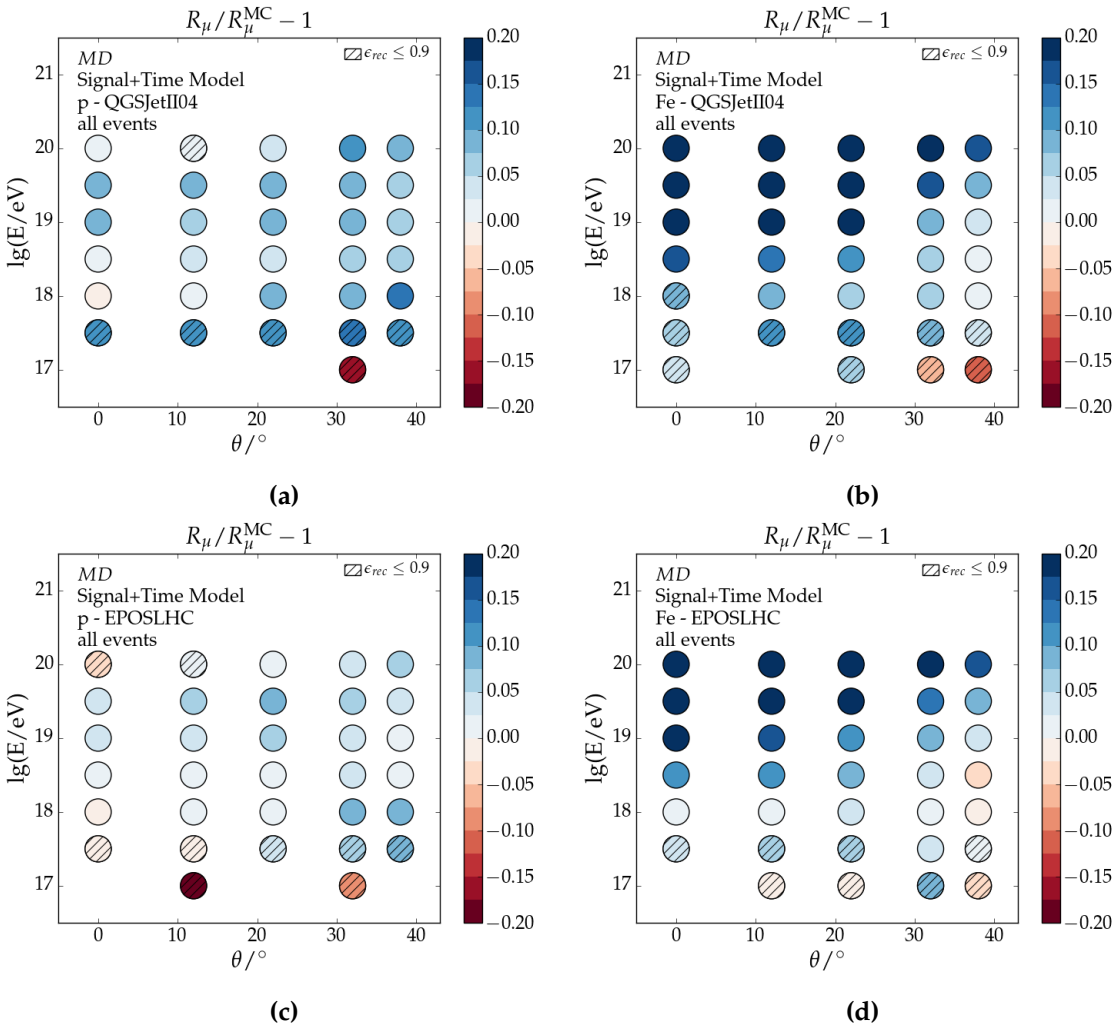
$R_\mu / R_\mu^{\mathrm{MC}} - 1$
MD
Signal+Time Model
p - QGSJetII04
all events
$\epsilon_{rec} \leq 0.9$
lg(E/eV)
$\theta / ^\circ$
(a)
$R_\mu / R_\mu^{\mathrm{MC}} - 1$
MD
Signal+Time Model
Fe - QGSJetII04
all events
$\epsilon_{rec} \leq 0.9$
lg(E/eV)
$\theta / ^\circ$
(b)
$R_\mu / R_\mu^{\mathrm{MC}} - 1$
MD
Signal+Time Model
p - EPOSLHC
all events
$\epsilon_{rec} \leq 0.9$
lg(E/eV)
$\theta / ^\circ$
(c)
$R_\mu / R_\mu^{\mathrm{MC}} - 1$
MD
Signal+Time Model
Fe - EPOSLHC
all events
$\epsilon_{rec} \leq 0.9$
lg(E/eV)
$\theta / ^\circ$
(d)

Figure C.16

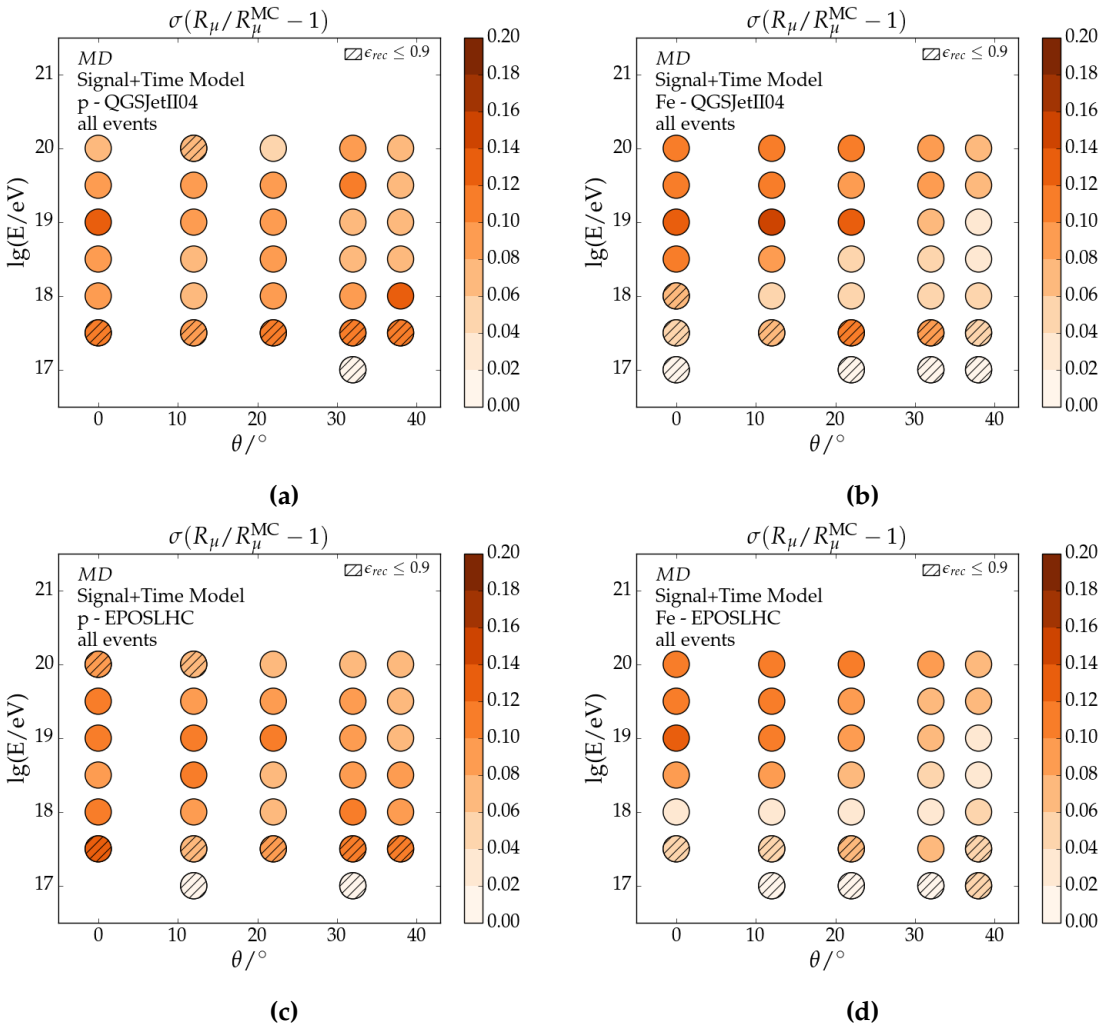
$\sigma(R_\mu/R_\mu^{\mathrm{MC}}-1)$
$\epsilon_{rec} \leq 0.9$
MD
Signal+Time Model
p - QGSJetII04
all events
Fe - QGSJetII04
p - EPOSLHC
Fe - EPOSLHC
lg(E/eV)
$\theta/^\circ$
(a)
(b)
(c)
(d)

Figure C.17

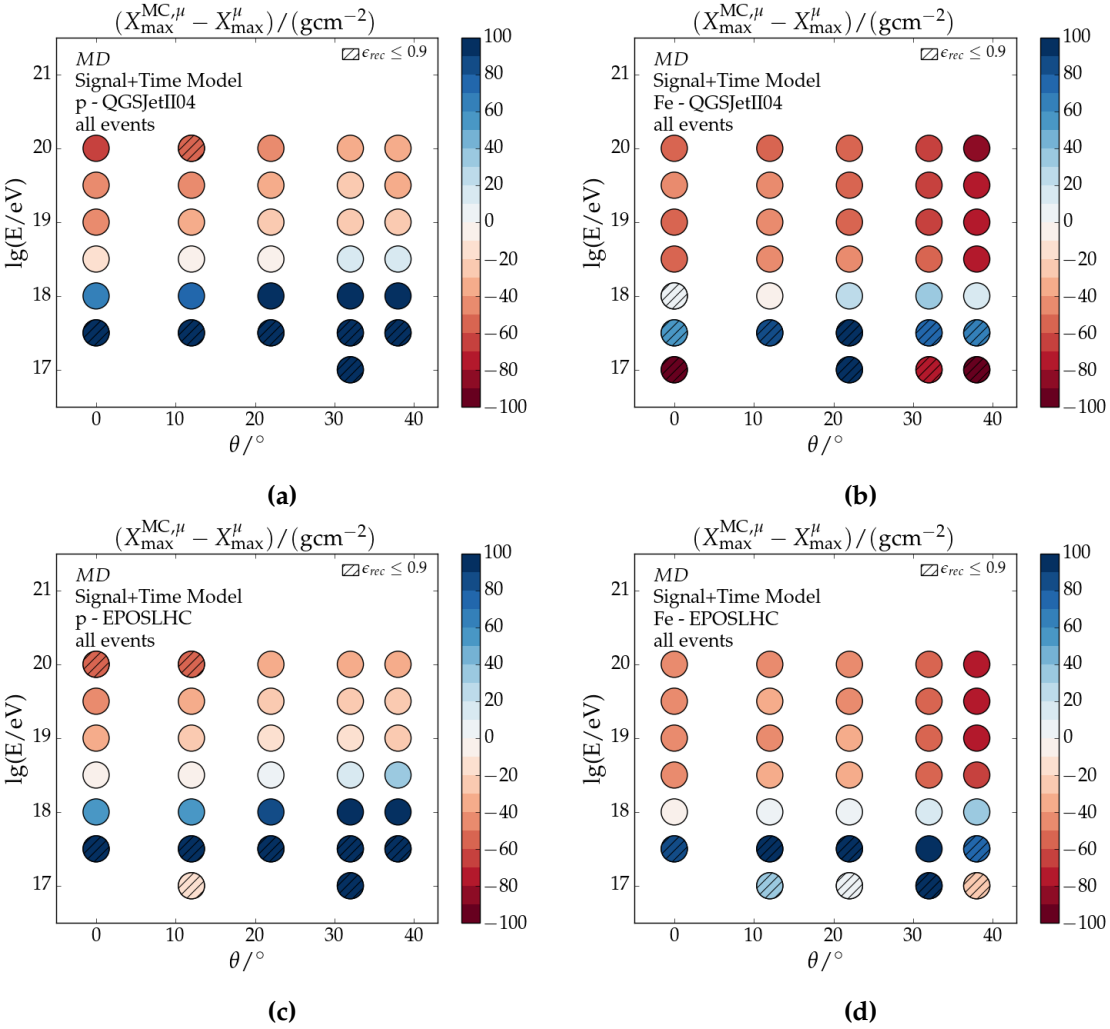
$(X_{max}^{MC,\mu} - X_{max}^{\mu})/(gcm^{-2})$
MD
Signal+Time Model
p - QGSJetII04
all events
$\epsilon_{rec} \leq 0.9$
lg(E/eV)
$\theta/^\circ$
(a)
Fe - QGSJetII04
(b)
p - EPOSLHC
(c)
Fe - EPOSLHC
(d)

Figure C.18

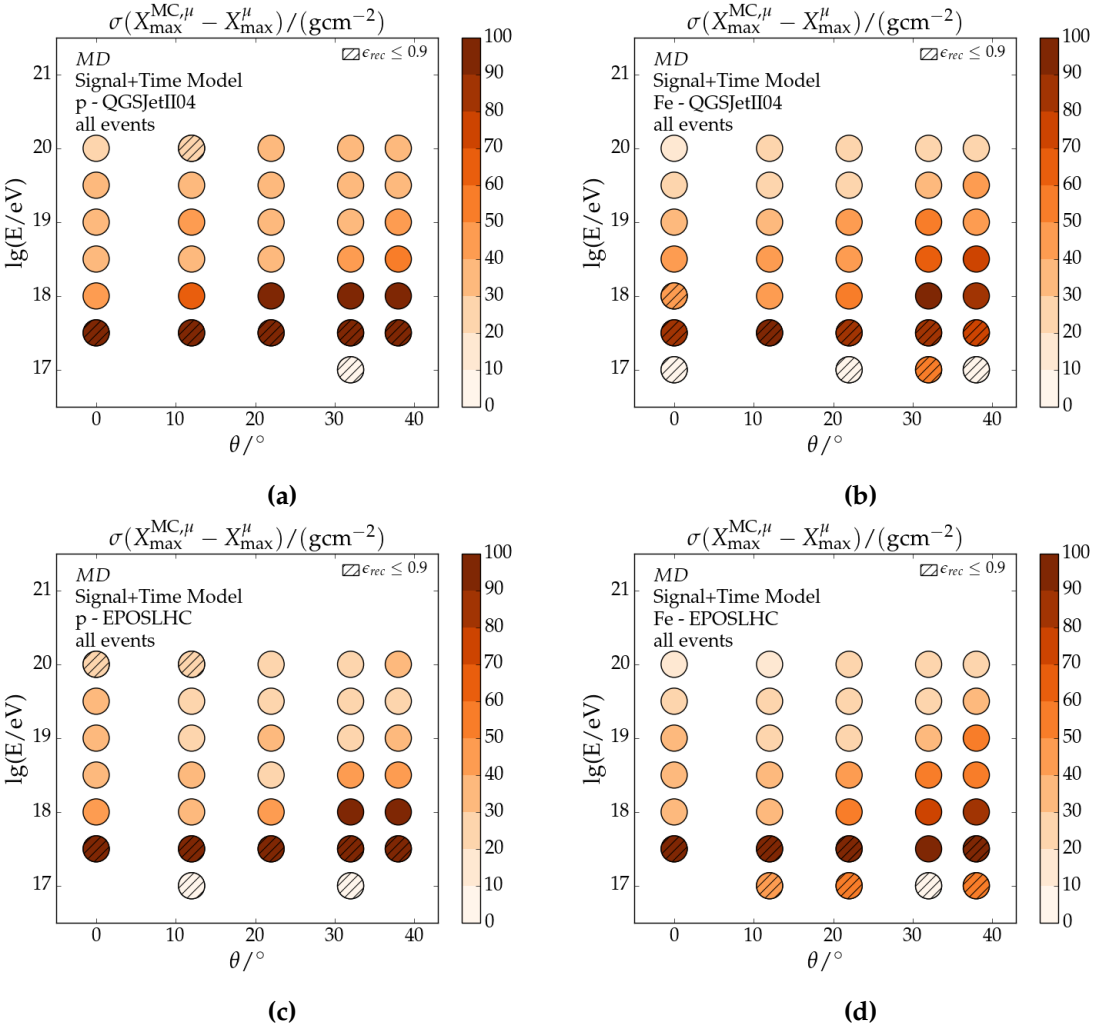
$\sigma(X_{\max}^{\mathrm{MC},\mu} - X_{\max}^{\mu})/(\mathrm{gcm}^{-2})$
MD
Signal+Time Model
p - QGSJetII04
all events
$\epsilon_{rec} \leq 0.9$
lg(E/eV)
$\theta/^\circ$
(a)
$\sigma(X_{\max}^{\mathrm{MC},\mu} - X_{\max}^{\mu})/(\mathrm{gcm}^{-2})$
MD
Signal+Time Model
Fe - QGSJetII04
all events
$\epsilon_{rec} \leq 0.9$
lg(E/eV)
$\theta/^\circ$
(b)
$\sigma(X_{\max}^{\mathrm{MC},\mu} - X_{\max}^{\mu})/(\mathrm{gcm}^{-2})$
MD
Signal+Time Model
p - EPOSLHC
all events
$\epsilon_{rec} \leq 0.9$
lg(E/eV)
$\theta/^\circ$
(c)
$\sigma(X_{\max}^{\mathrm{MC},\mu} - X_{\max}^{\mu})/(\mathrm{gcm}^{-2})$
MD
Signal+Time Model
Fe - EPOSLHC
all events
$\epsilon_{rec} \leq 0.9$
lg(E/eV)
$\theta/^\circ$
(d)

Figure C.19

C.3 WCD and MD

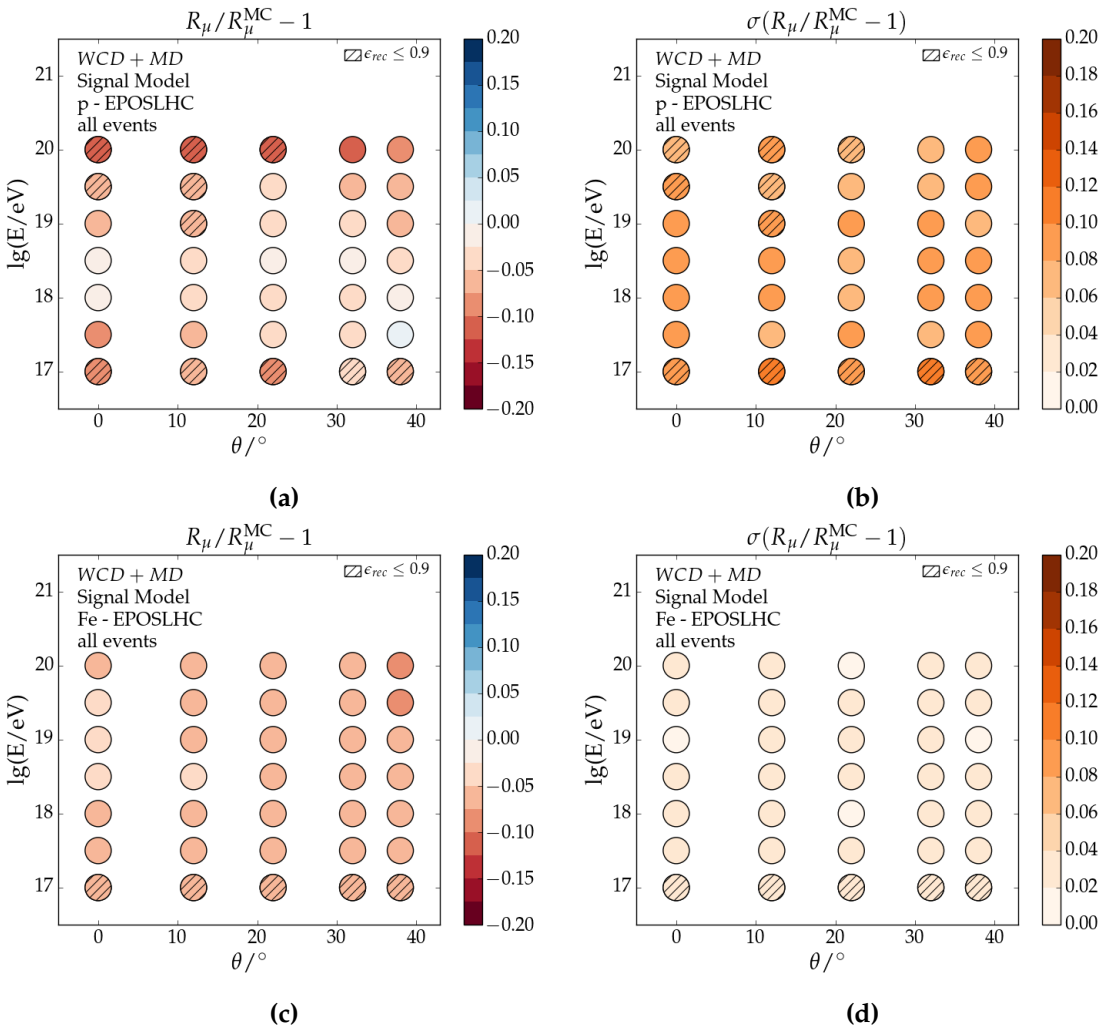

Figure C.20

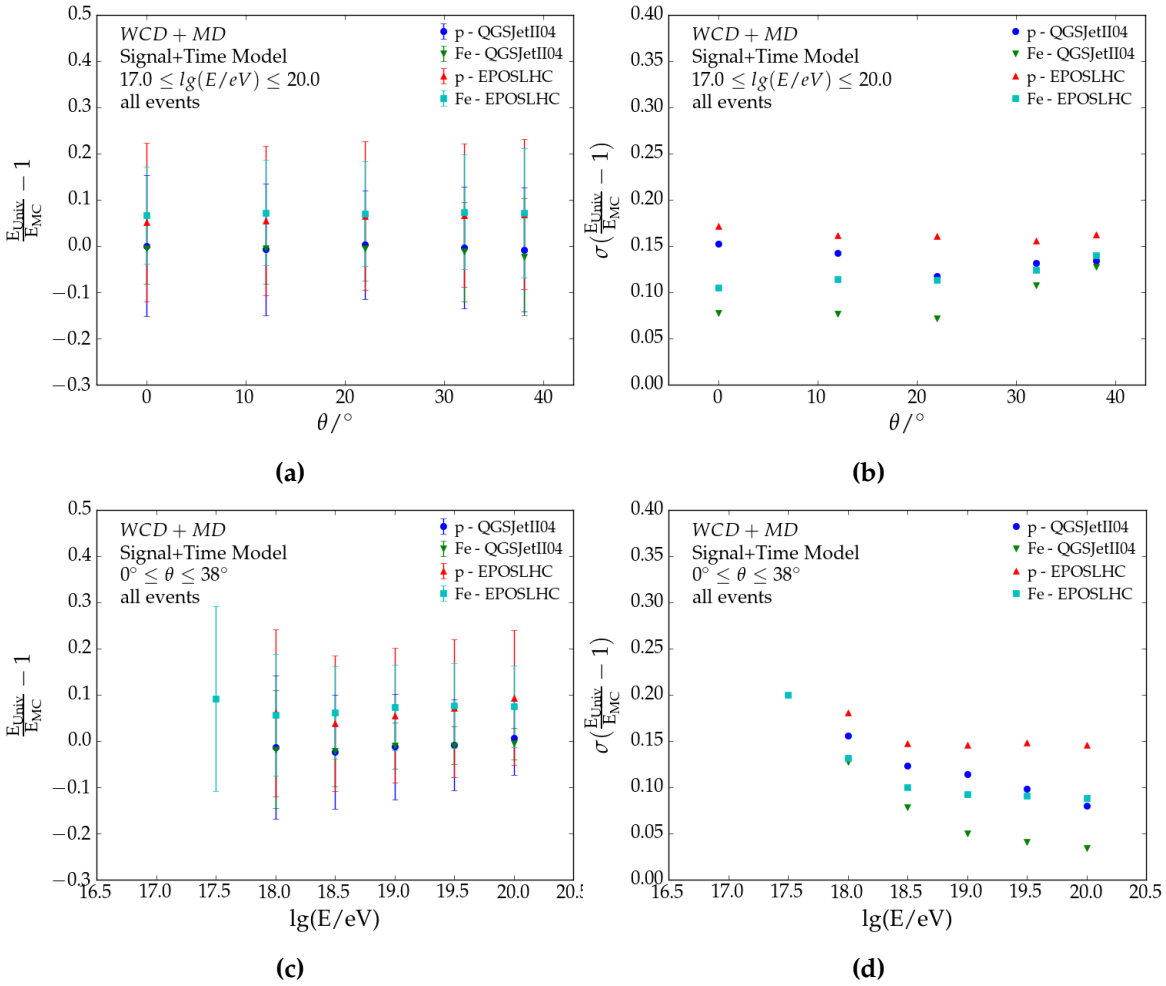

Figure C.21: Energy bias (*Left*) and resolution (*Right*) with respect to true shower **Top)** zenith and **Bottom)** energy.

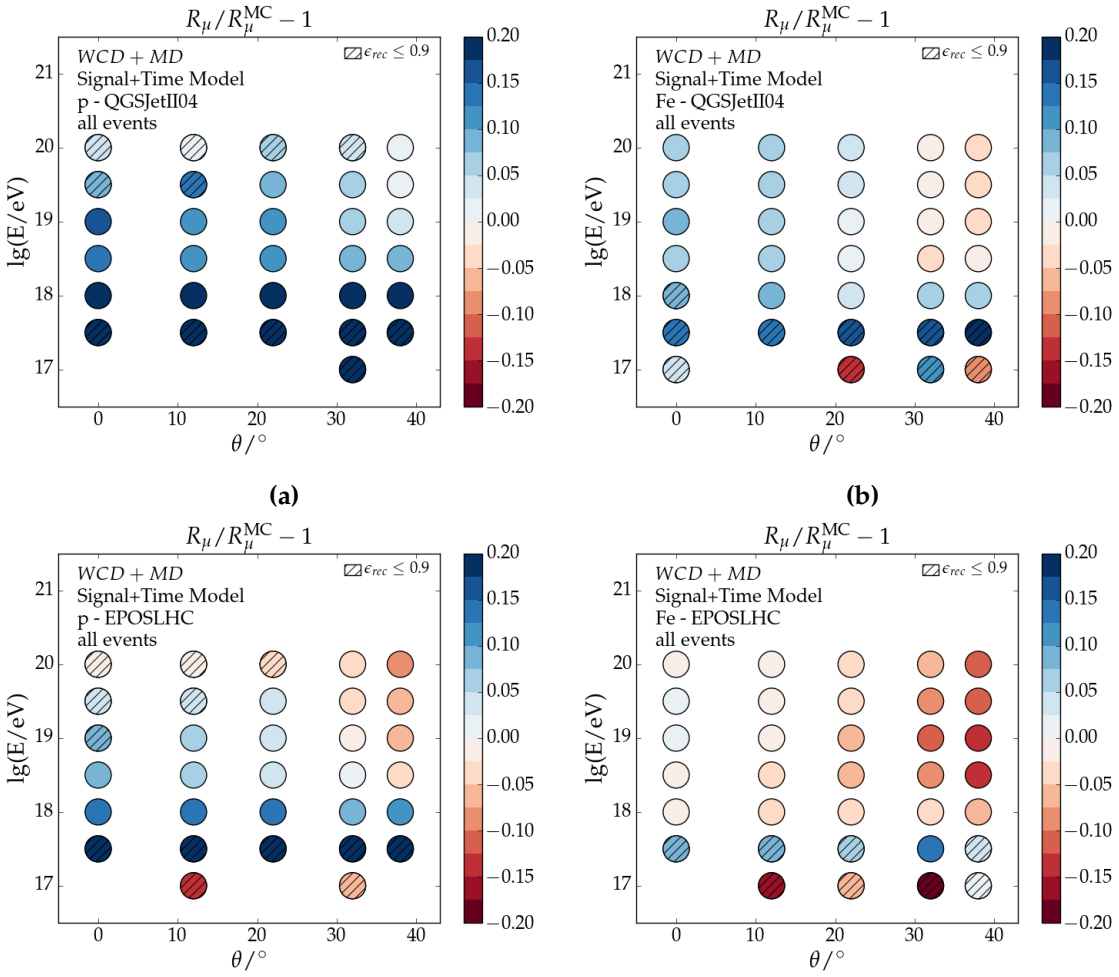
$R_\mu / R_\mu^{\mathrm{MC}} - 1$
$WCD + MD$
Signal+Time Model
p - QGSJetII04
all events
$\epsilon_{rec} \leq 0.9$
lg(E/eV)
$\theta / ^\circ$
(a)
$R_\mu / R_\mu^{\mathrm{MC}} - 1$
$WCD + MD$
Signal+Time Model
Fe - QGSJetII04
all events
$\epsilon_{rec} \leq 0.9$
lg(E/eV)
$\theta / ^\circ$
(b)
$R_\mu / R_\mu^{\mathrm{MC}} - 1$
$WCD + MD$
Signal+Time Model
p - EPOSLHC
all events
$\epsilon_{rec} \leq 0.9$
lg(E/eV)
$\theta / ^\circ$
(c)
$R_\mu / R_\mu^{\mathrm{MC}} - 1$
$WCD + MD$
Signal+Time Model
Fe - EPOSLHC
all events
$\epsilon_{rec} \leq 0.9$
lg(E/eV)
$\theta / ^\circ$
(d)

Figure C.22

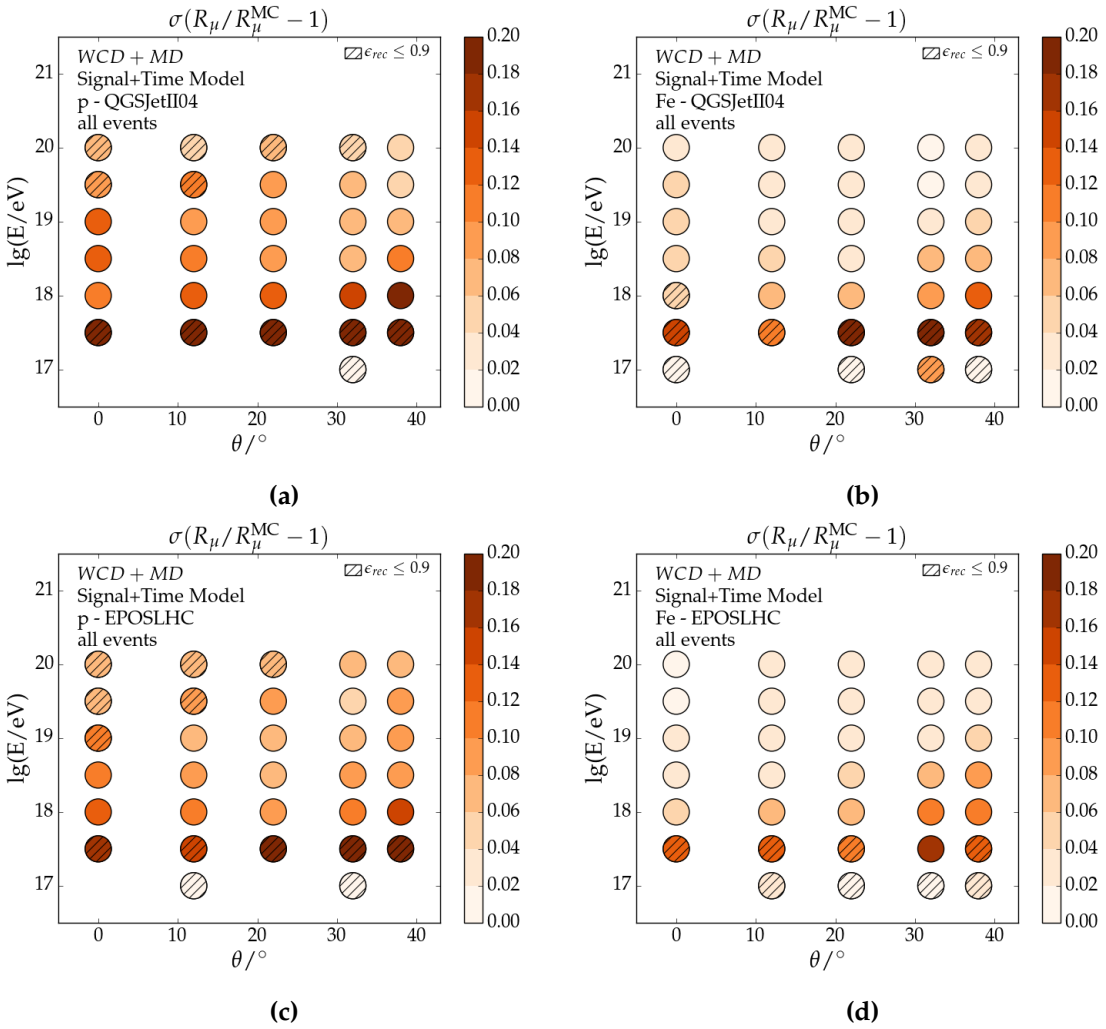
$\sigma(R_\mu/R_\mu^{\mathrm{MC}}-1)$
$WCD + MD$
Signal+Time Model
p - QGSJetII04
all events
$\epsilon_{rec} \leq 0.9$
lg(E/eV)
$\theta/^\circ$
(a)
$\sigma(R_\mu/R_\mu^{\mathrm{MC}}-1)$
$WCD + MD$
Signal+Time Model
Fe - QGSJetII04
all events
$\epsilon_{rec} \leq 0.9$
lg(E/eV)
$\theta/^\circ$
(b)
$\sigma(R_\mu/R_\mu^{\mathrm{MC}}-1)$
$WCD + MD$
Signal+Time Model
p - EPOSLHC
all events
$\epsilon_{rec} \leq 0.9$
lg(E/eV)
$\theta/^\circ$
(c)
$\sigma(R_\mu/R_\mu^{\mathrm{MC}}-1)$
$WCD + MD$
Signal+Time Model
Fe - EPOSLHC
all events
$\epsilon_{rec} \leq 0.9$
lg(E/eV)
$\theta/^\circ$
(d)

Figure C.23

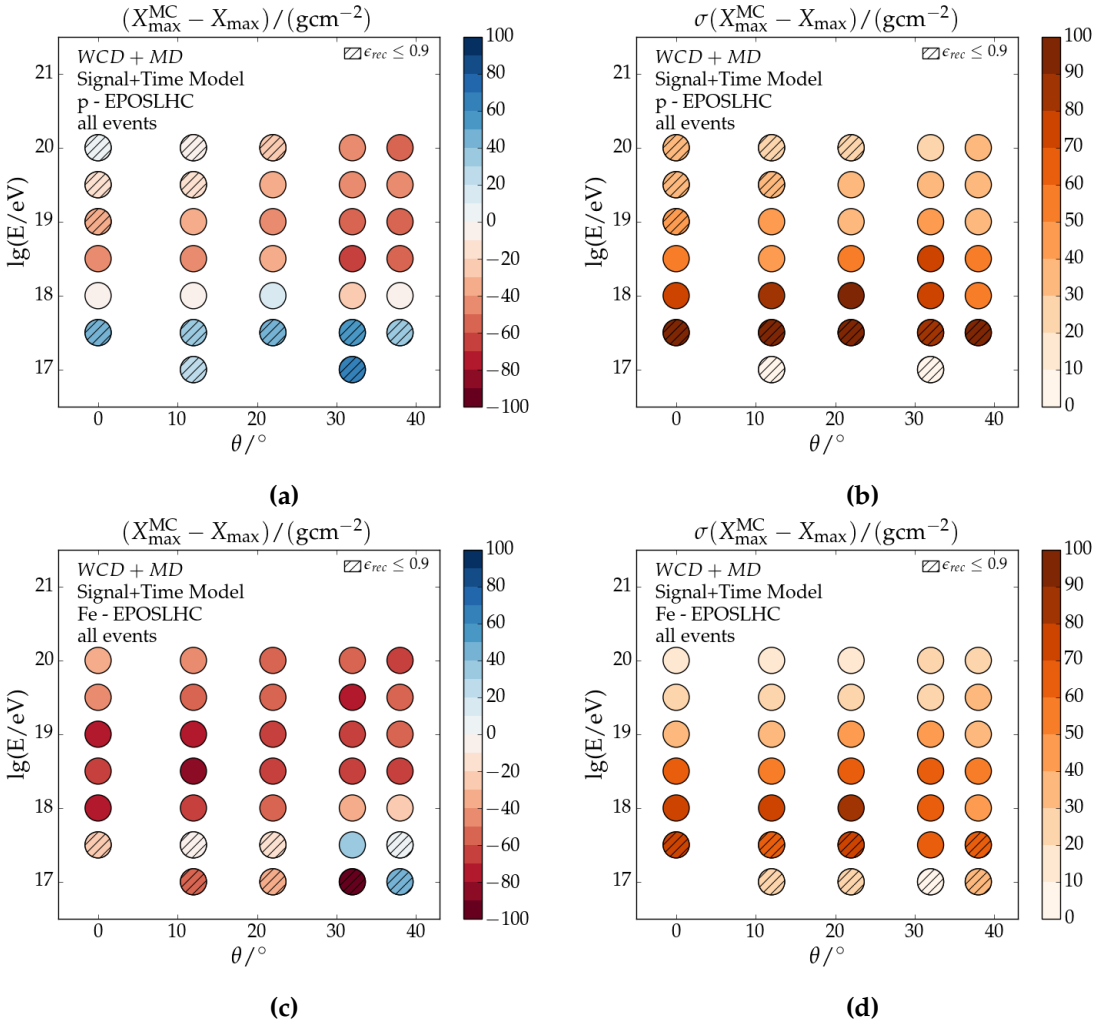
$(X^{MC}_{max} - X_{max})/(gcm^{-2})$
$\sigma(X^{MC}_{max} - X_{max})/(gcm^{-2})$
WCD + MD
Signal+Time Model
p - EPOSLHC
Fe - EPOSLHC
all events
$\epsilon_{rec} \leq 0.9$
lg(E/eV)
$\theta/^\circ$
(a)
(b)
(c)
(d)

Figure C.24

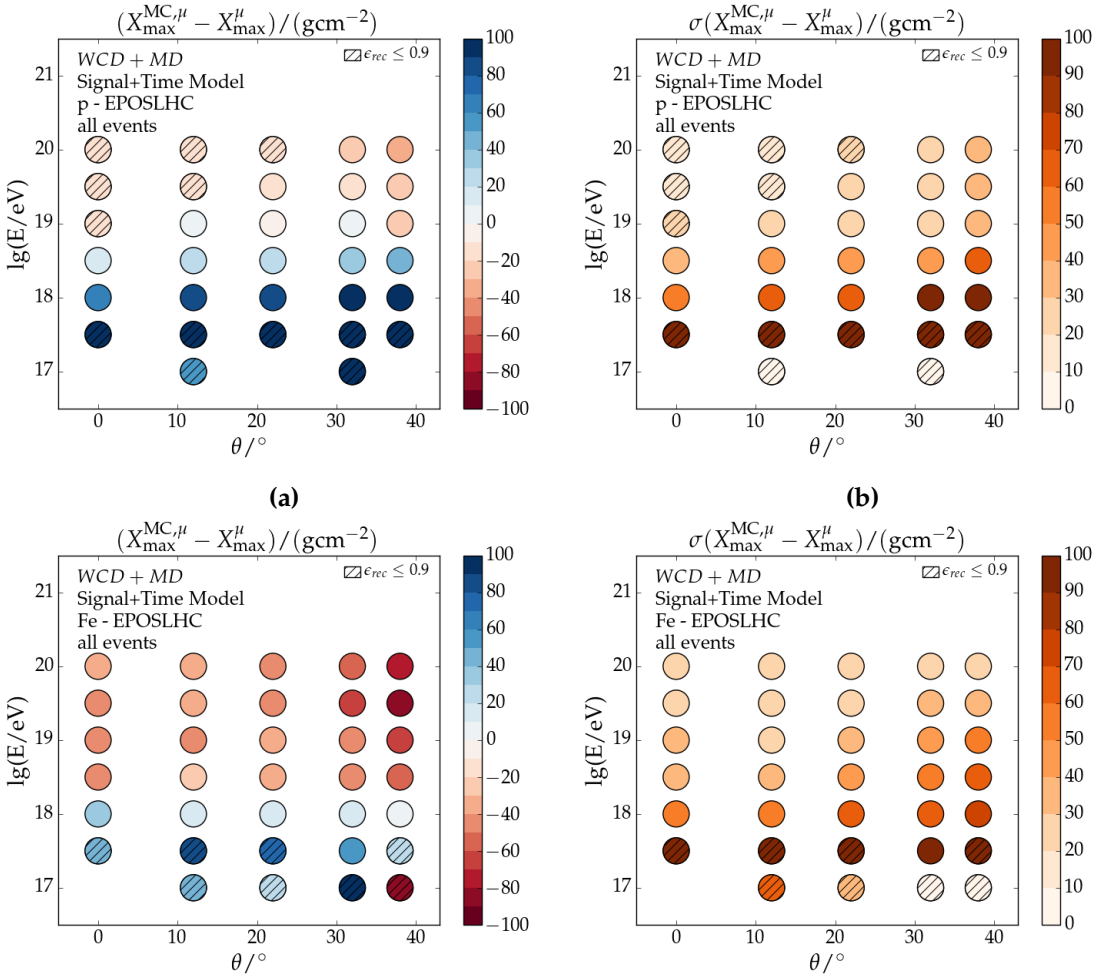
$(X^{\mathrm{MC},\mu}_{\mathrm{max}} - X^{\mu}_{\mathrm{max}})/(\mathrm{gcm}^{-2})$
$\sigma(X^{\mathrm{MC},\mu}_{\mathrm{max}} - X^{\mu}_{\mathrm{max}})/(\mathrm{gcm}^{-2})$
$WCD + MD$
Signal+Time Model
p - EPOSLHC
Fe - EPOSLHC
all events
$\epsilon_{rec} \leq 0.9$
lg(E/eV)
$\theta/^\circ$
(a)
(b)
(c)
(d)

Figure C.25

Acknowledgments

I would like to thank the two reviewers of this dissertation, Professors Supanitsky and Blümer, for facilitating this work. This work, although sometimes tedious, was scientifically very intriguing, it motivated me to give the best of my efforts. I consider myself lucky to have been presented with such a cool challenge.
Many thanks to the coordinators of this double degree program, Professors Blümer and Etchegoyen, for laying the foundations of this joint German-Argentine program through which I have now passed. I truly enjoyed this international and intercultural scientific exchange program which has taught me so much on an academic and personal level. To my advisor, Markus Roth, I have appreciated his constant support and interest for my work, as well as the trust and freedom that were given to me. His experience and insight have often helped me resolve bottlenecks during my work.
My sincerest gratitude to Sabine Bucher and Marie-Christine Kaufmann-Mundt for their outstanding administrative support. Preparations for conferences, workshops and my defense would not have gone smoothly without their help. I am also grateful for the technical support at ITeDA (mostly from Adrian Sedoski), at IKP and bwUniCluster. Without their resources, many of my results would not have been possible.

Immense appreciation to my family; their never-ending support pushed me through my darkest hours. My parents, Cornelis and Sawsan, always found the right words for me not to lose focus and remain positive. To my sister, Petra, frequently communicating with me about music, movies, games and even vacation. To my brothers, Paul en Filip, sharing their crazy project ideas and life experiences. To Elinor van Poyer, whom I also consider as family. Their care and understanding calmed me more than I could remember.

In Argentina, I am grateful for the warm company of the people in Buenos Aires, Bariloche and La Plata. I thank Ana Botti, Belen Andrada, Nicolas Gonzalez, Isabel Goos and Ana Laura M"uller for their company. Special appreciation goes to Adrian Sedoski, Alejandro Almela and Eugenia Iglesias. Their humor, care, openness and energy lifted my spirits countless times. To Federico Suarez, my first office mate, and his family. Our daily 'Mate time' and weekly squash matches provided a sense of balance in an unfamiliar environment. He also welcomed me to his family, which I truly valued. His advice, care and pragmatic solutions often helped me pass through many struggles. To Flavia, among my closest friends. I have shared some of my most joyful moments with her. Her warmth, care, humor, 'Merienda time' and persistency sparked some of my most cherished experiences. Throughout the worst of my struggles, she always stood by to lift me up. She helped me with my thesis, as well as

lending her ear when I needed it most. Words will never be able to express the immense of joy she has given me.

In Germany, I had the pleasure to do many things with wonderful people there. To David Schmidt, for his welcome company and many fruitful discussions. To Maximilian Reininghaus and William Painter, for the many activities we have shared. I would also like to thank Maximilian for being such a cool office mate while coming to Argentina. To Darko Veberic, for the refreshing amount of energy during and after work. To Tanguy Pierog and Detlef Maurel, for our weekly squash duels. To Martin Schimassek and Alexander Streich, for the fun and interesting conversations. To Sarah Müller and Daniela Mockler, for introducing me to sportive activities and helping me find my groove. Also, to Daniela, for the evening discussions after work. To Maximilian Stadelmaier, Steffen Hahn, Felix Schlüter and Alvaro Taboada, for the good times and company. To the many other colleagues and friends with whom I had meaningful contact, but are not explicitly mentioned here.

I consider myself lucky to have been surrounded by so much good. My sincerest thanks to all of you.

Special thanks to Argentinian Asado and German beers.

Bibliography

[1] V. F. Hess, Beobachtungen der durchdringenden Strahlung bei sieben Freiballonfahrten, Phys. Z. 13 (1912) 1084.

[2] J. Clay, P. van Alphen, C. Hooft, Results of the Dutch Cosmic Ray Expedition 1933: II. The magnetic latitude effect of cosmic rays a magnetic longitude effect, Physica 1 (7–12) (1934) 829 – 838. doi:10.1016/S0031-8914(34)80277-7.

[3] E. R. Thomas K. Gaisser, Ralph Engel, Cosmic Rays and Particle Physics, second edition Edition, Cambridge University Press, 2016.

[4] J. Blümer, R. Engel, J. R. Hörandel, Cosmic rays from the knee to the highest energies, Progress in Particle and Nuclear Physics 63 (2) (2009) 293–338. doi:10.1016/j.ppnp.2009.05.002.
URL http://dx.doi.org/10.1016/j.ppnp.2009.05.002

[5] P. Auger, P. Ehrenfest, R. Maze, J. Daudin, R. A. Fréon, Extensive cosmic-ray showers, Rev. Mod. Phys. 11 (3-4) (1939) 288–291. doi:10.1103/RevModPhys.11.288.

[6] W. Heitler, The Quantum Theory of Radiation, 3rd Edition, Oxford University Press, Oxford, 1954.

[7] B. Rossi, High Energy Particles, Prentice-Hall, Englewood Cliffs, NJ, 1952.

[8] J. Linsley, Evidence for a Primary Cosmic-Ray Particle with Energy 10^{20} eV, Phys. Rev. Lett. 10 (4) (1963) 146–148. doi:10.1103/PhysRevLett.10.146.

[9] K. Greisen, End to the cosmic-ray spectrum?, Phys. Rev. Lett. 16 (17) (1966) 748–750. doi:10.1103/PhysRevLett.16.748.

[10] G. T. Zatsepin, V. A. Kuz'min, Upper Limit of the Spectrum of Cosmic Rays, JETP Lett. 4 (1966) 78 – 80.

[11] D. M. Edge, A. C. Evans, H. J. Garmston, R. J. O. Reid, A. A. Watson, J. G. Wilson, A. M. Wray, The cosmic ray spectrum at energies above 1017ev, Journal of Physics A: Mathematical, Nuclear and General 6 (10) (1973) 1612–1634. doi:10.1088/0305-4470/6/10/019.
URL https://doi.org/10.1088%2F0305-4470%2F6%2F10%2F019

[12] M. I. Pravdin, N. A. Dyachkovsky, Y. A. Egorov, N. N. Efremov, A. V. Glushkov, A. A. Ivanov, S. P. Knurenko, V. A. Kolosov, A. D. Krasilnikov, I. T. Makarov, A. K. Makarov, A. A. Mikhailov, Z. E. Petrov, V. P. Prohorova, A. V. Saburov, I. Y. Sleptsov, G. G. Struchkov, The cosmic rays energy spectrum of the Yakutsk EAS Array, in: Proc. 31st Int. Cosmic Ray Conf., 2009, p. 3.

[13] N. Chiba *et al.* (AGASA Collab.), Akeno giant air shower array (AGASA) covering 100-km^2 area, Nucl. Instrum. Meth. A311 (1992) 338–349. doi:10.1016/0168-9002(92)90882-5.

[14] R.U. Abbasi *et al.* (HiRes Collab.), High Resolution Fly's Eye Collab., First observation of the greisen-zatsepin-kuzmin suppression, Phys. Rev. Lett. 100 (2008) 101101. doi:10.1103/PhysRevLett.100.101101.

[15] P. Sokolsky (HiRes Collab.), Final Results from the High Resolution Fly's Eye (HiRes) Experiment (2010). arXiv:astro-ph/1010.2690.

[16] N. Sakaki (AGASA Collab.), Cosmic ray energy spectrum above 3×10^{18} eV observed with AGASA, in: Proc. 27th Int. Cosmic Ray Conf., Hamburg, Germany, 2001, p. 4.

[17] A. Aab *et al.* (Pierre Auger Collab.), The Pierre Auger Cosmic Ray Observatory, Nucl. Instrum. Meth. A798 (2015) 172–213. arXiv:astro-ph.IM/1502.01323, doi:10.1016/j.nima.2015.06.058.

[18] Y. Tsunesada (Telescope Array Collab.), Highlights from Telescope Array, in: Proc. 32th Int. Cosmic Ray Conf., Beijing, China, 2011, p. 10.

[19] S. E. S. Ferreira, M. S. Potgieter, Long-term cosmic-ray modulation in the heliosphere, The Astrophysical Journal 603 (2) (2004) 744–752. doi:10.1086/381649.
URL https://doi.org/10.1086%2F381649

[20] M. Tanabashi, K. Hagiwara, K. Hikasa, K. Nakamura, Y. Sumino, F. Takahashi, J. Tanaka, K. Agashe, G. Aielli, C. Amsler, M. Antonelli, D. M. Asner, H. Baer, S. Banerjee, R. M. Barnett, T. Basaglia, C. W. Bauer, J. J. Beatty, V. I. Belousov, J. Beringer, S. Bethke, A. Bettini, H. Bichsel, O. Biebel, K. M. Black, E. Blucher, O. Buchmuller, V. Burkert, M. A. Bychkov, R. N. Cahn, M. Carena, A. Ceccucci, A. Cerri, D. Chakraborty, M.-C. Chen, R. S. Chivukula, G. Cowan, O. Dahl, G. D'Ambrosio, T. Damour, D. de Florian, A. de Gouvêa, T. DeGrand, P. de Jong, G. Dissertori, B. A. Dobrescu, M. D'Onofrio, M. Doser, M. Drees, H. K. Dreiner, D. A. Dwyer, P. Eerola, S. Eidelman, J. Ellis, J. Erler, V. V. Ezhela, W. Fetscher, B. D. Fields, R. Firestone, B. Foster, A. Freitas, H. Gallagher, L. Garren, H.-J. Gerber, G. Gerbier, T. Gershon, Y. Gershtein, T. Gherghetta, A. A. Godizov, M. Goodman, C. Grab, A. V. Gritsan, C. Grojean, D. E. Groom, M. Grünewald, A. Gurtu, T. Gutsche, H. E. Haber, C. Hanhart, S. Hashimoto, Y. Hayato, K. G. Hayes, A. Hebecker, S. Heinemeyer, B. Heltsley, J. J. Hernández-Rey, J. Hisano, A. Höcker, J. Holder, A. Holtkamp, T. Hyodo, K. D. Irwin, K. F. Johnson, M. Kado, M. Karliner, U. F. Katz, S. R. Klein, E. Klempt, R. V. Kowalewski, F. Krauss, M. Kreps, B. Krusche, Y. V. Kuyanov, Y. Kwon, O. Lahav, J. Laiho, J. Lesgourgues, A. Liddle, Z. Ligeti, C.-J. Lin, C. Lippmann, T. M. Liss, L. Littenberg, K. S. Lugovsky, S. B. Lugovsky, A. Lusiani, Y. Makida, F. Maltoni, T. Mannel, A. V. Manohar, W. J. Marciano, A. D. Martin, A. Masoni, J. Matthews, U.-G. Meißner, D. Milstead, R. E. Mitchell, K. Mönig, P. Molaro, F. Moortgat, M. Moskovic, H. Murayama, M. Narain, P. Nason, S. Navas, M. Neubert, P. Nevski, Y. Nir, K. A. Olive, S. Pagan Griso, J. Parsons, C. Patrignani, J. A. Peacock, M. Pennington, S. T. Petcov, V. A. Petrov, E. Pianori, A. Piepke, A. Pomarol, A. Quadt, J. Rademacker,

G. Raffelt, B. N. Ratcliff, P. Richardson, A. Ringwald, S. Roesler, S. Rolli, A. Romaniouk, L. J. Rosenberg, J. L. Rosner, G. Rybka, R. A. Ryutin, C. T. Sachrajda, Y. Sakai, G. P. Salam, S. Sarkar, F. Sauli, O. Schneider, K. Scholberg, A. J. Schwartz, D. Scott, V. Sharma, S. R. Sharpe, T. Shutt, M. Silari, T. Sjöstrand, P. Skands, T. Skwarnicki, J. G. Smith, G. F. Smoot, S. Spanier, H. Spieler, C. Spiering, A. Stahl, S. L. Stone, T. Sumiyoshi, M. J. Syphers, K. Terashi, J. Terning, U. Thoma, R. S. Thorne, L. Tiator, M. Titov, N. P. Tkachenko, N. A. Törnqvist, D. R. Tovey, G. Valencia, R. Van de Water, N. Varelas, G. Venanzoni, L. Verde, M. G. Vincter, P. Vogel, A. Vogt, S. P. Wakely, W. Walkowiak, C. W. Walter, D. Wands, D. R. Ward, M. O. Wascko, G. Weiglein, D. H. Weinberg, E. J. Weinberg, M. White, L. R. Wiencke, S. Willocq, C. G. Wohl, J. Womersley, C. L. Woody, R. L. Workman, W.-M. Yao, G. P. Zeller, O. V. Zenin, R.-Y. Zhu, S.-L. Zhu, F. Zimmermann, P. A. Zyla, J. Anderson, L. Fuller, V. S. Lugovsky, P. Schaffner, Particle Data Group, Review of particle physics, Phys. Rev. D 98 (2018) 030001. doi:10.1103/PhysRevD.98.030001.
URL https://link.aps.org/doi/10.1103/PhysRevD.98.030001

[21] Hörandel, J. R. et al., Estimation of the cosmic ray composition with the kascade hadron calorimeter, in: Proc. 25th Int. Cosmic Ray Conf., 1997, p. 4.

[22] J. R. Horandel, Cosmic rays from the knee to the second knee: 10**4 to 10**18-eV, Mod. Phys. Lett. A22 (2007) 1533–1552, [,63(2006)]. arXiv:astro-ph/0611387, doi:10.1142/S0217732307024139.

[23] A. Haungs *et al.*, KCDC — The KASCADE Cosmic-ray Data Centre, J. of Phys.: Conf. Series 632 (1) (2015) 012011.
URL http://stacks.iop.org/1742-6596/632/i=1/a=012011

[24] R. Aloisio, V. Berezinsky, P. Blasi, Ultra high energy cosmic rays: implications of Auger data for source spectra and chemical composition, JCAP 1410 (10) (2014) 020. arXiv:1312.7459, doi:10.1088/1475-7516/2014/10/020.

[25] M. Unger, G. R. Farrar, L. A. Anchordoqui, Origin of the ankle in the ultra-high energy cosmic ray spectrum and of the extragalactic protons below it, Phys. Rev. D 92 (12) (2015) 123001. arXiv:astro-ph.HE/1505.02153, doi:10.1103/PhysRevD.92.123001.

[26] T. K. Gaisser, T. Stanev, S. Tilav, Cosmic Ray Energy Spectrum from Measurements of Air Showers, Front. Phys.(Beijing) 8 (2013) 748–758. arXiv:1303.3565, doi:10.1007/s11467-013-0319-7.

[27] B. Peters, Primary cosmic radiation and extensive air showers, Il Nuovo Cimento (1955-1965) 22 (4) (1961) 800–819. doi:10.1007/BF02783106.
URL https://doi.org/10.1007/BF02783106

[28] V. Berezinsky, Transition from galactic to extragalactic cosmic rays, in: Proc. 30th Int. Cosmic Ray Conf., Mérida, Mexico, 2007, p. 14. arXiv:astro-ph/0710.2750.

[29] A. Aab, et al., Pierre Auger, Combined fit of spectrum and composition data as measured by the Pierre Auger Observatory, JCAP 1704 (04) (2017) 038, [Erratum: JCAP1803,no.03,E02(2018)]. arXiv:1612.07155, doi:10.1088/1475-7516/2018/03/E02,10.1088/1475-7516/2017/04/038.

[30] A. Aab, et al., Pierre Auger, An Indication of anisotropy in arrival directions of ultra-high-energy cosmic rays through comparison to the flux pattern of extragalactic gamma-ray sources, Astrophys. J. 853 (2) (2018) L29. arXiv:1801.06160, doi:10.3847/2041-8213/aaa66d.

[31] A. Aab, et al., Pierre Auger, Observation of a Large-scale Anisotropy in the Arrival Directions of Cosmic Rays above 8×10^{18} eV, Science 357 (6537) (2017) 1266–1270. arXiv:1709.07321, doi:10.1126/science.aan4338.

[32] A. M. Hillas, Cosmic Rays: Recent Progress and some Current Questions, in: Conference on Cosmology, Galaxy Formation and Astro-Particle Physics on the Pathway to the SKA Oxford, England, April 10-12, 2006, 2006, p. 12. arXiv:astro-ph/0607109.

[33] Lorenzo Cazon, Probing High-Energy Hadronic Interactions with Extensive Air Showers, in: Proc. 36th Int. Cosmic Ray Conf., Madison, United States of America, 2019, p. 16.

[34] J. Matthews, A Heitler model of extensive air showers, Astropart. Phys. 22 (5-6) (2005) 387 – 397. doi:10.1016/j.astropartphys.2004.09.003.

[35] A. Haungs, et al., KCDC - The KASCADE Cosmic-ray Data Centre, J. Phys. Conf. Ser. 632 (1) (2015) 012011. arXiv:1504.06696, doi:10.1088/1742-6596/632/1/012011.

[36] P. Abreu *et al.* (Pierre Auger Collab.), Interpretation of the Depths of Maximum of Extensive Air Showers Measured by the Pierre Auger Observatory, JCAP 1302 (2013) 026. arXiv:1301.6637, doi:10.1088/1475-7516/2013/02/026.

[37] R. Engel, D. Heck, T. Pierog, Extensive air showers and hadronic interactions at high energy, Ann. Rev. Nucl. Part. Sci. 61 (2011) 467–489. doi:10.1146/annurev.nucl.012809.104544.

[38] L. N. and, The observation of a muon deficit in simulations from data of the pierre auger observatory, Journal of Physics: Conference Series 409 (2013) 012107. doi:10.1088/1742-6596/409/1/012107.
URL https://doi.org/10.1088%2F1742-6596%2F409%2F1%2F012107

[39] Müller, Sarah, for the Pierre Auger Collaboration, Direct measurement of the muon density in air showers with the pierre auger observatory, EPJ Web Conf. 210 (2019) 02013. doi:10.1051/epjconf/201921002013.
URL https://doi.org/10.1051/epjconf/201921002013

[40] F. Gesualdi, et al., Pierre Auger, Muon deficit in air shower simulations estimated from AGASA muon measurements (**not published yet**), unpublished (2019) 11.

[41] H. P. Dembinski, et al., EAS-MSU, IceCube, KASCADE-Grande, NEVOD-DECOR, Pierre Auger, SUGAR, Telescope Array, Yakutsk EAS Array, Report on Tests and Measurements of Hadronic Interaction Properties with Air Showers, EPJ Web Conf. 210 (2019) 02004. arXiv:1902.08124, doi:10.1051/epjconf/201921002004.

[42] R. Abbasi, et al., Pierre Auger, Telescope Array, Report of the Working Group on the Composition of Ultra High Energy Cosmic Rays, JPS Conf. Proc. 9 (2016) 010016. arXiv:1503.07540, doi:10.7566/JPSCP.9.010016.

[43] X. Bertou *et al.* (Pierre Auger Collab.), Calibration of the surface array of the Pierre Auger Observatory, Nucl. Instrum. Meth. A568 (2006) 839–846.

[44] A. Bridgeman, Determining the Mass Composition of Ultra-high Energy Cosmic Rays Using Air Shower Universality, Dissertation, Karlsruhe Institute of Technology (2018).

[45] T. K. Gaisser, A. M. Hillas, Reliability of the Method of Constant Intensity Cuts for Reconstructing the Average Development of Vertical Showers, in: Proc. 15th Int. Cosmic Ray Conf., Vol. 8, Plovdiv, Bulgaria, 1977, p. 353.

[46] A. Aab (Pierre Auger Collab.), Prototype muon detectors for the AMIGA component of the Pierre Auger Observatory, JINST 11 (02) (2016) P02012. arXiv:physics.ins-det/1605.01625, doi:10.1088/1748-0221/11/02/P02012.

[47] F. S. A. M. Botti, Characterization of AMIGA binary signals with SiPMs, Auger internal note GAP-2018-049 (2018).

[48] Ana Martina Botti (Pierre Auger Collab.), The AMIGA underground muon detector of the Pierre Auger Observatory - performance and event reconstruction, in: Proc. 36th Int. Cosmic Ray Conf., Madison, United States of America, 2019, p. 8.

[49] D. Schmidt, Sensitivity of AugerPrime to the masses of ultra-high-energy cosmic rays, Dissertation, Karlsruhe Institute of Technology (2018).

[50] A. Aab *et al.* (Pierre Auger Collab.), The Pierre Auger Observatory Upgrade - Preliminary Design Report (2016). arXiv:astro-ph.IM/1604.03637".

[51] P. Abreu *et al.* (Pierre Auger Collab.), Advanced functionality for radio analysis in the Offline software framework of the Pierre Auger Observatory, Nucl. Instrum. Meth. A635 (2011) 92–102. arXiv:1101.4473, doi:10.1016/j.nima.2011.01.049.

[52] P. Auger, Antennas for the detection of radio emission pulses from cosmic-ray induced air showers at the pierre auger observatory, Journal of Instrumentation 7 (10) (2012) P10011–P10011. doi:10.1088/1748-0221/7/10/p10011.
URL https://doi.org/10.1088%2F1748-0221%2F7%2F10%2Fp10011

[53] O. Kambeitz, Radio Detection of Horizontal Extensive Air Showers, Ph.D. thesis, KIT, Karlsruhe (2016). doi:10.5445/IR/1000055758.

[54] D. Veberič, M. Roth, Offline reference manual: Sd reconstruction, Auger internal note GAP-2005-035, an updated version is shipped with the Offline software distribution (2005).

[55] P. Lipari, The Concepts of 'Age' and 'Universality' in Cosmic Ray Showers, Phys. Rev. 79 (2008) 063001. arXiv:0809.0190.

[56] S. Lafebre, R. Engel, H. Falcke, J. Hörandel, T. Huege, J. Kuijpers, R. Ulrich, Universality of electron-positron distributions in extensive air showers, Astropart. Phys. 31 (2009) 243–254. arXiv:0902.0548.

[57] M. Ave, N. Busca, L. Cazon, F. Schmidt, T. Yamamoto, Can EPOS Reproduce the Auger SD and Hybrid Data?, Auger internal note GAP-2007-098 (2007).

[58] M. Ave, R. Engel, J. Gonzalez, D.Heck, D. Maurel, T. Pierog, M. Roth, Prediction of the tank response $S(r, \Delta X, E|\theta, \phi)$ from shower universality, Auger internal note GAP-2011-087 (2011).

[59] M. Ave, R. Engel, M. Roth, A. Schulz, A generalized description of the signal size in extensive air shower detectors and its applications, Astropart. Phys. 87 (2017) 23 – 39. doi:https://doi.org/10.1016/j.astropartphys.2016.11.008.

[60] D. Heck, R. Engel, The ehistory option of the air-shower simulation program corsika, Tech. rep., Karlsruhe Institute of Technology, 51.53.01; LK 02; Wissenschaftliche Berichte, FZKA-7495 (Oktober 2009) (2009). doi:10.5445/IR/270078292.

[61] D. Heck, J. Knapp, J. Capdevielle, G. Schatz, T. Thouw, CORSIKA: A Monte Carlo Code to Simulate Extensive Air Showers, Report FZKA 6019, Karlsruhe (1998).

[62] N. N. Kalmykov, S. S. Ostapchenko, A. I. Pavlov, Quark-gluon-string model and EAS simulation problems at ultra-high energies, Nucl. Phys. B Proc. Suppl. 52B (3) (1997) 17–28.

[63] T. Pierog, I. Karpenko, J. M. Katzy, E. Yatsenko, K. Werner, EPOS LHC: Test of collective hadronization with data measured at the CERN Large Hadron Collider, Phys. Rev. C 92 (2015) 034906. doi:10.1103/PhysRevC.92.034906.

[64] S. Argirò, S. Barroso, J. Gonzalez, L. Nellen, T. Paul, T. Porter, L. P. Jr., M. Roth, R. Ulrich, D. Veberič, The Offline software framework of the Pierre Auger Observatory, Nucl. Instrum. Meth. A580 (2007) 1485–1496. doi:http://dx.doi.org/10.1016/j.nima.2007.07.010.

[65] D. Maurel, Mass composition of ultra-high energy cosmic rays based on air shower universality, Dissertation, Karlsruhe Institute of Technology (2013).

[66] S. Mueller, Measurement of the Cosmic Ray Composition with Air Showers Detected by the AMIGA Extension at the Pierre Auger Observatory, Dissertation, Karlsruhe Institute of Technology (2018).

[67] F. Sanchez, B. Wundheiler, J. M. Figueira, D. Ravignani and M. Canziani, Timing studies for the prototype AMIGA detectors, Auger internal note GAP-2016-069 (2016).

[68] A. Aab, et al., Pierre Auger, Muon counting using silicon photomultipliers in the AMIGA detector of the Pierre Auger observatory, JINST 12 (03) (2017) P03002. arXiv:1703.06193, doi:10.1088/1748-0221/12/03/P03002.

[69] J. Hulsman, Shower universality, https://gitlab.ikp.kit.edu/shower-universality/bariloche-universality/ (2019).

[70] L. G. Dedenko, A. V. Lukyashin, T. M. Roganova, G. F. Fedorova, Testing of almost all the hadronic interaction models by comparing calculated muon energy spectrum with data, EPJ Web Conf. 208 (2019) 07004. doi:10.1051/epjconf/201920807004.

[71] T. Pierog, LHC Data and Extensive Air Shower, talk presented at ISVHECRI, Berlin, Germany (2012).

[72] S. J. Sciutto, AIRES: A System for air shower simulations. User's guide and reference manual. Version 2.2.0, User Manual (1999)arXiv:astro-ph/9911331.

[73] J. A. J. Matthews, R. Mesler, B. R. Becker, M. S. Gold, J. D. Hague, A Parametrization of Cosmic Ray Shower Profiles Based on Shower Width, J. Phys. G37 (2010) 025202. arXiv:0909.4014, doi:10.1088/0954-3899/37/2/025202.

[74] J. Abraham *et al.* (Pierre Auger Collab.), Trigger and aperture of the surface detector array of the Pierre Auger Observatory, Nucl. Instrum. Meth. A613 (2010) 29–39.

[75] C. Bleve, Atmospheric effects on extensive air showers observed with the Surface Detector of the Pierre Auger Observatory, preprint submitted to Elsevier (12 2008).

[76] B. Keilhauer, Investigation of Atmospheric Effects on the Development of Extensive Air Showers and their Detection with the Pierre Auger Observatory, Dissertation, Karlsruhe University, Karlsruhe, Germany (2003).

[77] M. Ave, R. Engel, J. Gonzalez, D.Heck, D. Maurel, T. Pierog, M. Roth, Prediction of the tank response $S(r, \mathrm{DX}, E|\theta, \phi)$ from shower universality, Auger internal note GAP-2011-087 (2011).

[78] K. Greisen, Progress in elementary particle and cosmic ray physics, Vol. 3, North-Holland Publishing, Amsterdam, 1956.

[79] L. Cazon, R. Conceicao, M. Pimenta, E. Santos, A model for the transport of muons in extensive air showers, Astropart. Phys. 36 (2012) 211–223. arXiv:1201.5294, doi:10.1016/j.astropartphys.2012.05.017.

[80] M. Ave, M. Roth, A. Schulz, A generalized description of the time dependent signals in extensive air shower detectors and its applications, Astropart. Phys. 88 (2017) 46 – 59. doi:https://doi.org/10.1016/j.astropartphys.2017.01.003.

[81] A. Schulz, Measurement of the Energy Spectrum and Mass Composition of Ultra-high Energy Cosmic Rays, Dissertation, Karlsruhe Institute of Technology (2016).

[82] R. Ulrich, J. Blumer, R. Engel, F. Schussler, M. Unger, On the measurement of the proton-air cross section using air shower data, New J. Phys. 11 (2009) 065018. arXiv:0903.0404, doi:10.1088/1367-2630/11/6/065018.

[83] T. Pierog, Air Shower Simulation with a New Generation of post-LHC Hadronic Interaction Models in CORSIKA, PoS ICRC2017 (2018) 1100. doi:10.22323/1.301.1100.

[84] A. Aab *et al.* (Pierre Auger Collab.), Muons in air showers at the Pierre Auger Observatory: Measurement of atmospheric production depth, Phys. Rev. D90 (2014) 012012. arXiv:1407.5919, doi:10.1103/PhysRevD.90.012012,10.1103/PhysRevD.90.039904.

[85] A. Castellina, Pierre Auger, AugerPrime: the Pierre Auger Observatory Upgrade, EPJ Web Conf. 210 (2019) 06002. arXiv:1905.04472, doi:10.1051/epjconf/201921006002.

[86] T. Suomijärvi, Pierre Auger, New electronics for the surface detectors of the Pierre Auger Observatory, PoS ICRC2017 (2018) 450. doi:10.22323/1.301.0450.

[87] D. Veberic, Estimation of the Total Signal in Saturated Stations of Pierre Auger Surface Detector, in: Proceedings, 33rd International Cosmic Ray Conference (ICRC2013): Rio de Janeiro, Brazil, July 2-9, 2013, 2013, p. 0633.
URL http://www.cbpf.br/%7Eicrc2013/papers/icrc2013-0633.pdf

[88] D. Ravignani, A. D. Supanitsky, D. Melo, B. Wundheiler, A method to reconstruct the muon lateral distribution with an array of segmented counters with time resolution, PoS ICRC2015 (2016) 399. arXiv:1510.01266, doi:10.22323/1.236.0399.

[89] A. D. Supanitsky, A. Etchegoyen, G. Medina-Tanco, I. Allekotte, M. G. Berisso, M. C. Medina, Underground Muon Counters as a Tool for Composition Analyses, Astropart. Phys. 29 (2008) 461–470. arXiv:0804.1068, doi:10.1016/j.astropartphys.2008.05.003.

[90] D. Veberič, Maximum-likelihood reconstruction of photon returns from simultaneous analog and photon-counting lidar measurements, Appl. Opt. 51 (2) (2012) 139–147. doi:10.1364/AO.51.000139.
URL http://ao.osa.org/abstract.cfm?URI=ao-51-2-139

[91] M. Ave, P. Bauleo, T. Yamamoto, Signal fluctuations in the auger surface detector array, Auger internal note GAP-2003-030 (2003).

[92] L. M. Bueno, P. Billoir, I. C. Maris, Signal variance for the TOTd and MoPS triggers, Auger internal note GAP-2014-035 (2014).

[93] R. Hiller, M. Roth, An update on the signal accuracy using the infill array, Auger internal note GAP-2012-012 (2012).

[94] B. Wundheiler, Pierre Auger, The AMIGA Muon Counters of the Pierre Auger Observatory: Performance and Studies of the Lateral Distribution Function, PoS ICRC2015 (2016) 324. doi:10.22323/1.236.0324.

[95] Z. Zong, Pierre Auger, First results from the AugerPrime engineering array, PoS ICRC2017 (2018) 449. doi:10.22323/1.301.0449.

[96] A. W. D. Supanitsky, M. Zha, Fluctuations in Pulse Shape, Auger internal note GAP-2005-015 (2005).

[97] L. Collica, Pierre Auger, Measurement of the Muon Production Depths at the Pierre Auger Observatory, Eur. Phys. J. Plus 131 (9) (2016) 301. arXiv:1609.02498, doi:10.1140/epjp/i2016-16301-6.

[98] F. James, Minuit Reference Manual, CERN Program Library Office CERN-IT Division CH-1211 Geneva 23 Switzerland (1998).

[99] R. Brun, F. Rademakers, ROOT: An object oriented data analysis framework, Nucl. Instrum. Meth. A389 (1997) 81–86. doi:10.1016/S0168-9002(97)00048-X.

[100] E. Varela, Pierre Auger, The low-energy extensions of the Pierre Auger Observatory, J. Phys. Conf. Ser. 468 (2013) 012013. doi:10.1088/1742-6596/468/1/012013.

[101] D. Ravignani, The formulas of the angular resolution, Auger internal note GAP-2017-003 (2017).

[102] C. Bonifazi *et al.* (Pierre Auger Collab.), The angular resolution of the Pierre Auger Observatory, Nucl. Phys. Proc. Suppl. 190 (2009) 20–25, arXiv astro-ph/0901.3138. doi:10.1016/j.nuclphysbps.2009.03.063.

[103] D. C. Hoaglin, F. Mosteller, J. W. Tukey, Understanding Robust and Exploratory Data Analysis, John Wiley and Sons, 1983.

[104] F. Fenu, Pierre Auger, The cosmic ray energy spectrum measured using the Pierre Auger Observatory, PoS ICRC2017 (2017) 9–16[PoSICRC2017,486(2018)]. doi:10.22323/1.301.0486.

[105] M. Mallamaci, Pierre Auger, Measurements of the depth of maximum muon production and of its fluctuations in extensive air showers above $1.510^{19} eV$ at the Pierre Auger Observatory, PoS ICRC2017 (2018) 509, [,73(2017)]. doi:10.22323/1.301.0509.

[106] A. Aab, et al., Pierre Auger, Highlights from the Pierre Auger Observatory, PoS ICRC2017 (2018) 1102, [35,1102(2017)]. arXiv:1710.09478, doi:10.22323/1.301.1102.